
**Derivation of Effective Models using Self-Similar
Continuous Unitary Transformations in Real Space**

Inaugural-Dissertation
zur
Erlangung des Doktorgrades
der Mathematisch-Naturwissenschaftlichen Fakultät
der Universität zu Köln

vorgelegt von
Alexander Antonius Reischl
aus Pforzheim

2006

Berichterstatter:

Prof. Dr. G.S. Uhrig

Prof. Dr. E. Müller-Hartmann

Vorsitzender der Prüfungskommission: Prof. Dr. M. Braden

Tag der mündlichen Prüfung:

2. Juni 2006

Contents

1. Introduction	9
2. Self-similar continuous unitary transformations in real space	13
2.1. CUTs: general concept	13
2.2. Generators	15
2.2.1. Wegner's generator	15
2.2.2. Mielke-Knetter-Uhrig generator	16
2.2.3. Example: Two-level problem	19
2.3. Self-similar CUTs in real space	22
2.3.1. Physical motivation	23
2.3.2. Setup of the flow equations	24
2.3.3. Formulation with local operators	25
2.3.4. Transformation of the Hamiltonian	28
2.3.5. Transformation of observables	30
2.4. Different unitary transformations	32
2.5. Implementation on a computer	34
2.5.1. Program and data structures	34
2.5.2. Symmetries	35
2.5.3. Calculation of the flow equation	36
2.5.4. Numerical solution of the differential equation	41
2.6. Summary	42
3. Effective t-J-model derived from the Hubbard model	43
3.1. Fermionic Hubbard model	44
3.2. Method	47
3.2.1. Reference ensemble	48
3.2.2. Two explicit examples for self-similar CUTs in real space	49
3.2.3. Comparison to perturbation theory	52
3.2.4. Comparison of different unitary transformations	54
3.2.5. Higher truncation schemes	57
3.3. Results	60

3.3.1. Properties of the CUT	61
3.3.2. Effective model	67
3.4. Discussion	76
3.5. Summary and outlook	78
4. One-dimensional spin systems	81
4.1. Spin ladder	81
4.1.1. Method	83
4.1.2. Dispersion	86
4.1.3. Two-triplon continuum and bound states	94
4.1.4. Multi-triplon continua	98
4.1.5. Discussion	100
4.2. Spin chain	102
4.2.1. Model and method	102
4.2.2. Dispersion	109
4.2.3. Spectral weight	114
4.3. Summary and outlook	117
5. Bosonic atoms in an optical lattice	119
5.1. Bosonic Hubbard model	120
5.1.1. Non-interacting approximation	123
5.1.2. CUT treatment	125
5.1.3. Dispersion and phase diagram	129
5.2. Experiment and relevant observable	133
5.3. Spectral weights at zero and finite temperature	137
5.3.1. Finite temperature	140
5.3.2. Results	144
5.4. Entropy	145
5.4.1. Entropy in a harmonic trap	146
5.4.2. Tonks-Girardeau regime	146
5.4.3. Reliability of the approximation for finite temperatures	148
5.4.4. CUT treatment	150
5.5. Discussion	154
5.6. Summary and outlook	155
6. Summary	157
6.1. Outlook	159
A. The Lanczos technique	161
A.1. Liouville formulation of the Lanczos technique	162

B. Entropy of bosons in a three-dimensional harmonic oscillator and in the Tonks-Girardeau regime	163
References	167
Abstract	175
Zusammenfassung	177
Danksagung	179
Erklärung	181
Teilpublikationen	181
Lebenslauf	183

1. Introduction

The development of quantum mechanics in the beginning of the last century has led to important progress in the understanding of the physical behavior of solids. Especially the electronic properties of solids are governed by quantum mechanics to a large extent. Many insights can already be gained by treating the electrons as independent particles. The electronic contribution to the specific heat and the occurrence of energy bands can be explained in this way to mention but two effects. Including the interactions of the electrons in an average way and using still a one-particle description yields an excellent description of most band structures in real crystals [1].

The phenomenology of real crystals is much richer than what can be explained within a one-particle description. Superconductivity and in particular the properties of the high- T_c materials cannot be explained without the interaction of the particles. The Mott transition between an insulator and a metal is also due to interactions. Also the magnetic behavior of solids is governed by the correlation of the electrons in the crystal to a large extent. Already these examples show that an appropriate theory of many solids has to deal with the correlations of electrons. In particular, strong correlations lead to a great variety of phenomena that are observed in the phase diagrams of solid matter. This explains the need for a quantum theory of strongly correlated many-body systems.

The complexity found in correlated materials poses a formidable challenge to theoretical physics. In most cases a detailed description of a certain material is too complicated. Therefore, theoretical solid state physics studies the behavior of paradigmatic models. These models are simplifications of the true Hamiltonian of the material or the class of materials of interest. However, they contain the relevant contributions to describe many of the physical effects qualitatively.

The paradigmatic model for correlated electrons is the Hubbard model. The complicated Hamiltonian of the crystal is reduced to a model containing only a single localized orbital. Electrons are allowed to hop between neighboring sites. On the same site they strongly repel each other. The local interaction accounts for the screened electron-electron interaction. The competition between kinetic and interaction energy is at the basis of many phenomena found in strongly correlated materials. The Hubbard model is assumed to describe at least parts of this phenomenology because it contains these two important ingredients in a simplified form. Although being very simple this model is very hard to solve. Exact solutions are only possible in one or infinite dimensions [2, 3].

The Heisenberg model is among the most important models to describe magnetism. It can be

derived from the Hubbard model for half filling as an effective model describing only the magnetic degrees of freedom. The Hilbert space is reduced to the subspace with lowest energy. The degrees of freedom that describe the charge dynamics are neglected. The interactions between the spins of the electrons are created by virtual charge excitations. Thus, the Heisenberg model deals only with the magnetic interaction of localized magnetic moments. An exact solution can only be found in one or infinite dimensions.

A main purpose of quantum many-body theory is to develop techniques to solve these and other models. The aim is to understand the materials behind the models. At present, there exists a set of well established techniques in many body theory. Green's function methods [4] rely on the calculation of the propagators or susceptibilities. They can be applied in a perturbative way or by a systematic resummation of selected diagrams to infinite order. The aim is the direct calculation of the Green's function which describes the propagation of a particle in the system. Also susceptibilities can be calculated in this way. Starting from a Hamiltonian the method provides results that are frequency dependent.

Another very successful approach in many-body theory is the renormalization group [5]. It has been originally applied in the description of critical phenomena. It focuses on low energy properties and is therefore especially useful to determine the phase diagram. The renormalization group has been introduced originally to treat collective bosonic degrees of freedom. In solid state physics many phenomena are based on the fermionic behavior of the constituents. The low energy behavior of electrons is strongly influenced by the existence of a Fermi surface. In recent years the renormalization group has been generalized to fermionic degrees of freedom [6–9]. This approach is known under the name of "functional renormalization group". In the case of strongly correlated systems the renormalization flow often leads to divergent behavior of the couplings. Whereas the phase diagram can be determined in a reliable way, the divergence of coupling constants hinders a quantitative interpretation of the results in the symmetry broken phase. The continuation of the flow into the symmetry broken phase is the topic of current research [10]. Renormalization group methods focus on the low energy excitations of the system.

Another approach to many-body systems are numerical methods. In many cases numerical methods are the first means to obtain information about a complex system. Even for complicated Hamiltonians numerical analysis yields exact results. The calculations are only restricted by the computing resources at hand. A drawback of numerical results is that they sometimes allow only limited insight into the mechanisms that produce the physical behavior.

Our understanding of correlated systems is far from being complete. There is a strong need for new methods that complement the existing ones. The objective of this thesis is to investigate a relatively new method, namely continuous unitary transformations (CUTs) [11–15]. The basic idea is to construct an effective Hamiltonian systematically that describes the original system. The technical tool for this task is to set up a differential equation describing the evolution of a set of couplings that are chosen to describe the system. The original and the effective Hamiltonian are linked by a unitary transformation. Unitary transformations have been used to derive effective models for a long time. The CUT method puts the derivation of the effective

model on a systematic basis.

The above mentioned methods are well-established in quantum many-body theory. They have accumulated an impressive amount of results. The CUT is of course not meant to supersede these methods. But, the method of CUTs can complement these approaches in some aspects. It is an advantage that the CUTs yield an effective Hamiltonian. This effective Hamiltonian allows further calculations. This is not possible for example for the above mentioned Green's function methods. The CUT describes processes on all energy scales. It does not focus on very low energies like renormalization group approaches. It allows insight into the relevant processes determining the physical behavior. The effective Hamiltonian is given in terms of certain quasiparticles. Their properties can be analyzed within the one-, two- and higher particle sectors. The method shows how the final physical behavior is generated. The CUTs give also access to the description of observables. This is indispensable if one finally aims at the explanation of experimental results.

The aim of the present thesis is to make a methodological investigation of a special realization of the CUT method. We apply the CUT in a self-similar fashion just as it has been done in the original work by *Wegner* [11]. This means that the coefficients of operators in the CUT scheme are not given by a perturbative expansion but renormalized according to the differential equation that defines the CUT. The set of operators in the CUT has to be restricted to keep the method numerically tractable. In this thesis the couplings to describe the effective model are chosen according to their locality. The local approach is very common in solid state physics. The paradigmatic models like the Hubbard and Heisenberg model for strong correlations are phrased in terms of operators that deal with localized Wannier orbitals.

The aim of the transformation is to map the given Hamiltonian onto an effective Hamiltonian which is in some sense easier to treat. The use of the Mielke-Knetter-Uhrig (MKU) generator [12, 13] is an important ingredient to simplify the structure of the effective Hamiltonian. The CUT in the MKU scheme ensures that the effective Hamiltonian is quasiparticle number conserving. This makes the effective Hamiltonian easily amenable to numerical techniques like Lanczos diagonalization.

The present approach is a novel realization of the CUT technique. Therefore, we present the method and its central concepts in detail and discuss the physical motivation of this approach. The transformation of the Hamiltonian and of observables is discussed. The diagonalization of the Hamiltonian gives insight in the energy properties of the system. The study of observables is necessary to understand experimental results that usually probe the system with a certain observable. To check the reliability of the method we compare its results to perturbative CUT calculations and other methods. We will not only reproduce known results but we will also calculate new ones to underline the efficiency of this method.

Thesis overview

The next chapter, Chap. 2, is devoted to the presentation of the method. Important points of the concept are discussed in this chapter. The need for a truncation scheme is explained. The notion of a reference state and the extension of operators are introduced. These concepts are necessary to define the truncation scheme. Various generators are studied. The MKU generator is used mostly in this thesis. Its properties, in particular the relation to the quasiparticle concept, are described. This section defines how the Hamiltonian and observables are transformed according to the CUT scheme. To this end a simple example and the implementation of this technique on a computer are described in detail.

Chapter 3 deals with the Hubbard model. There, the CUT method is used to map the Hubbard model onto an effective Hamiltonian that conserves the number of double occupancies. The effective model is a generalized t - J model. A worked-out example gives insight into the functioning of the method. The conditions necessary to carry out the transformation are studied and the coefficients of the effective model are presented.

The Heisenberg model in one dimension is studied in Chapter 4. It is applied to two different geometries, namely ladders and chains. The Heisenberg model on the ladder is treated for intermediate and large ratios of the leg and the rung coupling. The dispersion and two-particle properties including bound states are calculated. For the isotropic Heisenberg ladder the convergence of the transformation becomes an issue. It leads us to the study of multi-particle continua. The overlap of continua of different quasiparticle number plays a crucial role in the question if the transformation is physically reasonable and possible. For the spin chain we calculate the one-particle energies for various values of the dimerization. An observable is transformed and the results for the respective spectral weights are discussed.

Chapter 5 applies the CUTs to the bosonic Hubbard model. Very recently this model has found an artificial realization in atom traps [16, 17]. This has spurred the research on the bosonic version of the Hubbard model. The chapter concentrates on the explanation of absorption experiments performed on atom gases in traps. The observable describing the experimental situation is transformed and the corresponding spectral weights are calculated. The experimental result of large spectral weight at high energies is explained by considering the effect of finite temperatures in the trap. These findings are further corroborated using thermodynamic considerations. The last chapter summarizes the results.

2. Self-similar continuous unitary transformations in real space

Continuous unitary transformations (CUTs) are a way to systematically derive effective Hamiltonians for many-body problems. The underlying concept of an optimally chosen change of basis is intuitive. The CUT used in this thesis are non-perturbative and self-similar. The choice of a suitable generator of the transformation is central in the setup of the flow equation.

The generator that is mostly applied in this thesis is the so-called MKU generator. It allows to construct a quasiparticle number conserving effective Hamiltonian. The structure of the Hamiltonian imposed by the quasiparticle concept is of crucial importance for the construction and the analysis of the effective Hamiltonian.

The second important ingredient in the construction of a CUT is the truncation scheme. Regarding this point, the guiding idea in this work is to encode the effective Hamiltonian in operators that are as local as possible. This results in a self-similar realization of the flow equation. The effective Hamiltonian is incorporated in operators that are chosen mainly by their locality.

This section is organized as follows. Section 2.1 explains the general properties of CUTs. The properties of the Wegner and the MKU generator are discussed in Sec. 2.2. A central part of the thesis is Section 2.3. There, the method is described. The discussion is focused on the version of the CUT that is used throughout the thesis. A physical motivation of the particular approach is given and the method is explained in detail. The following Section, Sec. 2.5, presents technical details of the implementation on a computer. A summary is given in Sec. 2.6.

2.1. CUTs: general concept

The subject of this thesis is the method of continuous unitary transformations (CUTs). The method has been introduced by *Wegner* [11] and independently by *Glazek* and *Wilson* [18, 19]. This section introduces CUTs in general. Later on, the discussion will specialize on the variant of CUTs that is used in this work, namely self-similar CUTs in real space.

Unitary transformations are widely used in physics to map a given problem to an effective Hamiltonian which is simpler, i. e. closer to diagonality. The original problem shall be given in the form of a Hamiltonian H , the effective Hamiltonian is denoted by H_{eff} . In a one-step transformation the mapping of H onto H_{eff} is done with a single unitary transformation operator

U

$$H_{\text{eff}} = U H U^{-1}. \quad (2.1.1)$$

Since a unitary transformation realizes a change of basis the Hamiltonian H and the effective Hamiltonian H_{eff} have the same eigenvalues. There are many successful applications of such one-step unitary transformations. Examples in condensed matter physics include Fröhlich's [20] derivation of an effective electron-electron interaction by eliminating the electron-phonon interaction, the Schrieffer-Wolff transformation [21] to map the Anderson model onto the Kondo model and the derivation of low energy effective models for the Hubbard model [22–24].

The concept of a one-step transformation is now generalized to a continuous unitary transformation. The Hamiltonian is considered to depend on the flow parameter l . Its transformation is governed by the flow equation

$$\frac{\partial H(l)}{\partial l} = [\eta(l), H(l)]. \quad (2.1.2)$$

The flow of the Hamiltonian is generated by the anti-hermitian operator $\eta(l)$. The anti-hermiticity of the generator $\eta(l)$ ensures that the transformation of $H(l)$ is unitary. The original Hamiltonian fixes the initial condition of Eq. (2.1.2)

$$H(l = 0) = H. \quad (2.1.3)$$

The flow equation Eq. (2.1.2) produces a whole set of unitarily equivalent Hamiltonians $H(l)$. For all values of l the transformed Hamiltonian $H(l)$ can be used as an effective Hamiltonian for the initial problem. Usually, the flow equation is integrated up to $l = \infty$ and the corresponding $H(\infty)$ is referred to as the effective Hamiltonian

$$H(l = \infty) = H_{\text{eff}}. \quad (2.1.4)$$

The continuous realization of the unitary transformation can be superior to one-step transformations. The transformation is permanently adjusted to the flowing Hamiltonian. This leads to effective Hamiltonians that have less singular interactions than those found by single step transformations [25].

The aim of the transformation is an effective Hamiltonian which is in some respect simpler than the original problem. For typical generators this is indeed the case. If one inspects Eq. (2.1.2) one recognizes that the transformation stops if the generator η and the Hamiltonian H commute

$$[\eta(\infty), H(\infty)] = 0. \quad (2.1.5)$$

This is only the case if the Hamiltonian has a definite structure. The transformation brings the Hamiltonian closer to diagonality. The detailed properties of the effective Hamiltonian will depend on the choice of the generator.

In basic quantum-mechanics one often exploits the fact that the Hamiltonian commutes with another operator. Then, one can find a common eigenbasis for the operators. One can classify the eigenstates of the Hamiltonian by the quantum numbers of the other operator. The Hamiltonian is already block-diagonal with respect to the quantum numbers of this operator. The situation is

somewhat different in Eq. (2.1.2) because the generator is an anti-hermitian operator. However, we will also find that the effective Hamiltonian is structured by the relation in Eq. (2.1.5).

Like in any change of basis all operators and hence also observables have to be subjected to the same transformation. The flow equation for an observable \mathcal{O} reads

$$\frac{\partial \mathcal{O}(l)}{\partial l} = [\eta(l), \mathcal{O}(l)]. \quad (2.1.6)$$

While the transformation will simplify the Hamiltonian this is not the case for the observable. The observable will generally become more complicated. However, the effective observable can also be classified according to the structure which is imposed on the Hamiltonian. This will be further explained in Sec. 2.3.5.

The method of CUTs has been invented more than ten years ago and has been applied to various systems. At this point we want to highlight some references that are connected to the self-similar approach in real space which is the topic of the present thesis. This list of references cannot be exhaustive. For further references we refer to two overview articles by *Wegner* [14, 15]. The different approaches to CUTs can be grouped into perturbative and self-similar treatments. Perturbative treatments of CUTs are presented in Refs. [13, 26–33]. Their relation to the present approach is described in Sec. 3.2.3. A self-similar truncation scheme is used in Refs. [31, 34–40]. The method has been applied to a wide range of systems. These include the Hubbard model (see Refs. [26, 39, 40]) and one-dimensional spin models (see Refs. [13, 41, 42] and references therein) which are both also treated in the present thesis. Also many other systems have been the subject of CUT studies, e. g. the Lipkin-Meshkov-Glick model [31–33] or impurity models Refs. [36, 43–46], to mention only two.

2.2. Generators

The transformation depends crucially on the choice of the generator η . The aim of the transformation is to bring the Hamiltonian closer to diagonality. Then, the problem is easier tractable than the starting Hamiltonian. If full diagonalization is not feasible also partial diagonalization can be a decisive step towards the solution. Partial diagonalization of the Hamiltonian means the decoupling of certain sectors of the Hilbert space.

Here, two generators are presented, namely the generator originally introduced by *Wegner* and the MKU generator. It is also possible to use other generators or variants of the two above mentioned generators. In addition, one can use different generators, one after the other. The result of a first transformation is an effective Hamiltonian. One can use this Hamiltonian as the starting point for a second transformation with another generator.

2.2.1. Wegner's generator

In Wegner's original scheme [11] the Hamiltonian is split into a diagonal part H_d and a non-diagonal part H_{nd}

$$H = H_d + H_{nd}. \quad (2.2.7)$$

The splitting of the Hamilton operator into a diagonal part H_d and a non-diagonal part H_{nd} is not unique. There is a freedom to define which operators are said to be diagonal and which are not [14]. The generator η_W is

$$\eta_W(l) = [H_d(l), H_{nd}(l)] = [H_d(l), H(l)] \quad (2.2.8)$$

and thus the flow equation is

$$\frac{\partial H(l)}{\partial l} = [\eta_W(l), H(l)] = [[H_d(l), H_{nd}(l)], H(l)]. \quad (2.2.9)$$

The right-hand side of the flow equation vanishes if $H_d(l)$ commutes with $H_{nd}(l)$.

The transformation induced by η_W is quite robust. It has been shown that the choice of η_W as the generator will lead to diagonalization up to degenerate subspaces. This applies to finite [11] as well as to infinite matrices [31]. Formally, the Wegner generator solves the problem. However, in an actual calculation it is possible only in rare cases to take into account all operators that appear in the flow equation. The set of operators has to be truncated. In such a situation the choice of η_W might not be optimal.

2.2.2. Mielke-Knetter-Uhrig generator

This section describes the CUT using the generator introduced by *Mielke* [12] and *Knetter* and *Uhrig* [13]. The fundamental idea is to use a counting operator Q in the definition of the generator. The operator Q counts the number of quasiparticle excitations. In the following the CUT approach based on this idea will be labeled with the abbreviation ‘‘MKU’’ standing for Mielke, Knetter and Uhrig. The quasiparticle number will be the fundamental quantity to organize the problem in the MKU approach. The choice of the quasiparticle has to be motivated by the physical situation. If a system can be successfully described in terms of this quasiparticle depends decisively on this choice. The analysis of the spectral weight in channels with low quasiparticle number allows to judge the appropriateness of the quasiparticle picture.

The MKU generator η_{MKU} is defined using an eigenbasis of Q via its matrix elements [13]

$$(\eta_{MKU}(l))_{i,j} = \text{sgn}(q_i - q_j) H_{i,j}(l), \quad (2.2.10)$$

where sgn is the sign-function. The use of an eigenbasis of Q allows to assign the eigenvalue q_i to each state i . An operator in H commuting with Q does not contribute to η_{MKU} . On the other hand, operators not commuting with Q contribute to η_{MKU} . The flow equations using the MKU generator have been shown to converge for finite matrices [13]. The transformation leads to an effective Hamiltonian commuting with Q

$$[H_{\text{eff}}, Q] = 0. \quad (2.2.11)$$

This means that subspaces of different eigenvalues of q_i are decoupled. Typically, there exists a maximum number n by which the number of quasiparticles can be changed by the action of the

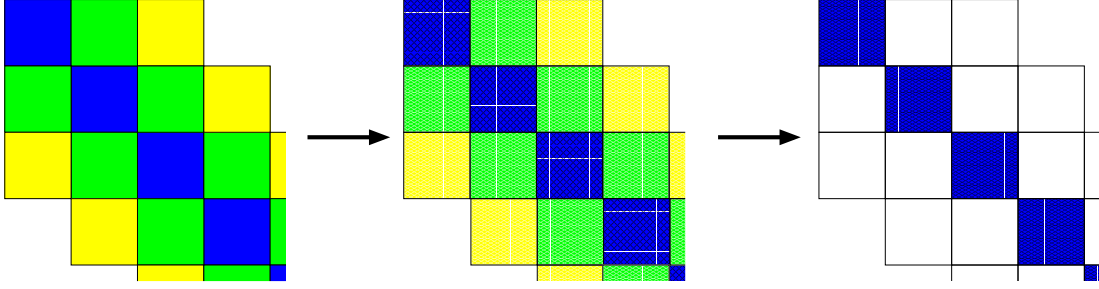


Fig. 2.1: The MKU-generator preserves the block-band structure of the Hamiltonian during the flow. On the left a schematic picture of the initial Hamiltonian is shown. It gets renormalized during the flow. The transformation finally yields the effective Hamiltonian on the right. The final Hamiltonian is block-band diagonal. The blocks group different terms with a definite action on the number of quasiparticles.

Hamiltonian. The initial Hamiltonian has a block-band structure. The MKU generator preserves this block-band structure [12, 13, 29]. The conservation of the block-band structure is illustrated in Fig. 2.1. The number n which limits the change of the number of quasiparticles for the initial Hamiltonian also holds for the flowing Hamiltonian $H(l)$. When full block-diagonalization is achieved for $l = \infty$ the effective Hamiltonian does not change the number of quasiparticles any more. The effective Hamiltonian is block-diagonal.

The conservation of block-band diagonality is an important feature of the MKU generator. It reduces the number of operators that are involved during the flow. It also imposes a constraint on their structure. In view of an actual calculation this is a clear advantage.

The effective Hamiltonian conserves the number of quasiparticles. This observation is essential for the method of MKU flow equations. The problem to solve H_{eff} at the end is simplified by this quasiparticle conservation. The groundstate of the effective problem is the quasiparticle vacuum. The one-particle subspace is separated from the remaining Hilbert space. Its diagonalization yields the one-particle energies. Generally, all n -particle sectors can be treated separately as the transformation achieves block-diagonality. A mathematically detailed discussion of the structure of the effective Hamiltonian can be found in Ref. [29].

It is useful to use the language of the counting operator for the whole formalism of the CUT. Not only the effective Hamiltonian at the end of the flow but also the flowing Hamiltonian is most conveniently described using the quasiparticle number. It is therefore useful to separate the operators in the Hamiltonian according to their effect on the quasiparticle number. If an operator creates i quasiparticles and annihilates j it is said to belong to the $\{i, j\}$ -block.

A picture illustrating the structure of the Hamiltonian is shown in Fig. 2.2. The structure is given by the action of the operators in the Hamiltonian on the quasiparticle number. The terms in the Hamiltonian are grouped into blocks that create and annihilate a definite number of quasiparticles. The terms in the $\{0, 0\}$ -block create and destroy zero quasiparticles. For a system with a unique groundstate the $\{0, 0\}$ -block is just a single constant, namely the groundstate

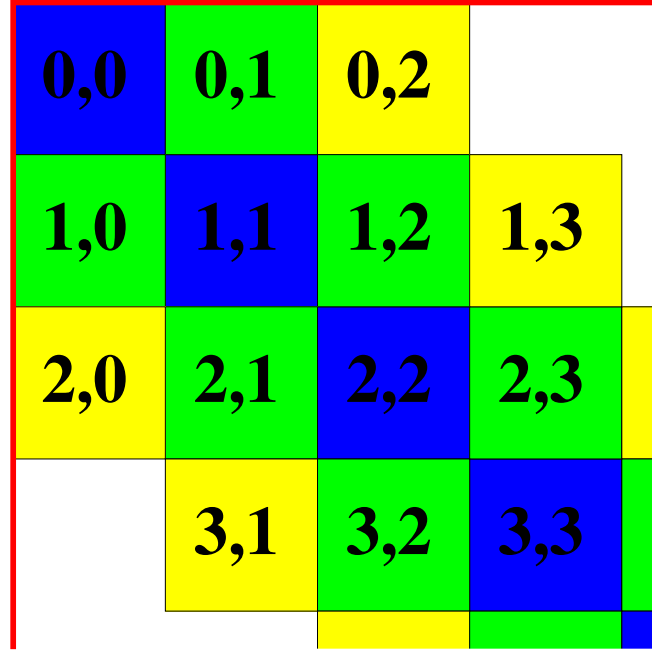


Fig. 2.2: Block-structure of the Hamiltonian. Here, the case of a Hamiltonian changing the quasiparticle number by at most 2 is shown.

energy. Operators that create quasiparticles out of the vacuum belong to $\{n, 0\}$ -blocks. In Fig. 2.2 a Hamiltonian is sketched that changes the number of quasiparticles by at most 2. The one-particle dispersion is given by operators in the $\{1, 1\}$ -block, interactions of two particles are in the $\{2, 2\}$ -block, and so on.

Note that the illustration in Fig. 2.2 should be viewed as a scheme organizing the structure of the Hamiltonian rather than a large matrix. For example, the terms belonging to the $\{1, 1\}$ -block do not only act on one-particle states. They annihilate the vacuum, but they do not annihilate states with more than one particle. Therefore, they have to be taken into account when diagonalizing the two-particle sector. This is evident in the formalism of second quantization. It is just restated here to avoid confusion in the presentation of the quasiparticle structure of the Hamiltonian.

The quasiparticle concept is also important for the solution of the effective Hamiltonian H_{eff} . The operator H_{eff} commutes with Q . It is diagonal up to subspaces with fixed quasiparticle number. For a non-degenerate ground state the $\{0, 0\}$ -block is just the energy of the groundstate. Generally, the derivation of H_{eff} has turned the original problem into a few-body problem. This has to be contrasted with the many-body problem one usually starts with. The n -particle sector can be solved within this subspace handling only n particles. It is much easier to deal with a two-particle problem than to deal with a many-body problem, even though the two-particle

interaction becomes complicated.

All observables of interest have to be transformed with the same transformation. At the end of the flow, the observables do not conserve the particle number in general. They create or destroy particles in the system. The action of the observables can be classified according to the change of the number of quasiparticles [30, 47, 48]. At zero temperature one has to consider only those operators which do not annihilate the ground state. Also the calculation of spectral quantities like spectral densities and spectral weights can be classified according to the number of quasiparticles involved.

The CUT using the MKU generator reformulates the Hamiltonian in the effective quasiparticle description. The computational effort to describe many-particle subspaces increases drastically with the particle number. The reason is that the number of terms that have to be taken into account increases. Typically, the sectors with low numbers of quasiparticles can be described with sufficient accuracy. These are the zero-, one- and two-particle subspaces. Also higher subspaces can be treated [49], however only with increasing efforts. The quasiparticle picture is most appropriate if the system can be described by the sectors with low quasiparticle numbers. For a certain observable under study it can be checked how much of the physics is contained in the n -particle sector. As the observable is classified according to its action on the number of quasiparticles one can calculate the n -particle spectral weights. If a large part of the total spectral weight is contained in the lowest sectors the effective picture is appropriate. It describes the physics of the system under study. Sum rules can be used to check how much of the total weight is described by a certain quasiparticle sector. In actual calculations it is advisable to use sum rules to check the quality of the applied quasiparticle picture.

A particular property of MKU flow equations is that they sort the eigenvalues in ascending order of the quasiparticle number of the corresponding eigenvector [12, 13]. The quasiparticle number is measured with the counting operator Q . The example presented in the next section illustrates this fact. This property of MKU flows can lead to convergence problems. If the initial Hamiltonian has a sequence of multi-particle continua that are not ordered energetically with respect to the number of quasiparticles it can be impossible to reorganize the Hilbert space such that the energy levels are sorted according to the eigenvalues of Q . This issue will have to be discussed in the applications that are treated in the following chapters.

2.2.3. Example: Two-level problem

In this section the two-level problem is considered using CUTs. It is intended to illustrate some of the concepts discussed so far. It also shows the difference between the MKU and Wegner generator. The discussion of the two-level problem with a slightly different focus can also be found in Ref. [31].

The two-level problem in the language of a system with a single spin 1/2 reads

$$H_2 = E\mathbf{1}_2 - \frac{\omega}{2}\sigma^z + \frac{a}{2}\sigma^x \quad (2.2.12a)$$

$$= \begin{pmatrix} E - \frac{\omega}{2} & \frac{a}{2} \\ \frac{a}{2} & E + \frac{\omega}{2} \end{pmatrix}. \quad (2.2.12b)$$

Here, the σ^i are the Pauli matrices. The model contains an absolute energy constant E . The level spacing is ω . The size of the off-diagonal term is given by a . The CUT is now used to eliminate the off-diagonal term and thus to diagonalize the Hamiltonian.

MKU generator

For the MKU approach the counting operator is chosen to be

$$Q = (\mathbf{1} - \sigma^z)/2 = \begin{pmatrix} 0 & 0 \\ 0 & 1 \end{pmatrix}. \quad (2.2.13)$$

The first state is the quasiparticle vacuum since it has quasiparticle number $q_1 = 0$. For the second state, the number of quasiparticles is $q_2 = 1$. Thus, the MKU generator reads

$$\eta_{\text{MKU}}(l) = \text{sgn}(q_i - q_j) H_{i,j}(l) = -\frac{a(l)}{2} i\sigma^y = \begin{pmatrix} 0 & -\frac{a(l)}{2} \\ \frac{a(l)}{2} & 0 \end{pmatrix}. \quad (2.2.14)$$

From

$$\frac{\partial H(l)}{\partial l} = [\eta(l), H(l)] = -\frac{a(l)^2}{2}\sigma^z - \frac{\omega(l)a(l)}{2}\sigma^x \quad (2.2.15)$$

one reads the flow equations by comparing the coefficients on the left- and right-hand side. The flow equations close. They read

$$\partial_l E(l) = 0 \quad (2.2.16a)$$

$$\partial_l \omega(l) = a(l)^2 \quad (2.2.16b)$$

$$\partial_l a(l) = -\omega(l)a(l). \quad (2.2.16c)$$

The right-hand side of the flow equation is bilinear. The equations are solved by observing that $a(l)^2 + \omega(l)^2$ is a conserved quantity. Since convergence is proven for finite matrices we know that $a(\infty) = 0$ and therefore

$$\omega_{\text{MKU}}^{\text{eff}} = \omega(\infty) = \sqrt{\omega(0)^2 + a(0)^2}. \quad (2.2.17)$$

The eigenstate with $q_1 = 0$ has energy $E - \omega_{\text{eff}}/2$ and the eigenstate with $q_1 = 1$ has energy $E + \omega_{\text{eff}}/2$. Solving the differential equation explicitly yields the l -dependence of the coefficients $\omega(l)$ and $a(l)$. The solution reads

$$\omega(l) = \omega(\infty) \tanh \left(\omega(\infty)l + \text{arctanh} \left(\frac{\omega(0)}{\omega(\infty)} \right) \right), \quad (2.2.18)$$

$$a(l) = \text{sgn}(a(0))\omega(\infty) \sqrt{1 - \tanh^2 \left(\omega(\infty)l + \text{arctanh} \left(\frac{\omega(0)}{\omega(\infty)} \right) \right)}, \quad (2.2.19)$$

where sgn is the sign-function. The explicit solution confirms the exponential decay of the off-diagonal element $a(l)$ for large values of the flow parameter.

Wegner's generator

The problem can also be solved using Wegner's generator. The diagonal part is $H_d = E\mathbf{1}_2 - \frac{\omega}{2}\sigma^z$ and thus the generator reads

$$\eta_W = -\frac{a(l)\omega(l)}{2}i\sigma^y. \quad (2.2.20)$$

The flow equations read

$$\partial_l E(l) = 0 \quad (2.2.21a)$$

$$\partial_l \omega(l) = w(l)a(l)^2 \quad (2.2.21b)$$

$$\partial_l a(l) = -\omega(l)^2 a(l). \quad (2.2.21c)$$

They are cubic in the coefficients. Again, $a(l)^2 + \omega(l)^2$ is a conserved quantity. The Wegner flow equations are the same as the MKU flow equations up to a rescaling by $\omega(l)$. Therefore, one finds for the effective Hamiltonian

$$\omega_W^{\text{eff}} = \omega(\infty) = \text{sgn}(\omega(0))\sqrt{w(0)^2 + a(0)^2}. \quad (2.2.22)$$

Comparison

Both approaches solve the problem. However, the sorting property of η_{MKU} leads to a different sequence of the eigenstates for negative values of $\omega(0)$. In the MKU solution, the first state with $q_1 = 0$ has energy $E - \omega_{\text{eff}}/2$ and the state with $q_1 = 1$ has energy $E + \omega_{\text{eff}}/2$. The eigenvalues are sorted according to the quasiparticle number. The value of $\omega(\infty)$ is always positive.

In the Wegner approach $\omega(\infty)$ has the same sign as $\omega(0)$. The eigenvalues are not sorted. The off-diagonal term $a(l)$ is a monotonic decaying function as the right-hand side of Eq. (2.2.21c) has always the opposite sign of $a(l)$.

On the contrary, the behavior of $a(l)$ in the MKU approach can be non-monotonic. This is the case if $\omega(0)$ is negative. Then, the energies are in the wrong order according to the quasiparticle number of the states. The coefficients $a(l)$ and $\omega(l)$ in the MKU-scheme are shown in Fig. 2.3 for various values of $\omega(0)$. For all values of $\omega(0)$ the coefficient $a(l)$ approaches zero for large values of the flow parameter. The flow equations converge.

A monotonic decrease of $a(l)$ is found for positive $\omega(0)$. If $\omega(0)$ is negative the off-diagonal term displays non-monotonic behavior. The coefficient $a(l)$ has a maximum. The value of the maximum increases with increasing modulus $\omega(0)$. The eigenvalues are sorted according to the quasiparticle number. As long as $\omega(l) \leq 0$ the value of $a(l)$ increases. As soon as $\omega(l)$ is positive the correct order of levels is reached. Then, the off-diagonal term becomes smaller.

In more general many-body problems this behavior is also found. The reordering of energies according to their quasiparticle number will make the transformation more difficult or will even

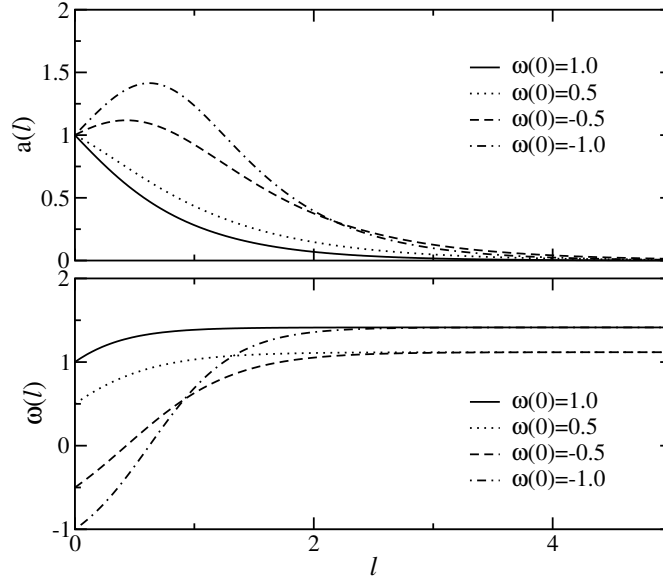


Fig. 2.3: Evolution of $a(l)$ and $\omega(l)$ in the flow for the MKU generator. The parameters are $a(0) = 1$ and $\omega(0) \in \{1, 0.5, -0.5, -1\}$. Non-monotonic behavior of $a(l)$ is found for negative values of $\omega(0)$. For $\omega(0) \leq 0$ the maximal value of the off-diagonal element $a(l)$ increases with decreasing $\omega(0)$. The maximum of $a(l)$ is at the l -value for which $\omega(l)$ changes sign.

hinder the transformation from converging. Non-monotonic behavior of the off-diagonal part of the Hamiltonian is found. All applications that are discussed in the following chapters are not exactly solvable. The Hamiltonian has to be truncated. In this situation special attention has to be paid to possible non-monotonic behavior of the off-diagonal elements because increasing off-diagonal elements imply increasing truncation errors. Therefore, this issue will show up again in the sections where applications of the CUT are described.

2.3. Self-similar CUTs in real space

Up to now the flow equations and generators have been described in a very general fashion. The flow equation, Eq. (2.1.2), is written down as a formal expression. We have not discussed so far the question how to calculate and solve the flow equations. The present section will further specify the method used in this thesis. It deals with the construction of the flow equation of the self-similar CUT in real space. As has been mentioned before, the flow equations generally do not produce a closed set of equations. A truncation scheme is introduced to make the CUT approach amenable for a numerical solution. The transformation of the Hamiltonian and the observables is described.

2.3.1. Physical motivation

Before we turn to the question how to set up the flow equations let us discuss the physical motivation for the local approach used in this thesis. The starting point of the method is a Hamiltonian formulated on a lattice. For the method to be applicable this Hamiltonian has to consist of local terms only. Infinite or long range interactions are beyond the applicability of the present treatment. In solid state physics local Hamiltonians are of great importance. A wide range of physical problems is formulated using localized Wannier states and local Hamiltonians in second quantization [1].

Note that local Hamiltonians do not necessarily describe local physics. An obvious example is a tight-binding Hamiltonian for non-interacting fermions that contains only hoppings to a few nearest neighbors. Although the Hamiltonian is very local the eigenstates are extended momentum eigenstates. If one includes interaction terms in the Hamiltonian a rich variety of phenomena are described by local Hamiltonians.

The first main concept of the present approach is to transform the Hamiltonian at hand into an effective Hamiltonian using local terms. This is done using the method of CUTs. They are a formal procedure to derive an effective Hamiltonian. The effective Hamiltonian given by the CUT is supposed to be closer to diagonality and thus easier to treat than the original problem. The effective Hamiltonian will contain additional terms. The local approach assumes that it is possible to encode the problem truthfully in rather local terms. It is implemented as a real-space CUT. Operators are denoted in real space and the truncation scheme is based on the locality of the terms.

The second central concept is the description of the system in terms of quasiparticles. The choice of the quasiparticles depends on the physical situation. The counting operator of the quasiparticles defines the MKU generator, see also Sec. 2.2.2. The quasiparticle description gives a clear physical picture of the transformation and the effective Hamiltonian. The advantages of the quasiparticle picture inherent to the MKU-CUT has already been described in the preceding section. The local approach is combined in a natural way with the quasiparticle picture. In addition, the quasiparticle structure of terms allows a deeper analysis of the effects and of the relevance of local terms.

In contrast to a perturbative CUT a *self-similar* strategy is adopted here. The terms that are included in the Hamiltonian have to be chosen using definite rules. In the self-similar CUT this is done using the structure of the operators. After the new terms have been included in the Hamiltonian the CUT represents a transformation within these terms. This motivates the naming “self-similar”. The differential equation given by the CUT represents flow equations for the coefficients of the Hamiltonian. This results in a non-perturbative dependence of the effective coefficients on the system parameters.

This local approach is promising under the following circumstances. The effective model has to incorporate the physics into local operators. The physically relevant processes have to be of a certain range only. This is the case for small correlation lengths. For a diverging correlation length, e. g. at a continuous phase transition, one has to be aware of a possible breakdown of

the transformation. The mapping might not be possible. This is signalled by a non-convergent behavior of the flow equation.

The local approach is particularly suited in physical situations with strong correlations. This is the type of problem where also strong-coupling expansions around the atomic limit are applied. The reasoning behind the strong-coupling expansion also suggests the use of the local CUT approach. If the most important terms are local correlations then an expansion using terms that include these processes is promising. A prominent model describing the physics of local correlations is the Hubbard model. At large coupling and half filling it describes insulating systems with short correlation lengths. We will apply the real-space CUT to the fermionic as well as to the bosonic Hubbard model in Chap. 3 and Chap. 5, respectively. Another application are spin liquids. These are spin models that display a gap between the groundstate and the first excited states. Spin liquids are realized by local spin Hamiltonians under certain conditions. Due to the presence of a gap the correlation length is typically of the order of only a few lattice spacings. The treatment of the spin ladder and the dimerized spin chain is presented in Chap. 4. These systems are spin liquids for appropriate choices of the coupling constants.

The formal properties and the implementation of the real space approach to self-similar CUTs are discussed in the following.

2.3.2. Setup of the flow equations

This section presents the implementation of the CUT approach. The central formula is the flow equation for the Hamiltonian. It is restated here

$$\frac{\partial H(l)}{\partial l} = [\eta(l), H(l)]. \quad (2.3.23)$$

The initial condition for this equation is the original Hamiltonian $H(0) = H$. The first step is the calculation of the commutator on the right-hand side. It will contain terms that are present in the original Hamiltonian and new terms. In most cases the number of newly generated terms proliferates. The flow equations do not close.

The proliferating number of terms has to be dealt with. The importance of the newly generated terms has to be judged in a certain way. Then, more important terms are kept and the others are discarded. One way to do this is to arrange the terms in perturbative order. An expansion parameter is assigned to the non-diagonal part of the Hamiltonian. Each term is of a certain order in this expansion parameter. Terms are kept up to a certain order. The resulting effective Hamiltonian contains coefficients that are given as a power series in the expansion parameter. This strategy has been successful, see e. g. Refs. [13, 26, 27, 29, 30, 50].

In contrast to this perturbative strategy we follow the self-similar setup of the CUT. As has been motivated in the preceding section the locality of a term is a measure for its importance if the correlation length is small. Terms are kept according to a truncation rule that implements this idea. The commutator on the right-hand side of the flow equation is computed explicitly. The terms meeting the truncation criterion are included in the Hamiltonian. The flow equation

constitutes a differential equation for the prefactors of the terms. The example of the two-level problem treated in Sec. 2.2.3 was our first application of self-similar CUTs.

The real-space implementation of the CUTs uses the locality of operators as the main truncation criterion. Therefore, a measure for the locality of an operator has to be defined. An indispensable prerequisite is a physically meaningful and in particular unique way to denote the operators. We define a sort of normal-ordering of the operator products¹. The normal-ordering will take place with respect to a reference ensemble. If this ensemble is unique it is a single *reference state*. If it consists of many states it is a *reference ensemble*.

First, we discuss the situation of a single reference state. It is constructed using a local reference state. The choice of this local reference state has to be motivated physically. The reference state is the state with no excitation present. Deviations from the reference state represent excitations. The full reference state is constructed as

$$|\text{ref}\rangle = \prod_i |0\rangle_i, \quad (2.3.24)$$

where $|0\rangle_i$ denotes the local reference state on site i . The case of a reference ensemble is encountered if there are several local states that have no excitation present. This situation will be further treated in Chap. 3. The above definition of the reference state is then generalized to the following expression for the reference ensemble

$$\hat{\rho}_0 := \prod_i \left(\frac{1}{N_{\text{ref}}} \sum_{\alpha \in \text{ref}} |\alpha\rangle_i \langle \alpha| \right), \quad (2.3.25)$$

where the sum extends over all local states that have no quasiparticle excitation present. Their number is N_{ref} .

A product of n local operators $o_{i_1, \alpha_1} \cdot \dots \cdot o_{i_n, \alpha_n}$ is normal-ordered if any expectation value for $m \in \{1, \dots, n\}$

$$\langle o_{i_m, \alpha_m} \rangle_{\text{ref}} := \text{Tr}(o_{i_m, \alpha_m} \hat{\rho}_0) \quad (2.3.26)$$

with the reference ensemble *vanishes*. Here, α_m labels the local operators. Local deviations from the reference ensemble are excitations. The normal-ordered notation as defined by Eq. (2.3.26) assures that operators really deal with those excitations. The creation and annihilation operators of the excitations and products of these operators constitute the algebra of local operators.

2.3.3. Formulation with local operators

This section introduces the operator algebra for a finite local Hilbert space for the case of a single reference state. This formalism is directly applicable to the spin-systems treated in Chap. 4 and for the bosonic Hubbard system in Chap. 5. In Chap. 3 the case of a reference ensemble is encountered. The minor modifications to treat this case are discussed in Chap. 3.2.1.

¹We use the expression “normal-ordering” while we are aware that we are in general not dealing with conventional normal-ordering. The applications of the method will not treat non-interacting fermions or bosons. Normal-ordering in the context of the present work refers to the standardized procedure to represent operators.

For illustration, we treat here a local Hilbert space of four states. The formalism is generalized straightforwardly to any finite number of states. Chapters 4 and 5 will also use a local basis with four states. Thus, for the sake of concreteness this dimension of the Hilbert space is used.

The four states are labeled $|n\rangle_i$ where $n \in \{0, 1, 2, 3\}$. The local operators can be denoted as 4x4 matrices. Next, we construct the basis for the local operator algebra. The state $|0\rangle$ is defined to be the local reference state. The full reference state is the product state

$$|\text{ref}\rangle = \prod_i |0\rangle_i. \quad (2.3.27)$$

A local operator is normal ordered if

$$\langle o_{i,\alpha} \rangle_{\text{ref}} = \langle 0 | o_{i,\alpha} | 0 \rangle_i \stackrel{!}{=} 0. \quad (2.3.28)$$

The creation operators of local excitations have the following matrix representations

$$e_{i,1}^\dagger = \begin{pmatrix} 0 & 0 & 0 & 0 \\ 1 & 0 & 0 & 0 \\ 0 & 0 & 0 & 0 \\ 0 & 0 & 0 & 0 \end{pmatrix}_i, \quad (2.3.29a)$$

$$e_{i,2}^\dagger = \begin{pmatrix} 0 & 0 & 0 & 0 \\ 0 & 0 & 0 & 0 \\ 1 & 0 & 0 & 0 \\ 0 & 0 & 0 & 0 \end{pmatrix}_i, \quad (2.3.29b)$$

$$e_{i,3}^\dagger = \begin{pmatrix} 0 & 0 & 0 & 0 \\ 0 & 0 & 0 & 0 \\ 0 & 0 & 0 & 0 \\ 1 & 0 & 0 & 0 \end{pmatrix}_i, \quad (2.3.29c)$$

where the basis consists of the states $|n\rangle_i$ with $n \in \{0, 1, 2, 3\}$. They create local excitations with flavor $\alpha \in \{1, 2, 3\}$. The annihilation operators $e_{i,\alpha}$ are the hermitian conjugates of Eq. (2.3.29). The operators $e_{i,\alpha}^\dagger$ correspond to creation operators of hard-core particles. The application of a creation operator annihilates any singly occupied states. The operators in Eq. (2.3.29) fulfill the commutation relations of hard-core particles

$$[e_{i,\alpha}, e_{j,\beta}^\dagger] = \delta_{i,j} \left(\delta_{\alpha,\beta} - e_{i,\beta}^\dagger e_{j,\alpha} - \delta_{\alpha,\beta} \sum_\gamma (e_{i,\gamma}^\dagger e_{j,\gamma}) \right). \quad (2.3.30)$$

Here, we have assumed that operators on different sites fulfill bosonic commutation relations. Fermionic operators anti-commute on different sites. Compared to the usual commutation relations of non-interacting particles the above equation contains additional contributions. This complicates analytical calculations with hard-core operators. For example, a usual Bogoliubov transformation to diagonalize a bilinear Hamiltonian is not possible for hard-core particles. The

Bogoliubov transform conserves the commutation relations of non-interacting bosons but not the one for hard-core particles.

Using the operators in Eq. (2.3.29) one can construct nine additional operators of the type

$$e_{i,\alpha}^\dagger e_{i,\beta} \quad (2.3.31)$$

where α and β are $\in \{1, 2, 3\}$. Together with the creation and annihilation operators, $e_{i,\alpha}^\dagger$ and $e_{i,\alpha}$, this gives fifteen local operators. They are all normal ordered since the expectation value $\langle 0|o_{i,\alpha}|0\rangle_i$ vanishes, see Eq. (2.3.26).

The addition of the local four-dimensional identity-matrix $\text{Id}(4)$ makes this set of operators a basis of the operators of the local Hilbert space. Any local operator o_i can be decomposed into a linear combination of the basis

$$\left\{ \text{Id}(4), e_{i,\alpha}^\dagger, e_{i,\alpha}, e_{i,\alpha}^\dagger e_{i,\beta} \mid \alpha, \beta \in \{1, 2, 3\} \right\}. \quad (2.3.32)$$

The role played by this basis becomes clear if one notes that the following operator is *not* included in the operator basis

$$\begin{pmatrix} 1 & 0 & 0 & 0 \\ 0 & 0 & 0 & 0 \\ 0 & 0 & 0 & 0 \\ 0 & 0 & 0 & 0 \end{pmatrix}_i. \quad (2.3.33)$$

The reason is that the expectation value in Eq. (2.3.26) does not vanish. This operator projects onto the reference state, i. e. it does not deal with the excitations defined by Eq. (2.3.29).

If the operator (2.3.33) appears in the calculation it has to be rewritten in the normal-ordered form

$$\begin{aligned} \begin{pmatrix} 1 & 0 & 0 & 0 \\ 0 & 0 & 0 & 0 \\ 0 & 0 & 0 & 0 \\ 0 & 0 & 0 & 0 \end{pmatrix}_i &= \text{Id}(4)_i - \begin{pmatrix} 0 & 0 & 0 & 0 \\ 0 & 1 & 0 & 0 \\ 0 & 0 & 0 & 0 \\ 0 & 0 & 0 & 0 \end{pmatrix}_i - \begin{pmatrix} 0 & 0 & 0 & 0 \\ 0 & 0 & 0 & 0 \\ 0 & 0 & 1 & 0 \\ 0 & 0 & 0 & 0 \end{pmatrix}_i - \begin{pmatrix} 0 & 0 & 0 & 0 \\ 0 & 0 & 0 & 0 \\ 0 & 0 & 0 & 0 \\ 0 & 0 & 0 & 1 \end{pmatrix}_i \\ &= \text{Id}(4)_i - e_{i,1}^\dagger e_{i,1} - e_{i,2}^\dagger e_{i,2} - e_{i,3}^\dagger e_{i,3}. \end{aligned} \quad (2.3.34)$$

The local operators are labeled with a site index when they are used to write down the Hamiltonian. Consequently, also products of local normal-ordered operators belonging to different sites are normal-ordered. The expectation value with respect to the reference ensemble of each separate factor vanishes.

Terms acting on several sites are composed of the local operator basis in Eq. (2.3.32). As the operator basis is normal-ordered it is clear that all operators apart from the identity deal with quasiparticles. As usual in second quantization, the identity operator is dropped when writing down products of local operators. Then, the distance between the remaining normal-ordered local operators is a measure for the locality of the induced process. This is further explained in the next section.

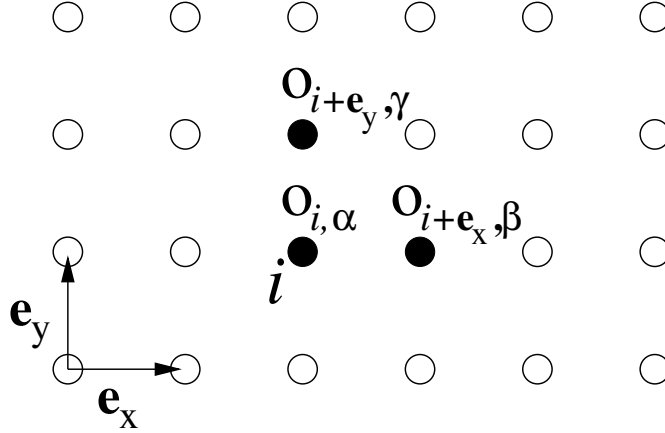


Fig. 2.4: The operator in Eq. (2.3.35) on a square lattice. Filled sites are affected by the term.

2.3.4. Transformation of the Hamiltonian

The previous section defined a physically motivated unique way to denote operators. This is necessary to implement reasonable truncation rules for the real-space CUT. The motivation to use the locality of terms for the truncation scheme has been given in Sec. 2.3. Here, we describe how this concept is implemented in a CUT calculation as a criterion for the terms that are kept in the Hamiltonian.

The Hamiltonian is a sum of products that are composed of local operators. Also products of normal-ordered operators are normal-ordered. The prefactor of a product of local operators will be called the *coefficient* of this term.

On the basis of the normal-ordering and of the induced standardized notation we define a measure for the locality of a term, namely its *extension* d . Consider the following example in two dimensions

$$\sum_i o_{i,\alpha} o_{i+\mathbf{e}_x,\beta} o_{i+\mathbf{e}_y,\gamma}. \quad (2.3.35)$$

Local operators are denoted by $o_{i,\alpha}$. In this notation i is the site index and α labels the various local operators. The local operators are normal-ordered. The above term is illustrated in Fig. 2.4. It contains operators that act on three different sites. They are depicted as filled circles in Fig. 2.4. These sites will be called the *cluster* belonging to this term. On all other sites the term acts as the identity. The Hamiltonian is translationally invariant because the term is summed over the index i .

The maximal taxi cab distance² d of two sites in this cluster is the *extension* of this term. This definition of the extension is applicable in any dimension. In particular, in one dimension the

²The taxi cab distance of two points is the minimal number of bonds on the square lattice that connect these two points.

taxi-cab metric coincides with the usual euclidian metric. The extension of the term Eq. (2.3.35) is $d = 2$.

The extension of the cluster belonging to a term is the measure of its locality. For a truncation scheme, a certain maximal extension is defined. Terms that meet this criterion, i. e. which have an extension smaller or equal to the maximal extension, are kept. If the extension of a term is larger than the maximal extension this term is discarded.

It has to be emphasized that the use of clusters to define the truncation does not turn our approach into a finite cluster calculation. It is a self-similar calculation in the thermodynamic limit. Only the decision which terms are kept is based on their locality. By translational invariance, the operators appear on the whole lattice as it is denoted by the sum over lattice sites i in Eq. (2.3.35). There are no such things as finite size effects. The Hamiltonian after the transformation is the thermodynamically correct effective Hamiltonian.

Additional conditions on the terms retained can be imposed. The maximal size of a calculation is usually restricted by the computer resources at hand. Therefore, it can be useful to impose certain additional restrictions on the terms kept. The number of local operators different from the identity can be restricted to a maximal number. A calculation using this criterion will be performed in Chap. 3 for the fermionic Hubbard model. One can also impose different maximal extensions for different blocks of the Hamiltonian. A term is attributed to a certain block according to its action on the number of quasiparticles, see Sec. 2.2.2. In certain problems it is necessary to keep one block, e. g. the dispersion terms, to a larger extension than it is possible for more complicated terms. This can be done using different maximal extensions for different blocks. This strategy is adopted for the spin systems in Chap. 4.

The complete prescription for the *self-similar* CUT calculation in real space reads:

- Define a truncation scheme. The truncation scheme is given by a maximal extension and possibly by additional constraints. Normal-ordered operators that meet the truncation criteria are kept during the calculation. The truncation rule limits the number of possible terms. Hence, the flow equation closes.
- Calculate $[\eta(\ell), H(\ell)]$ to obtain the differential equation for the coefficients of the terms in H . Terms that are not present in the original Hamiltonian start with initial coefficients zero at $\ell = 0$. The differential equation has to be set up only once for each truncation scheme. It has to be solved for each set of initial conditions separately.
- The numerical integration of the flow equation yields the effective model. For $\ell \rightarrow \infty$ it conserves the number of quasiparticles.

A worked out example for the self-similar CUTs in real space will be given in Sec. 3.2.2. The various steps in this calculation will be described in detail. It has to be noted that the flowing Hamiltonian can be used as an effective model for all $l \in [0, \infty]$. If the flow equations are not integrated up to $l = \infty$ there are terms still present that change the number of quasiparticles. In this case these terms have to be treated by some other means or they can be neglected if

they are sufficiently small. This will be the case for the bosonic Hubbard model discussed in Chap. 5. The integration of the flow equation up to $l = \infty$ requires that the flow equation converges. Generally, non-convergence can be due to an insufficient approximation or due to the breakdown of the mapping. It can be impossible for given parameters to perform the mapping to a quasiparticle conserving effective Hamiltonian. This can be due to overlapping multi-particle continua. It can also be due to a phase transition where the applied quasiparticle picture breaks down. In these cases the flow equations will not converge.

The flow equations are solved numerically. An analytic solution is usually not feasible because of the large dimension of the system of differential equations. Using numerical integration the transformation cannot be carried out until $l = \infty$. Therefore, one needs to measure the extent to which the unitary transformation has already eliminated the terms that contribute in the generator. For the MKU generator these are the terms that change the number of quasiparticles. The *residual off-diagonality* (ROD) is defined as the sum of the squares of all coefficients that contribute to the generator. This definition applies both to the MKU as well as to the Wegner generator. In a numerical integration of the differential equation the residual off-diagonality will not vanish exactly. Therefore, a small but non-zero value is defined for which the flow is stopped as soon as the residual off-diagonality falls below this value.

2.3.5. Transformation of observables

The effective Hamiltonian allows to access energy properties of the system. If one wants to explain experiments one also has to transform the observables that are relevant for the experiment. The application of the operators that represent the observable introduce excitations in the system. This allows also the calculation of spectral densities belonging to the susceptibility of this excitation.

The general setup of the flow equations for an observable is very similar to the previously described case of the Hamiltonian. The total effect of the observable is a sum of the local observables

$$\mathcal{O}(l) = \sum_{\mathbf{r} \in i} \mathcal{O}(l, \mathbf{r}). \quad (2.3.36)$$

The observable depends on the flow parameter l . It is transformed with the same generator as the Hamiltonian, see Eq. (2.1.6). The observable is also formulated using normal-ordered operators. In this work only observables acting locally or linear combinations of such observables are considered.

The fact that the observable acts on a definite position necessitates a modification of the truncation scheme. The truncation scheme for the Hamiltonian is based on the extension of a term. The way in which the extension is calculated for terms in the Hamiltonian is not directly applicable for the observable. The motivation to use the local approach to CUTs presented in Sec. 2.3.1 applies also to the observable. Therefore, the truncation scheme for the observable will also rely on the locality of the terms. The change in the truncation scheme is the only difference for the calculation of the effective observable.

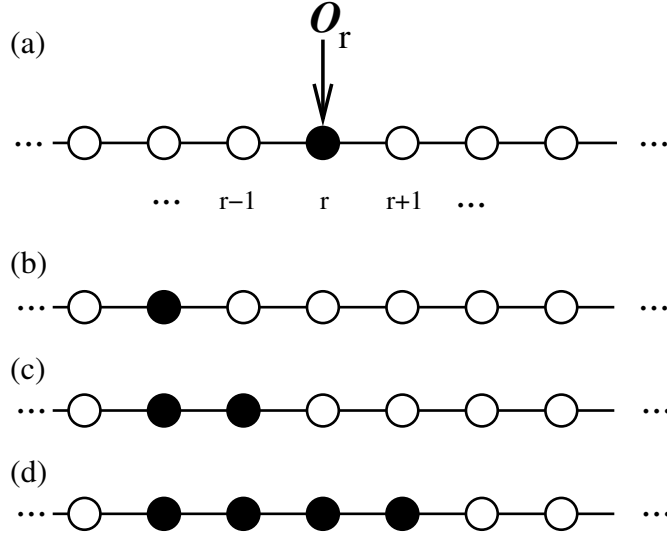


Fig. 2.5: Terms of the local observable $\mathcal{O}(l, \mathbf{r})$. The arrow indicates the site on which the local observable acts. Filled circles: sites on which a non-trivial operator acts; “non-trivial” means that the operator is different from the identity. Open circles: sites on which the term under study does not act, i.e., the term acts as the identity on these sites. (a) At $l = 0$ the observable is composed of local terms that act only on one site of the lattice. (b) A term acting only at the site $\mathbf{r} - 2$. Its coefficient is different from the coefficient of the same local operator acting on the site \mathbf{r} . The reason is that the local observable acts at a definite site. (c) and (d) More complicated terms appear during the flow. The observable extension of the terms in (a)-(d) is $d_{\mathcal{O}} = 0, 2, 3, 4$, respectively. Terms beyond a certain extension are omitted.

The operator of the *local* observable is bound to a definite site in the system. As an example we consider a local observable that acts for $l = 0$ only on one site of the lattice. The discussion of this section is straightforwardly generalized to bond-centered observables.

Figure 2.5 illustrates the action of the local observable at $l = 0$. For clarity, a one-dimensional lattice is shown. The local observable is centered at the site \mathbf{r} . The sites on which the observable acts are shown as filled circles. The state of the sites shown as empty circles is not altered by the observable. In the course of the flow, contributions to the observable appear which do not act on the site on which the initial local observable is centered. The initially local process spreads out in real space for $l \rightarrow \infty$. Examples are sketched in Fig. 2.5b-d.

The terms in the observable are generally written using the normal-ordered operators introduced in Sec. 2.3.4

$$\mathcal{O}(l, \mathbf{r}) = \sum_{\{i, \alpha\}} \hat{c}(l, \{i, \alpha\}) o_{i_1+r, \alpha_1} \cdots o_{i_n+r, \alpha_n} \quad (2.3.37)$$

with the multi-index $\{i, \alpha\}$ summing over all combinations of site indices $\{i\}$ and operator indices $\{\alpha\}$. The observable $\mathcal{O}(l, \mathbf{r})$ acts on the site \mathbf{r} . The coefficient of a term in the observable depends on its position relative to this site.

In order to avoid proliferation, also the terms in the observable have to be truncated. Like for the terms in the Hamiltonian we introduce a measure for the extension of the terms in the observable. Also for the observable the truncation scheme relies on the locality of the terms. It has to be taken into account that the local observable has a definite site \mathbf{r} on which it acts. The *observable extension* of a term in the *observable* $d_{\mathcal{O}}$ is defined as the sum of the distances of *all* its local operators to the site \mathbf{r} .

Figures 2.5a-d are used to motivate this definition of the observable extension. The terms in Fig. 2.5a and Fig. 2.5b both act only at a single site. The observable initially acts at site \mathbf{r} . Since the second term acts on a site that is two lattice spacings away from the site \mathbf{r} it has to be generated through multiple application of the commutator to the observable at $l = 0$. The observable extension of this term is $d_{\mathcal{O}} = 2$ whereas the term in Fig. 2.5a has $d_{\mathcal{O}} = 0$. The term in Fig. 2.5c is generated in an even more complicated process. This is reflected in its larger observable extension $d_{\mathcal{O}} = 3$. The different complexity of the terms Fig. 2.5a and b would not be captured if only the maximum distance of a local operator to the site \mathbf{r} would be taken as a measure for the observable extension. Finally, the term shown in Figure 2.5c has $d_{\mathcal{O}} = 4$.

The terms appearing in the observable are truncated by choosing a maximum value for the observable extension $d_{\mathcal{O}}$. In a calculation with maximum observable extension $d_{\mathcal{O}} = 3$ the terms in Fig. 2.5a through c are kept. The last term in the figure is discarded. This term meets the truncation criterion only if the maximum observable extension is $d_{\mathcal{O}} \geq 4$.

Once the local effective observables $\mathcal{O}(l = \infty, \mathbf{r})$ are known, the total effective expression \mathcal{O}^{eff} is given by the sum over all sites, see Eq. (2.3.36). The transformation of observables completes the description of the method of self-similar CUTs in real space. Before we turn to the implementation of the method on a computer in Sec. 2.5, the next section discusses the relation between different unitary transformations.

2.4. Different unitary transformations

The subject of the present section is to briefly discuss the relation of the self-similar CUT scheme to perturbative schemes. In addition, we will address the question of the uniqueness of the transformation.

The unitary transformation reaching block-diagonality is not unique. This fact has also been discussed in the context of perturbative transformations by *Stein* in Ref. [26]. It can be easily understood by considering the effective Hamiltonian. Let U_0 be the unitary transformation that transforms the original Hamiltonian H into H_{eff} . An additional unitary transformation shall be applied. It is given by U_1 . The transformation U_1 does not mix the subspaces with different quasiparticle number. Such a transformation is given by any basis change *within* the quasiparticle subspaces. This is sketched in Fig. 2.6. The successive application of U_0 and U_1 to the original Hamiltonian also reaches block-diagonality. Since there are infinitely many different basis changes within the blocks, there are also infinitely many unitary transformations that achieve block-diagonality.

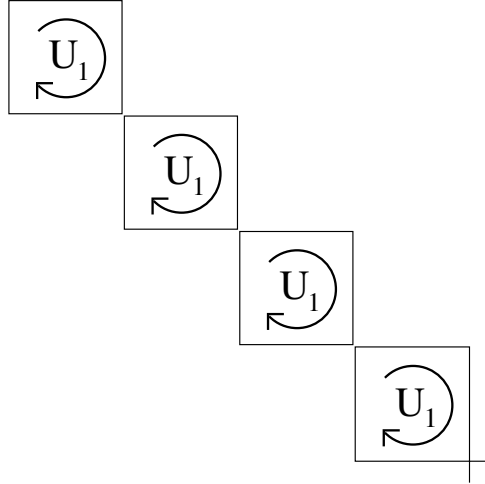


Fig. 2.6: Sketch of a unitary transformation within the blocks of fixed quasiparticle number. Assume that a transformation U_0 has been found that achieves block diagonality of the effective Hamiltonian. Then, any additional transformation U_1 that acts only within the subspaces of fixed quasiparticle number can be performed after U_0 . The combined transformation still has the property to block-diagonalize the given Hamiltonian.

Furthermore, the effective Hamiltonian can be different because the coefficients of the effective Hamiltonian can be changed by the additional unitary transformation. This has to be kept in mind when comparing the results of different unitary transformations. An example for this fact is discussed in Sec. 3.2.4.

The perturbative and the self-similar approaches to CUTs are not completely unrelated³. Perturbative CUTs organize the right-hand side of the flow equation using an expansion parameter that is assigned to the non-diagonal part of the original Hamiltonian. Let us consider one definite parameter of the effective model. A certain set of terms is necessary for the perturbative derivation of this parameter. The set of terms in the perturbative calculation depends on the specified parameter and on the order to which it is calculated. A self-similar CUT contains the results of the perturbative calculation if all operators are taken into account that are necessary for the perturbative expansion. That means that the series expansion of the coefficients given by the self-similar transformation coincides with the perturbative CUT result. However, there are situations where the self-similar approach yields reliable results whereas it is hard to achieve convergence of the perturbative expansion. In other circumstances the perturbative expansion is better behaved than the self-similar transformation. Further discussions on how the two approaches compare are found in Sec. 3.2.3 and Sec. 4.

³For references on perturbative CUTs see e. g. Refs. [13, 26, 27, 29, 30, 50].

```
struct op
{
    short opno;      operator number  $\alpha$ 
    short posx;     x-coordinate of position index  $i$ 
    short posy;     y-coordinate of  $i$ 
};
```

Fig. 2.7: Representation of the local operator $o_{i,\alpha}$ in the programming language C.

2.5. Implementation on a computer

This section presents the central features concerning the computer implementation of the self-similar real-space CUT. Readers that are not interested in the details of the programming may skip it. However, it might serve as a resource for someone who implements a CUT calculation.

The basic structure of the programs that perform the calculation is discussed in this section. The method splits into two steps. First, one has to setup the flow equation and, second, one has to solve this differential equation. The second step, the solution of the differential equation is rather straightforward. The implementation of the differential equation solver is briefly commented in Sec. 2.5.4.

The first step is the computationally more sophisticated one. The flow equation is constructed by calculating commutators of terms. This requires the implementation of some features of the algebra of operators. The number of terms in a calculation can be very large. To make such calculations feasible we point out ways to reduce the computational efforts. The use of symmetries is one important tool to minimize the actual operations that are needed.

A further motivation to discuss the implementation at some length is the versatility of the present approach. Each problem that can be treated by a CUT approach and that is formulated with local operators can be tackled using these programs. All projects of this thesis are solved using basically the same sort of program. Only certain modifications have been necessary to accomplish the adjustment to the particular problem.

2.5.1. Program and data structures

The first program constructs the flow equation. It reads in an initial Hamiltonian and generates the differential equation. Effective Hamiltonians involving a large number of terms have to be treated in order to achieve a good description of the system. An implementation using a computer algebra system like Mathematica or Maple is not advisable due to the insufficient performance of these high level languages. Therefore, an implementation in C/C++ has been chosen.

To calculate the commutators that determine the flow equation the program has to be able to perform some algebra with the terms in the Hamiltonian. The basic entities with which

```
struct term
{
    fraction prefactor;
    short rank;
    struct op ops[MaxRank];
};
```

Fig. 2.8: A term is a product of local operators. It consists of a prefactor stored as an exact fraction and of the array of local operators. The rank is the number of local operators in a term. The maximal number of operators in a term is given by MaxRank.

the program deals are the local operators $o_{i,\alpha}$, see Sec. 2.3.4. The terms in the Hamiltonian are products of local operators. The data structures representing these objects are depicted in Figs. 2.7 and 2.8.

Local operators are implemented as structures of the type “op”. They consist of the operator number and the position of the operator. Figure 2.7 displays the corresponding data structure. This example encodes the position in two indices assuming that the lattice is two-dimensional. Terms are represented with the data structure “term” shown in Fig. 2.8. Each term has a prefactor. It is implemented as an exact fraction of two integer values⁴. It is advisable to keep exact fractions as prefactors. Then, the resulting flow equations are exact and not affected by rounding errors. This allows the exact treatment of small systems and, perhaps even more importantly, simplifies checks of the consistency of the data.

The program is able to multiply, to add, and to sort terms. In addition, equal terms can be identified and combined. The Hamiltonian and the observables are lists of terms. They are stored in an array variable in the program. The program appends new terms that meet the truncation criterion to the existing array during the calculation.

To make extensive calculations possible one has to spend some considerations on efficiency. The means to increase the efficiency presented here lead to a considerable acceleration of the calculation process. The speed gains are not marginal but reach orders of magnitude. The use of these efficiency considerations led to a reduction of the necessary computation time of at least a factor of 100 for the applications in this thesis.

2.5.2. Symmetries

Before we turn to the actual calculation of the commutators the role of symmetries to minimize the computational cost is discussed. Terms in the Hamiltonian that are related by symmetry carry the same coefficient. The use of symmetries reduces the number of terms that have to be treated. Instead of taking into account all terms of a symmetry class one can instead treat only

⁴In fact, integers of type “long long int” are used for the numerator and denominator of the fraction.

one *representative*.

The symmetry groups of the Hamiltonian and of the observables can be different. However, the considerations in this chapter apply to observables in exactly the same way if the appropriate symmetry groups are used. For simplicity, we will discuss the symmetries of the Hamiltonian.

Typical symmetries encountered in solid state physics are spin rotation symmetry, particle-hole symmetry and the space group of the underlying lattice. For simplicity, this section treats discrete symmetries⁵. Let G be the discrete symmetry group of the Hamiltonian. The full symmetry group G can be a product of various subgroups. The number of group elements is l_G . The Hamiltonian is divided into subsets of terms that are related by symmetry. These subsets are called classes. For each class one can define a representative. The choice of the representative has to be unique. Instead of treating all terms in a class separately only the representative has to be taken into account.

The Hamiltonian is an array of terms. It can be rewritten using representatives

$$H = \sum_{i=1}^N f_i h_i = \sum_G \sum_{j=1}^{N_s} \tilde{f}_j \tilde{h}_j \quad (2.5.38)$$

where N is the number of terms h_i without reduction by symmetry. The coefficient of h_i is f_i . The number of representatives is N_s . The representatives are \tilde{h}_j with coefficients \tilde{f}_j .

Note that the coefficient of a representative \tilde{f}_j can be different from the corresponding f_i in the unsymmetrized Hamiltonian. To see this, consider a representative \tilde{h}_j with coefficient \tilde{f}_j . Let h_i be the corresponding term in the Hamiltonian. If the sum over the symmetry group contains the representative several times, the absolute value of the coefficient f_j is $\text{abs}(f_j) = \text{abs}(\tilde{f}_j s_j)$. Here, the factor s_j is the multiplicity of \tilde{h}_j in $\sum_G \tilde{h}_j$. This equation only holds for the absolute value of the coefficient since some symmetry operations can lead to a change of the sign of the coefficient. This has to be taken into account when retrieving the full set of symmetry related terms from the representative. As an example consider the unity operator. It transforms identically under all symmetries. Therefore, $f_{\text{Id}} = \tilde{f}_{\text{Id}} l_G$.

The CUT calculation is performed for the representatives only. The reduction of the number of terms to be treated is significant. The largest calculations in this work could only be done using the symmetry reduction. For the Hubbard model the value of l_G is 64. The number of terms in the Hamiltonian is not reduced by the same factor. The reduction is nevertheless significant especially for large calculations.

2.5.3. Calculation of the flow equation

The purpose of the first program is to calculate the differential equations that embody the flow equation of the coefficients. The central task is the calculation of commutators. Here, the procedure of setting up the flow equations is described. Some hints are given how to fulfill this

⁵The technique to reduce the number of terms in the Hamiltonian works also for continuous symmetries, e. g. spin rotation symmetry. Also continuous symmetries relate only a finite number of terms in the Hamiltonian by symmetry. The value of l_G is in this case the maximum number of symmetry related terms.

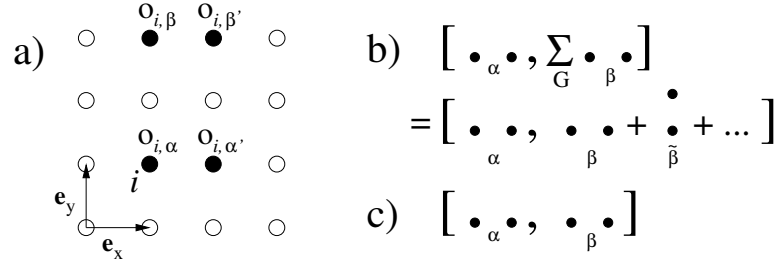


Fig. 2.9: a) Sketch of the representatives. Their local operators act on one site and the nearest neighbor in x -direction. (b) The commutator involves a sum over the symmetry group. (c) A commutator of the two representatives will not give the same result.

task efficiently. A MKU CUT is considered first. Then, the small variations are pointed out that appear for a Wegner generator.

The Hamiltonian is given as an array of terms. Newly generated terms are appended to the array. In a MKU type of CUT the generator is very similar to the Hamiltonian. One just has to determine the correct prefactors in Eq. (2.2.10). The generator is not stored separately. The prefactors are inserted when needed. Thus, one has to calculate the commutators of those terms in the Hamiltonian that contribute to the generator with the Hamiltonian itself. To make use of the symmetry one observes that

$$\left[\sum_G \tilde{f}_i \tilde{h}_i, \sum_G \tilde{f}_j \tilde{h}_j \right] = \sum_G \left[\tilde{f}_i \tilde{h}_i, \sum_G \tilde{f}_j \tilde{h}_j \right]. \quad (2.5.39)$$

Since the Hamiltonian itself is a sum over the symmetry group one can drop this sum and calculate the flow equation only for the representatives.

It is not possible to take the second sum over the symmetry group in Eq. (2.5.39) out of the commutator and to calculate the commutators only with the representatives. The reason is explained using Fig. 2.9. Let the terms $o_{i,\alpha} o_{i+\mathbf{e}_x,\alpha'}$ and $o_{i,\beta} o_{i+\mathbf{e}_x,\beta'}$ be two different representatives. These terms are shown in Fig. 2.9a embedded in the square lattice. Let the symmetries of the square lattice constitute the symmetry group G . The correct calculation of the commutator Eq. (2.5.39) is sketched in Fig. 2.9b. The second term in the commutator is summed over the symmetry group. The second line shows two terms in this sum. Note especially the second term which is labeled with $\tilde{\beta}$. It is directed along the y -direction of the lattice. Therefore, the result of the commutator will contain terms whose local operators act on sites which are not collinear. On the other hand, the commutator of the two representatives will only contain terms on collinear sites in the x -direction. This commutator is sketched in Fig. 2.9c. It cannot give the correct result for Eq. (2.5.39).

The procedure to calculate the contribution of a pair of terms \tilde{h}_i and \tilde{h}_j is sketched in Fig. 2.10. After taking the representatives \tilde{h}_i and \tilde{h}_j one first has to calculate the sum of \tilde{h}_j over the symmetry group. The commutator is calculated and assigned to the variable **res**. The commutation

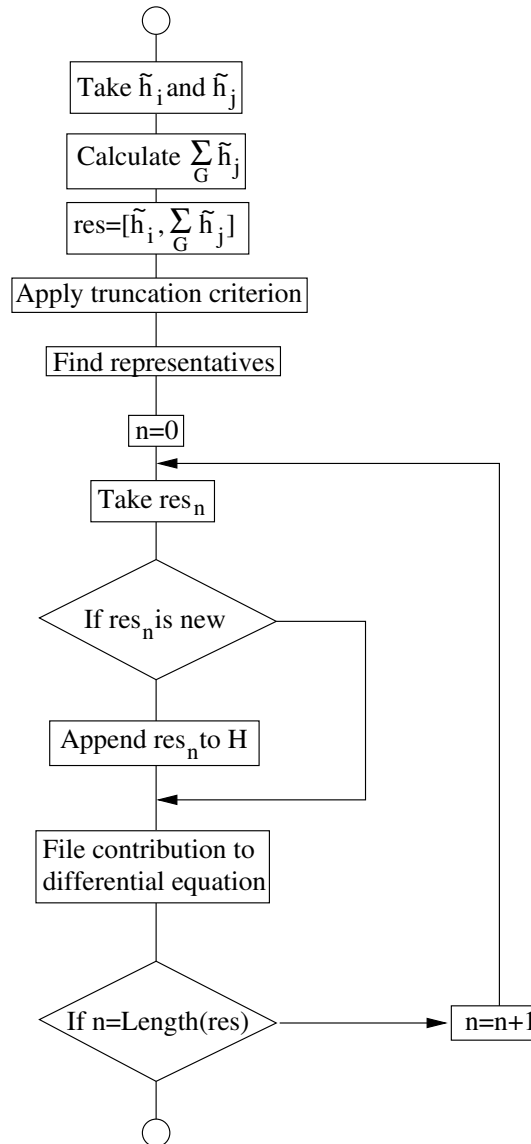


Fig. 2.10: Schematic representation of the calculation of the commutator of a pair of terms \tilde{h}_i and \tilde{h}_j .

procedure also yields terms that do not meet the truncation criterion. These terms are discarded. In a next step the representatives for all terms in the result are found. It might be necessary to combine equal contributions after this step.

Next, the result has to be examined in view of its contributions to the flow equation. To this end, the terms in the result are treated one after the other. If a term is already present in the Hamiltonian the contribution from the commutator of \tilde{h}_i and \tilde{h}_j is filed into the proper

differential equation. If a term is not yet contained in the Hamiltonian it is appended to it. Then, the contribution to the differential equation can be stored. In this step one has to take care of prefactors originating from the definition of the MKU generator, see Eq. (2.2.10). The MKU generator contains a sign-function that depends on the change of the number of quasiparticles. If a term decreases the number of quasiparticles its contribution to the generator has to include an additional minus sign.

In the course of the calculation it frequently happens that terms have to be looked up in the array representing the Hamiltonian. It has to be checked whether a certain term is already present or not. In addition, for a given term its position in the array has to be found. As searching and sorting is computationally quite costly it is favorable to define a hash function for the terms that are allowed in the Hamiltonian. A hash function attributes a unique hash value to all terms that are allowed in the Hamiltonian. The hash value is typically an integer number. Searching for a certain term is easily accomplished if one stores together with each hash value the position of the corresponding term in the Hamiltonian. This causes some more implementation work but speeds up the program significantly. In the local approach to CUTs one has a finite number of local operators. Let n be this number. For the case of a local basis of four states that was presented in Sec. 2.3.3 $n = 16$ holds. A hash value in this case can be defined as an integer in base n where the digits are given by the number of the corresponding local operator. This hash function has been used in Chap. 3. It is appropriate if all terms that are taken into account are defined using rather local clusters. In the application to spin systems in Chap. 4 the terms in some blocks have to be taken into account to larger distance than others. In this case a hash function is used that is especially adapted to handle this problem. It treats the terms of different blocks separately.

The calculation of the commutators has to be performed until the whole flow equation is set up. This is achieved by repeating the above procedure for all terms in the Hamiltonian.

2.5.3.1. Calculation of commutators

What is left to discuss is the computation of a commutator of two operators. The operators are given as products of local operators. In this part of the program, efficiency is a central issue. The problem is the calculation of a commutator of local operators

$$\left[\sum_r o_{r+i_1, \alpha_1}^L \cdots o_{r+i_m, \alpha_m}^L, \sum_{r'} o_{r'+j_1, \beta_1}^R \cdots o_{r'+j_n, \beta_n}^R \right] \quad (2.5.40)$$

where r and r' are site indices and α_i and β_i determine the local operator. The superscripts mark operators on the left (L) and on the right (R) side of the commutator. The final result is most efficiently calculated using the product rule for commutators. Using the product rule the commutators of products are reduced to commutators of elementary local operators. The result

reads

$$\begin{aligned} \sum_r \sum_{r'} \sum_k \sum_l & (-1)^\xi o_{r+i_1, \alpha_1}^L \cdots o_{r+i_k, \alpha_k}^L o_{r+i_1, \alpha_1}^R \cdots o_{r+i_{l-1}, \alpha_{l-1}}^R [o_{r+i_k, \alpha_k}^L, o_{r+j_l, \beta_l}^R]_\epsilon \\ & \times o_{r+j_{l+1}, \beta_{l+1}}^R \cdots o_{r+j_n, \beta_n}^R o_{r+i_{k+1}, \alpha_{k+1}}^L \cdots o_{r+i_m, \alpha_m}^L. \end{aligned} \quad (2.5.41)$$

The ξ encodes a possible sign. The symbol $[\dots, \dots]_\epsilon$ denotes a commutator or anti-commutator for $\epsilon = 1$ and $\epsilon = -1$, respectively. This (anti-)commutator will produce a Kronecker-symbol for the positional indices such that one of the sums over r and r' disappears. The (anti-)commutators of local operators can be calculated from their representation as finite matrices in Eq. (2.3.29). These commutators are previously calculated and stored in an array in the program so that they can be looked up quickly.

The commutator of products of local terms in Eq. (2.5.40) could also be calculated by implementing only the product rule for operators. A recursive application of the product rule yields the same result as Eq. (2.5.41). However, a recursive implementation is not efficient enough and therefore not advisable.

If each pair of two local operators on different sites fulfills bosonic commutation relations there are only commutators in Eq. (2.5.41). Thus $\epsilon = 1$ holds for all contributions. In addition, the value of ξ is always zero since the product rule for bosonic operators contains no minus sign. One can also calculate the value of ξ if local operators with fermionic commutation relations are present. However, for fermionic operators a , b , and c the following product rule must be used

$$[a, bc] = \{a, b\}c - b\{a, c\}, \quad (2.5.42)$$

where curly brackets denote the fermionic anti-commutator. Then, also these anti-commutators can be simplified using product rules. For fermionic operators a and b and a bosonic operator d the following relations hold

$$\{a, bd\} = \{a, b\}d - b\{a, d\}, \quad (2.5.43)$$

$$\{a, db\} = d\{a, b\} + [a, d]b. \quad (2.5.44)$$

The result in Eq. (2.5.41) for products involving also operators of fermionic type can include a sign change. The sign encoded in ξ is calculated by tracking how the present term is produced by the product rules. Note that only the second terms in Eq. (2.5.42) and Eq. (2.5.43) carry a minus sign. If a commutator or anti-commutator has to be used, can be determined from the type of operators involved. This determines the value of ϵ in Eq. (2.5.41).

2.5.3.2. Wegner's generator

The Wegner generator is given in Eq. (2.2.8). The generator itself involves a commutator. Again, the right-hand side of the flow equation is given by the commutator of the generator and the Hamiltonian. A straightforward implementation of the Wegner generator is done as

follows. The flow equation Eq. (2.2.9) for the Wegner generator reads $\partial_l H(l) = [\eta_W(l), H(l)] = [[H_d(l), H_{nd}(l)], H(l)]$. This can be implemented by the following set of equations

$$\frac{\partial H(l)}{\partial l} = [\eta_W(l), H(l)] \quad (2.5.45a)$$

$$\eta_W(l) = [H_d(l), H_{nd}(l)]. \quad (2.5.45b)$$

Equation (2.5.45a) is a first order differential equation. The equation Eq. (2.5.45b) defining the generator is a usual equation. It gives the coefficients of the generator as a sum over terms that are bilinear in the coefficients of the Hamiltonian. Using this implementation of the Wegner scheme the double commutator in the definition of the flow equation is avoided. The equation (2.5.45) is set up in the same way as the flow equation for the MKU scheme. The right-hand side of Eq. (2.5.45a) involves bilinear combinations of the coefficients of the Hamiltonian and the generator. The flow equation Eq. (2.2.9) involves cubic terms in the coefficients. This cubic relation has been substituted by the bilinear equations Eq. (2.5.45).

2.5.4. Numerical solution of the differential equation

The final step in the CUT calculation is the solution of the differential equations. The flow equations are ordinary first order differential equations. Their solution yields the coefficients of the effective Hamiltonian. In the MKU CUT the right-hand side consists of terms that are bilinear in the coefficients of the Hamiltonian. If the Wegner scheme is implemented as described in Sec. 2.5.3.2 the right-hand side consists of products of the coefficients of the Hamiltonian and the generator. The differential equation for the coefficients of the Hamiltonian is supplemented by an equation for the generator. The flow equations for an observable Eq. (2.1.6) are also first order differential equations. They are linear in the coefficients of the observable. They also contain the coefficients of the generator. Therefore, they have to be solved together with the flow equations for the Hamiltonian.

A Runge-Kutta method with adaptive step size control is used to solve the differential equations [51]. The functional behavior of the coefficients is smooth if the mapping to the effective model works. Divergencies of the coefficients appear if the transformation is not possible. Reasons for such behavior have been discussed in Sec. 2.3.4. The only problem is the large size of the set of differential equations. They contain up to several ten thousands of coefficients in the problems treated in this thesis. This leads to a sizeable computational cost for each Runge-Kutta step. Especially in cases of slow convergence of the CUT this implies long run times of the numerical integration. The solution of the largest set of differential equations in this thesis took several days of computing time on Sun UltraSPARC workstations. The computation time to solve the differential equation is thus comparable to the time it takes to set up the equations. However, this first step of setting up the flow equation can be done in parallel on many computers. A parallelization of the differential equation on separate computers is not possible. Therefore, the programs solving the differential equations took the longest real time. Technically, it is possible to parallelize the solution of the differential equation using packages

like OpenMP [52]. This would lead to a substantial increase in the performance of the program.

2.6. Summary

In this section the method of self-similar CUTs in real space was presented. CUTs in general are an approach to many-body physics that allows to derive effective Hamiltonians that are simpler to solve than the original problem.

The CUT approach presented here relies on the following prerequisites. Depending on the physical problem at hand one has to define a reference state or ensemble. Quasiparticles are elementary deviations from the reference ensemble. The MKU generator induces a transformation such that the effective Hamiltonian is block-diagonal in the quasiparticle number. The quasiparticle counting operator Q commutes with H_{eff} .

The real space approach of the CUT was described in detail. It formulates the effective Hamiltonian using terms that are as local as possible. The reference ensemble defines the normal-ordering of operators. Normal-ordering is a unique way to denote operators. The physical situation is reflected in the normal-ordering since the choice of the reference ensemble and the quasiparticles is motivated by the actual physical situation under study.

We have introduced the extension of a normal-ordered term as a measure for its locality. It is the central criterion to truncate the proliferating number of terms appearing in the construction of the flow equation. The truncation scheme applied in this thesis selects terms of a certain form. The resulting flow equations are self-similar. Their solution yields the coefficients of the effective Hamiltonian in a non-perturbative way. The residual off-diagonality (ROD) measures the size of the terms that still contribute to the generator during the flow.

The last section, Sec. 2.5, introduces the computational techniques that are necessary to implement the flow equation method on a computer. It also describes means to optimize the efficiency of the calculation. Efficiency is a crucial condition for a good description of the physical system since this often requires the treatment of effective Hamiltonians with many terms.

3. Effective t - J -model derived from the Hubbard model

The Hubbard model is a paradigmatic model in condensed matter physics. It describes the physics of correlated electrons in a lattice. The very successful determination of energy bands in solids using band theory relies on an effective one-particle description. The Hubbard model goes beyond this one-particle description by including a true correlation term. It includes beside one-particle hopping terms only an additional two-particle on-site interaction. The use of the Hubbard model aims at situations where correlations are central to the physics of the system and therefore the one-particle descriptions fail. It was first introduced to describe ferromagnetism in systems with electron correlations that are not negligible [53–56]. The Hubbard model has been used to describe the Mott metal-insulator transition [57, 58]. The Mott transition is a prototypic example for the failure of band theory. Mott insulators have an odd number of electrons but do not conduct as predicted by band theory. They display gapful behavior that is caused by the electronic correlation. In the case of strong coupling and half filling the Hubbard model can be mapped onto a pure spin Hamiltonian. In second order in perturbation theory one finds an antiferromagnetic Heisenberg model [22, 59]. Although the Hubbard model has been introduced to describe ferromagnetism it gives more naturally rise to antiferromagnetic behavior. A prominent application of the Hubbard model in recent years is the description of the electronic properties of high- T_c cuprates [60].

In this chapter the method of continuous unitary transformations is used to treat the insulating regime of the Hubbard model. In particular, the aim is to provide a systematic and controlled non-perturbative derivation of a generalized t - J -model. The t - J -model and its generalizations describe the physics of the Hubbard model restricted to the subspace of states with smallest expectation value of the interaction. This is the subspace of states with minimal number of doubly occupied sites.

A particle number conserving self-similar CUT is used to derive the t - J -model. The truncation scheme follows the local approach motivated in the previous chapter. The terms retained are chosen according to their locality. This is appropriate for the insulating regime of the phase diagram. Also the limits of validity of the mapping itself are studied. The mapping corresponds to the elimination of charge fluctuations. Whether the mapping is possible depends on the extent of these charge fluctuations and thus on the energy cost of charge fluctuations.

The focus of this chapter lies on the derivation of the effective model itself. We will not aim at a solution of the effective model. The step from the Hubbard model to the t - J model is a

substantial simplification. Nevertheless, the effective Hamiltonian is still very complicated and its solution is a field of study in its own. The reduction of the Hubbard model to the t - J model is quite common by now. However, our results reach beyond what has been done before [22–24, 26, 59, 61]. First, the results are calculated in a non-perturbative way. The coefficients of the effective model are stable with respect to the truncation scheme. The results for the effective spin model obtained by perturbative treatments [22–24, 26, 61] are reliable only for very large interactions. Up to now only the effective spin model has been derived in a systematic perturbative expansion. Second, matrix elements of hole motion and interaction are discussed in a systematic way beyond the zeroth order. The present approach is the first to treat the charge part of the effective model systematically beyond the leading order in perturbation theory. The main coefficients of the effective model will be given explicitly.

The chapter is organized as follows. First the model is introduced in Sec. 3.1. The description of the method is placed in Sec. 3.2. It includes a discussion of the relation of the self-similar results to perturbative results in Sec. 3.2.3 and a remark on the possible difference between various unitary transformations in Sec. 3.2.4. Section 3.3 presents the properties of the transformation as well as the results for the effective Hamiltonian. The results of the CUT are discussed in Sec. 3.4 and finally summarized in Sec. 3.5.

3.1. Fermionic Hubbard model

The Hubbard model¹ consists of electrons with spin moving on a lattice [53–56]. The electrons repel each other if they are on the same site. We will only consider the Hubbard model in two dimensions on a square lattice. The model is defined by the Hamiltonian

$$H = H_U + H_t \quad (3.1.1)$$

which is composed of the interaction and the kinetic energy

$$H_U = U \sum_i (n_{i,\uparrow} - \frac{1}{2})(n_{i,\downarrow} - \frac{1}{2}) = \frac{U}{2} \left(\hat{D} - \frac{N}{2} \right) \quad (3.1.2a)$$

$$H_t = t \sum_{\langle i,j \rangle, \sigma} (c_{i,\sigma}^\dagger c_{j,\sigma} + \text{h.c.}). \quad (3.1.2b)$$

where N is the number of sites, $c_{i,\sigma}^\dagger$, $c_{i,\sigma}$ are creation and annihilation operators of an electron on site i with spin $\sigma \in \{\uparrow, \downarrow\}$ and $n_{i,\sigma} = c_{i,\sigma}^\dagger c_{i,\sigma}$ is the number operator. Hopping is only possible between nearest neighbor (NN) sites as indicated by $\langle i, j \rangle$ in the sum in H_t . The bare hopping coefficient is given by t . The bare bandwidth without interactions is $W = 2zt$ where z is the coordination number. For the square lattice the bandwidth is $W = 8t$. Later all energies will be most conveniently given in units of the bandwidth W . H_U describes the repulsion of electrons

¹In the discussion of the fermionic Hubbard model we will drop the specification 'fermionic'. With 'Hubbard model' always the fermionic model is addressed. When the particles involved are bosons we will always write 'bosonic Hubbard model'.

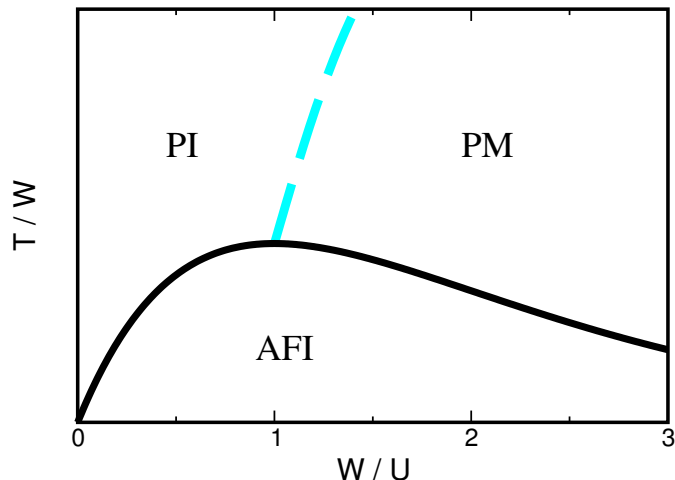


Fig. 3.1: Schematic phase diagram of the Hubbard model at half filling in higher dimensions $d > 2$. The tick labels at the x -axis are indicative only. The bare bandwidth is denoted by W , the Hubbard repulsion by U , the temperature by T ; PI stands for paramagnetic insulator, PM for paramagnetic metal and AFI for antiferromagnetic insulator. The dashed line indicates the transition or the crossover from insulator to metal.

of opposite spin on the same site. The interaction, Eq. (3.1.2a), leads to a complex interplay of magnetic and charge degrees of freedom. It is useful to rewrite the interaction part using the operator

$$\hat{D} := \sum_i [n_{i,\uparrow}n_{i,\downarrow} + (1 - n_{i,\uparrow})(1 - n_{i,\downarrow})] \quad (3.1.3)$$

which counts the number of double occupancies (DOs) of particles *and* holes. The interaction H_U is rewritten using the operator \hat{D} in Eq. (3.1.2a). In the subsequent sections only the two-dimensional case is treated. Before, some general comments are made regarding the Hubbard model also in other dimensions.

Phase diagram

At half filling the Hubbard model displays insulating behavior in the limit of strong interactions. In the opposite limit of vanishing interaction it describes free electrons and the conductivity is finite. In-between an intricate metal-insulator transition (MIT) takes place. In one dimension the Hubbard model can be solved exactly by Bethe ansatz [2, 62]. The transition to the Mott insulating state takes place already at $U = 0$. Any non-vanishing interacting makes the system insulating.

Figure 3.1 shows a schematic phase diagram of the Hubbard model at half filling for dimensions $d > 2$. The figure summarizes the currently assumed picture. This picture is motivated by various mean-field computations, in particular in infinite dimensions [3, 57]. In the limit of

infinite dimensions, the dynamical mean-field theory (DMFT) allows to make statements about the value of the critical interaction where the transition from the insulating to the metallic phase takes place [3, 57, 63, 64].

For large repulsion U , a double occupancy is energetically costly. Therefore, the system is insulating at half filling. The localized electrons interact only via their spin degree of freedom. The size of the magnetic exchange J is equal to $4t^2/U$ in lowest order of perturbation theory in t/U [59]. This magnetic interaction sets the energy scale for the transition between a long-range antiferromagnetically ordered phase (AFI) and a disordered insulating phase (PI). The AFI phase stays insulating for larger values of t/U . It is insulating for values of t/U for which the system is metallic at higher temperatures. The insulating behavior of the AFI phase is due to the breaking of the translational symmetry. Hence it resembles rather a band insulator than a genuine Mott-Hubbard insulator [65]. The system undergoes an insulator-metal transition for increasing bandwidth only for temperatures at which the antiferromagnetic long-range order is suppressed. The conducting region is a paramagnetic metal (PM). The transition from the PI to the PM phase is therefore a transition between two phases which are magnetically disordered. The MIT is a first order transition in infinite dimensions and for not too large temperatures [3]. In finite dimensions, it is possible that the transition is still first order. However, it might also be the case that the system undergoes a crossover only. In the case of two dimensions there is no long-range order at finite temperatures due to the Mermin-Wagner theorem [66]. The AFI phase collapses to the line where $T = 0$. At finite temperatures, only the disordered phases exist.

Elimination of charge fluctuations

The aim of the present chapter is to use a CUT to eliminate charge fluctuations. This can be done only in a certain parameter regime. If the interaction is such that the system is a paramagnetic metal, charge excitations cost zero energy. The elimination of the charge fluctuations is not possible. The transformation is only feasible in the range of parameters where the system is insulating. The phase diagram in Fig. 3.1 shows that the derivation of the effective model requires a certain minimal value of the interaction U . If the interaction U is too small the Hubbard model cannot be mapped onto the effective model.

The effective model is a generalized t - J -model. Charge fluctuations involving the change of the number of DOs are eliminated. The degrees of freedom that are described by the effective model are those of the spins of the electrons and of doped charge carriers. Although the effective model is derived at half filling it keeps track of the dynamics of holes and double occupancies. This is necessary since we have to know how virtual intermediate states evolve and they generically contain charge excitations. The parts of the effective model which describe the dynamics of holes apply also to holes inserted externally by doping. In this sense, the effective model describes also the physics in a vicinity of half filling. The t - J -model describes the remaining degrees of freedom without the precondition of a certain long range order. The state of the spins and of doped charges has to remain unspecified. The reference ensemble may not favor a certain spin

or charge order. These conditions have to be fulfilled in the set up of the CUT.

3.2. Method

In the half filled case, in the limit of infinite U the electrons are fixed on their lattice site by the constraint of having no DO. Reducing U from this limit the electrons are gradually allowed to move producing DOs intermediately. But the physics remains still rather local. In the following, we want to map the Hubbard model for finite U in a systematic way onto an effective model that conserves the number of DOs. The guiding idea will be that the physics can be incorporated into an effective model that contains operators that describe rather local processes. The truncation scheme will rely on the local approach to CUTs described in Chap. 2. The extension of a term decides if it is kept in the flow equations or not. The discussion in the previous section showed that the mapping to a DO conserving effective Hamiltonian will break down for too large values of t/U .

The aim of the transformation is to eliminate charge fluctuations. Charge fluctuations are local deviations from half filling. Such a deviation is either an empty sites or a doubly occupied site. Both types of deviations are called double occupancies (DO). The operator \hat{D} defined in Eq. (3.1.3) counts the number of DOs. The effective Hamiltonian has to conserve the number of DOs. Therefore, a MKU CUT is used with the counting operator \hat{D} . The DOs are the quasiparticles of the MKU scheme. As described in Sec. 2.2.2 the corresponding MKU generator reads

$$\eta(\ell) = [\hat{D}, H(\ell)] = 2\text{sgn}(q_i - q_j) H_{i,j}(\ell). \quad (3.2.4)$$

Except for an overall factor [67], the above η coincides with η in Refs. [12,13], where it was defined using the *sign* of the change in the number of quasiparticles.

It is useful to classify the operators in the kinetic part of the Hamiltonian according to their effect on the number of DOs

$$H_t = T_0 + T_{+2} + T_{-2} \quad (3.2.5a)$$

$$T_0 = t_0 \sum_{\langle i,j \rangle, \sigma} \left[(1 - n_{i,\sigma}) c_{i,\bar{\sigma}}^\dagger c_{j,\bar{\sigma}} (1 - n_{j,\sigma}) + n_{i,\sigma} c_{i,\bar{\sigma}}^\dagger c_{j,\bar{\sigma}} n_{j,\sigma} + \text{h.c.} \right] \quad (3.2.5b)$$

$$T_{+2} = t_{+2} \sum_{\langle i,j \rangle, \sigma} \left[n_{i,\sigma} c_{i,\bar{\sigma}}^\dagger c_{j,\bar{\sigma}} (1 - n_{j,\sigma}) + n_{j,\sigma} c_{j,\bar{\sigma}}^\dagger c_{i,\bar{\sigma}} (1 - n_{i,\sigma}) \right] \quad (3.2.5c)$$

$$T_{-2} = t_{-2} \sum_{\langle i,j \rangle, \sigma} \left[(1 - n_{i,\sigma}) c_{i,\bar{\sigma}}^\dagger c_{j,\bar{\sigma}} n_{j,\sigma} + (1 - n_{j,\sigma}) c_{j,\bar{\sigma}}^\dagger c_{i,\bar{\sigma}} n_{i,\sigma} \right], \quad (3.2.5d)$$

where $\bar{\sigma} = -\sigma$. The projection operators $1 - n_{i,\sigma}$ and $n_{i,\sigma}$ ensure that T_n changes the number of DOs by n . The Hamiltonian, Eq. (3.1.1), changes the number of DOs only by a single, finite absolute value, namely 2. Thus the MKU generator in Eq. (3.2.4), which is usually defined with a sign function, can also be expressed as the commutator $[\hat{D}, H(\ell)]$. The only difference between the matrix elements $\text{sgn}(d_i - d_j) H_{ij}$ and $(d_i - d_j) H_{ij}$ in an eigenbasis of \hat{D} is a factor of 2. The

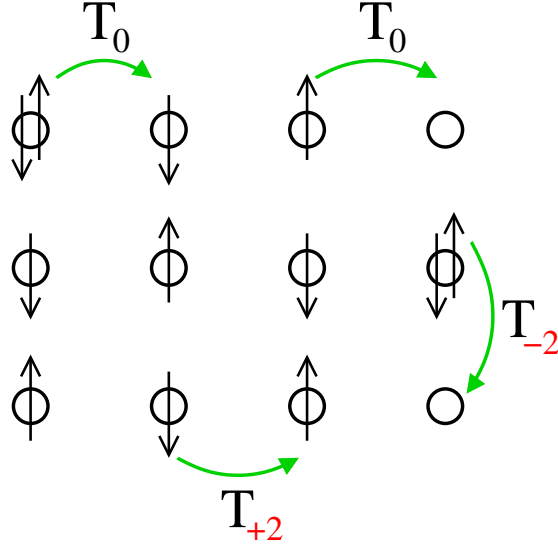


Fig. 3.2: Illustration of various hopping processes. The change in the number of DOs is given by the subscript of the operators T_n .

MKU CUT preserves the block-band structure of the Hamiltonian. In the flow equations no terms will appear that change the number of DOs by a value other than 0, -2 and 2.

The action of the operators T_0 , T_{+2} and T_{-2} is illustrated in Fig. 3.2. A hopping process of a σ electron does not change the number of DOs if the initial and the final site are both empty or both occupied by electrons with spin $-\sigma$. These are the processes represented by the two terms in Eq. (3.2.5b). The number of DOs is increased by two if an electron on a singly occupied site hops onto a site which is occupied by an electron of opposite spin. After this process the initial site is empty and the final site is doubly occupied. Both contribute one quasiparticle excitation. The reverse process reduces the number of DOs by two. More complicated terms are created during the flow. They are also easily classified using the counting operator \hat{D} of DOs.

3.2.1. Reference ensemble

The local basis consists of four states: the empty site $|0\rangle$, two singly occupied states with spin up and spin down, $|\uparrow\rangle$ and $|\downarrow\rangle$, and the state with two electrons, $|\uparrow\downarrow\rangle$. The two singly occupied states, $|\uparrow\rangle$ and $|\downarrow\rangle$, are half filled. They form the set of two local reference states. Here we encounter the case of a true reference *ensemble*. This possibility has been pointed out in Sec. 2.3.2. The reference ensemble is represented by the statistical operator

$$\hat{\rho}_0 := \prod_i \frac{1}{2} (|\uparrow\rangle_{ii}\langle\uparrow| + |\downarrow\rangle_{ii}\langle\downarrow|). \quad (3.2.6)$$

The index i indicates the site of the local state. The reference ensemble in our approach is magnetically completely disordered and without any intersite correlations. It contains the up-

$\mathbf{1}$	$\bar{n} = n_\uparrow + n_\downarrow - \mathbf{1}$	$\sigma^+ = c_\uparrow^\dagger c_\downarrow$	$c_\downarrow c_\uparrow$
$\sigma^z = n_\uparrow - n_\downarrow$	$2n_\uparrow n_\downarrow - \bar{n}$	$\sigma^- = c_\downarrow^\dagger c_\uparrow$	$c_\uparrow^\dagger c_\downarrow^\dagger$
$(1 - n_\downarrow)c_\uparrow$	$(1 - n_\uparrow)c_\downarrow$	$n_\uparrow c_\downarrow$	$n_\downarrow c_\uparrow$
$(1 - n_\downarrow)c_\uparrow^\dagger$	$(1 - n_\uparrow)c_\downarrow^\dagger$	$n_\uparrow c_\downarrow^\dagger$	$n_\downarrow c_\uparrow^\dagger$

Table 3.1: Local operators. The operators in the first two lines have an even number of fermionic operators, those in the last two lines an odd number of fermionic operators; the usual spin operators are $S^z = \sigma^z/2, S^\pm = \sigma^\pm$.

spin and down-spin electrons with the same weight. The reference ensemble constitutes the quasiparticle vacuum in the calculation. This reference ensemble fulfills the condition that the effective Hamiltonian must not rely on a certain magnetic order in the subspace without any DO.

Normal-ordering

The reference ensemble implies the normal-ordered notation of local operators. A local operator o_i is normal-ordered if

$$\langle o_i \rangle_{\text{ref}} := \text{Tr}(o_i \hat{\rho}_0) = \frac{1}{2}(i \langle \uparrow | o_i | \uparrow \rangle_i + i \langle \downarrow | o_i | \downarrow \rangle_i) \quad (3.2.7)$$

vanishes. Table 3.1 gives the local operator basis in normal-ordered form. The operator $\bar{n} = n_\uparrow + n_\downarrow - \mathbf{1}$ counts the number of electrons relative to half filling. The Hubbard operator $2n_\uparrow n_\downarrow - \bar{n}$ counts the number of DOs. The empty state $|0\rangle$ and the doubly occupied state $|\uparrow\downarrow\rangle$ yield $\langle 0 | 2n_\uparrow n_\downarrow - \bar{n} | 0 \rangle = \langle \uparrow\downarrow | 2n_\uparrow n_\downarrow - \bar{n} | \uparrow\downarrow \rangle = 1$ whereas expectation values with $|\uparrow\rangle$ or $|\downarrow\rangle$ vanish. For the spin operator σ^z the sum in Eq. (3.2.7) is zero as well. All other operators in Table 3.1 are non-diagonal in the local basis and thus normal-ordered with respect to the reference ensemble. Also terms which are products of normal-ordered local operators on different sites are normal-ordered.

3.2.2. Two explicit examples for self-similar CUTs in real space

The present section gives two examples for the self-similar CUT scheme. It is intended to illustrate the concepts described in the method section. There are two examples in this section. The first presents a minimal model that includes the NN effective spin coupling. The second effective model keeps all the operators on neighboring sites.

3.2.2.1. Minimal truncation

Starting with H_t and H_U the generator η reads

$$\eta(\ell) = [\hat{D}, H(\ell)] = [\hat{D}, T_{+2} + T_{-2}] = 2T_{+2} - 2T_{-2}. \quad (3.2.8)$$

To set up the flow equation we have to calculate

$$\frac{\partial}{\partial \ell} H(\ell) = [\eta(\ell), H(\ell)] = [\eta(\ell), H_U(\ell) + H_t(\ell)]. \quad (3.2.9)$$

The first contribution to the flow equation

$$[\eta(\ell), H_U(\ell)] = -2U(\ell)T_{+2} - 2U(\ell)T_{-2} \quad (3.2.10)$$

produces the suppression of terms changing the number of DOs as intended. The second contribution reads

$$\begin{aligned} [\eta(\ell), H_t(\ell)] &= [2T_{+2} - 2T_{-2}, T_0 + T_{+2} + T_{-2}] \\ &= 32t_{+2}t_{-2} \cdot \frac{1}{2} \hat{D} \end{aligned} \quad (3.2.11a)$$

$$+16t_{+2}t_{-2} \sum_{\langle i,j \rangle} \mathbf{S}_i \cdot \mathbf{S}_j \quad (3.2.11b)$$

$$-4t_{+2}t_{-2} \sum_{\langle i,j \rangle} \bar{n}_i \bar{n}_j \quad (3.2.11c)$$

$$+8t_{+2}t_{-2} \sum_{\langle i,j \rangle} (c_{i,\uparrow}^\dagger c_{i,\downarrow}^\dagger c_{j,\downarrow} c_{j,\uparrow} + h.c.) \quad (3.2.11d)$$

$$+ \dots \quad (\text{three site terms}).$$

Only terms with maximal extension up to $d = 1$ are kept. The extension of an operator is defined in Sec. 2.3.4. It measures the maximum taxi cab distance of two local operators in a term. Terms with extension up to $d = 1$ are found in Eqs. (3.2.11)a through d. In Eq. (3.2.11) the terms containing operators on three different sites are omitted. Their extension is $d = 2$. The term in Eq. (3.2.11a) will renormalize the strength of the Hubbard interaction U . The next line, Eq. (3.2.11b), generates the Heisenberg exchange

$$H_{\text{NN}} = J_1(\ell) \sum_{\langle i,j \rangle} \mathbf{S}_i \cdot \mathbf{S}_j \quad (3.2.12)$$

with the initial condition $J_1(0) = 0$. To get a minimal model for the NN exchange we neglect the terms in Eqs. (3.2.11c) and (3.2.11d). The exchange term H_{NN} will not produce a contribution to η since it does not change the number of DOs. As a further simplification we neglect the terms that would arise from the commutator $[\eta, H_{\text{NN}}]$. The resulting CUT will be called *minimal* model.

Exploiting that operators related by hermitian conjugation have the same real coefficient we know $t_{+2} = t_{-2}$. Thus the differential equations for this truncation read

$$\partial_\ell U(\ell) = 32t_{+2}(\ell)^2 \quad (3.2.13a)$$

$$\partial_\ell t_0(\ell) = 0 \quad (3.2.13b)$$

$$\partial_\ell t_{+2}(\ell) = -2U(\ell)t_{+2}(\ell) \quad (3.2.13c)$$

$$\partial_\ell J_1(\ell) = 16t_{+2}(\ell)^2. \quad (3.2.13d)$$

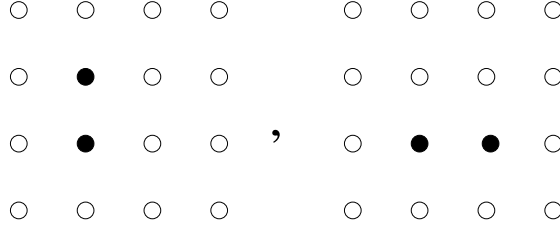


Fig. 3.3: Clusters in the square lattice that define the NN truncation scheme. Filled circles indicate the two clusters defining the truncation rule of the NN truncation. Only terms fitting on these clusters are kept.

Using the conserved quantity $s = \sqrt{64t_{+2}(\ell)^2 + 4U(\ell)^2}$ we obtain for this truncation

$$U(\ell) = \frac{s}{2} \tanh(s\ell + C) \quad (3.2.14a)$$

$$t_0(\ell) = t_0(0) \quad (3.2.14b)$$

$$t_{+2}(\ell) = t_{-2}(\ell) = (s/8)\sqrt{1 - \tanh^2(s\ell + C)} \quad (3.2.14c)$$

$$J_1(\ell) = s [\tanh(s\ell + C) - 2U_0/s] / 4 \quad (3.2.14d)$$

where $C = \operatorname{arctanh}(2U_0/s)$. The effective model is obtained in the limit $\ell \rightarrow \infty$. Since $t_{+2}(\infty) = 0$ it contains only terms conserving the number of DOs

$$H_{\text{eff}} = T_0 + U(\infty)\frac{1}{2}\hat{D} + J_1(\infty)\sum_{\langle i,j \rangle} \mathbf{S}_i \cdot \mathbf{S}_j. \quad (3.2.15)$$

Strictly at half filling, Eq. (3.2.15) reduces to a Heisenberg model with effective coupling $J_{1,\text{eff}} = J_1(\infty)$

$$J_{1,\text{eff}} = \frac{U}{2}\sqrt{1 + 16(t/U)^2} - \frac{U}{2} \quad (3.2.16a)$$

$$= \frac{4t^2}{U} + \mathcal{O}(t^4/U^3). \quad (3.2.16b)$$

For small t/U this reproduces the well-known second order result [22, 59] $J_1^{(2)} = \frac{4t^2}{U}$. Note that the final results are given in t and U denoting the initial, bare values. For clarity we use $t_0 = t$ and $U_0 = U$ to denote the initial values while solving the flow equation. The result in Eq. (3.2.16) coincides with the result one gets from diagonalization of a two-site cluster for the splitting between the singlet and the triplet state and thus for J . This is purely coincidental. Taking into account *all* operators on NN sites in the CUT leads to a different result as is shown in the following section.

3.2.2.2. The NN truncation

The NN truncation relies only on the extension of the terms that appear in the flow equation. The extension of a term has been defined in Sec. 2.3.4 as the maximal distance between two

local operators measured in the taxi cab metric. The maximal extension for the NN truncation is $d = 1$. The truncation rule for the NN truncation can be visualized by the two clusters shown in Fig. 3.3. All terms are kept that contain only local operators on two neighboring sites. Thus, the terms in Eqs. (3.2.11c) and (3.2.11d) have to be included in the Hamiltonian

$$H_V = V(\ell) \sum_{\langle i,j \rangle} \bar{n}_i \bar{n}_j \quad (3.2.17)$$

$$H_{\text{pair}} = V_{\text{pair}}(\ell) \sum_{\langle i,j \rangle} (c_{i,\uparrow}^\dagger c_{i,\downarrow}^\dagger c_{j,\downarrow} c_{j,\uparrow} + h.c.) . \quad (3.2.18)$$

H_V describes interactions of electrons on NN sites, H_{pair} the hopping of two electrons between site i and j . These terms do not change the number of DOs. Thus, they generate no new contributions in η . Calculating $[\eta, H_{\text{NN}} + H_V + H_{\text{pair}}]$ and neglecting again terms that do not fit on NN sites we obtain the closed flow equation

$$\partial_\ell U(\ell) = 32t_{+2}(\ell)^2 \quad (3.2.19a)$$

$$\partial_\ell t_0(\ell) = 0 \quad (3.2.19b)$$

$$\partial_\ell t_{+2}(\ell) = -2U(\ell)t_{+2}(\ell) + t_{+2}(\ell)(2V(\ell) - 2V_{\text{pair}}(\ell) - 3J(\ell)/2) \quad (3.2.19c)$$

$$\partial_\ell J_1(\ell) = 16t_{+2}(\ell)^2 \quad (3.2.19d)$$

$$\partial_\ell V(\ell) = -4t_{+2}(\ell)^2 \quad (3.2.19e)$$

$$\partial_\ell V_{\text{pair}}(\ell) = 8t_{+2}(\ell)^2 . \quad (3.2.19f)$$

The truncation criterion ensures that the flow equations close since only a finite number of terms can meet the truncation criterion. The solution for J_1 is

$$J_1^{\text{NN}}(\ell) = \frac{2r}{7} \tanh(2r\ell + D) - \frac{2}{7}U_0 \quad (3.2.20)$$

where $r = \sqrt{28t_0^2 + U_0^2}$ and $D = \text{arctanh}(U_0/r)$. This yields in the limit $\ell \rightarrow \infty$ the effective NN spin-coupling of the NN truncation

$$J_{1,\text{eff}}^{\text{NN}} = \frac{2}{7} \sqrt{U^2 + 28t^2} - \frac{2}{7}U , \quad (3.2.21)$$

where the final result is given in the bare parameters recalling $t_0 = t, U_0 = U$. As expected the result is different from the result from the exact diagonalization of a finite two site cluster. The exact diagonalization deals with a finite system only whereas the CUT is a renormalization procedure in the thermodynamic limit where the terms kept are chosen according to their locality.

3.2.3. Comparison to perturbation theory

The CUT calculations for the minimal and the NN truncation yield non-divergent results for all values of t/U . They reproduce the leading order of the perturbative expansion. The result for J_1 up to sixth order in perturbation theory reads

$$J_1 = \frac{4t^2}{U} - \frac{24t^4}{U^3} + \frac{331t^6}{U^5} + \mathcal{O}(t^8/U^7) . \quad (3.2.22)$$

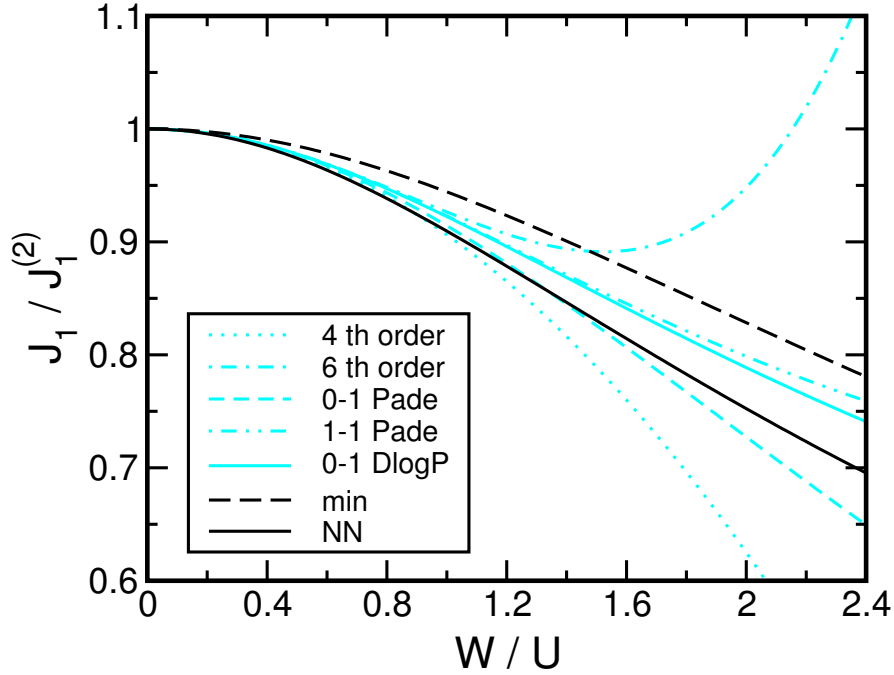


Fig. 3.4: Results for the Heisenberg coupling J_1 from the minimal and the NN truncation compared to perturbation theory. All curves are plotted relative to $J_1^{(2)} = 4t^2/U$. The numbers in the legend in front of Padé or DlogP indicate the degree of the polynomials in $x = t^2/U^2$ in the numerator and denominator of the Padé approximant. Recall that $W = 8t$ holds.

We have calculated the sixth order term using the perturbation theory presented in Ref. [23] where the fourth order term is given. Figure 3.4 compares the results for the Heisenberg coupling J_1 . All results are given relative to the second order $J_1^{(2)} = 4t^2/U$.

The perturbative results are truncated power series in the expansion parameter t/U . They are shown as gray dotted and dashed-dotted curves. For large values of t/U they are dominated by the contribution with the highest power of the expansion parameter. They exhibit strongly divergent behavior even if the fourth and sixth order is included. In addition, Fig. 3.4 shows the results of various Padé-approximants derived from the series of the perturbation theory [68]. The dashed and the dashed-dotted gray curve represent a $0-1$ and a $1-1$ Padé-approximant, respectively. The solid gray curve shows a Dlog-Padé-approximant.

The dashed and solid black lines show the result for J_1 from the minimal and the NN truncation, respectively. They do not show divergent behavior. The results are meaningful also for large values of t/U . Already the minimal model correctly reproduces the leading order behavior of the perturbation theory. The results of the Padé-approximants support that the CUT results of the minimal and the NN truncation lie in the reasonable range of values. It is remarkable that CUT calculations with rather few couplings involved produce these results. The result for J_1 is

reasonable for small and also intermediate and rather large values of the bandwidth W . They reproduce the perturbative behavior for small t/U and they do not show divergent behavior for large t/U . Thus, the self-similar approach to CUTs provides a tool to derive an effective Hamiltonian also in cases where perturbative treatments are not easy to control.

The CUT calculation will be further improved by taking into account more terms on more complex site configurations leading to higher truncation schemes. The agreement of calculations with various numbers of operators will be a probe for the accuracy of the results.

Generally, the result of a self-similar CUT calculation will reproduce the result for a certain coefficient of a perturbative calculation if all operators are taken into account that appear in the intermediate steps of the perturbative derivation of this coefficient. Therefore, the minimal and the NN calculation reproduce the second order of the expansion of the Heisenberg coupling J_1 . Higher orders of the perturbative expansion will be reproduced only if more terms on larger clusters are taken into account. In Sec. 3.2.5 two higher truncation schemes are introduced that reproduce the fourth and sixth order of the perturbation theory.

The NN truncation does not give the perturbative result for *all* terms in second order. Additional terms on larger clusters are necessary to reproduce all second order processes. The reason is that we have omitted certain terms in Eq. (3.2.11). There are three site processes that appear already in second order in t/U . These are truncated in the NN truncation scheme. The set of terms necessary to reproduce the perturbative result is different for different terms. This has to be kept in mind when comparing the results of a self-similar CUT to perturbative results.

3.2.4. Comparison of different unitary transformations

In Sec. 2.4 it has been pointed out that the unitary transformation leading to block-band diagonality is not unique. Any additional unitary transformation within the blocks conserves block-band diagonality. This fact has also been observed by *Lenz* and *Wegner* in Ref. [25] and by *Stein* in Ref. [26]. The effective Hamiltonians of two different unitary transformations are generically different. This fact is illustrated in the present section by comparing two different *perturbative* realizations of unitary transformations. The present section is a digression from the discussion of the self-similar approach to the Hubbard model. Yet it presents some facts that are interesting for the application of unitary transformations in general. We will return to the main track of the discussion in Sec. 3.2.5.

The Hubbard Hamiltonian is separated into an unperturbed part H_U and a perturbation V

$$H_0 = H_U \tag{3.2.23}$$

$$V = H_t = T_0 + T_{+2} + T_{-2}. \tag{3.2.24}$$

A unitary transformation is constructed which eliminates terms changing the number of double occupancies to a given order in t/U . The effective Hamiltonian consists of a sum of products of the operators T_0 , T_{+2} and T_{-2} . In the approach followed by *Stein* in Ref. [26] the effective Hamiltonian is constructed using a continuous unitary transformation with the generator

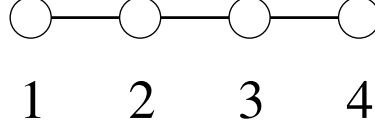


Fig. 3.5: Finite cluster of four linearly arranged sites. Site numbers range from 1 to 4.

Eq. (3.2.4). We will only consider the case of a half filled Hubbard model. Then, the effective Hamiltonian for the subspace without any DO can be cast into the form of a spin Hamiltonian. To illustrate the structure of the effective Hamiltonian the leading orders are given explicitly. The resulting effective Hamiltonian [26] reads in second order in t/U

$$\frac{H_{\text{eff,Stein}}^{(2)}}{1/U} = T_2 T_{-2} - T_{-2} T_2 \quad (3.2.25)$$

and in fourth order

$$\begin{aligned} \frac{H_{\text{eff,Stein}}^{(4)}}{1/U^3} = & \frac{1}{4} T_0 T_0 T_2 T_{-2} - \frac{1}{4} T_0 T_0 T_{-2} T_2 - T_0 T_2 T_0 T_{-2} + \frac{1}{2} T_0 T_2 T_{-2} T_0 \\ & + T_0 T_{-2} T_0 T_2 - \frac{1}{2} T_0 T_{-2} T_2 T_0 + T_2 T_0 T_0 T_{-2} - T_2 T_0 T_{-2} T_0 \\ & + \frac{1}{2} T_2 T_2 T_{-2} T_{-2} + \frac{1}{4} T_2 T_{-2} T_0 T_0 - T_2 T_{-2} T_2 T_{-2} - T_{-2} T_0 T_0 T_2 \\ & + T_{-2} T_0 T_2 T_0 - \frac{1}{4} T_{-2} T_2 T_0 T_0 + T_{-2} T_2 T_{-2} T_2 - \frac{1}{2} T_{-2} T_{-2} T_2 T_2. \end{aligned} \quad (3.2.26)$$

Each operator T_0 , T_{+2} and T_{-2} carries a factor of t .

The perturbation theory introduced by *Takahashi* [23] is a different perturbative unitary transformation that realizes a mapping onto a DO conserving effective model. There are also other approaches that can be used, see Ref. [26] and references therein. We will concentrate on the two methods of *Stein* and *Takahashi* because they provide a particularly simple way of deriving the effective model.

For simplicity, we will consider the Hubbard model at half filling on a finite cluster. The cluster is shown in Fig. 3.5. It consists of a chain of four sites. The perturbative expansion of Stein and Takahashi differ in eighth order in the case of half filling. Away from half filling the

first differences appear already in fourth order. The difference in eighth order reads

$$\begin{aligned}
\frac{H_{\text{eff,Tak}}^{(8)} - H_{\text{eff,Stein}}^{(8)}}{1/U^7} &= +\frac{35}{16}T_{-2}T_2T_{-2}T_0T_0T_2T_{-2}T_2 - \frac{35}{32}T_{-2}T_0T_0T_2T_{-2}T_2T_{-2}T_2 \\
&- \frac{35}{32}T_{-2}T_2T_{-2}T_2T_{-2}T_0T_0T_2 - \frac{7}{8}T_{-2}T_0T_2T_{-2}T_2T_{-2}T_0T_2 \\
&+ \frac{7}{16}T_{-2}T_0T_2T_{-2}T_0T_2T_{-2}T_2 + \frac{7}{16}T_{-2}T_2T_{-2}T_0T_2T_{-2}T_0T_2 \\
&+ \frac{17}{24}T_{-2}T_2T_{-2}T_{-2}T_2T_2T_{-2}T_2 - \frac{17}{48}T_{-2}T_2T_{-2}T_2T_{-2}T_{-2}T_2T_2 \\
&- \frac{17}{48}T_{-2}T_{-2}T_2T_2T_{-2}T_2T_{-2}T_2. \tag{3.2.27}
\end{aligned}$$

The difference is written in the complicated form of products of T_n -operators. It is not obvious if Eq. (3.2.27) is equal to zero or not. Therefore, it is rewritten in the spin language. It reads

$$\begin{aligned}
\frac{H_{\text{eff,Tak}}^{(8)} - H_{\text{eff,Stein}}^{(8)}}{t^8/U^7} &= -\frac{74}{3}\mathbf{S}_1 \cdot \mathbf{S}_2 + \frac{31}{3}\mathbf{S}_1 \cdot \mathbf{S}_3 - \frac{62}{3}\mathbf{S}_1 \cdot \mathbf{S}_4 + \frac{148}{3}\mathbf{S}_2 \cdot \mathbf{S}_3 + \frac{31}{3}\mathbf{S}_2 \cdot \mathbf{S}_4 \\
&- \frac{74}{3}\mathbf{S}_3 \cdot \mathbf{S}_4 - \frac{124}{3}(\mathbf{S}_1 \cdot \mathbf{S}_2)(\mathbf{S}_3 \cdot \mathbf{S}_4) + \frac{296}{3}(\mathbf{S}_1 \cdot \mathbf{S}_3)(\mathbf{S}_2 \cdot \mathbf{S}_4) \\
&- \frac{172}{3}(\mathbf{S}_1 \cdot \mathbf{S}_4)(\mathbf{S}_2 \cdot \mathbf{S}_3). \tag{3.2.28}
\end{aligned}$$

Indices denote the sites within the cluster shown in Fig. 3.5. In the spin language it is clear that the above operator has non-vanishing matrix elements. This implies that also the perturbative expansion of the spin couplings will be different in the two approaches. For example consider the coefficient of the following two-spin term

$$H_{12} = J_{12}\mathbf{S}_1 \cdot \mathbf{S}_2. \tag{3.2.29}$$

The coefficient J_{12} differs by $-74/3t^8/U^7$ in eighth order in the two perturbative schemes, see Eq. (3.2.28).

The perturbative expansion of the coefficients of the effective model can be different for different unitary transformation. This has to be kept in mind when comparing the results of different perturbative approaches. In Ref. [26] *Stein* compares the CUT approach to the perturbative approach used by *MacDonald* and coworkers [24]. Also in this case differences are found in the formulation with T_0 , T_{+2} and T_{-2} operators.

The value of any physical quantity is unique. Its perturbative expansion has unique coefficients. The differences found above in the coefficients of the effective model are compatible with this statement. We have calculated the eigenvalues of the system using both approaches. They agree up to the order to which the expansion was carried out. The results of the two approaches are in agreement with each other and with the expansion of the exact eigenenergies. However, there are differences in higher orders. The eigenvalues display differences which are of tenth order in the expansion parameter. Yet this is not in contradiction with the uniqueness of physical quantities because all *reliably determined* orders agree.

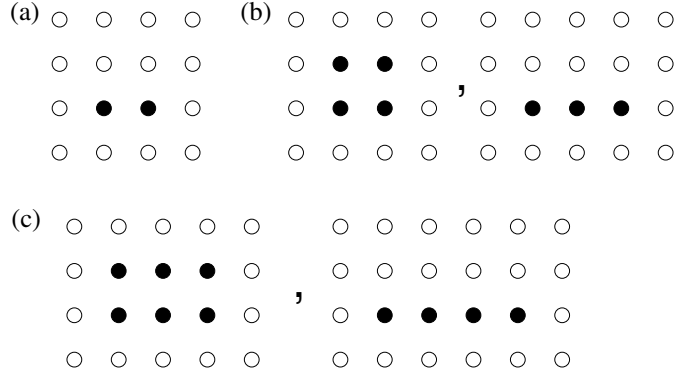


Fig. 3.6: Various clusters defining the operators to be kept in the CUT. Only one of the various clusters that are related by the point group symmetry of the two-dimensional square lattice is shown.

A similar conclusion can be found in the case of the elimination of the electron-phonon coupling treated by *Lenz* and *Wegner* [25]. The resulting electron-electron interaction differs from the one found by *Fröhlich* [20]. However, the matrix elements which correspond to physical quantities, like for instance energies, are the same.

There is a freedom in the choice of a unitary transformation achieving block-diagonality. This freedom is represented in the operator Eq. (3.2.28). If one adds multiples of this operator to the effective Hamiltonian the resulting eigenvalues remain unchanged in the given order of the perturbative expansion. It is an important point that agreement in perturbation theory can only mean agreement up to a certain order. The addition of Eq. (3.2.28) to the effective Hamiltonian changes higher orders of physical quantities.

We have tried to exploit this fact by adding multiples of the operator Eq. (3.2.28) to the effective Hamiltonian. In this way one can adjust for one chosen quantity the next order in the perturbative expansion to have the correct value. The correct values are known for the finite system shown in Fig. 3.5. Thus one can tune the eighth order result to contain also the correct tenth order of the perturbative expansion. However, we did not succeed in defining a precise way of improving the results in this way. One can only tune the coefficients of a single eigenvalue. There was no systematic way to improve the result for the whole system. In the end one would have liked to give a general prescription also for many-body systems where the exact solution is not known. Since this has not been possible it was decided to stick to the CUTs as defined in the method section, Sec. 2. They provide a systematic way to derive the effective Hamiltonian without artificial adjustments.

3.2.5. Higher truncation schemes

The truncation scheme relies on the locality of the terms. Figure 3.6 shows the clusters defining the various truncation schemes. The sites that belong to the clusters are depicted as filled circles

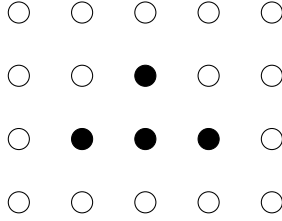


Fig. 3.7: A term affecting the filled sites in this graph has extension $d = 2$. It complies with a truncation scheme that is defined by a maximal extension 2. Such a term is discarded in the plaquette truncation scheme.

within the two-dimensional square lattice. Only one representative is shown for different clusters that are related by the point-group symmetry of the square lattice. We use the clusters that are necessary for a perturbative derivation of the spin Hamiltonian from the Hubbard model as a guideline for the choice of the clusters defining the truncation. This leads to a definition of the truncation scheme which differs slightly from the one relying only on the extension of terms.

In second order the NN Heisenberg exchange is the only effective spin coupling. For its perturbative derivation a cluster of two neighboring sites is sufficient. Thus, the NN truncation is defined by the cluster given in Fig. 3.6a. The cluster in Fig. 3.6a represents the two possible clusters of NN sites on the two-dimensional square lattice. In fourth order in the electron hopping further hopping processes contribute to the effective spin couplings. The cluster of four sites on a plaquette of the square lattice and the linear cluster of three sites cover all hopping processes relevant for the derivation of the spin couplings in fourth order. They are depicted in Fig. 3.6b.

The present truncation scheme is motivated by the correspondence to a perturbative derivation of the spin couplings. This truncation scheme is not the same as taking all terms with extension $d = 2$ into account. This is illustrated by the cluster shown in Fig. 3.7. In the derivation of the spin couplings only processes contribute that return to a state that has the same local electron occupation as the initial state. A hopping process in fourth order linking all sites on the cluster in Fig. 3.7 will not leave the electron occupation unchanged. Therefore it is discarded in the present truncation scheme that is defined by the clusters in Fig. 3.6b. Yet, there are processes in fourth order that link the sites of the cluster in Fig. 3.6b. These processes would give a contribution to a CUT defined only by a maximal extension $d = 2$.

The double plaquette and the linear chain of four sites depicted in Fig. 3.6c are representatives for the clusters necessary for accounting fully of the 6th order of the spin Hamiltonian. The calculation for the clusters in Fig. 3.6c has been the largest possible. To have an additional comparison, we have also performed calculations keeping only the operators which affect at most four different sites on the clusters of Fig. 3.6c. In summary, the various truncation schemes are

- (i) **minimal** model: only H_U, H_t, H_{NN}
- (ii) **NN**: cluster used in 2nd order perturbation theory, Fig. 3.6a.

Calculation	#operators in H	# of terms in DE
(i) minimal	4	3
(ii) NN	6	8
(iii) plaquette	172	10,364
(iv)	2,217	1,341,736
(v) double-plaquette	26,251	304,514,721

Table 3.2: Number of operators in the Hamiltonian reduced by the symmetries given in the main text for various approximation schemes. This number coincides with the number of differential equations. In the last column the total number of all bilinear terms on the right-hand side of the differential equations is listed.

(iii) **plaquette** and three-site chain: clusters used in 4th order, Fig. 3.6b.

(iv) operators on up to four different sites on the clusters of Fig. 3.6c.

(v) **double-plaquette** and four site chain: clusters used in 6th order, see Fig. 3.6c.

The NN truncation (ii) yields the leading order result for the NN spin coupling J_1 , the plaquette truncation (iii) yields the correct result in 4th order, and the double plaquette truncation (v) yields the correct result in 6th order. We have confirmed that our implementation complies with these checks.

The use of symmetries is essential to reduce the computational cost for setting up and solving the flow equations. For the implementation of symmetries in the CUT scheme see Sec. 2.5.2. The symmetry group G used for the Hubbard model consists of the point-group symmetry of the square lattice, i.e., rotations about multiples of $\pi/2$ and reflections about the axes and diagonals. Additionally, terms which are related by hermitian conjugation, by particle-hole transformation, and by flipping $\sigma \rightarrow -\sigma$ all spin indices carry the same coefficient. The particle-hole symmetry is only present at half filling. In a calculation for a Hubbard model doped away from half filling this particular symmetry cannot be used. Table 3.2 shows the number of terms, reduced by the symmetries, in the Hamiltonian of each calculation. The third column of Tab. 3.2 lists the total number of all bilinear terms on the right-hand side of the differential equation. The number of variables and the number of differential equations is growing fast with the size of the cluster defining the truncation rule. This renders both the set up of the flow equation and its numerical integration computationally costly.

The double-plaquette calculation takes the largest amount of computation time. As discussed in Sec. 2.5 it is possible to split the calculation of the flow equation into separate runs. For the double plaquette, about 65 separate runs have been performed, each with a CPU time below 10 hours and less than 0.5 Gbyte memory on Sun UltraSPARC workstations. The solution of the differential equation has taken typically 120 hours of CPU time and about 2.5 Gbyte on Sun UltraSPARC workstations.

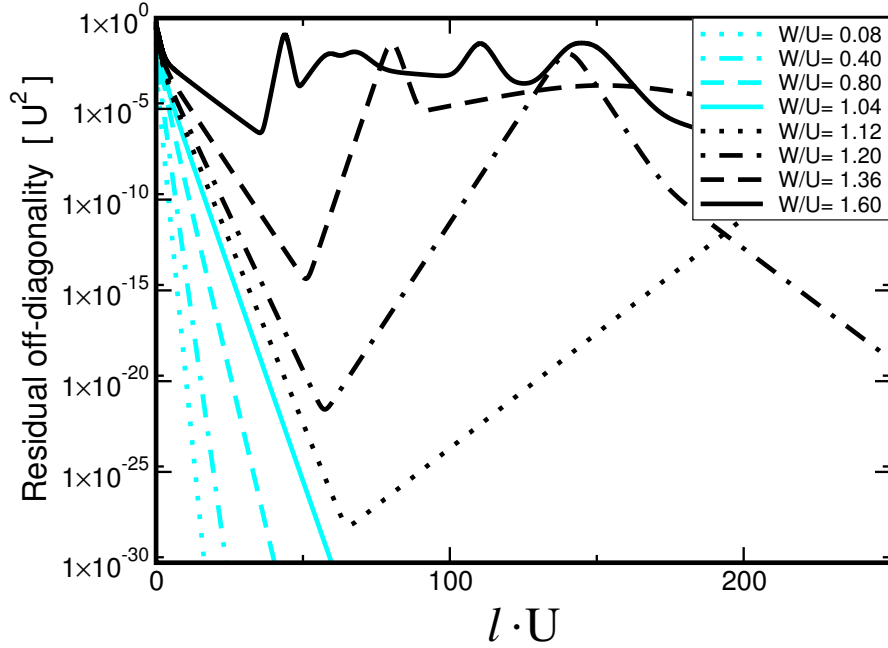


Fig. 3.8: Evolution of the residual off-diagonality in the double-plaquette calculation (ν) for various values of W/U .

3.3. Results

The results of the calculations with various truncation schemes are discussed in this section. Before the coefficients of the effective Hamiltonian are presented we highlight certain properties of the CUT. They enable us to analyze the limitations of the construction of the t - J -model. First, the behavior of the residual off-diagonality is discussed and, second, the importance of operators of different extension. These quantities give insight in the convergence of the CUT itself and in the locality of the effective model. For increasing W/U we find that rather extended terms give sizeable contributions to the effective model.

An additional criterion for the possibility of the mapping to a DO conserving effective model will be found in the analysis of the apparent gap Δ_{app} . The apparent gap Δ_{app} is the energy cost that separates quasiparticle excitations from the ground state sector of the Hilbert space. The sector with zero quasiparticles is not a single state, but an ensemble. Therefore, the calculation of the gap is more complicated than in a situation with a unique reference state. The operator Lanczos technique is applied to calculate the separation of different quasiparticle sectors as function of the hopping parameter.

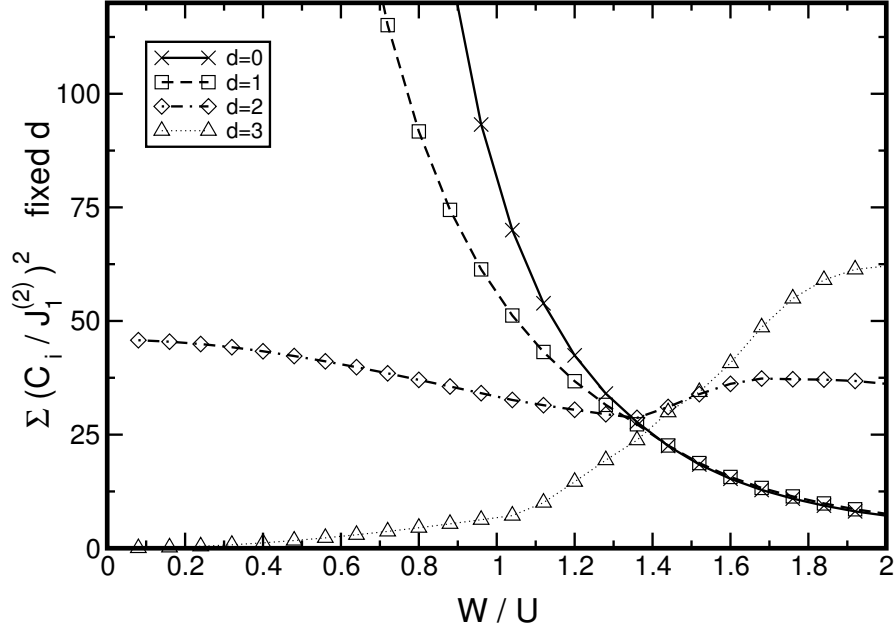


Fig. 3.9: Distribution of coefficients as function of W/U according to the spatial extension d of the respective terms in the double-plaquette calculation (v). The sum of the squares of the coefficients are plotted relative to the second order Heisenberg exchange $J_1^{(2)} = 4t^2/U$.

3.3.1. Properties of the CUT

The residual off-diagonality (ROD) has been defined in Sec. 2.3.4 as the sum of the squares of all coefficients that change the number of quasiparticles. The ROD measures the extent to which the unitary transformation has eliminated the terms that change the number of DOs. The ROD of the calculations with truncation scheme (i) to (iv) show exponential convergence. The unitary transformation is carried out to very low values of the ROD without problems. Since the integration is done numerically one cannot perform the transformation until $l = \infty$. Therefore the flow is stopped at a value of the flow parameter l where the ROD has fallen below a low threshold. Typically this value is $10^{-18}U^2$. The remaining very small coefficients of off-diagonal terms are neglected.

The ROD of the double-plaquette calculation (v) is shown in Fig. 3.8 for various values of W/U . It displays non-monotonic behavior for larger values of W/U . At $l = 0$ the operators in T_{+2} and T_{-2} in Eq. (3.2.5) contribute to the residual off-diagonality. Written with the operators in Table 3.1 these are $4 \cdot 2 = 8$ terms (hopping forth and back in x- and y-direction, with spin up or down) in T_{+2} and T_{-2} each. Therefore the curves in Fig. 3.8 for the residual off-diagonality start at $l = 0$ with the value $8t_{+2}^2 + 8t_{-2}^2 = 16t^2$.

The ROD shows exponential decay for values of the bandwidth up to $W/U = 1.04$. The curve for $W/U = 1.12$ displays non-monotonic behavior. It falls below $10^{-27}U^2$ to rise again up to

$10^{-3}U^2$ for $l * U \approx 270$. Non-monotonic behavior occurs for all values of $W/U \geq 1.12$. An uprise in the ROD has already been observed in the case of the two-level model discussed in Sec. 2.2.3. The ROD increases if states are not ordered according to their quasiparticle number. In the present case the uprise signals that the intended transformation cannot be performed in a well-controlled way. The sectors with different double occupancy cannot be separated. Thus it is not possible to make the number of DOs a conserved quantity. The next section analyzes the dependence of the apparent gap on W/U . It will be shown that the non-monotonic behavior of the ROD appears only in a parameter range where the mapping is no longer possible. For parameters $W/U \lesssim 0.9$, where the mapping is possible according to $\Delta_{\text{app}} > 0$, we find an exponential decrease of the residual off-diagonality down to values where the calculation is limited by the numerical accuracy of the computer implementation.

This conclusion is supported by the distribution of coefficients over terms of various extensions d . The distribution of coefficients on the extensions is a measure of the locality of the effective model. The truncation scheme limits the maximal possible extension. If the terms with maximal extension constitute a large fraction of the total coefficients it is doubtful that the effective model captures all relevant terms. In this case even terms with larger extension should be incorporated into the effective model.

Figure 3.9 shows the distribution of coefficients over various values of the extension. The figure shows the sum of the squares of all coefficients C_i of terms with the definite extension d at the end of the flow. They are given as functions of W/U . The results are given in units of $J_1^{(2)} = 4t^2/U$ which is a natural scale for the parameters defining the effective model. The Hubbard repulsion term H_U is the only term with extension $d = 0$. Its coefficient is large for small W/U . The relevance of the most local terms with $d = 0$ and $d = 1$ decreases for increasing W/U . Whereas the contribution of terms with extension $d = 2$ stays fairly constant there is a clear increase of the $d = 3$ contribution around $W/U = 1.2$. This is also the maximal extension possible in the double-plaquette calculation. The increase of the coefficients with the largest possible extension indicates that for values larger than $W/U = 1.2$ one should take into account even more extended terms. However, the behavior of the ROD and especially the analysis of the apparent gap in the following section will put more restrictive conditions on the parameter regime where the mapping to the effective model is possible. Figure 3.9 shows on the other hand that the double-plaquette calculation includes all relevant terms for values up to $W/U = 0.9$. The coefficients with extension $d = 3$ constitute only a minor contribution in this parameter range.

Apparent charge gap

In the setup of the CUT for the Hubbard model we have argued that the mapping to a DO conserving effective model is not possible for large bandwidth W . The behavior of the ROD and the distribution of coefficients on the extension have supported this view. The present section studies the possibility of the mapping further. Below we calculate the apparent charge gap Δ_{app} within the effective model. The apparent charge gap is the energy gap of a DO propagating

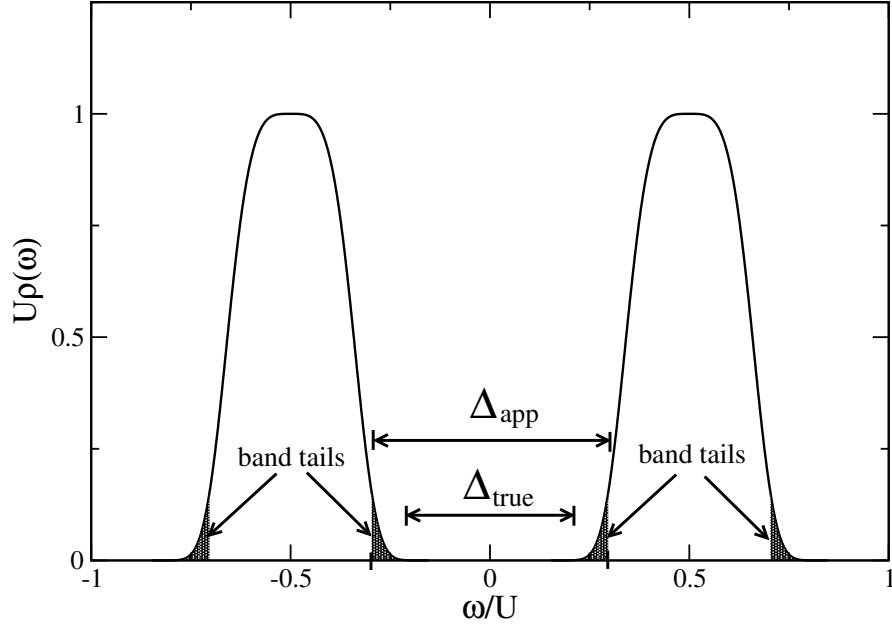


Fig. 3.10: Schematic density of states displaying band tails. An approximate numerical treatment will find an apparent gap Δ_{app} which is larger than the true gap Δ_{true} . This is due to the appearance of band tails.

in the spin background given by the reference ensemble. The DO can be a hole or a double occupation of a site. Since the paramagnetic reference ensemble is not the true ground state the apparent charge gap Δ_{app} is *not* the true charge gap. The apparent charge gap measures the separation of energy scales. This separation governs the convergence of the mapping as it is performed here. We will discuss this issue and its physical significance in more detail in the Discussion in Sec. 3.4.

The apparent gap has to be calculated for the effective Hamiltonian given by the CUT. This effective Hamiltonian is a generalized t - J model including a large number of terms. An additional complication is that the DO is propagating in a paramagnetic background given by the reference ensemble.

Before we describe the calculation of the apparent gap it is instructive to look at some results that are known for related problems. The problem of a single particle propagating in a spin background has been treated by *Brinkman* and *Rice* [69]. In this work the cases of ferromagnetic, antiferromagnetic and random spin background are treated. The density of states is calculated within the so-called retraceable path approximation. The authors point out that it is to be expected that the density of states exhibits Lifshitz tails. A schematic density of states for this physical situation is shown in Fig. 3.10. There are two Hubbard bands centered at energy $\omega = \pm U/2$. The density of states $\rho(\omega)$ consists of a central region and so-called Lifshitz tails [69–72]. Most of the weight is situated in the central region. The weight in the band tails is small.

The true gap is labeled with Δ_{true} in Fig. 3.10.

The small weight in the band tails is difficult to describe with an approximate numerical method. Therefore, it is well possible that a numerical treatment finds a larger value for the gap, namely an apparent gap Δ_{app} , and not Δ_{true} . Such an approximate treatment correctly describes most of the weight which is situated in the band center. But it does not capture the band tails. The band tails can lead to finite lifetime effects if different bands overlap. This would not be described by the approximate treatment. However, the effect of the band tails is expected to be small because their spectral weight is small. The appearance of band tails is a generic feature of the one-particle dynamics in a spin background, see e.g. Refs. [71, 73–76].

Coming back to our present problem, the apparent gap is the lowest energy cost of a DO moving in the spin background. The dispersion of a single DO is now determined using the Lanczos method, see Appendix A and Refs. [77, 78]. The spin background is given by the reference ensemble. It is possible that band tails are present. These band tails contain only little spectral weight. It is difficult to capture this spectral weight in a numerical treatment like the Lanczos technique. The small weight in the band tails is only detected in high Lanczos coefficients. Since the present calculation has to deal with complicated effective Hamiltonians it is well possible that the band tails are not correctly described. Nevertheless, the Lanczos calculation gives important insight in the possibility of the mapping to the effective model. For the same reason that the band tails are hard to detect, namely their low spectral weight, it is expected that they play only a minor role in the possibility of the mapping. The CUT will break down if the sectors with different DO overlap considerably. A considerable overlap will be captured in the following Lanczos calculation.

The Lanczos technique is applied within the Liouville or projection formalism, see Appendix A and Ref. [79]. This is the appropriate technique in the present situation. One does not have to deal with simple states in a Hilbert space but with ensembles derived from the paramagnetic reference ensemble in Eq. (3.2.7) by the application of operators. As usual in the Heisenberg picture, the dynamics of operators in the frequency domain is captured by the commutation with the Hamiltonian.

The Lanczos algorithm starts from the operator \mathcal{O}_0 which generates a single DO with momentum k

$$\mathcal{O}_0 := \frac{1}{\sqrt{N}} \sum_{\mathbf{r}} e^{i\mathbf{k}\mathbf{r}} n_{\mathbf{r},\downarrow} c_{\mathbf{r},\uparrow}^\dagger \quad (3.3.30)$$

where the number of sites is denoted by N and the sum extends over the whole lattice. A real space representation of the action of this initial operator on the reference ensemble is sketched in Fig. 3.11a. The operator Eq. (3.3.30) introduces a DO at a certain site in the lattice. This site is then occupied by a spin-up and a spin-down electron. On the other sites the reference ensemble is not changed. These sites are depicted by shaded circles in Fig. 3.11a.

The Lanczos method constructs iteratively a series of basis states $\{\mathcal{O}_n\}$. This is done by application of the Liouville operator $\mathcal{L} := [H, \cdot]$ to the operators \mathcal{O}_n . The application of \mathcal{L} derived from the effective Hamiltonian *after* the CUT does not change the number of DOs. Hence its action on the initial vector is (i) to shift the DO and/or (ii) to change the spin

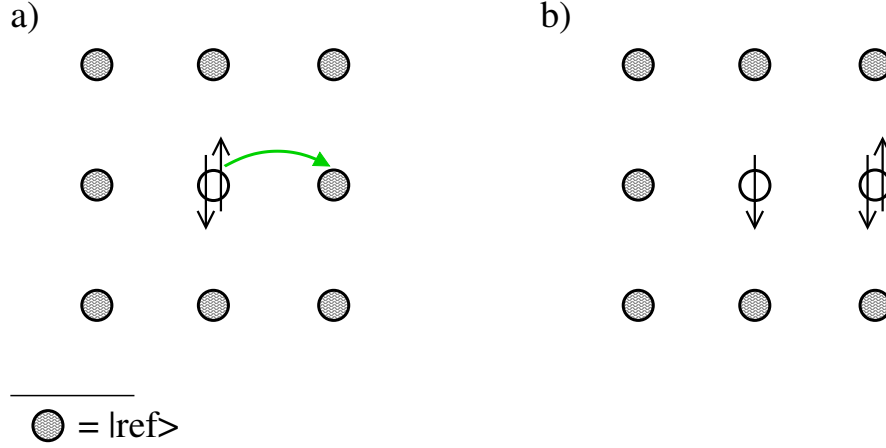


Fig. 3.11: a) Sketch of the action of the initial operator on the reference ensemble. Shaded sites represent the local reference ensemble. Black arrows indicate spin directions. A hopping process is shown as a gray (green) arrow. b) Situation after the hopping. For further explanation, see text.

background. The situation after the movement of the DO is shown in Fig. 3.11b in real space. The DO, which was situated originally on the central site, has moved to the right. Note that it does not leave the initial site in the reference state. The initial site of the DO is occupied by an electron with opposite spin of the moving electron. This is one unique state as opposed to the local reference ensemble. The application of the Liouville operator can also change the spin background since the effective Hamiltonian does not only consist of pure hopping terms.

The iteratively built basis $\{\mathcal{O}_n\}$ describes a single DO (charge excitation) at momentum \mathbf{k} including its magnetic dressing. In this basis the Liouville operator is a tridiagonal matrix. The lowest energy in this subspace defines the (apparent) dispersion E_k of a single charge excitation relative to the paramagnetic ensemble. Hence the evaluation of the lowest accessible energy in any truncated subspace of $\{\mathcal{O}_n\}$ provides an upper bound to E_k . The apparent charge gap Δ_{app} is finally given by

$$\Delta_{\text{app}} = 2 \min_k E_k, \quad (3.3.31)$$

where the factor of 2 is put to account for the creation of a particle and a hole. For vanishing hopping $\Delta_{\text{app}} = U$ holds. The apparent charge gap Δ_{app} is not the true charge gap because the paramagnetic spin background is not the true ground state. But Δ_{app} is a measure of the separation of energies between sectors of different double occupancy.

Numerically, one has to restrict the above procedure to truncated basis sets. The general Liouville approach is explained in Appendix A. Here we give the details that are special for the present problem. We construct a sequence of basis sets, labeled by the integer n , by applying the Liouville operator $\mathcal{L}_0 := [T_0, \cdot]$ (cf. Eq. (3.2.5b)) iteratively to the initial operator Eq. (3.3.30). The first basis $n = 1$ consists only of the single operator \mathcal{O}_0 . The subsequent basis sets are generated by applying T_0 ($n - 1$) times. All components of the \mathcal{O}_n are products of the local

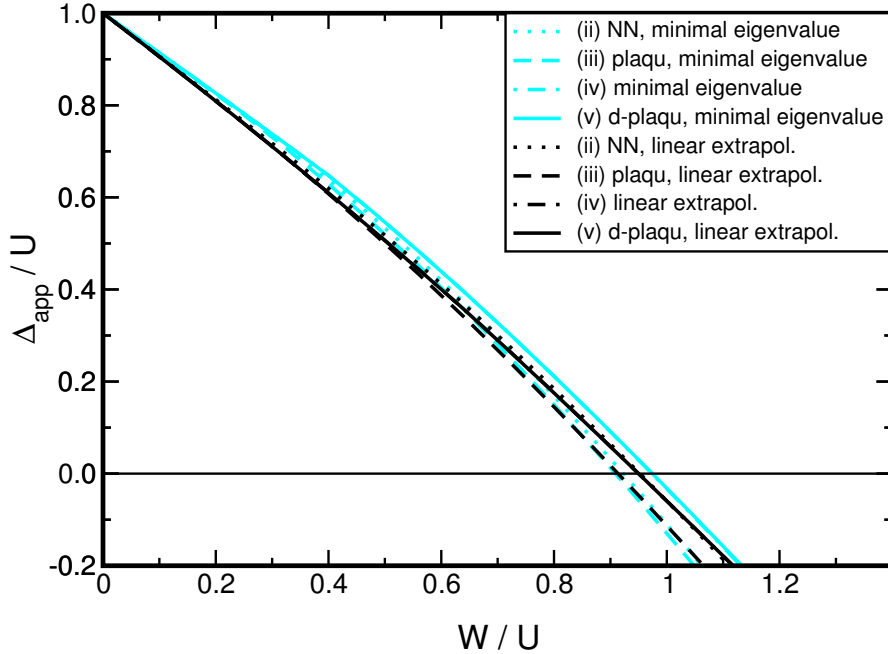


Fig. 3.12: Apparent charge gap as calculated with Lanczos diagonalization. Gray (cyan) lines show the minimal eigenvalues, black lines the result of a linear extrapolation.

operators in Tab. 3.1. They are independent vectors from the basis of all operators. For each basis set the lowest eigenvalue of the matrix representation of the Hamiltonian is an upper bound to the lowest energy E_k of a single DO.

The calculation is done for \mathbf{k} -values on the high symmetry lines in \mathbf{k} -space from $(0, 0) - (\pi/a, \pi/a) - (\pi/a, 0) - (0, 0)$. Figure 3.12 shows the results of the Lanczos calculation. The computational effort grows with the number of terms in the Hamiltonian. For the effective Hamiltonians (iv) and (v) it has only been possible to do the calculation up to the basis set $n = 6$, whereas for the NN (ii) and plaquette (iii) Hamiltonians the $n = 7$ calculation has been feasible. In Fig. 3.12 gray (cyan) lines show the smallest eigenvalue found for all momenta k in the largest possible Lanczos calculation. An additional estimate for the gap is found by extrapolating the lowest eigenvalues at momentum $(\pi/a, \pi/a)$ for each basis set as function of $1/n$ to $n \rightarrow \infty$.

The lowest eigenvalue at momentum $(\pi/a, \pi/a)$ is usually also the minimum of the dispersion except for $n = 5, 6$ or 7 where the whole dispersion becomes very flat. The result from a fit linear in $1/n$ is included in Fig. 3.12 by black lines. For the minimal eigenvalues as well as for the extrapolated ones the result for the Hamiltonian (iv) is covered by the double-plaquette result (v), since the coefficients of the Hamiltonians nearly coincide. The lowest eigenvalues for the Hamiltonians (iv) and (v) are larger than the lowest eigenvalues for the Hamiltonians (ii) and (iii) because larger values of n have been accessible for the latter.

A first guess for the gap is that it is reduced by the free bandwidth W . This would lead to $\Delta_{\text{app}}/U = 1 - W/U$, see e.g. Ref. [57]. So one expects that the gap closes around $W/U = 1$. The apparent charge gap calculated within the effective model using Lanczos diagonalization displays a similar behavior. The gap decreases almost linearly from $\Delta_{\text{app}}/U = 1$ at $W/U = 0$. There is, however, a certain downward curvature so that it closes at about $W/U \approx 0.9$.

We find that the apparent charge gap Δ_{app} becomes even negative for values of $W/U \gtrsim 0.92$. Once excitation energies become negative the CUT does not work because the limit $\ell \rightarrow \infty$ does not exist any longer. The #DO-changing processes can no longer be eliminated because they constitute no longer vacuum fluctuations around a stable vacuum. The negativity of excitation energies signals that the chosen reference ceases to be a physically reasonable reference.

At this point we have to recall that the true minimum might even be lower. The discussion of Lifshitz tails shows that the density of states in related problems displays tails with low spectral weight. Also in the present problem band tails are possibly present. They might be detected only in further iterations within the Lanczos procedure. The linear extrapolation corroborates the results from the linear eigenvalues to a certain extent. But we could not identify a clear asymptotic behavior for large values of n . Other extrapolation schemes, for instance as function of $1/\sqrt{n}$, point towards an earlier closing of the apparent charge gap. Therefore, the value $W/U \approx 0.9$ for the closing of the gap must be seen as a rough estimate. The determination of a possible power law, by which the gap closes, is beyond the scope of the present study.

The above findings are discussed in more detail in Sect. 3.4. In the remaining part of this chapter, we have to keep in mind that the mapping to the effective model conserving the number of DOs is not possible for $W/U \gtrsim 0.9$. For completeness, we will present the coefficients of the generalized t - J model up to values $W/U = 1.6$ to illustrate in which way the results are affected by the breakdown of the mapping. As a reminder of the breakdown, the definitely unphysical region beyond $W/U \approx 1$ will be shaded in the figures.

3.3.2. Effective model

The effective model conserves the number of DOs. This leads to a significant reduction of the size of the Hilbert space. At half filling the local Hilbert space has two states instead of the four states included in the original Hubbard model. The number of states grows like 2^N instead of 4^N for a lattice of N sites. Also away from half filling the model is considerably simplified. States with a finite number of DOs are separated from each other. The application of the Hamiltonian will not produce additional particle-hole pairs. The problem can be solved within the subspace of a fixed number of DOs. Thus, the conservation of the number of DOs leads to a simplification of the problem also in the case of the dynamics of charges.

On the other hand the effective Hamiltonian contains more terms. Especially for the double-plaquette calculation the number of terms is beyond any treatment that does not rely on numerics. However, the derivation of the effective model makes it possible to reduce the problem by neglecting terms with small coefficients. The quantitative calculation of the effective coefficients puts this procedure on a firm basis. Before, ad-hoc simplifications had to be made [60].

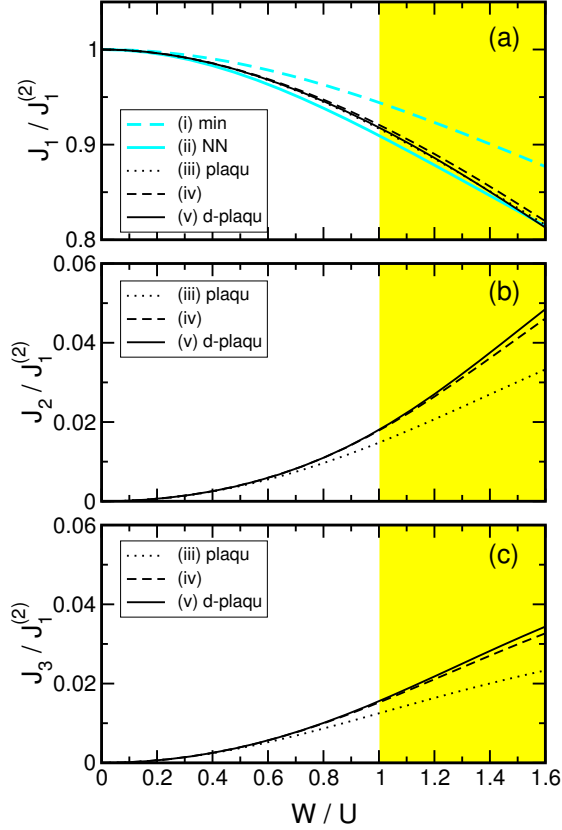


Fig. 3.13: Couplings of two-spin operators relative to $J_1^{(2)}$ as function of W/U .

In the following, we will first discuss the effective spin model. Second, the terms relevant for the one- and two-quasiparticle sector are described. These terms describe the motion of a single DO and the interaction of two DOs. Of course, the coefficients cannot be discussed exhaustively. The focus lies naturally on the most relevant coefficients.

3.3.2.1. Effective spin model

At half filling the effective Hamiltonian for the sector with no DO can be put in the form of a pure spin Hamiltonian. There are various two-spin couplings of the Heisenberg type

$$H_{2\text{-spin}} = \sum_{i,j} J_{|i-j|} \mathbf{S}_i \cdot \mathbf{S}_j. \quad (3.3.32)$$

The coefficients $J_{|i-j|}$ rapidly decrease with increasing distance between the sites i and j . The largest couplings are found for adjacent sites. Figure 3.13 displays the coefficients of various two-spin couplings. The Heisenberg NN exchange J_1 is shown in Fig. 3.13a, the exchange couplings between second and third nearest neighbors, J_2 and J_3 , are depicted in Fig. 3.13b and Fig. 3.13c,

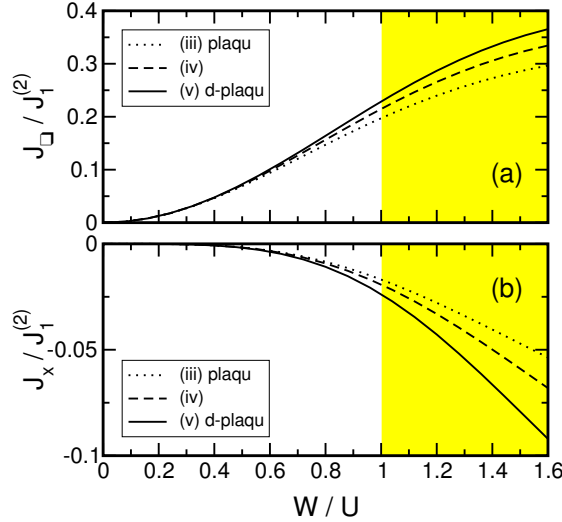


Fig. 3.14: Couplings of four-spin operators relative to $J_1^{(2)}$ as function of W/U .

respectively. Second nearest neighbor sites reside on diagonally opposite sites of the plaquettes of the square lattice. Third nearest neighbor sites are two lattice spacings away from each other and are connected by two consecutive unidirectional bonds. The coefficients are shown in units of $J_1^{(2)} = 4t^2/U$. The leading order $J_1^{(2)}$ of the Heisenberg NN exchange gives a reasonable energy scale to compare the various contributions to the spin Hamiltonian. Already the minimal calculation reproduces the correct leading order behavior of the perturbative expansion. For larger values of W/U the coupling J_1 is renormalized slightly to lower values $\approx 0.92J_1^{(2)}$ for $W/U = 1$. The perturbative corrections in Fig. 3.4 display a strong influence of higher order terms. On the contrary, the self-similar CUT calculation displays a regular development of the results. Already the NN calculation yields a very reasonable result for larger values of W/U . The results for larger calculations converge with good accuracy to a reliable quantitative result for J_1 . The convergence of the various calculations shows that the terms retained are sufficient to determine J_1 . Note that the dotted curve of the plaquette calculation (iii) is almost hidden by the double-plaquette result (v).

The couplings J_2 and J_3 behave like $(t/U)^4$ for small W/U . Their absolute convergence is as good as for J_1 . But due to their small values – both are smaller than $0.02J_1^{(2)}$ for $W/U < 1$ – the relative differences between calculations on different clusters are still discernible. In a further simplification of the effective model these terms could be dropped because of the small size of their coefficients.

There are not only exchange terms between two spins but also between four or more spins. Exchange between an odd number of spins is not generated since such terms would change sign under time reversal. The first term that one encounters in perturbation theory [23] in fourth

order is the following ring exchange operator

$$H_{\square} = J_{\square} \sum_{\langle i,j,k,l \rangle} \left[(\mathbf{S}_i \cdot \mathbf{S}_j)(\mathbf{S}_k \cdot \mathbf{S}_l) + (\mathbf{S}_i \cdot \mathbf{S}_l)(\mathbf{S}_j \cdot \mathbf{S}_k) - (\mathbf{S}_i \cdot \mathbf{S}_k)(\mathbf{S}_j \cdot \mathbf{S}_l) \right] \quad (3.3.33)$$

where $\langle i, j, k, l \rangle$ label the sites around a plaquette of the square lattice in cyclic order. We mention that this four-spin operator can be rewritten in the following way

$$H_{\square} = \frac{J_{\square}}{4} \sum_{\langle i,j,k,l \rangle} \left(P_{ijkl} + P_{ijkl}^{-1} \right) - \frac{J_{\square}}{2} \sum_{\langle i,j \rangle} \mathbf{S}_i \cdot \mathbf{S}_j - \frac{J_{\square}}{4} \sum_{\langle\langle i,j \rangle\rangle} \mathbf{S}_i \cdot \mathbf{S}_j, \quad (3.3.34)$$

where P_{ijkl} is the permutation operator. In the literature one also finds the permutation operator $\sum_{\langle i,j,k,l \rangle} P_{ijkl} + P_{ijkl}^{-1}$ in parametrizations of effective spin models. In 6th order an additional independent four-spin operator reads

$$H_{\times} = J_{\times} \sum_{\langle i,j,k,l \rangle} (\mathbf{S}_i \cdot \mathbf{S}_k)(\mathbf{S}_j \cdot \mathbf{S}_l). \quad (3.3.35)$$

The coefficients J_{\square} and J_{\times} are shown in Fig. 3.14. The ring exchange J_{\square} is the most important modification of the pure NN Heisenberg model. Its value is larger than $0.2J_1^{(2)}$ for $W/U = 1$. The relevance of the ring exchange in the CuO_2 -planes of La_2CuO_4 was proposed early [80, 81]. First experimental signs of a possible relevance of the ring exchange have been found in the line shape of infrared absorption experiments [82]. Clear evidence for a significant ring exchange term in La_2CuO_4 has been found by inelastic neutron scattering [83]. Theoretically the ring exchange has been derived from the three-band Hubbard model [84–86] and the single-band Hubbard model [23, 24]. The influence of ring-exchange on the Raman line shape has been computed in Refs. [80, 81, 87, 88].

The coefficients of the effective spin model are smooth functions of W/U up to $W/U = 1.6$. They do not suffer from the breakdown of the unitary transformation at $W/U \approx 0.9$. The vanishing of the apparent gap Δ_{app} and the slow drop of the residual off-diagonality for $W/U \gtrsim 1$ do not give rise to an anomalous behavior of the effective spin coefficients. The effective spin couplings are determined already for small values of the flow parameter l . They are fixed at the time the problems for other coefficients set in. The convergence of the results for values $W/U \lesssim 1$ is very good, i.e., the couplings do not change much as function of the cluster size for the larger clusters. The results of this section fix the effective spin model quantitatively.

3.3.2.2. Effective charge model

The unitary transformation deals also with the motion and interaction of charges. In the course of the transformation charge excitations (DOs) are created virtually. After the transformation, DOs can be introduced externally by doping or thermal fluctuations. Note that generically the effective model displays a finite U term. So DOs are not suppressed. But due to the disentanglement of the sectors of different number of DOs there is no direct influence of these sectors on one another. For instance, the magnetism strictly at half filling is not influenced by the physics of the sector with a particle-hole pair (two DOs in our counting).

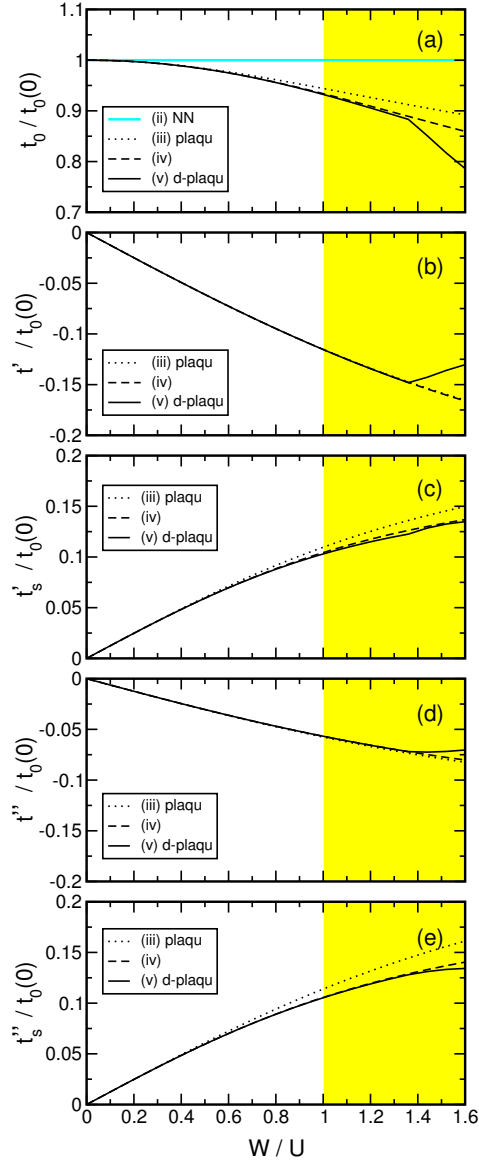


Fig. 3.15: Effective hopping coefficients between (a) NN sites, (b) NNN sites, (c) spin-dependent NNN hopping, (d) 3NN sites and (e) spin-dependent 3NN hopping.

Also in an effective model conserving the number of DO the sectors of different DO influence certain physical quantities. Thermal expectation values are influenced by the presence of sectors of different number of DOs. Also spectral properties are influenced by the presence of these sectors. The spectral weight will be distributed over a number of sectors. Additional contributions stem from Hubbard bands corresponding to more than one DO. Besides the lower (one hole)

and the upper (one electron) Hubbard band there are Hubbard bands with two or more DOs. Preliminary estimates of the spectral weight in this band indicate that it is below the order of one percent [89]. Yet it is a strong point of the approach chosen that the concept allows to discuss such subtle effects.

In the following the most important terms of the effective charge model are presented. One-quasiparticle terms describe the dynamics of a single hole or doubly occupied site. These terms build the $\{1, 1\}$ -block as classified in Sec. 2.2.2. The $\{2, 2\}$ -block consists of interaction terms of two DOs. In order not to be lost in a proliferating number of terms we will present results for terms which are at most of order t^2/U in the limit of weak hopping.

Figure 3.15 shows the coefficient of various one-quasiparticle terms. They correspond to hoppings of DOs. The NN hopping T_0 is shown in Fig. 3.15a. All single particle coefficients are given relative to the initial unrenormalized value $t_0(0) = t$ for the NN hopping. The next relevant processes besides NN hopping are hopping processes between next-nearest neighbor (NNN) sites and third-nearest neighbor sites (3NN). The NNN sites lie on diagonally opposite corners of the plaquettes of the two-dimensional square lattice. The NNN hopping T'_0 reads

$$T'_0 = t' \sum_{\langle\langle i,j \rangle\rangle;\sigma} \left[(1 - n_{i,\sigma}) c_{i,\bar{\sigma}}^\dagger c_{j,\bar{\sigma}} (1 - n_{j,\sigma}) - n_{i,\sigma} c_{i,\bar{\sigma}}^\dagger c_{j,\bar{\sigma}} n_{j,\sigma} + \text{h.c.} \right] \quad (3.3.36)$$

where $\langle\langle i,j \rangle\rangle$ stands for NNN sites and $\bar{\sigma} = -\sigma$. The spin-dependent NNN hopping $T'_{s,0}$ reads

$$T'_{s,0} = t'_s \sum_{\langle i,k,j \rangle;\alpha,\beta} \left\{ \begin{aligned} & [(1 - n_{i,\alpha}) c_{i,\bar{\alpha}}^\dagger \boldsymbol{\sigma}_{\bar{\alpha},\bar{\beta}} c_{j,\bar{\beta}} (1 - n_{j,\beta})] \cdot \mathbf{S}_k \\ & + [n_{i,\alpha} c_{i,\bar{\alpha}}^\dagger \boldsymbol{\sigma}_{\bar{\alpha},\bar{\beta}} c_{j,\bar{\beta}} n_{j,\alpha}] \cdot \mathbf{S}_k + \text{h.c.} \end{aligned} \right\} \quad (3.3.37)$$

where $\langle i,k,j \rangle$ stands for three sites wherein i and j are NNN and k is a nearest neighbor to both i and j . The symbol $\boldsymbol{\sigma} = (\sigma_x, \sigma_y, \sigma_z)$ stands for the vector made out of the three Pauli-matrices; \mathbf{S}_k represents the usual $S = 1/2$ spin vector at site k . Hopping and spin-dependent hopping between 3NN is also generated in second order in t/U . A pair of 3NN sites is connected by two unidirectional consecutive bonds. The distance of two 3NN sites is two lattice spacings. The couplings read

$$T''_0 = t'' \sum_{\langle\langle\langle i,j \rangle\rangle\rangle;\sigma} \left[(1 - n_{i,\sigma}) c_{i,\bar{\sigma}}^\dagger c_{j,\bar{\sigma}} (1 - n_{j,\sigma}) - n_{i,\sigma} c_{i,\bar{\sigma}}^\dagger c_{j,\bar{\sigma}} n_{j,\sigma} + \text{h.c.} \right] \quad (3.3.38)$$

where $\langle\langle\langle i,j \rangle\rangle\rangle$ stands for 3NN sites and

$$T''_{s,0} = t''_s \sum_{\langle\langle\langle i,k,j \rangle\rangle\rangle;\alpha,\beta} \left\{ \begin{aligned} & [(1 - n_{i,\alpha}) c_{i,\bar{\alpha}}^\dagger \boldsymbol{\sigma}_{\bar{\alpha},\bar{\beta}} c_{j,\bar{\beta}} (1 - n_{j,\beta})] \cdot \mathbf{S}_k \\ & + [n_{i,\alpha} c_{i,\bar{\alpha}}^\dagger \boldsymbol{\sigma}_{\bar{\alpha},\bar{\beta}} c_{j,\bar{\beta}} n_{j,\alpha}] \cdot \mathbf{S}_k + \text{h.c.} \end{aligned} \right\} \quad (3.3.39)$$

where $\langle\langle\langle i,k,j \rangle\rangle\rangle$ stands for three sites wherein i and j are 3NN and k is a nearest neighbor to both i and j , so k is just the site between i and j . All these hoppings, Eqs. (3.3.36)-(3.3.39)

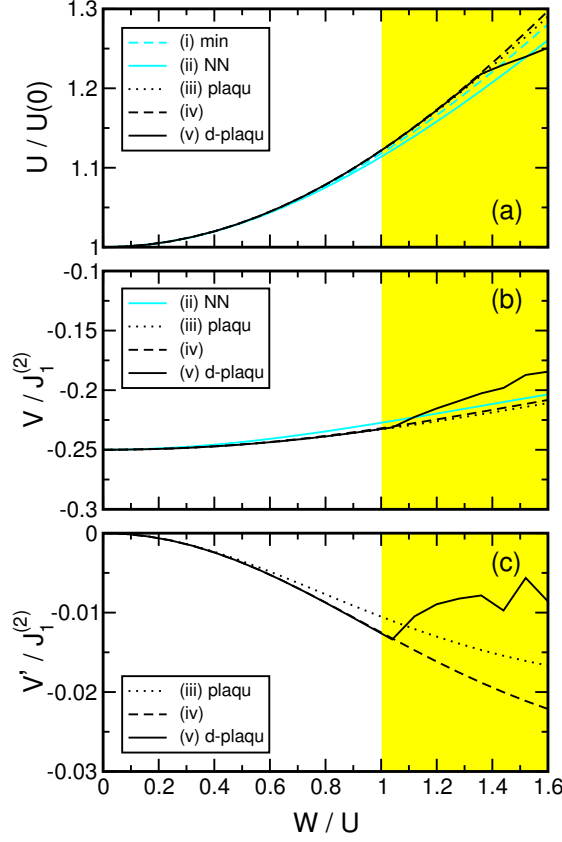


Fig. 3.16: Hubbard repulsion U (a) and NN interaction V (b) and NNN interaction V' (c) between holes or double occupancies.

conserve the number of DOs. Figures 3.15a-e show the coefficients of the NN hopping t_0 (T_0 from Eq. (3.2.5b)), NNN hopping t' , spin-dependent NNN hopping t'_s , 3NN hopping t'' and spin-dependent 3NN hopping t''_s , respectively.

The NN hopping t_0 shown in Fig. 3.15a remains unchanged from its initial value for the NN truncation. Including more terms reduces the effective t_0 . At $W/U \approx 1.36$, the double plaquette calculation (v) shows a sudden change of slope. This is related to the non-monotonic behavior of the residual off-diagonality. But the value $W/U \approx 1.36$ is already beyond the point $W/U \approx 0.9$ where the apparent gap Δ_{app} becomes negative and the mapping is no longer possible. The signs of t' (NNN hopping) and of t'' (3NN hopping) are opposite to the sign of t (NN hopping). The value of t' is approximately two times t'' because it is generated from the two possible hopping processes to go from one corner of a plaquette to the opposite corner. In contrast, there is only one process to generate t'' in second order. The results for the calculations (iii)–(v) lie almost on top of each other for the coefficients t , t' and t'' until spurious behavior sets in at larger values of W/U .

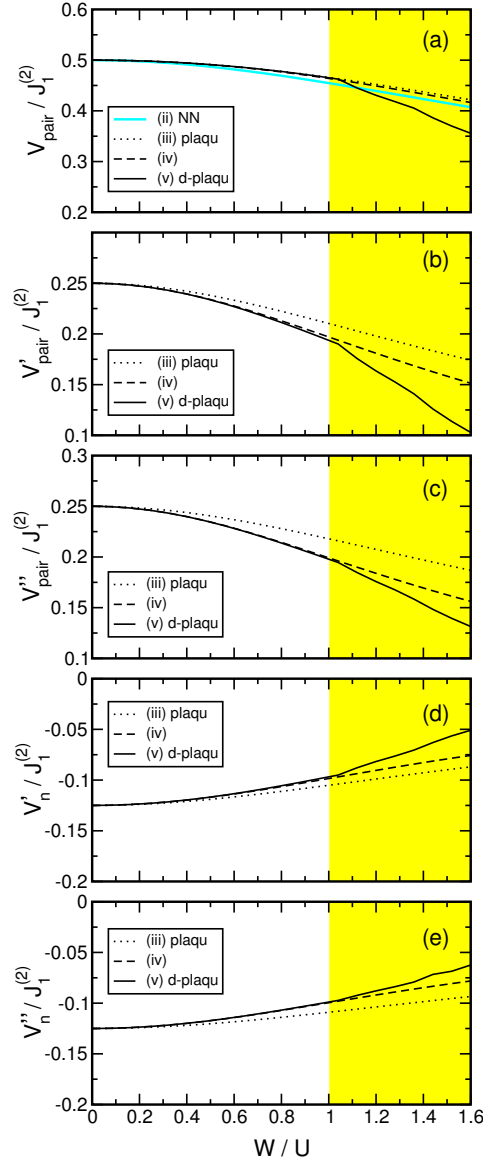


Fig. 3.17: Further coefficients of interactions of two DO that are of second order in t/U . For explanation, see text.

The coefficients of the spin-dependent hoppings t'_s and t''_s are shown in Fig. 3.15c and e. They increase quadratically for small W/U just like t' which leads to the linear behavior in units of t_0 depicted in Fig. 3.15. These hoppings are terms which involve three sites. Their coefficients have approximately the same value since it does not matter very much whether the three sites are aligned linearly or form an angle of 90° . We emphasize that both coefficients t'_s and t''_s

are of similar size as t' . This implies that the commonly used phenomenological description in terms of a t - t' - J -model is not justified. If an extension of the most simple t - J -model is used the NNN and 3NN hoppings, t' and t'' , and the spin-dependent hoppings t'_s , t''_s should all be included. Investigations of the importance of spin-dependent hopping are reported in e. g. Refs. [90–94]. The spin-dependent hopping is found to influence the dispersion measured by angle-resolved photoemission [92] and the spectral weight distribution measured by optical conductivity [90, 93, 94].

Figures 3.16 and 3.17 show the coefficients from the $\{2, 2\}$ -block. They describe interactions between quasiparticles. At least two holes or two doubly occupied sites or one hole and one doubly occupied site must be present for these interactions to be effective. In Fig. 3.16a, the Hubbard repulsion U is shown in units of its unrenormalized value. All calculations show a slight increase of the effective U with W/U . It is interesting to note that this basic quantity neither diverges nor stays constant in the process of the disentanglement of the various sectors of double occupancy.

The density-density interactions for NN sites is described by

$$H_V = V \sum_{\langle i,j \rangle} \bar{n}_i \bar{n}_j \quad (3.3.40)$$

where $\bar{n}_i = n_{i,\uparrow} + n_{i,\downarrow} - 1$. Similarly, the operator for density-density interactions for NNN sites reads

$$H_{V'} = V' \sum_{\langle\langle i,j \rangle\rangle} \bar{n}_i \bar{n}_j. \quad (3.3.41)$$

The coefficients V and V' are shown in Fig. 3.16b and 3.16c. They are given in units of the second order scale $J_1^{(2)} = 4t^2/U$. The attractive interaction V is proportional to $-t^2/U = -J_1^{(2)}/4$ as expected from perturbation theory. It represents a sizeable contribution at all W/U . In contrast, the parameter V' coupling NNN sites, which is of fourth order in t/U , turns out to be very small [60]. This fact justifies our choice to focus otherwise on the terms which appear already in second order in t .

There are two additional types of operators that are created in second order in t/U . The first type consists of operators which destroy or create two electrons at the same site. Figure 3.17a shows the coefficient V_{pair} of

$$H_{\text{pair}} = V_{\text{pair}} \sum_{\langle i,j \rangle} (c_{i,\uparrow}^\dagger c_{i,\downarrow}^\dagger c_{j,\downarrow} c_{j,\uparrow} + h.c.). \quad (3.3.42)$$

Figure 3.17b and c show the coefficients V'_{pair} and V''_{pair} of

$$\begin{aligned} H'_{\text{pair}} = & V'_{\text{pair}} \sum_{\langle i,k,j \rangle, \sigma} \left[c_{k,\sigma}^\dagger c_{k,\bar{\sigma}}^\dagger c_{i,\bar{\sigma}} c_{i,\sigma} n_{i,\sigma} c_{j,\sigma} (1 - n_{j,\bar{\sigma}}) \right. \\ & \left. + c_{k,\sigma}^\dagger c_{k,\bar{\sigma}}^\dagger c_{i,\bar{\sigma}} (1 - n_{i,\sigma}) c_{j,\sigma} n_{j,\bar{\sigma}} + h.c. \right], \end{aligned} \quad (3.3.43)$$

and

$$\begin{aligned}
H''_{\text{pair}} = & V''_{\text{pair}} \sum_{\langle\langle i,k,j \rangle\rangle, \sigma} \left[c_{k,\sigma}^\dagger c_{k,\bar{\sigma}}^\dagger c_{i,\bar{\sigma}} n_{i,\sigma} c_{j,\sigma} (1 - n_{j,\bar{\sigma}}) \right. \\
& \left. + c_{k,\sigma}^\dagger c_{k,\bar{\sigma}}^\dagger c_{i,\bar{\sigma}} (1 - n_{i,\sigma}) c_{j,\sigma} n_{j,\bar{\sigma}} + \text{h.c.} \right]. \quad (3.3.44)
\end{aligned}$$

The operators H'_{pair} and H''_{pair} describe processes where two electrons from sites i and j are transferred to site k . They do not change the number of DOs since at one site (with local operator $c_{i,\sigma}(1 - n_{i,\bar{\sigma}})$) a DO is created while at another ($c_{i,\sigma} n_{i,\bar{\sigma}}$) a DO is annihilated. The local operator $c_{k,\uparrow}^\dagger c_{k,\downarrow}^\dagger$ turns an empty site into a doubly occupied site and thus does not change the number of DOs in our counting. Both the coefficients V'_{pair} and V''_{pair} change only slightly on passing from calculation (iii) to calculation (iv); the difference between (iv) and (v) is minute so that we consider the final result as reliable for not too large W/U where the mapping to the generalized t - J models is possible.

The last type of operators created in second order in t/U are correlated hopping terms. We classify them as interactions because they have a non-vanishing effect only if at least two double occupancies or holes are present. The operator

$$\begin{aligned}
V'_{n,0} = & V'_n \sum_{\langle i,k,j \rangle; \alpha, \beta} \left[(1 - n_{i,\alpha}) c_{i,\alpha}^\dagger c_{j,\bar{\beta}} (1 - n_{j,\beta}) \bar{n}_k \right. \\
& \left. + n_{i,\alpha} c_{i,\alpha}^\dagger c_{j,\bar{\beta}} n_{j,\beta} \bar{n}_k + \text{h.c.} \right] \quad (3.3.45)
\end{aligned}$$

describes a process of a DO hopping between the NNN sites i and j if and only if there is a DO on the site k . The corresponding operator for a 3NN process is

$$\begin{aligned}
V''_{n,0} = & V''_n \sum_{\langle\langle i,k,j \rangle\rangle; \alpha, \beta} \left[(1 - n_{i,\alpha}) c_{i,\alpha}^\dagger c_{j,\bar{\beta}} (1 - n_{j,\beta}) \bar{n}_k \right. \\
& \left. + n_{i,\alpha} c_{i,\alpha}^\dagger c_{j,\bar{\beta}} n_{j,\beta} \bar{n}_k + \text{h.c.} \right]. \quad (3.3.46)
\end{aligned}$$

The coefficients V'_n and V''_n are shown in Fig. 3.17d and e.

The above results define the quasiparticle dynamics of the effective Hamiltonian in a systematic way. Within the $\{1, 1\}$ -block we emphasize the importance of spin-dependent hoppings. All the values for the hopping coefficients and the interactions show excellent convergence in the relevant region up to $W/U \approx 0.9$. For values $W/U > 0.9$ the coefficients display anomalous behavior. This effect is most striking for the coefficient V' of the $\{2, 2\}$ -block. It is shown Fig. 3.16c. We attribute this spurious behavior to the breakdown of the mapping of the Hubbard model to a generalized t - J -model without specifying the state of the spin degrees of freedom.

3.4. Discussion

In the derivation of the effective t - J -model, one does not aim at the solution of the complete problem of the Hubbard model. The CUT is designed to disentangle the energetically low-lying

dynamics, i.e., the dynamics of the spins and of the doped holes, from processes involving more double occupancies. So no particular state in spin space is assumed, but an effective model without processes changing the number of double occupancies is derived. In this calculation, the paramagnetic ensemble at half filling serves as the reference ensemble.

The general consideration presented in Sec. 3.1 suggested that the reduction to the effective model without charge fluctuations cannot be defined for too large W/U . This view is verified by the actual calculations. The reduction of the Hubbard model to a generalized t - J model is possible as long as the apparent gap Δ_{app} remains positive. The appearance of negative values for Δ_{app} is an artefact. It indicates that the paramagnetic reference ensemble does no longer represent a phase which is stable against fluctuations involving double occupancies. In this case the reduction to an effective model without virtual double occupancies is no longer possible.

The apparent gap in the present context measures the separation of blocks of different double occupancy. It is calculated using the reference ensemble. Since the reference ensemble is not the true ground state the apparent gap is not the energy difference between two eigenstates of the system. For a qualitative understanding it is helpful to consider a modified system where the apparent and the true gap coincide. This situation is realized for a Hubbard model on the Bethe lattice in the limit of infinite coordination number $Z \rightarrow \infty$, cf. Refs. [3, 57, 63, 64, 95]. For infinite dimensional lattices it is assumed that long-range order can be completely suppressed by frustration, e.g., in the generalizations of fcc lattices to infinite dimensions [96, 97]. Since the magnetic couplings J scale with the inverse coordination number Z^{-1} there are *no* magnetic correlations *at all* once the static sublattice magnetization is suppressed [98]. The paramagnetic reference ensemble represents the highly degenerate magnetic ground state in infinite dimensions without long-range order. The apparent gap and the true charge gap are identical. Their closure signals a real insulator-to-metal transition. In finite dimensions the closure of the apparent gap signals only a *crossover* from well-separated to non-separated energy scales.

The crossover from well-separated energy scales to non-separated energy scales in finite dimensions can be studied in the purified form of a insulator-to-metal phase transition in the infinite dimensional Hubbard model. Indeed, similar behavior is found. The single-particle gap Δ vanishes in infinite dimensions at about $1.1W - 1.2W$ [63, 95, 99–101]. It disappears roughly linearly as function of U [63, 95]. These similarities corroborate the view that the infinite dimensional model is an illustration for the crossover in finite dimensions.

Coming back to the two-dimensional Hubbard model one can still use the apparent gap to quantify the separation of sectors of different double occupancy. The vanishing of the apparent gap marks the region of the crossover from insulator to metal. The validity of our approach is clear for small values of W/U . The only approximation used is the truncation of processes of a spatial range $d \geq 4$. The remaining question is to know up to which ratio of W/U the results are reliable. Our findings in finite dimensions illustrate that the answer to this question is difficult already on the conceptual level. The apparent gap Δ_{app} measuring the separation of energy scales does not compare the energies of real eigenstates. The validity of the mapping of the Hubbard model to a generalized t - J -model is not limited by a sharply defined transition but

by a gradual crossover.

An estimate up to which ratio of W/U the mapping is reasonable can be obtained from the closure of the apparent gap at around $W/U \approx 0.9$. A better estimate for the region of validity should compare Δ_{app} to the size of the coefficients of the neglected operators. But these coefficients are not available. Hence we take the operators with the *maximal* extension considered, that is $d = 3$, as an estimate for the importance of the neglected operators. The root mean square of the coefficients of the operators with extension $d = 3$ is compared to Δ_{app} . These two quantities become equal for $W/U \approx 0.85$. If in addition we take the uncertainty of the extrapolation procedure into account we arrive at the conservative estimate that the generalized t - J -model can be used up to $W/U \approx 0.8$ which includes the commonly assumed parameters [60] for cuprate planes $t/J \approx 3$ which translates to $W/U \approx 0.7$. Up to $W/U \approx 0.8$, the quantitative results provided in Sec. 3.3.2 are reliable.

The possibility to map a Hubbard model in a systematic and controlled way to a generalized t - J model depends essentially on local physics. The breakdown of this mapping does not represent a real physical phase transition in finite dimensions. We suppose that the breakdown of the mapping manifests itself as a crossover in physical properties. It is plausible, for instance, that the nature of the elementary excitations changes: holes and magnetic modes for large values of the interaction become fermionic quasiparticles at small values of the interaction.

3.5. Summary and outlook

In this chapter the method of self-similar CUTs in real space was applied to the Hubbard model. The MKU generator is chosen such that the number of double occupancies is a conserved quantity in the effective model. The effective Hamiltonian represents thus a generalized t - J model. The calculation relies on a reference *ensemble*. The reference ensemble is constructed from the two local singly occupied states. The vacuum represented by the reference ensemble does not have any magnetic correlations. The t - J -model is derived without the assumption of a particular magnetic state. The truncation scheme uses the extension of a term in real space as a measure for its locality.

The effective model contains spin terms and terms determining the dynamics of doped charge carriers. Besides the NN Heisenberg exchange further two-spin terms and four-spin terms are taken into account. It is shown that two-spin couplings other than the Heisenberg term are small whereas the four-spin ring exchange J_{\square} gives a sizeable contribution to the effective spin model. Results for the size of the coefficients for NN hopping, NNN and 3NN hopping and spin-dependent NNN and 3NN hopping are obtained. It is found that the spin-dependent NNN and 3NN hopping is as important as the spin-independent one. This fact should be accounted for in phenomenological parametrizations of experimental Fermi surfaces. In addition, the size of the interactions between holes and double occupancies on NN and NNN sites are calculated. Various truncation schemes show very good convergence of the coefficients of the effective model in the relevant parameter region $W \lesssim 0.8U$.

The results of the present chapter are not only concerned with the parameters of the effective model but also with the possibility of its derivation. The fundamental result is that for $U \gtrsim 1.3W$ the mapping of the Hubbard model to a generalized t - J -model is possible. The parameters of the effective model can be determined reliably by the CUT. They are governed mainly by local physics. On the other hand, the reduction of the Hubbard model to an effective model without charge fluctuations is not possible for $U \lesssim 1.2W$. Here, the sectors of different number of double occupancies cannot be disentangled. The derivation of the effective Hamiltonian for the Hubbard model represents a successful application of self-similar CUTs in real space. It establishes that the method developed in Chapter 2 can be applied to many-body problems and provides good quantitative results.

Further work in this direction could include the effect of doping onto the effective model. The present treatment contains also the dynamics of double occupancies and holes that are introduced in the half filled Hubbard model, e.g. by doping. However, it does not treat the effect of a finite percentage of double occupancies or holes. A systematic treatment of the influence of doping is lacking at present. An additional focus of future research could be the relevance of trans-Hubbard bands. The Hubbard model contains not only the dynamics of a single DO but also the excitation of multiple DOs. Their contribution to the spectral weight is not yet clear though first estimates indicate that it is very small.

4. One-dimensional spin systems

Low dimensional spin systems provide a fascinating wealth of phenomena to be studied using the techniques of quantum many-body physics. This section will apply self-similar CUTs in real space to two generic one-dimensional spin systems, namely the spin ladder and the dimerized spin chain. A lot is known about them such that these results can be used to test the CUT method.

The starting point for the CUT is a representation of the spin systems in a dimer basis. The isotropic system is found by setting the interaction between the dimers to unity. The advantage of starting from a dimerized state is that in this case the system has a large gap. The transformation can be set up without problems. The ladder system is treated in Sec. 4.1. This section introduces the dimer basis which is used to reformulate the Hamiltonian. Complex behavior is found if the interaction between the dimers is increased. For the spin ladder we will investigate the energy properties of one- and two-particle excitations. A comparison to established results will help to judge the quality of the mapping.

The investigation of the spin chain in Sec. 4.2 is also built upon the dimer basis formulation. For large dimerization the spin gap is large. The homogeneous limit of the spin chain is gapless. This limit is very difficult to describe using real space CUTs. For the spin chain the one-triplon dispersion is calculated. It will be investigated how the convergence properties of the CUT change if the dimerization is decreased. Using the spectral weight of the transformed observable S_z we will discuss the lifetime effects resulting from the overlap of different multi-triplon continua.

4.1. Spin ladder

The spin ladder is composed of pairs of spins that are linearly arranged to form a ladder as shown in Fig. 4.1. The Hamiltonian reads

$$\begin{aligned} H &= J_{\perp} H_{\perp} + J_{\parallel} H_{\parallel} \\ &= \sum_i [J_{\perp} \mathbf{S}_{1,i} \mathbf{S}_{2,i} + J_{\parallel} (\mathbf{S}_{1,i} \mathbf{S}_{1,i+1} + \mathbf{S}_{2,i} \mathbf{S}_{2,i+1})] , \end{aligned} \quad (4.1.1)$$

where 1 and 2 denote the left and right leg of the ladder. The rung is denoted by the index i . The spins interact antiferromagnetically. The couplings J_{\perp} and J_{\parallel} are larger than zero. The spin ladder Hamiltonian is realized in telephone number compounds like $\text{Sr}_{14}\text{Cu}_{24}\text{O}_{41}$ and $\text{La}_6\text{Ca}_8\text{Cu}_{24}\text{O}_{41}$ [102, 103]. The structure of the first of these compounds is shown in Fig. 4.2. Layers composed out of spin ladders and spin chains are separated by Sr atoms. Adjacent spin

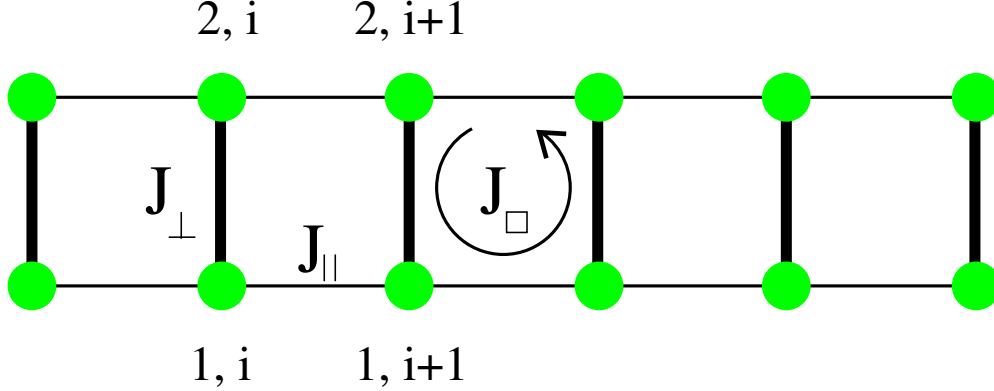


Fig. 4.1: The spin ladder consists of sites on two legs 1 and 2. The index i labels the sites in ladder direction. The spin coupling of the rungs is given by J_{\perp} , the coupling in leg direction by J_{\parallel} . A possible four-spin exchange is given by J_{\square} .

ladders in one layer are only weakly coupled due to 90° exchange. In addition, the coupling of a site to the adjacent ladders is frustrated.

The four-spin exchange is an important modification of the Heisenberg model in two dimensions [83]. This has been confirmed in Sec. 3 of the present thesis by a derivation of the effective spin model from a one-band model. Similar results can be achieved starting from a three-band model [80, 81, 87, 88, 104]. Experiments on two-dimensional spin systems support the importance of four-spin exchange terms [83]. In experimental realizations of spin ladders the four spin exchange is important as well. The analysis of experiments shows that the minimal spin model contains a four-spin exchange term [48, 103, 105–110]. Its size is typically about 10% – 20% of the rung coupling J_{\perp} [108–110]. Theoretical derivations of the effective spin model support this interpretation of the experiments [84]. The four-spin exchange couples the spins on the corners of one plaquette. The four-spin term reads

$$H_{\square} = J_{\square} \sum_i \left[(\mathbf{S}_{1,i} \cdot \mathbf{S}_{1,i+1})(\mathbf{S}_{2,i} \cdot \mathbf{S}_{2,i+1}) + (\mathbf{S}_{1,i} \cdot \mathbf{S}_{2,i})(\mathbf{S}_{1,i+1} \cdot \mathbf{S}_{2,i+1}) - (\mathbf{S}_{1,i} \cdot \mathbf{S}_{2,i+1})(\mathbf{S}_{1,i+1} \cdot \mathbf{S}_{2,i}) \right]. \quad (4.1.2)$$

The ladder Hamiltonian Eq. (4.1.1) can be considered in two limits. For small ratio $x = J_{\parallel}/J_{\perp}$ it represents weakly interacting rungs. For $x = 0$ the ground state is the product state of local rung singlets. The spin gap Δ is equal to J_{\perp} . Small finite coupling in leg direction introduces a finite dispersion $\Delta(k)/J_{\perp} = 1 + x \cos(k)$ where x is again the ratio of leg and rung coupling. For $J_{\parallel} \gg J_{\perp}$ the model Eq. (4.1.1) describes two weakly coupled chains. Keeping this in mind one can identify some properties of spin chains in the results for larger values of x . The spin gap is finite for any non-zero value of J_{\perp}/J_{\parallel} [111–113]. Therefore there is no phase transition for any finite value of x in the spin ladder.

If one includes the four-spin exchange Eq. (4.1.2) there are several phase transitions for varying

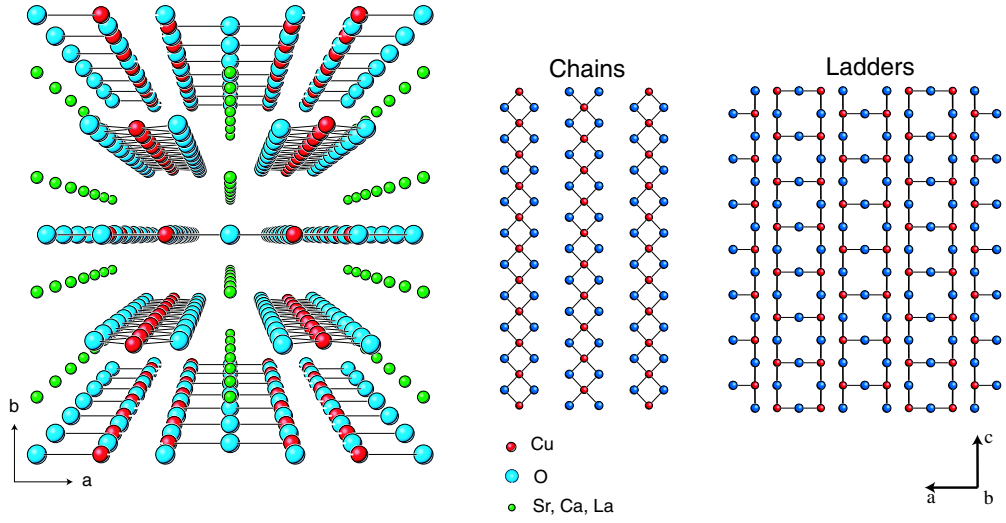


Fig. 4.2: Schematic view of the telephone number compound $\text{Sr}_{14}\text{Cu}_{24}\text{O}_{41}$. The figures are taken from Ref. [102]. On the left a three-dimensional view on the material is shown. It consists of planes formed by chain or ladder structures. These structures are shown on the right. In between the layers there are Sr atoms.

ratio J_{\square}/J_{\perp} . The spin gap Δ is reduced for increasing four-spin exchange. At a finite value of J_{\square} the spin gap closes and a phase transition from the rung singlet phase to a phase with dominant staggered dimer correlations occurs [114, 115]. The critical value of J_{\square} depends on the ratio of leg and rung coupling x . For $x = 1$ the transition takes place at $x_{\square} = J_{\square}/J_{\perp} \approx 0.25$. One also finds phases with scalar chiral order, so-called dominant vector chirality and dominant collinear spin order on varying the size of the four-spin exchange [115].

4.1.1. Method

A local operator basis is used to set up the local approach of the self-similar CUT. The operator basis is motivated by the rung singlet phase. For $x = 0$ the ground state is the product state of local rung singlets. The ground state of a local dimer is the singlet state as we deal with antiferromagnetic spin couplings. The local excited states are the three triplets with magnetic quantum number $\{1, 0, -1\}$. For finite leg coupling the local triplets are dressed. These quasiparticles are called *triplons* [116].

The local basis consists of four states, namely the singlet and the three local triplets. The Hamiltonian is now written in this local operator basis [117]. Then, the local CUT approach is implemented using the techniques described in Sec. 2. For small x and x_{\square} the spin gap is finite. The most relevant processes are captured by terms that are rather local. For larger couplings the description in terms of rather local triplon operators will break down.

$2\mathcal{T}_0$	
$ t^{0,\pm 1}, s\rangle$	\longrightarrow $ s, t^{0,\pm 1}\rangle$
$ t^0, t^{\pm 1}\rangle$	\longrightarrow $ t^{\pm 1}, t^0\rangle$
$ t^{\pm 1}, t^{\pm 1}\rangle$	\longrightarrow $ t^{\pm 1}, t^{\pm 1}\rangle$
$ t^{\pm 1}, t^{\mp 1}\rangle$	\longrightarrow $ t^0, t^0\rangle - t^{\pm 1}, t^{\mp 1}\rangle$
$ t^0, t^0\rangle$	\longrightarrow $ t^1, t^{-1}\rangle + t^{-1}, t^1\rangle$
$2\mathcal{T}_2$	
$ s, s\rangle$	\longrightarrow $ t^0, t^0\rangle - t^1, t^{-1}\rangle - t^{-1}, t^1\rangle$

Table 4.1: Matrix elements of the operators \mathcal{T}_i in Eq. (4.1.5). The states denote product states on adjacent rungs. Here, s stands for the singlet state and t^i for the triplet with magnetic quantum number i . Matrix elements of \mathcal{T}_{-2} are fixed by the relation $\mathcal{T}_n^\dagger = \mathcal{T}_{-n}$.

It is useful to rewrite the Hamiltonian in units of the rung coupling J_\perp

$$\frac{H}{J_\perp} = H_\perp + xH_\parallel + x_\square H_\square. \quad (4.1.3)$$

The above Hamiltonian depends on the previously introduced ratios $x = J_\parallel/J_\perp$ and $x_\square = J_\square/J_\perp$. The operator H_\perp counts the number of local triplets. It is therefore diagonal in the local basis. In addition, it serves as the counting operator of triplets. This counting operator defines the MKU generator that is used in the following. The contributions H_\parallel and H_\square are non-diagonal in the local basis. The operator H_\parallel is written as

$$H_\parallel = T_{-2} + T_0 + T_2 \quad (4.1.4)$$

where

$$T_{0,\pm 2} = \sum_\nu \mathcal{T}_{0,\pm 2}(\nu), \quad (4.1.5)$$

and ν sums over all pairs of adjacent rungs. The local operators $\mathcal{T}_{0,\pm 2}(\nu)$ are defined by their action on a local basis as given in Tab. 4.1. Correspondingly, the four-spin exchange term is given by

$$H_\square = T_{-2}^\square + T_0^\square + T_2^\square \quad (4.1.6)$$

where

$$T_{0,\pm 2}^\square = \sum_\nu \mathcal{T}_{0,\pm 2}^\square(\nu). \quad (4.1.7)$$

The operators $T_{0,\pm 2}^\square$ are defined by their matrix elements in Tab. 4.2. Table 4.2 shows that the four-spin exchange has a finite matrix element $|s, s\rangle \rightarrow |s, s\rangle$. This means that the energy of the reference state itself is renormalized by the four-spin exchange in the form Eq. (4.1.6). It is advantageous to rewrite the four-spin exchange term in the following way. First we define

$$H_{\text{corr}} := J_\square \sum_i \left(\frac{3}{2} \mathbf{S}_{1,i} \mathbf{S}_{2,i} + \frac{9}{16} \right). \quad (4.1.8)$$

$2\mathcal{T}_0^\square$		
$ t^{0,\pm 1}, s\rangle$	\longrightarrow	$ s, t^{0,\pm 1}\rangle - \frac{3}{4} t^{0,\pm 1}, s\rangle$
$ s, s\rangle$	\longrightarrow	$\frac{9}{4} s, s\rangle$
$ t^0, t^{\pm 1}\rangle$	\longrightarrow	$\frac{1}{4} t^0, t^{\pm 1}\rangle$
$ t^{\pm 1}, t^{\pm 1}\rangle$	\longrightarrow	$\frac{1}{4} t^{\pm 1}, t^{\pm 1}\rangle$
$ t^{\pm 1}, t^{\mp 1}\rangle$	\longrightarrow	$\frac{1}{4} t^{\pm 1}, t^{\mp 1}\rangle$
$ t^0, t^0\rangle$	\longrightarrow	$\frac{1}{4} t^0, t^0\rangle$
$2\mathcal{T}_2^\square$		
$ s, s\rangle$	\longrightarrow	$- t^0, t^0\rangle + t^1, t^{-1}\rangle + t^{-1}, t^1\rangle$

Table 4.2: The four-spin part of the Hamiltonian H_\square is defined in terms of the operators \mathcal{T}_i^\square . The matrix elements of \mathcal{T}_i^\square are given in this table.

The term H_{corr} is used to compensate the purely local matrix elements in Table 4.2 connecting $|s, s\rangle \rightarrow |s, s\rangle$ and $|t^i, s\rangle \rightarrow |t^i, s\rangle$. The Hamiltonian is then rewritten as

$$\frac{H}{J_\perp} = (H_\perp - x_\square H_{\text{corr}}) + xH_\parallel + (x_\square H_\square + x_\square H_{\text{corr}}) \quad (4.1.9a)$$

$$= (H_\perp - x_\square H_{\text{corr}}) + xH_\parallel + x_\square \tilde{H}_\square, \quad (4.1.9b)$$

where we have introduced $\tilde{H}_\square = H_\square + H_{\text{corr}}$. The definition of \tilde{H}_\square is

$$\tilde{H}_\square = \tilde{\mathcal{T}}_0^\square + \tilde{\mathcal{T}}_2^\square + \tilde{\mathcal{T}}_{-2}^\square, \quad (4.1.10)$$

where the operators $\tilde{\mathcal{T}}_i^\square$ are given in Tab. 4.3. The two local matrix elements $|s, s\rangle \rightarrow |s, s\rangle$ and $|t^i, s\rangle \rightarrow |t^i, s\rangle$ are absent in \tilde{H}_\square . The Hamiltonian in its final form reads

$$\frac{H}{J_\perp} = (1 - 3x_\square) \left[H_\perp + \frac{x}{1 - 3x_\square} H_\parallel + \frac{x_\square}{1 - 3x_\square} \tilde{H}_\square \right] \quad (4.1.11a)$$

$$= (1 - 3x_\square) \left[H_\perp + \tilde{x} H_\parallel + \tilde{x}_\square \tilde{H}_\square \right]. \quad (4.1.11b)$$

The new variables \tilde{x} and \tilde{x}_\square are defined as

$$\tilde{x} = \frac{x}{1 - 3x_\square} \quad (4.1.12a)$$

$$\tilde{x}_\square = \frac{x_\square}{1 - 3x_\square}. \quad (4.1.12b)$$

The calculation is performed using the representation in Eq. (4.1.11b).

The operators T_i and \tilde{T}_i^\square change the number of triplets by i . The parts T_0 and \tilde{T}_0^\square are thus diagonal with respect to the counting operator H_\perp . The Hamiltonian contains only terms that change the number of triplets by an even number. Terms that change the number of triplets by an odd number are odd with respect to a reflection about the centerline of the ladder and therefore vanish.

$2\tilde{T}_0^\square$	
$ t^{0,\pm 1}, s\rangle$	\longrightarrow $ s, t^{0,\pm 1}\rangle$
$ t^0, t^{\pm 1}\rangle$	\longrightarrow $4 t^0, t^{\pm 1}\rangle$
$ t^{\pm 1}, t^{\pm 1}\rangle$	\longrightarrow $4 t^{\pm 1}, t^{\pm 1}\rangle$
$ t^{\pm 1}, t^{\mp 1}\rangle$	\longrightarrow $4 t^{\pm 1}, t^{\mp 1}\rangle$
$ t^0, t^0\rangle$	\longrightarrow $4 t^0, t^0\rangle$
$2\tilde{T}_2^\square$	
$ s, s\rangle$	\longrightarrow $- t^0, t^0\rangle + t^1, t^{-1}\rangle + t^{-1}, t^1\rangle$

Table 4.3: The table lists the matrix elements of \tilde{T}_i^\square on product states of adjacent rungs. Remaining matrix elements can be found by hermitian conjugation.

4.1.1.1. Truncation scheme

In the local approach to CUTs the truncation scheme relies on the extension of the terms. The truncation scheme is defined by a maximal extension. Terms with a larger extension are discarded. For the spin ladder it will turn out that it is appropriate to define not only one maximal extension for all operators but to keep terms of different blocks up to different maximal extensions. The reason is that one only obtains a good one particle dispersion by including terms in the $\{1, 1\}$ -block of an extension which is not too low. But it is not possible to take into account all blocks that are necessary for a good description of the system up to the same extension. Therefore, the truncation scheme for the ladder is defined by a set of maximal extensions. Terms that contain n triplet annihilation or creation operators need to have extension d_n or less to be included in the flow equation. This is illustrated in Fig. 4.3. The flowing Hamiltonian contains only terms with an even number of triplet operators. The $\{1, 1\}$ -, $\{0, 2\}$ - and $\{2, 0\}$ -blocks are kept up to extension d_2 . If one takes into account an off-diagonal block connecting to a N -particle subspace it is advantageous to include also the $\{N, N\}$ -block in the calculation. Only then true N -particle interactions are included. Therefore, an additional truncation criterion is imposed in order to restrict the size of the block matrix in Fig. 4.3. Thereby, only off-diagonal blocks are taken into account for which also the corresponding diagonal $\{N, N\}$ -block is present. The figure shows a block matrix containing terms with at maximum four triplet annihilation or creation operators. The truncation criterion for the size of the block matrix is given by an integer N . In the case of Fig. 4.3, $N = 4$ holds. A truncation scheme is fully defined by fixing the size of the blockmatrix N and defining N maximal distances $d = \{d_2, d_4, \dots, d_{2N}\}$.

4.1.2. Dispersion

The effective Hamiltonian is block diagonal. The one-triplon energies are given by the coefficients in the $\{1, 1\}$ -block. This block contains hopping terms of single triplons. It is diagonalized by a

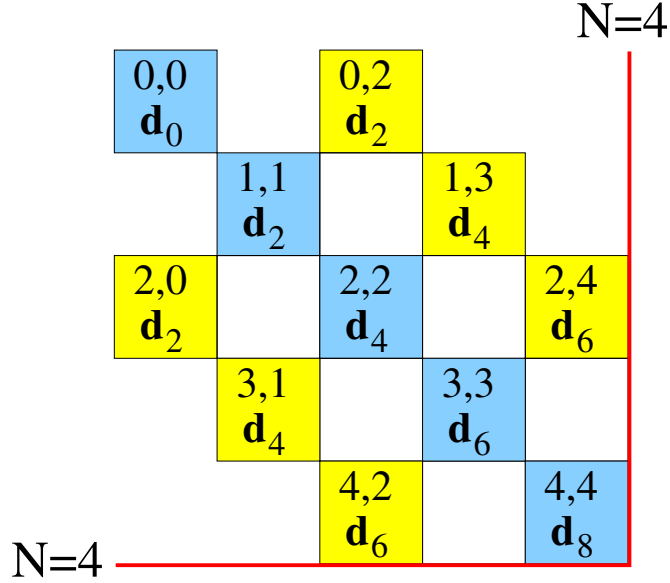


Fig. 4.3: The truncation scheme for the spin ladder introduces different maximal extensions for terms with different number of triplet operators. The figure gives the names of the blocks and the corresponding maximal extension. Note that the action of the Hamiltonian in the $\{0,0\}$ -block is only a number so that d_0 does not matter.

Fourier transform. The dispersion is given by

$$\omega(k) = \langle k | H_{\text{eff}} | k \rangle - E_0 \quad (4.1.13)$$

where $|k\rangle$ is a one-triplon momentum eigenstate with momentum k and E_0 is the ground state energy. The dispersion of the spin ladder has been calculated by various methods [41, 111, 118, 119]. We will discuss the dispersion for two values of x , namely $x = 0.5$ and $x = 1.0$. The results for the one-triplon dispersion for $x = 0.5$ are shown in Fig. 4.4. The figure includes the result from a perturbative CUT (PCUT) treatment to high order [120]. The PCUT result is shown as a thin black line. For the present intermediate values of $x = 0.5$ the PCUT calculation is very accurate. Figure 4.4 shows self-similar CUT results from two different truncations, namely $N = 2, d = \{d_2 = 10, d_4 = 6\}$ and $N = 3, d = \{d_2 = 10, d_4 = 6, d_6 = 3\}$.

The dispersion for $N = 2, d = \{10, 6\}$ shows significant deviations from the PCUT result. Obviously, this calculation omits terms that are necessary to determine the one-triplon energies. It is not sufficient to relax the truncation criterion for terms with two or four triplet operators. The result for the truncation $N = 2, d = \{d_2 = 10, d_4 = 8\}$ (not shown) lies on top of the calculation with $N = 2, d = \{d_2 = 10, d_4 = 6\}$.

The result improves if the size of the blockmatrix is increased to $N = 3$. In the truncation schemes with blockmatrix size $N = 3$ also the $\{1,3\}$ - and $\{3,1\}$ -blocks and true three-particle interactions in the $\{3,3\}$ -block enter in the calculation. These contributions improve the result

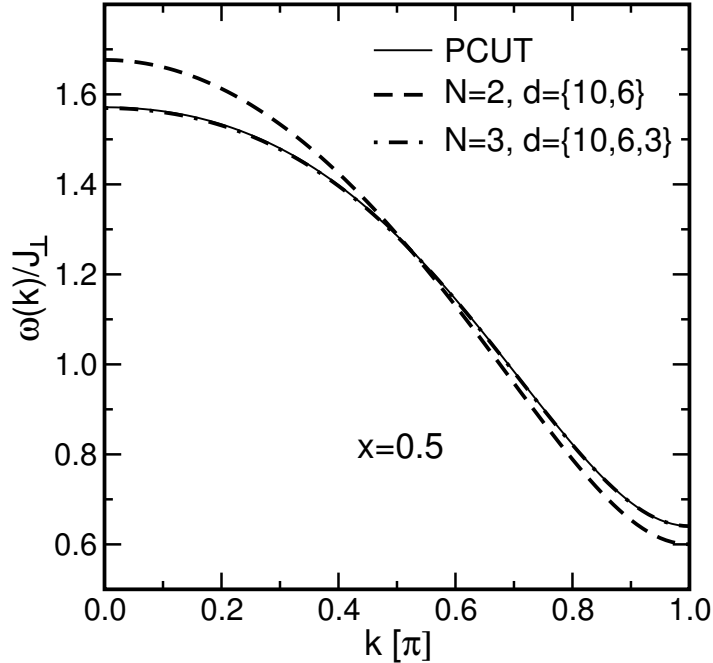


Fig. 4.4: Dispersion of a triplon in the antiferromagnetic Heisenberg ladder. The ratio of leg and rung coupling is $x = 0.5$.

for the dispersion. Figure 4.4 depicts the result from the truncation $N = 3, d = \{d_2 = 10, d_4 = 6, d_6 = 3\}$ as a dashed-dotted line. It is in excellent agreement with the PCUT result.

The dispersion at $x = 0.5$ displays a global minimum at $k = \pi$. The value of the gap is $\omega(k = \pi) = 0.64J_{\perp}$. The overall shape of the dispersion is dominated by the first Fourier coefficient of $\omega(k)$. The global maximum is at $k = 0$ with a value of $\omega(k = 0) = 1.57J_{\perp}$. The truncations $N = 3, d = \{10, 6, 4\}$, $N = 3, d = \{10, 8, 3\}$ and $N = 3, d = \{10, 8, 4\}$ yield results for the dispersion at $x = 0.5$ that coincide with the result for $N = 3, d = \{10, 6, 3\}$ within less than 0.1%. Thus, the result for the dispersion does not change any more on changing the truncation scheme. The self-similar approach to CUTs yields reliable and accurate results for intermediate values of x .

Next, we consider the situation for a large ratio of J_{\perp}/J_{\parallel} , namely $x = 1$. The results for the corresponding dispersion are shown in Fig. 4.5. The result from the PCUT is included as a thin solid line. Note that the PCUT result is covered by the other results. It is identified best in the inset close to the gray (cyan) dashed curve. The inset shows a magnification of the region of small momentum. The dispersion from the $N = 3, d = \{10, 6, 4\}$ truncation is shown as gray (cyan) solid curve. It shows large deviations from the PCUT result. The truncation $N = 3, d = \{10, 6, 3\}$ did not converge. This shows that the calculations with blockmatrix size $N = 3$ are not sufficient to describe the system at $x = 1$. Figure 4.5 shows that calculations

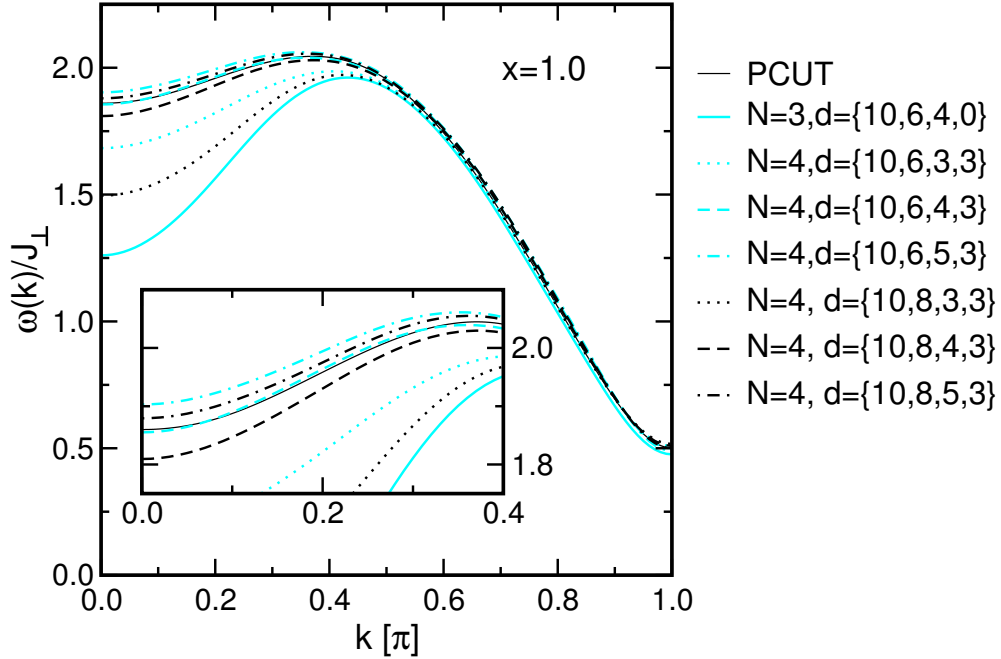


Fig. 4.5: One-triplon dispersion for $x = 1.0$ in units of the rung coupling J_{\perp} . Various results from the self-similar CUT scheme are compared to the dispersion given by a perturbative CUT treatment [120]. The inset shows a magnification of the region with small momentum k .

with $N = 4$ lead to increasing agreement of the self-similar CUT with the PCUT.

The dispersion at $x = 1$ exhibits a local minimum at $k = 0$. This dip is caused by the closeness of the three-particle continuum. This is further explained in Sec. 4.1.4. It can also be viewed as a precursor of chain physics. In the limit of $x \rightarrow \infty$ the two legs of the spin ladder behave like two independent spin chains. The dispersion of the spin chain is symmetric around $k = 0.5$ with a minimum at $k = 0$ and at $k = \pi$. For the homogeneous spin chain the minima have the value $\omega(k = 0) = \omega(k = \pi) = 0$. The dip at $k = 0$ for $x = 1$ in the ladder dispersion is a precursor of the chain-like behavior for large x . The spin chain is the topic of Sec. 4.2.

The results for $N = 4$ are in better agreement with the PCUT than the results for $N = 3$. The series $N = 4, d = \{10, 6, d_6, 3\}$ and $d_6 = 3, 4, 5$ is shown as dotted, dashed and dashed-dotted gray (cyan) curves. The dip value at $k = 0$ increases in this series. The results for $N = 4, d = \{10, 6, 4, 3\}$ and $N = 4, d = \{10, 6, 5, 3\}$ show good agreement with the PCUT result. However, the largest truncation of this series, namely $N = 4, d = \{10, 6, 5, 3\}$, is already above the PCUT result. In the series $N = 4, d = \{10, 8, d_6, 3\}$ with $d_6 = 3, 4, 5$ we find a similar behavior in the dip value. These results are shown as black curves in Fig. 4.5. If we compare the first series with $d_4 = 6$ and the second with $d_4 = 8$ we find that the second series lies systematically below the results of the first series. Thus the result for $N = 4, d = \{10, 8, 5, 3\}$ lies closer to the PCUT result than the result for $N = 4, d = \{10, 6, 5, 3\}$. Unfortunately, it is

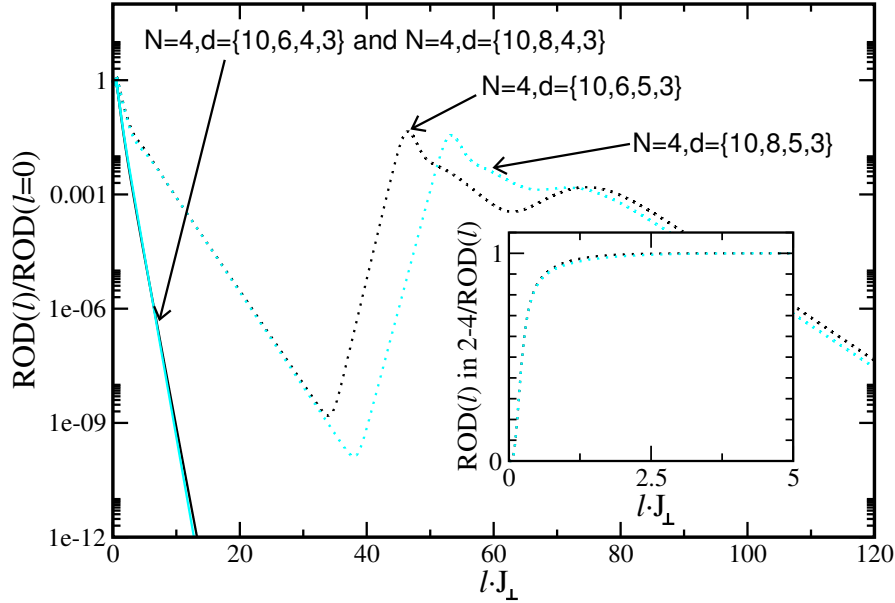


Fig. 4.6: The ROD for various calculations. The truncation schemes with $d_6 = 5$ lead to a pronounced non-monotonic behavior of the ROD. The inset shows the relative ROD which stems from the coefficients of terms in the $\{2, 4\}$ - and $\{4, 2\}$ -block for the calculations with $d_6 = 5$. These coefficients contribute almost the total ROD for values of the flow parameter of $l/U > 2.5$.

computationally costly to increase the value of d_8 because the number of possible terms in the Hamiltonian is growing very fast if d_8 is increased.

The self-similar CUT yields good results for a value of x as high as $x = 1$. However, the agreement is less good than for the intermediate value $x = 0.5$. The behavior of the results of various truncations is encouraging because they appear to converge systematically to the correct results for increasing maximal extension. However, there are still some differences between the results of the different truncation schemes. Further caveats are found in the behavior of the ROD. The ROD is defined as the sum of the coefficients squared that contribute to the generator, see Sec. 2.3.4. The ROD is shown in Fig. 4.6. It is exponentially decreasing for the calculations with $d_6 < 5$. This is shown in Fig. 4.6 for $N = 4, d = \{10, 6, 4, 3\}$ and $N = 4, d = \{10, 8, 4, 3\}$. The exponential decrease of the ROD for these truncations pertains to lowest numerical values. The calculations $N = 4, d = \{10, 6, 5, 3\}$ and $N = 4, d = \{10, 8, 5, 3\}$ both show a non-monotonic behavior of the ROD. A similar behavior has been found in the Hubbard model for too large values of the hopping amplitude.

The main contributions to the ROD come from coefficients of the $\{2, 4\}$ - and $\{4, 2\}$ -block. The inset of Fig. 4.6 shows the relative contribution to the ROD of the coefficients in the $\{2, 4\}$ - and $\{4, 2\}$ -blocks. For values of the flow parameter $l/U > 2.5$ these blocks contain almost the total ROD. This stems from the fact that the 2- and the 4-particle continuum overlap significantly for

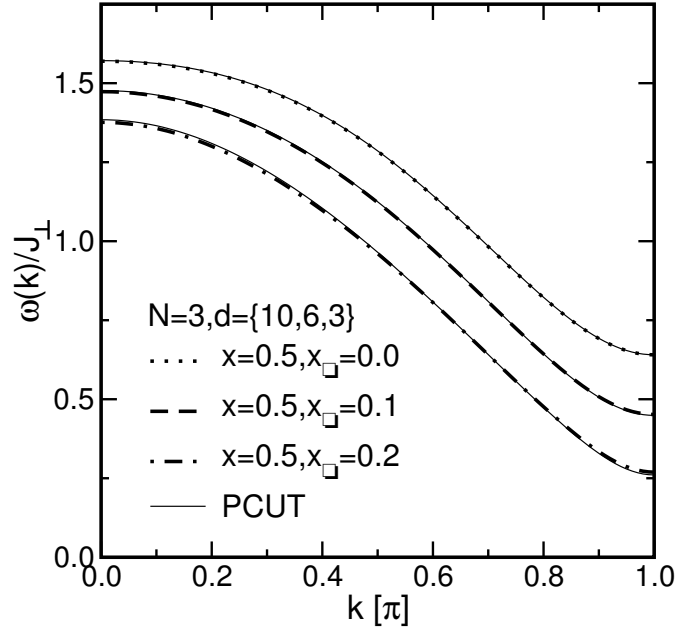


Fig. 4.7: One-triplon dispersion for $x = 0.5$ and various values of x_{\square} . PCUT results are taken from Ref. [120].

$x = 1.0$ as will be further discussed in Sec. 4.1.4. In this case the transformation using the MKU generator is not well-defined as this generator tries to sort the energy eigenstates according to their quasiparticle number.

Already the toy model in Sec. 2.2.3 displayed an uprise of the ROD in cases where the eigenenergies were not sorted according to the quasiparticle number. This does not lead to severe problems if the flow equation is solved exactly. If there are truncations involved the uprise in the ROD indicates that the results of the transformation have to be interpreted with caution. The problems in the transformation show up only for larger truncation schemes. These truncations describe the multi-particle continua more accurately. The transformation is hindered by the overlap of higher continua.

The coefficients that determine the dispersion are in the $\{1, 1\}$ -block. They are fixed already for small values of the flow parameter. The dispersion does not change in the non-monotonic region of the ROD. The $\{2, 2\}$ -block and higher diagonal blocks are influenced by the convergence problems in the $\{2, 4\}$ - and $\{4, 2\}$ -blocks. We will see later in Sec. 4.1.3 that these coefficients change in the non-monotonic region of the ROD.

4.1.2.1. Dispersion with finite four-spin exchange

The inclusion of the four-spin exchange in the Hamiltonian is motivated by experimental observations, see Ref. [41] and references therein. The experimentally relevant value of the four-spin

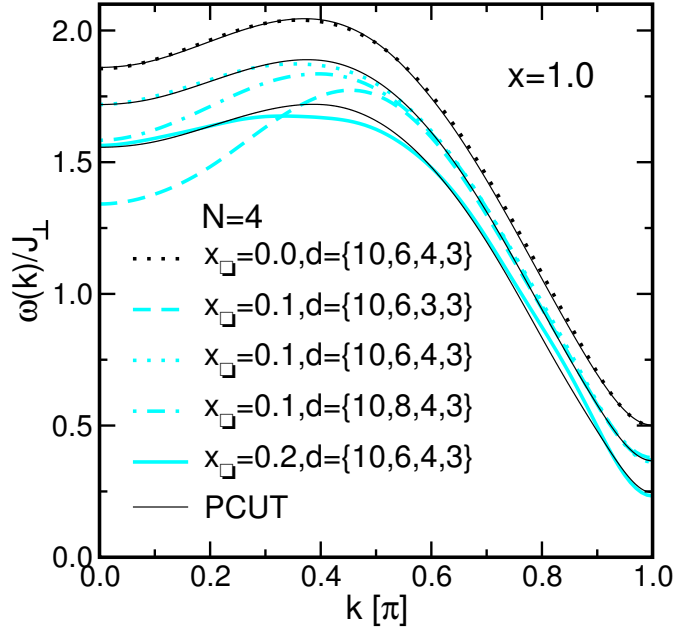


Fig. 4.8: One-triplon dispersion for $x = 1.0$ and various values of x_{\square} .

exchange is about $x_{\square} = 0.2$. This section is intended to show how the four-spin exchange is included in the calculation and how it affects the dispersion of the spin ladder.

The four-spin exchange is given in Eq. (4.1.2) in spin language and reformulated in the triplon basis using Tab. 4.3. Using this basis it can be written in terms of the local operators that are also used to formulate the Hamiltonian without the four-spin exchange. The matrix elements in the second and fifth line in Tab. 4.3 are not present in the Hamiltonian without four-spin exchange. They have to be included in the initial Hamiltonian. Then, the flow equations are calculated in the very same way as without four-spin exchange. The value of the four-spin exchange fixes the corresponding initial conditions. From the calculational point of view the inclusion of new terms in the Hamiltonian corresponds only to a change of the initial conditions in the flow equation. This flexibility is a major advantage of the self-similar CUT method.

Figure 4.7 compares the results for $x = 0.5$ and various values of the four-spin exchange to the findings from the PCUT [120]¹. The self-similar CUT calculation is done with the truncation scheme defined by $N = 3, d = \{10, 6, 3\}$ which is sufficient for the value $x = 0.5$. Figure 4.7 shows the excellent agreement with the PCUT result for $x = 0.5$ and values of the four-spin exchange $x_{\square} = 0.1$ and $x_{\square} = 0.2$.

The situation is more complicated for large values of x . The dispersion for $x = 1$ and finite four-spin exchange is shown in Fig. 4.8. The figure shows the results for $x_{\square} = 0.1$ for three

¹Note that our definition of the four-spin exchange coincides with the one in Ref. [41] but differs by a factor of two from the one in Ref. [120].

truncations, namely $N = 4, d = \{10, 6, 3, 3\}$, $N = 4, d = \{10, 6, 4, 3\}$ and $N = 4, d = \{10, 8, 4, 3\}$. The calculation for $N = 4, d = \{10, 8, 3, 3\}$ cannot be carried out since the ROD diverges during the flow. The three results shown for $x_{\square} = 0.1$ agree only for momenta $k \gtrsim 0.6$. They show strong differences especially at $k = 0$. The reason is again the closeness of the three-particle continuum. The extrapolations used to determine the PCUT result are also more complicated for small k values if one includes the four-spin exchange [120]. However, reliable results can still be extracted from the PCUT at these values of x and x_{\square} [41]. The self-similar CUT does not give a conclusive dispersion for $x = 1.0$ and $x_{\square} = 0.1$. The situation is even worse for larger four-spin exchange. For $x_{\square} = 0.2$ the truncation $N = 4, d = \{10, 6, 4, 3\}$ is the only one of the above mentioned truncation schemes that converges. It gives a reasonable result in comparison to the PCUT curve. However, there is no reliable finding within the self-similar CUT scheme for these parameters because this truncation scheme is the only calculation that converges.

Without four-spin exchange we have found reliable results for the dispersion for $x = 1.0$. The inclusion of the four-spin exchange makes the transformation more challenging. For $x = 0.5$ the dispersion can be determined up to the experimentally relevant ratio $x_{\square}/x = 0.2$. For $x = 1.0$ there is no conclusive finding for the dispersion already for $x_{\square}/x = 0.1$.

4.1.2.2. Dispersion from Wegner's generator

Most of the results in this thesis are found using the MKU generator. In this section we want to compare the dispersion of the MKU generator with the one found using Wegner's generator. Wegner's generator is defined in Sec. 2.2.1. The implementation is described in Sec. 2.5. The results for the dispersion for $x \in \{0.6, 0.8, 1.0\}$ are shown in Fig. 4.9. The figure shows results from the self-similar CUT using the MKU generator (dashed curves), using the Wegner generator (dotted curve) and PCUT results (thin solid curves). The self-similar CUT schemes all use the same truncation scheme $N = 3, d = \{10, 4, 3\}$. The Wegner transformation can be truncated using the same truncation criteria as the MKU transformation. There are additional blocks in the Hamiltonian because it does not stay band-diagonal as it is the case using a MKU generator. Nevertheless, all terms can be grouped according to their number of triplet creation and annihilation operators and then be truncated according to the chosen maximal extensions d_n and size N of the blockmatrix. The PCUT results are taken from Ref. [120]. Recall that the perturbative approach is also realized using a MKU generator.

Up to $x = 0.6$ the three approaches coincide. The PCUT and the self-similar CUT with MKU and with Wegner generator lie on top of each other. For $x = 0.8$ the dispersion from the Wegner generator is slightly higher at small k values than the other results. For $x = 1.0$ the differences are most drastic. The two MKU approaches yield dispersions that have a dip at $k = 0$. The value at $k = 0$ is $\omega(k = 0)/J_{\perp} \approx 1.8$. The difference between the self-similar MKU-CUT and the PCUT is $\approx 0.15J_{\perp}$. The self-similar CUT using Wegner's generator yields a dispersion for $x = 1$ which is much higher in energy.

We will see in Sec. 4.1.4 that at about $x = 1$ the multi-triplon continua start to overlap. At this point an important difference in the properties of the MKU and Wegner generator be-

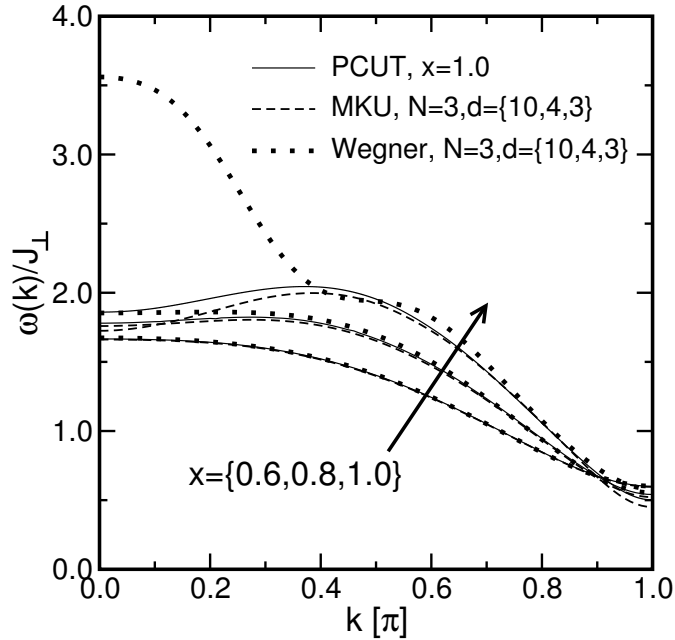


Fig. 4.9: Comparison of dispersions found using Wegner's generator and the MKU generator.

comes effective. The MKU generator sorts the energy eigenvalues according to the quasiparticle number, see Sec. 2.2.2 and Sec. 2.2.3. Therefore, the lowest energy eigenvalue is assigned to a one-triplon state. The Wegner generator does not have this property. It does not map the low energy states to the sector with low triplon number. In the Wegner scheme, it is to be expected that the low lying states at $k = 0$ are recovered in subsectors with higher triplon number. This finding underlines the strength of the quasiparticle scheme connected to the MKU generator. The single-particle states are really the elementary ones because they are energetically the lowest ones.

The MKU scheme yields a more easily interpretable physical picture. It is more appropriate for the description also of comparatively high-energy features within the effective Hamiltonian. An important advantage of the Wegner generator is its robustness [11, 31]. It yields converging flows also for parameters where the MKU scheme does not converge. Therefore, the Wegner generator is particularly successful in the determination of phase diagrams [36, 37, 39, 40].

4.1.3. Two-triplon continuum and bound states

Whereas the original Hamiltonian before the transformation is not quasiparticle conserving the effective model conserves the number of quasiparticles. Thus, the energy of two particles can be determined strictly within the two-particle subspace. The calculation of the two-triplon energies relies on the one-particle coefficients in the $\{1, 1\}$ -block and the true two-particle interactions

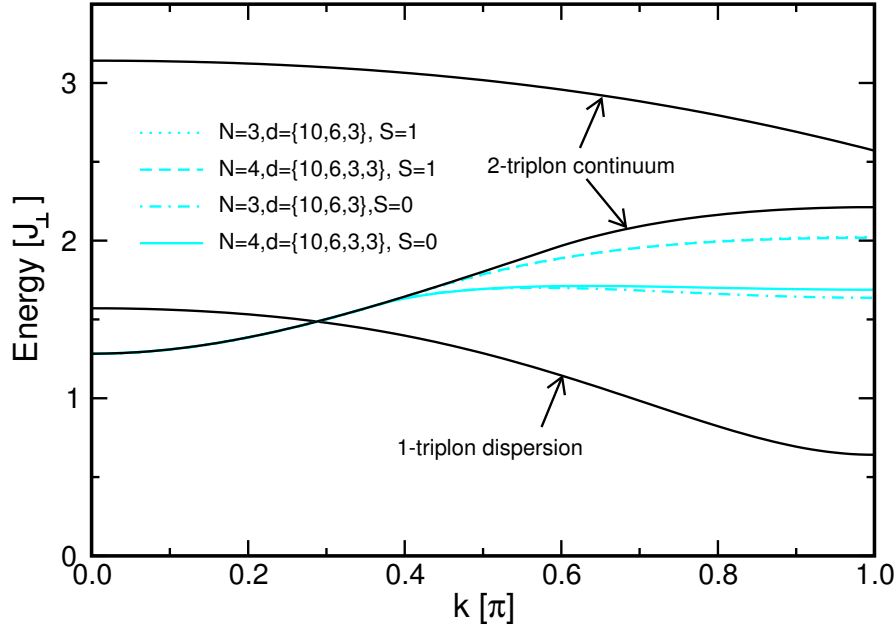


Fig. 4.10: Two-triplon continuum and bound states for $x = 0.5$. Black solid lines show the one-particle dispersion and the lower and the upper bound of the two-particle continuum. Results for the energy of two-particle bound states are included for two truncations in gray (cyan). The results for the $S = 1$ bound state are shown as dotted and dashed curves. The results of the two truncations coincide within the linewidth. The $S = 0$ bound state results are shown as dashed-dotted and solid curves for the two truncations.

which belong to the $\{2,2\}$ -block. A Lanczos algorithm is used to compute the two-triplon energies. For the description of the Lanczos technique see Appendix A. The accurate numerical calculation of the two-particle energies is decisively simplified by the quasiparticle number conservation. Otherwise matrix elements connecting to subspaces with different quasiparticle number would enhance the Hilbert space. This would make it much more difficult to calculate the eigenenergies.

The results of the Lanczos diagonalization for $x = 0.5$ are shown in Fig. 4.10. Energies are given in units of the rung coupling J_{\perp} . The figure shows the lower and the upper bound of the two-triplon continuum as black solid lines. In between these boundaries there exists a continuous distribution of two-particle states. The two triplons interact via the two-triplon interaction. The analysis of the interaction matrix elements shows that two triplons tend to attract each other and bound states form [106, 121–124].

All two-particle states can be grouped according to their total spin into $S = 0$, $S = 1$ and $S = 2$ states. For the value $x = 0.5$ the interactions are sufficiently strong to create an $S = 0$ and an $S = 1$ bound state below the two-triplon continuum [30, 41, 47, 103, 120, 125]. The existence of the bound states depends on the momentum k . For small k values there are no bound states.

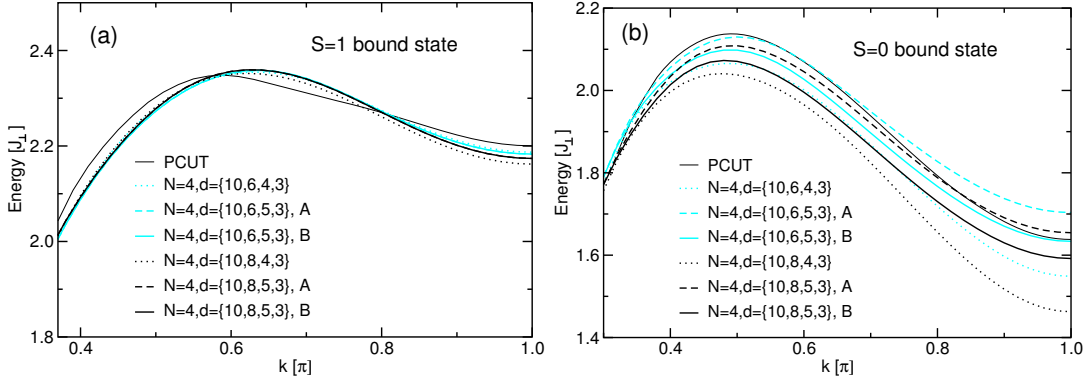


Fig. 4.11: Energy of the bound states for $x = 1.0$ for various truncations. (a) $S = 1$ bound state, (b) $S = 0$ bound state. See main text for further explanation.

The $S = 0$ bound state is present for values $k \gtrsim 0.38\pi$ and the $S = 1$ bound state for values $k \gtrsim 0.42\pi$. For all momenta the binding energy of the $S = 0$ bound state is larger than the binding energy of the $S = 1$ bound state. Figure 4.10 shows the results for the bound states of two different truncations, $N = 3, d = \{10, 6, 3\}$ and $N = 4, d = \{10, 6, 3, 3\}$. The results for the $S = 1$ bound state of these two calculations and the PCUT calculation of Ref. [120] agree with each other within the linewidth (for clarity, the PCUT result is not shown in Fig. 4.10). For the $S = 0$ bound state the truncation scheme $N = 3, d = \{10, 6, 3\}$ does not describe the $\{2, 2\}$ -block accurately enough. The truncation $N = 4, d = \{10, 6, 3, 3\}$ improves this result and coincides with the PCUT result within the linewidth. These results show that the self-similar real space CUT is capable to quantitatively describe the properties of complicated two-particle properties.

Increasing the leg coupling leads to an increasing dispersion of single triplons. In addition, the interaction and especially binding effects between two triplons become more pronounced. The results for the energy of the bound states for the value $x = 1.0$ are shown in Fig. 4.11. The figure shows the result of a PCUT calculation [41] together with the self-similar CUT results for truncations $N = 4, d = \{10, d_4, d_6, 3\}$ for $d_4 \in \{6, 8\}$ and $d_6 \in \{4, 5\}$. In Fig. 4.6 we have seen that the ROD for the truncations $N = 4, d = \{10, 6, 5, 3\}$ and $N = 4, d = \{10, 8, 5, 3\}$ display a pronounced non-monotonicity. Therefore, the figure shows two curves for these calculations, namely before and after the saw tooth in the ROD in Fig. 4.6. The curve labeled $N = 4, d = \{10, 6, 5, 3\}A$ is derived from the effective Hamiltonian at $l \cdot J_{\perp} = 30.13$ where the ROD falls below 10^{-8} times its initial value. The curve $N = 4, d = \{10, 6, 5, 3\}B$ is found for $l \cdot J_{\perp} = 161.37$ after the maximum in the ROD. At this point the ROD falls below 10^{-12} times its initial value. For the truncation $N = 4, d = \{10, 8, 5, 3\}$ the calculation A is stopped at $l \cdot J_{\perp} = 33.84$ and the calculation B is stopped at $l \cdot J_{\perp} = 233.10$. The ROD at these points is $\text{ROD}/\text{ROD}(l = 0) = 10^{-9}$ and 10^{-20} , respectively. For not too small values of the flow parameter the complete remaining ROD is situated in the $\{2, 4\}$ - and $\{4, 2\}$ -block, see Fig. 4.6. Therefore, one expects that the

coefficients of the $\{2,2\}$ -block change in the uprise of the ROD found for both truncations $N = 4, d = \{10, 6, 5, 3\}$ and $N = 4, d = \{10, 8, 5, 3\}$. The energies of the bound state in the $S = 0$ sector show that this is indeed the case.

The energy of the $S = 1$ bound state for $x = 1$ is shown in Fig. 4.11a. The figure compares the above mentioned calculations to the result of the PCUT. There is a small change in the energy of the bound state if we pass from the truncation $N = 4, d = \{10, d_4, 4, 3\}$ to $N = 4, d = \{10, d_4, 5, 3\}$ for $d_4 = 6$ and $d_4 = 8$. The calculations A and B for $d_6 = 5$ yield coinciding results. Thus we conclude that the interaction elements in the $S = 1$ sector are not influenced by the uprise of the ROD observed in Fig. 4.6. The results for $N = 4, d = \{10, 6, 5, 3\}$ and $N = 4, d = \{10, 8, 5, 3\}$ agree well. They both agree with the PCUT result within 2% accuracy.

The results for the $S = 0$ bound state are shown in Fig. 4.11b. The truncations $N = 4, d = \{10, 6, 4, 3\}$ and $N = 4, d = \{10, 8, 4, 3\}$ reproduce the PCUT result only qualitatively. In the case of the $S = 0$ bound state the calculations A and B before and after the saw tooth in the ROD display a difference. The dashed curves show the results in the first deep minimum of the ROD. They agree better with the PCUT result both for the $N = 4, d = \{10, 6, 5, 3\}$ and the $N = 4, d = \{10, 8, 5, 3\}$ truncation. The relative deviation of the $N = 4, d = \{10, 8, 5, 3\}$ result from the PCUT result is less than 2%. The energies found for the bound states are confirmed by density matrix renormalization group (DMRG) calculations [126].

The interaction elements in the $S = 0$ sector change when the flow equations are integrated over the hump in the ROD. Figure 4.11b shows the results after the hump as solid curves. The energy of the $S = 0$ is pushed to lower values for these calculations. The results for the B calculations are further away from the PCUT results. We conclude that the CUT cannot be carried out safely for values of the flow parameter where the pronounced increase in the ROD is observed. The most reliable results are found by stopping the flow in the minimum of the ROD and neglecting the small remaining ROD. This is legitimate because the influence of the neglected matrix elements is small as can be deduced from the smallness of the ROD. We will apply this strategy also in Chap. 5 in the cases where non-monotonic behavior of the ROD is found.

The reason for these problems lies in the re-ordering of the two- and four-particle energies. In the next section, Sec. 4.1.4, we will learn that the two- and four-particle continua have a considerable overlap for $x = 1.0$. In this situation it is impossible to sort the eigenenergies according to the quasiparticle number. The overlap of continua leads to finite lifetime effects since two-particle states can decay into four-particle states of the same energy.

For the $S = 0$ bound state the various truncations lead to slightly different results. Therefore, these results are not fully conclusive. To treat even larger truncations is not only hindered by the computational costs. A larger truncation scheme would also describe the multi-particle subspaces more accurately. We suppose that it would lead to more severe problems if one tries to disentangle the subspaces of especially two and four triplons. As we have seen in the case of the $S = 0$ bound state the convergence problems give rise to inaccuracies in the result. Thus, a larger truncation scheme does not necessarily lead to better results.

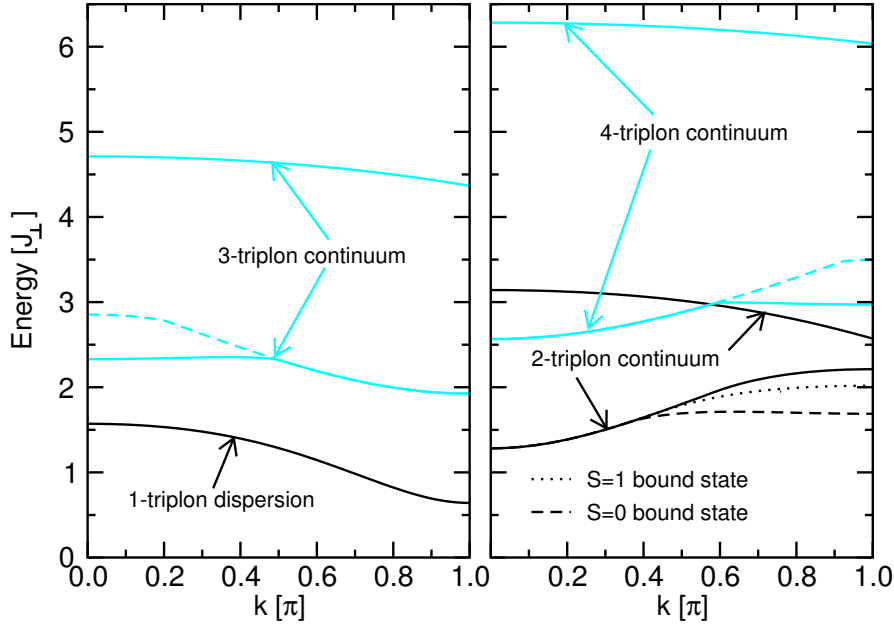


Fig. 4.12: Relative position of multi-triplon continua for $x = 0.5$. On the left, the sectors with odd number of triplons are shown. The right plot shows the sectors with even number of triplons. Note that the Hamiltonian of the spin ladder changes the triplon number only by an even number.

4.1.4. Multi-triplon continua

The Hamiltonian of the spin ladder can change the number of quasiparticles only by plus or minus two in a single application. This property is conserved during the flow using the MKU generator. Therefore, we present the one- and the three-particle continuum and the two- and four-particle continuum in separate graphs. The multi-triplon continua are calculated from the single triplon dispersion and the energies in the two-triplon sector. This includes also binding effects of two triplons as shown in the preceding section. True three- and four-particle interactions are neglected.

The resulting energy bands of the multi-triplon continua are shown in Fig. 4.12 for $x = 0.5$. The one- and three-particle sector are well separated. The lower boundary of the three-triplon continuum is shown as solid gray (cyan) line. It includes binding effects in the two-particle sector. With binding effects the lower boundary of the continuum may result from the combination of a two-triplon bound state and a single triplon. Without binding effects the three-triplon energies are calculated from the one-particle energies only. The dashed line gives the position of the lower edge without binding effects. Figure 4.12 shows that the substantial binding energy of the $S = 0$ bound state leads indeed to a lowering of the edge of the three-triplon continuum at low momentum values.

The right-hand side of Fig. 4.12 shows the two- and four-triplon continuum. The dashed gray

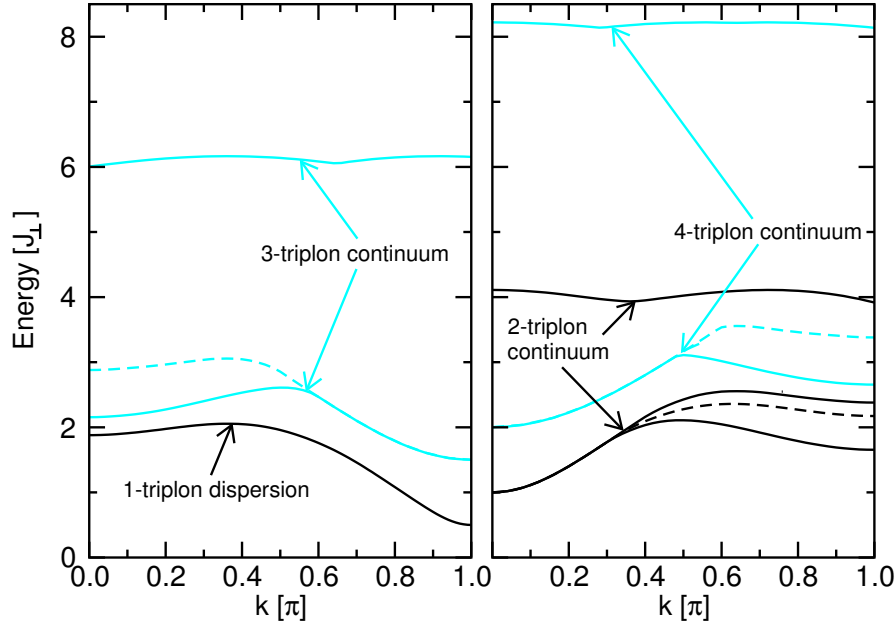


Fig. 4.13: Multi-triplon continua for $x = 1.0$. One- and three-particle continua are shown on the left plot. Two- and four-triplon continua are shown on the right plot.

(cyan) curve represents the lower edge of the four-triplon continuum without binding effects in the two-triplon sector. The continua overlap for momenta $k \lesssim 0.6$. However, the preceding section did not find any effect of this overlap in the transformations for $x = 0.5$. The ROD decays monotonically for $x = 0.5$. A possible reason is that the overlap is quite small. In the local approach to CUTs operators are represented in real space. Especially the operators dealing with a larger number of quasiparticles are taken into account only up to a small extension. The finite range of operators in real space leads to a finite resolution of the k -space properties. In addition, the weight close to the boundary of multi-particle continua is very small [127]. The CUT can be carried out for $x = 0.5$ without problems although the momentum representation of the multi-triplon continua shows that the two- and four-triplon continua overlap slightly.

The multi-triplon continua for $x = 1$ are shown in Fig. 4.13. The three-triplon continuum on the left-hand side of Fig. 4.13 extends to lower energies. It comes close to the one-triplon dispersion. At low values of k the vicinity of the three-particle continuum pushes the one-particle energies to lower values. The one-triplon dispersion exhibits a dip at $k = 0$. The right-hand side shows the continua with even triplon number. There is a considerable overlap of the two- and four-triplon sector for all values of the momentum. The MKU generator tries to sort the energies according to quasiparticle number. However, for $x = 1$ we find that the continua of different particle number overlap. This leads to the observed behavior of the ROD in Fig. 4.6 and to the problems in the quantitative determination of the bound state energies.

4.1.5. Discussion

The present section treats the antiferromagnetic spin ladder starting from the dimerized limit within a self-similar CUT approach. For an intermediate value of the leg coupling, namely $x = 0.5$, we find that a quantitative description of one- and two-particle properties is possible. Also the determination of the energy of bound states is numerically reliable. For $x = 1.0$ the one-particle energies can be calculated with good accuracy. The one- and three-particle states are still separated by a finite energy gap. The strong overlap of the two- and four-particle continua hinders the elimination of the operators connecting these sectors of the Hilbert space. Because truncations have to be applied the transformation cannot be carried out in a well-controlled way.

The self-similar MKU CUT runs into problems in situations where continua of different particle numbers overlap. The MKU generator tries to sort the eigenvalues according to the quasiparticle number. This is not possible in the presence of strongly overlapping continua. Such a situation is found for the spin ladder for the parameter $x = 1.0$. In this case, states with two and four triplons have the same energy. This leads to finite lifetime effects because states with two-triplons can decay into four triplons.

In the PCUT scheme these problems do not hinder the transformation. The reason is that the perturbative treatment is an expansion around $x = 0$. Strictly at $x = 0$, there are no problems concerning the order of multi-particle continua. An n -particle state has the energy nJ_{\perp} . Therefore, the series expansion around $x = 0$ is well-defined. Problems occur if one tries to extrapolate the series into parameter regimes with overlapping continua [120]. The Padé extrapolated series have poles and special care has to be taken to extract meaningful results. The problems related to finite lifetime effects are circumvented by sophisticated extrapolation techniques.

The self-similar CUT scheme is more susceptible to the problems originating from the overlap of different continua. The overlap of the continua is not an artefact. Therefore, the MKU scheme necessarily has difficulties in re-ordering the energy levels according to the quasiparticle number. In this sense the self-similar CUT scheme has a higher sensibility to capture the issue of the re-ordering process. It explicitly shows the complex physical situation. The ROD diverges if the transformation cannot be carried out at all. A strong non-monotonic behavior in the ROD signals that the transformation is demanding and might be flawed by inaccuracies. On the other hand the PCUT results might hide in some circumstances fingerprints of actual problems in the transformation. The overlap of subsectors of different quasiparticle number can lead to a non-analytic dependence of the energetic position of the continua [128]. Such a behavior cannot be captured within a perturbative approach. The self-similar approach will at least signal these problems in the behavior of the ROD. Then, one can devise some of the means described below to handle the problem.

In general, any system having a finite dispersion will have overlapping many-particle continua. For small bandwidths the overlap is present only between continua with large particle number. The crucial question for the present self-similar CUT scheme to work is, whether these continua have to be included in the derivation of the effective model. For the spin ladder we have seen

that the inclusion of the three-particle continuum is necessary to produce the dip in the one-particle dispersion. Correspondingly, four-particle operators have been necessary to find good results for the description of the two-particle energies. The problem depends of course on the parameter regime one is interested in. For the spin ladder the transformation is carried out safely for $x = 0.5$. The small overlap of the continua, see Fig. 4.12, did not affect the quality of the effective Hamiltonian. For $x = 1.0$ the overlap is larger and hinders a reliable determination of the effective model.

We want to point out some means how one could deal with the convergence problems that have been one focus of this chapter. The first possibility is to just stop the flow at a minimum of the ROD and neglect the remaining off-diagonal coefficients. This is legitimate if the remaining ROD is small. This has been done Sec. 4.1.3. We will also neglect the remaining off-diagonal coefficients in the case of the bosonic Hubbard model treated in Sec. 5 with the same justification.

Second, there are ways to treat the remaining off-diagonal part of the Hamiltonian after stopping the flow. For example, one can account for the off-diagonal part by perturbation theory. In this case, the block-diagonal terms are viewed as the unperturbed part of the Hamiltonian. Another possibility is to use a numerical technique such as Lanczos diagonalization also in the case of a non-blockdiagonal Hamiltonian. The Hilbert space is enlarged because one can not treat the sectors of different quasiparticle number separately. But, if the off-diagonal elements are not too large this might still be a viable path.

Finally, the transformation within the MKU scheme can be modified. One excludes from the generator the sectors that hinder a successful transformation. The transformation can then be carried out without the convergence problems encountered so far. However, the excluded block will not be transformed away and will still be present after the CUT. In a second step one can deal with the problematic block using Wegner's generator. The Wegner generator is more robust than the MKU generator and thus one can hope to eliminate the remaining off-diagonal block safely. In the end the combined transformation again produces a block-diagonal effective Hamiltonian. This procedure will be applied to the spin chain in the following section, Sec. 4.2.

4.2. Spin chain

The one-dimensional Heisenberg chain consists of spins of size one-half that are linearly arranged. Each site is connected to its two nearest neighbors via an isotropic spin coupling. Quantum effects play a dominant role because of the low dimensionality of the model and the small absolute value of the spin. Recent progress has been made in the calculation of spectral properties of the spin chain [129, 130]. These results have revived the discussion about the appropriate quasiparticle picture in this system. The question seemed to be settled with the spinon interpretation of the energy properties of the spin chain [131–135]. Spinons are excitation carrying spin one-half. In the spin chain they can only be created in pairs. The spinon formalism describes the continuum of states in the spectrum of the spin chain as a two-spinon continuum. The spinon language has been used to derive the spectral weight and the spectral density in the two-spinon channel [129]. An alternative quasiparticle picture has been put forward by *Uhrig* and *Schmidt* [130]. They start from the dimerized spin chain and describe the energy and spectral properties of the spin chain in terms of triplons. These are excitations of a disordered magnet with spin one². They find a surprisingly high spectral weight in the two-triplon channel. Practically the complete spectral weight is found in the two-triplon sector for the undimerized spin chain. At the same time the single triplon contribution goes to zero. These results rely on certain extrapolations that also include assumptions about the system. The dynamics of the system is not included in the study.

In this section we want to study if the triplon picture can also be constructed within the self-similar CUT in real space. The starting point is the fully dimerized chain. Then, the inter-dimer coupling is turned on. The one-triplon dispersion is calculated for various values of the dimerization. The dispersion relation of the undimerized chain is known exactly. It is gapless. From the discussion in the preceding section we know that this will cause problems in the convergence of the transformation. Nevertheless we will study down to which value of the dimerization one can find quantitative results using the self-similar CUT. The spectral weights for the observable S_z are calculated and compared to the results from the PCUT.

4.2.1. Model and method

The Hamiltonian of the dimerized spin chain reads

$$H = J_0 \sum_i [(1 + (-1)^i \delta) \mathbf{S}_i \mathbf{S}_{i+1}], \quad (4.2.14)$$

where J_0 is the average strength of the magnetic coupling. The dimerization δ leads to an alternation of strong bonds with coupling $J_0(1 + \delta)$ and weak bonds with coupling $J_0(1 - \delta)$. It is useful to rewrite the above Hamiltonian by separating explicitly the strong and the weak

²Magnons in contrast are excitations of an ordered magnet. In antiferromagnets there are two flavors of a magnon. The triplon has three flavors coming from the three S_z eigenstates of the underlying triplet excitation. There is one magnon per site while there are three triplons per two sites.

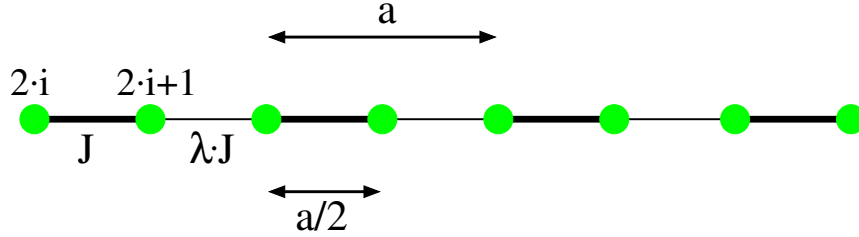


Fig. 4.14: Sketch of the spin chain.

bonds

$$\frac{H}{J} = \sum_i [\mathbf{S}_{2i}\mathbf{S}_{2i+1} + \lambda\mathbf{S}_{2i-1}\mathbf{S}_{2i}]. \quad (4.2.15)$$

where the parameters J and λ are related to J_0 and δ by the following relations

$$J = J_0(1 + \delta) \quad (4.2.16a)$$

$$\lambda = \frac{1 - \delta}{1 + \delta}. \quad (4.2.16b)$$

The system is sketched in Fig. 4.14. The strong bonds couple pairs of two spins to dimers. These dimers are connected via a coupling of strength λJ . The value of λ can be restricted to $\lambda \in [0, 1]$ as one can choose δ to be positive. A sign change in δ corresponds only to the exchange of strong and weak bonds. The distance between two dimers defines the lattice constant a . Note that the sites of the original lattice have a spacing of $a/2$. The dimerized spin chain displays a finite spin gap for any non-zero value of the dimerization. The spin gap vanishes if the dimerization is zero.

The starting point of the CUT is the fully dimerized system at $\lambda = 0$. The ground state is the product state of local singlets. This is the reference state for the setup of the self-similar CUT. Local triplets are excitations which cost the energy J at $\lambda = 0$. The gapless system is retrieved for $\lambda = 1$. The triplet number operator serves as a counting operator for the MKU scheme, see also Sec. 2.

Before the details of the calculation are described we want to give an account of the conventional picture of the excitations of the Heisenberg chain in terms of spinons. Then, the alternative interpretation in terms of triplon excitations is presented. This interpretation has been brought up using a perturbative CUT calculation [42, 130]. One aim of this section is to clarify if the triplon interpretation can also be supported within the present self-similar CUT scheme.

The homogeneous spin chain is exactly solvable by Bethe ansatz [131, 132, 136–140]. The

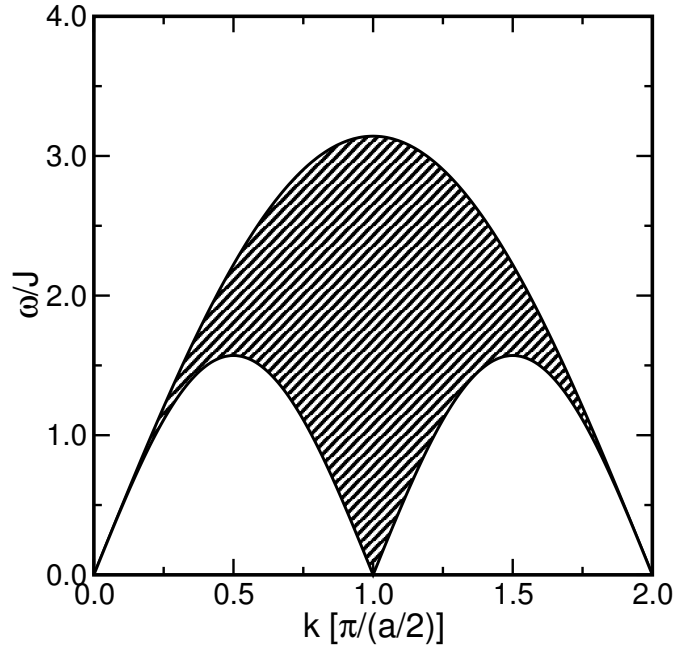


Fig. 4.15: The energies of the excited states of the spin chain as given by Bethe ansatz form a continuum.

solution motivates the spinon picture of the excitations of the spin chain. The Bethe ansatz solution gives the ground state and the excited states exactly. The support of the excitation spectrum is shown in Fig. 4.15. The dispersion of a single spinon reads

$$\omega(k) = J \frac{\pi}{2} \sin\left(\frac{a}{2}k\right), \quad (4.2.17)$$

where the momentum k lies in the interval $0 \leq k \leq \pi/(a/2)$. Spinons carry a spin $1/2$. They do not interact at $\delta = 0$ at infinite distance. At finite dimerization the spinons are confined by an attractive potential [141]. The total spin of the full system can only be changed by an integer. The total spin is fixed to be integer or half-integer. Therefore, a single spinon cannot be excited. The energies shown in Fig. 4.15 are two-spinon energies. The shaded area is the support of the two-spinon continuum.

The description in terms of triplons starts from the dimerized system. It is argued that the triplon description extends to the undimerized system at $\delta = 0$ [42, 130]. The dimerized system is successfully described in the triplet picture. For small λ or large dimerization already the leading order in perturbation theory yields the correct qualitative behavior. References [121, 142] show that the energy properties including the appearance of bound and anti-bound states for the dimerized system are correctly described by leading order perturbation theory. Using high order perturbation theory the results can be extrapolated to the undimerized system. This has been pointed out in Refs. [42, 130] using the PCUT method and has been verified in Refs. [143, 144] using a linked cluster series expansion.

The calculation of spectral properties using Bethe ansatz has been presented by *Karbach et al.* in 1997, Ref. [129]. This is much more difficult than the determination of the energy levels. The calculations depend on the studied observable. They describe the outcome of an experiment in which an external field couples to this observable. Therefore, the spectral quantities give important insight in the physics of the system including matrix element effects. The spectral weight in a channel with fixed particle number determines which part of the total weight is described by this number of particles. The finding of the Bethe ansatz solution is that 72.89% of the total intensity is found in the two *spinon*-continuum.

The spectral weight in terms of triplon excitations has been calculated in Refs. [42, 130, 143, 144]. It is found that the weight in the one-triplon channel vanishes upon approaching the undimerized chain. This behavior of the one-triplon weight is expected. It is found that the weight is almost completely shifted in the two-triplon channel. The two-triplon weight is larger than 99% of the total weight. Note that in the Bethe ansatz description the two-particle channel refers to two spinons whereas the triplon approach refers to two-triplon excitations. This result is remarkable. It suggests that the triplon approach incorporates more weight than the well-established spinon description in the channels with low particle number. In addition to the fact that the two-triplon spectral weight is larger than the two-spinon weight, it also comprises almost the total weight. This does not imply that one of the pictures – spinon or triplon – is wrong. Nevertheless, it would be a very interesting finding if triplons provided a valid description of the spin chain down to vanishing dimerization.

In this section we want to study if the result from the PCUT calculation can be reproduced within the self-similar CUT approach. The starting point for the self-similar CUT is the dimerized system as it is for the PCUT. The intra-dimer coupling does not conserve the number of triplons. It has to be transformed away. For finite dimerization δ the system is gapped. This facilitates the transformation. It is known that the dispersion of the spin chain becomes gapless at $\lambda = 1$ corresponding to $\delta = 0$. In the preceding section, Sec. 4.1, it has been shown that the overlap of continua of different quasiparticle number leads to convergence problems. Therefore, one has to be aware that the transformation will become increasingly challenging for large λ . Our aim is the calculation of the one-triplon dispersion and the spectral weight. Spectral densities will not be discussed. The results are compared to the PCUT results taken from Refs. [42, 120, 130].

4.2.1.1. Implementation of the CUT

The Hamiltonian in Eq. (4.2.15) couples strong bonds between sites $2i$ and $2i + 1$ with coupling strength J . Weak bonds between sites $2i - 1$ and $2i$ are coupled by λJ . The Hamiltonian is rewritten in terms of triplet operators on the strong bonds. The implementation of the technique is very much like the one used in Sec. 4.1 for the spin ladder. The local basis has four states, the singlet and the three triplets with flavor $\in \{1, 0, -1\}$. The part of the Hamiltonian acting

$4\mathcal{T}_0^a$		
$ t^{0,\pm 1}, s\rangle$	\rightarrow	$- s, t^{0,\pm 1}\rangle$
$4\mathcal{T}_0^b$		
$ t^0, t^{0,\pm 1}\rangle$	\rightarrow	$ t^{0,\pm 1}, t^0\rangle$
$ t^{\pm 1}, t^{\pm 1}\rangle$	\rightarrow	$ t^{\pm 1}, t^{\pm 1}\rangle$
$ t^{\pm 1}, t^{\mp 1}\rangle$	\rightarrow	$ t^0, t^0\rangle - t^{\pm 1}, t^{\mp 1}\rangle$
$ t^0, t^0\rangle$	\rightarrow	$ t^1, t^{-1}\rangle + t^{-1}, t^1\rangle$
$4\mathcal{T}_1$		
$ s, t^1\rangle, t^1, s\rangle$	\rightarrow	$ t^1, t^0\rangle - t^0, t^1\rangle$
$ s, t^0\rangle, t^0, s\rangle$	\rightarrow	$ t^1, t^{-1}\rangle - t^{-1}, t^1\rangle$
$ s, t^{-1}\rangle, t^{-1}, s\rangle$	\rightarrow	$ t^0, t^{-1}\rangle - t^{-1}, t^0\rangle$
$4\mathcal{T}_2$		
$ s, s\rangle$	\rightarrow	$ t^1, t^{-1}\rangle - t^0, t^0\rangle + t^{-1}, t^1\rangle$

Table 4.4: The action of the operators \mathcal{T}_j on states on adjacent dimers of the spin chain.

on the strong bonds is

$$\frac{H_{\text{strong}}}{J} = \sum_i \mathbf{S}_{2i} \mathbf{S}_{2i+1}. \quad (4.2.18)$$

Up to a constant this operator counts the triplet number and is therefore diagonal in the triplet basis. The Hamiltonian on the weak bonds reads

$$\frac{H_{\text{weak}}}{J} = \sum_i \lambda \mathbf{S}_{2i-1} \mathbf{S}_{2i}. \quad (4.2.19)$$

It is rewritten in terms of triplet operators as

$$\frac{H_{\text{weak}}}{J} = \sum_{n=-2}^2 T_n = \sum_{n=-2}^2 \sum_{\nu} \mathcal{T}_n(\nu). \quad (4.2.20)$$

The operators T_n change the number of triplets by n . They are composed of the local operators $\mathcal{T}_n(\nu)$ that act on the bond labelled by ν . The operators $\mathcal{T}_n(\nu)$ are defined in terms of their matrix elements on the product states of adjacent dimers in Tab. 4.4. Remaining matrix elements can be determined by hermitian conjugation.

The triplet number is changed by two at most. The Hamiltonian of the spin chain can change the triplon number also by ± 1 . This has not been possible in the case of the spin ladder, see Sec. 4.1. The truncation scheme is defined in the same way as for the ladder system in Sec. 4.1.1.1. It is illustrated in the sketch of the block structure of the Hamiltonian in Fig. 4.16. Different maximal extensions are defined for different numbers of triplet operators. The block with zero triplet operators acts only as a constant. Therefore, there is no need to define a truncation d_0 . As the quasiparticle number can be changed also by one there are additional

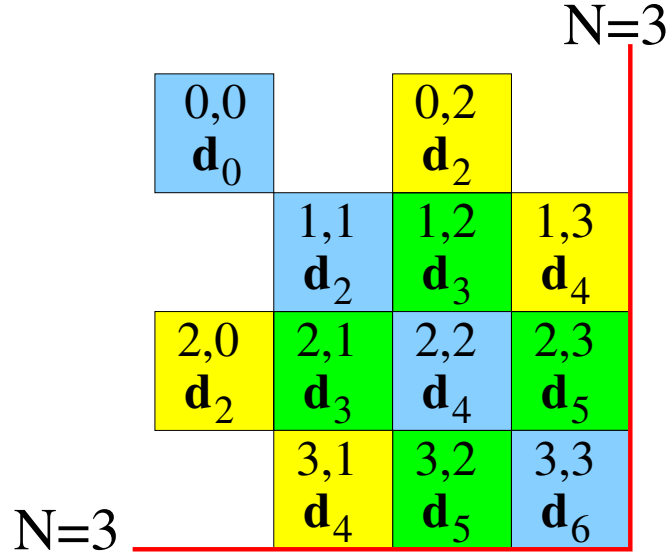


Fig. 4.16: The Hamiltonian of the spin chain changes the triplet number by ± 1 and ± 2 . The matrix sketches the definition of the truncation scheme for the spin chain. It denotes the names of the blocks together with the corresponding maximal extensions.

blocks. They have to be truncated with a certain maximal extension. Note that there are no operators with only a single triplet operator due to spin conservation. The maximal size of the block matrix is fixed by N . The truncation scheme is defined by the size N of the block matrix and the $2n - 1$ maximal extensions d_2, \dots, d_{2N} .

4.2.1.2. Observable

The local observable that is studied reads

$$\mathcal{O}_{\text{loc}}^{S=1}(r) = S_r^z = \mathcal{T}_{-1}^{S=1} + \mathcal{T}_0^{S=1} + \mathcal{T}_1^{S=1}. \quad (4.2.21)$$

The action of the observable is sketched in Fig. 4.17. The local observable acts on one specific site. This site can be the left or the right site of a strong bond. The parameter r denotes the site on which the local observable acts.

The observable induces $S = 1$ excitations. The operators $\mathcal{T}_n^{S=1}$ are defined via the matrix elements given in Tab. 4.5. The observable is the sum over the local observables

$$\mathcal{O}^{S=1} = \sum_r \mathcal{O}_{\text{loc}}^{S=1}(r) = \sum_r S_r^z. \quad (4.2.22)$$

The transformation deals with the coefficients of the local observable. The full, translationally invariant observable is recovered by summation over the lattice sites. The matrix elements given in Tab 4.5 depend on the site on which the observable acts.

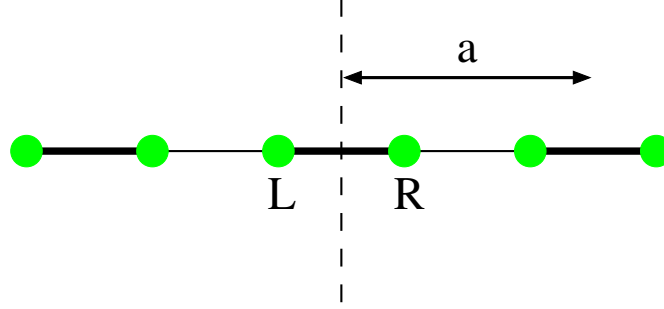


Fig. 4.17: Sketch of the action of the observable. The local observable can act on the left (L) or right (R) site within a strong bond. The strong bonds are depicted by thick lines.

The general aspects of the transformation of an observable are described in Sec. 2.3.5. The observable is transformed with the same generator as the Hamiltonian. But, one has to introduce a separate truncation scheme for the observable. The reason is that the local untransformed observable is connected to a certain site of the lattice. Contributions to the effective observable with large distance to this original site are less important. Therefore, the maximum of the sum of the distances of all local operators within the effective observable is restricted by the observable extension $d_{\mathcal{O}}$. There are also contributions with a single triplet operator in the observable. The truncation scheme for the observable is defined by a maximal size $N_{\mathcal{O}}$ of the block matrix of the observable and $2N_{\mathcal{O}}$ maximal observable extensions $d_{\mathcal{O},1}, \dots, d_{\mathcal{O},2N_{\mathcal{O}}}$. The maximal observable extension $d_{\mathcal{O},n}$ restricts the extension of terms with n triplet operators in the observable.

In our study of the S_z observable the quantity of interest is the spectral weight I_n in the n -particle channel. At zero temperature one obtains the spectral weights I_n by summing the squares of the coefficients of the terms that excite the respective number of particles from the vacuum. The spectral weights will be discussed in Sec. 4.2.3.

$\mathcal{O}_{\text{loc}}^{S=1} = S_L^z$		$\mathcal{O}_{\text{loc}}^{S=1} = S_R^z$	
$2\mathcal{T}_0^{r,S=1}$		$2\mathcal{T}_0^{r,S=1}$	
$ t^{-1}\rangle$	\rightarrow	$- t^{-1}\rangle$	
$ t^1\rangle$	\rightarrow	$ t^1\rangle$	
$2\mathcal{T}_1^{r,S=1}$		$2\mathcal{T}_1^{r,S=1}$	
$ s\rangle$	\rightarrow	$ t^0\rangle$	
$ t^0\rangle$	\rightarrow	$ s\rangle$	

Table 4.5: The observable $\mathcal{O}^{S=1} = S_r^z$ with $r \in \{L, R\}$ is defined by the matrix elements given in this table. The left panel gives the matrix elements of $\mathcal{O}^{S=1} = S_L^z$ and the right panel those of $\mathcal{O}^{S=1} = S_R^z$.

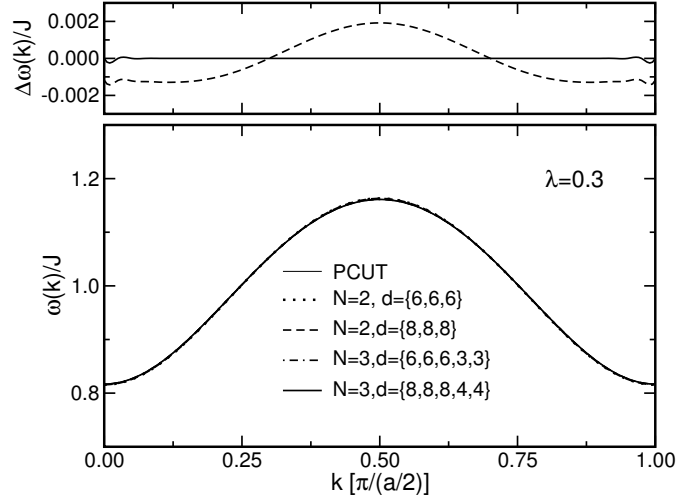


Fig. 4.18: Dispersion for $\lambda = 0.3$. The various truncations show excellent agreement between one another and with the PCUT result. The top graph shows the difference between the self similar CUT and the PCUT dispersion.

4.2.2. Dispersion

The dispersion consists of the momentum dependent one-particle energies. Within the effective model the dispersion is fixed by the coefficients of the $\{1, 1\}$ -block. The hopping amplitudes are Fourier transformed to obtain the momentum space representation. The results for $\lambda = 0.3$ are shown in Fig. 4.18. The figure shows the dispersion for truncations with $N = 2$ and $N = 3$. For $N = 2$ the maximal extensions used are $d = \{6, 6, 6\}$ and $d = \{8, 8, 8\}$ and for $N = 3$ the truncations $d = \{6, 6, 6, 3, 3\}$ and $d = \{8, 8, 8, 4, 4\}$ are shown. The dispersion has the overall shape of a cosine. The minima of the dispersion are found at $k = 0$ and $k = \pi$ (in units of $a/2$). The mutual agreement of the various calculations is excellent. They agree perfectly with the PCUT result. The difference of the self-similar calculation and the PCUT is shown in the top view graph. The truncations with $N = 2$ and $N = 3$ lie on top of each other. The deviation of the $N = 2$ calculation from the PCUT result is of the order of $0.002J$. The $N = 3$ calculations practically coincide with the PCUT result. The tiny wiggles around $k \approx 0$ and $k \approx \pi$ are extremely small. They are due to the extrapolations used in the PCUT result. For $\lambda = 0.3$ the dimerization is still quite strong. The one-triplon gap is large. Therefore the transformation can be carried out without any problem.

The results from the same truncations are shown in Fig. 4.19 for the value $\lambda = 0.6$. The shape of the dispersion is still cosine like. With increasing λ the bandwidth increases. The two calculations with $N = 2$ and the two calculations with $N = 3$ lie on top of each other. There is a small difference between the $N = 2$ and the $N = 3$ calculations. The deviation is best seen in the inset where the difference between the self-similar results and the PCUT result is

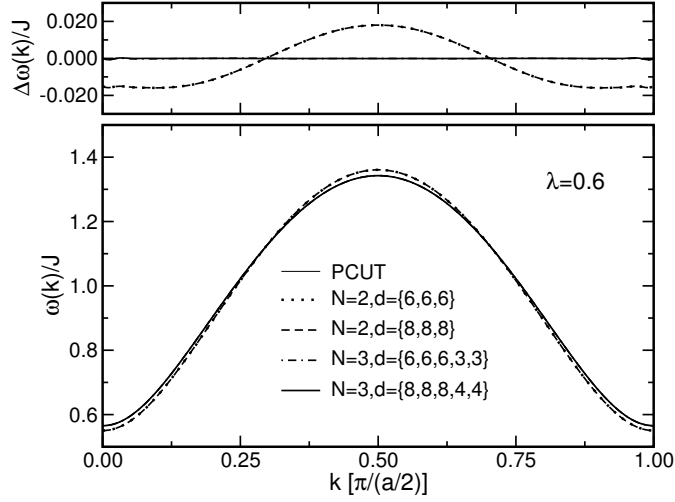


Fig. 4.19: Dispersion for $\lambda = 0.6$. The top graph shows the deviation of the results of the self-similar CUT from the PCUT result.

plotted. The calculations with $N = 2$ show a small deviation from the PCUT. The difference is approximately $0.02J$. Increasing the size of the block matrix to $N = 3$ leads to a nearly perfect agreement of the self-similar CUT and PCUT results.

Increasing the coupling λ leads to the same problems that we have encountered in the study of the spin ladder. The bandwidth increases and the energies of the continua with different quasiparticle number overlap. It becomes problematic to disentangle the sectors with different quasiparticle number. The situation is more severe for the spin chain because the quasiparticle number can be changed by one or by two. The one-particle subspace is therefore not only linked to the three-particle subspace but also to the two-particle subspace. In the case of the spin ladder the triplon number could be changed only by two. In addition, the dispersion of the spin chain is gapless for $\lambda = 1.0$. At least at this point, the continua of all particle numbers overlap.

The problems are signalled by the behavior of the convergence of the flow equation. While for $\lambda = 0.3$ all flow equations converged exponentially, this is no longer the case for $\lambda = 0.6$. The residual off-diagonality (ROD) is defined in Sec. 2.3.4 as the sum of the squares of all coefficients that contribute to the generator. The ROD for $\lambda = 0.6$ is shown in Fig. 4.20. The truncations $N = 2, d = \{6, 6, 6\}$ and $N = 2, d = \{8, 8, 8\}$ are shown as dotted and dashed curve, respectively. The ROD for these two truncations lie on top of each other. The ROD for $N = 3, d = \{6, 6, 6, 3, 3\}$ is shown as dashed-dotted line. The two truncation schemes with $N = 2$ and the one with $N = 3, d = \{6, 6, 6, 3, 3\}$ converge monotonically for $\lambda = 0.6$. The ROD for $N = 3, d = \{8, 8, 8, 4, 4\}$ shows a pronounced non-monotonic behavior. The ROD decreases by a factor of 10^{-8} before it rises again by nearly the same factor. The inset shows the contribution of coefficients in the $\{2, 3\}$ -block to the total ROD. Already for not too small values of the flow parameter l , the main contribution to the ROD results from the $\{2, 3\}$ -block. The dispersion

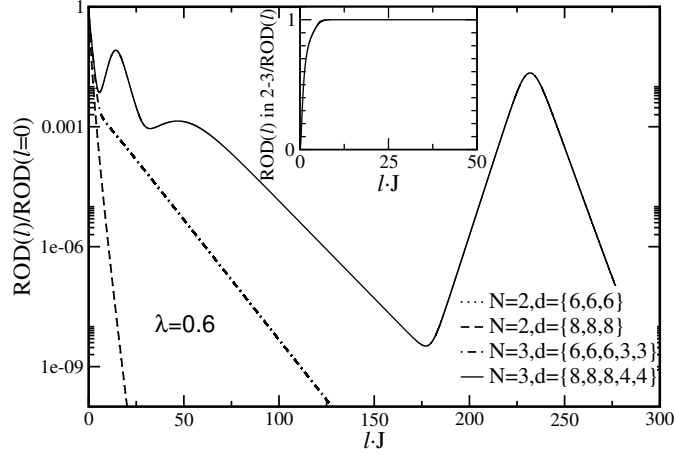


Fig. 4.20: The ROD relative to its initial value $\text{ROD}(l=0)$ for $\lambda = 0.6$. The RODs for the two calculations with $N = 2$ are on top of each other. The inset shows the contribution of coefficients of the $\{2,3\}$ -block for the $N = 3, d = \{8, 8, 8, 4, 4\}$ truncation.

does not change anymore for these values of the flow parameter. The dispersion is not influenced by the convergence problems in the $\{2,3\}$ -block. It remains the same if the flow is stopped at values of the flow parameter around the minimum in the ROD at $lJ \approx 175$ or if it is stopped at larger values.

The convergence problems will become more severe if λ is increased further. At $\lambda = 1.0$ the conditions are most challenging. The exact dispersion is gapless. All multi-particle continua overlap. Although we do not expect the self-similar CUT to work without problems in this situation it is now tried to determine the dispersion at $\lambda = 1.0$. The flow equations of the truncation schemes $N = 2, d = \{6, 6, 6\}$ and $N = 2, d = \{8, 8, 8\}$ diverge. The truncations $N = 3, d = \{6, 6, 6, 3, 3\}$ and $N = 3, d = \{8, 8, 8, 4, 4\}$ display a pronounced minimum before the ROD increases again. The ROD is shown in Fig. 4.21. The figure includes the diverging ROD of the $N = 2, d = \{8, 8, 8\}$ truncation as dotted curve. The contribution of the $\{2,3\}$ -block in the ROD of the $N = 3$ calculations is shown in the inset. This is the dominant contribution to the ROD already for small values of the flow parameter l . Therefore, the dispersion is determined already for small values of l and not influenced by the later occurring convergence problems.

The dispersion for the truncations $N = 3, d = \{6, 6, 6, 3, 3\}$ and $N = 3, d = \{8, 8, 8, 4, 4\}$ is found by stopping the flow at $lJ = 100$ where $\text{ROD}/\text{ROD}(l=0) = 7 \cdot 10^{-5}$ and at $lJ = 60$ where $\text{ROD}/\text{ROD}(l=0) = 2 \cdot 10^{-4}$, respectively. They are shown in Fig. 4.22 as thick dotted and dashed line. The quality of the result can be judged more easily by looking at the difference to the exact result $\omega(k) = J \frac{\pi}{2} \sin(k)$. This difference is shown in the upper graph. The deviations are of the order of $0.05J$. For k -values around $k = 0.5\pi$ the agreement is quite good. The differences increase towards the values $k = 0$ and $k = \pi$. At these k -points the exact dispersion is zero. The slope of the dispersion is linear. The self-similar CUT scheme encodes the one-

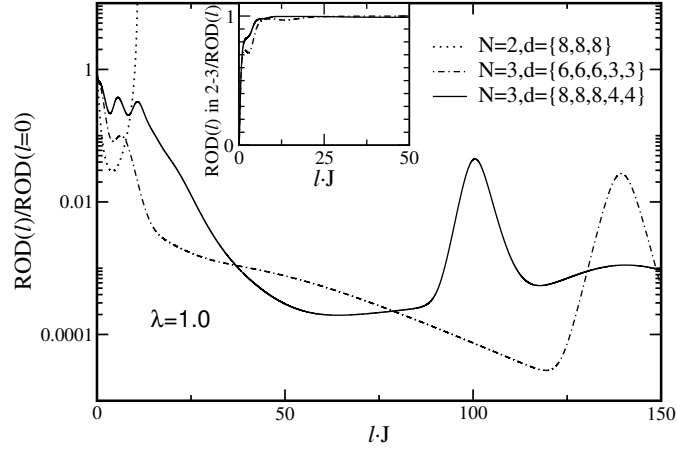


Fig. 4.21: ROD for $\lambda = 1.0$. The inset shows the relative contribution of the $\{2,3\}$ -block to the total ROD for the calculations with $N = 3$.

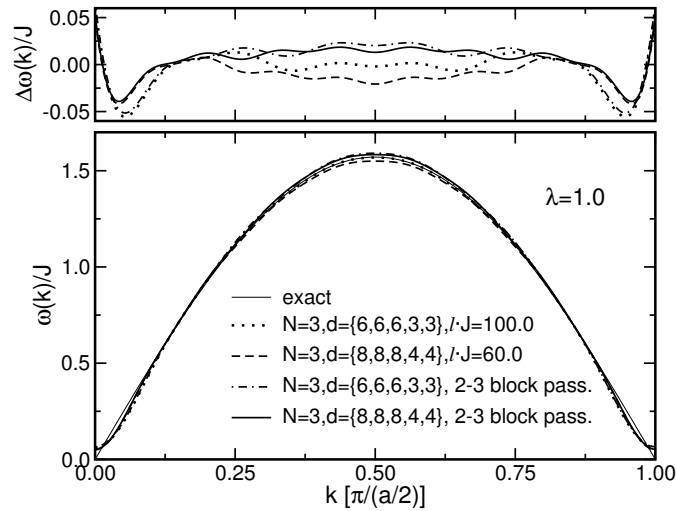


Fig. 4.22: The dispersion for $\lambda = 1.0$. The thin solid line shows the exact result. The results from the self-similar CUT are shown as thick lines. The inset shows the deviations from the exact result.

particle properties in the hopping amplitudes in the $\{1,1\}$ -block. In momentum space they represent prefactors of $\cos(nk)$. The linear behavior at $k = 0$ and $k = \pi$ can only be reproduced if one includes infinitely many of these cosine contributions to the dispersion. This is clearly not possible within our local approach to self-similar CUTs. Therefore, the deviations are largest at $k = 0$ and $k = \pi$. Nevertheless the results even for $\lambda = 1.0$ agree surprisingly well with the exact result. However, we assume that the determination of two- and more particle properties would be plagued by the convergence problems in the $\{2,3\}$ -block.

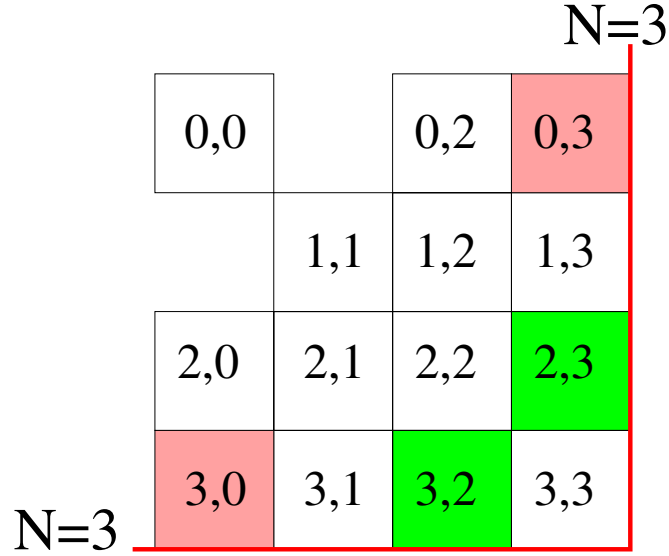


Fig. 4.23: A sketch to illustrate the passive transformation of the $\{2, 3\}$ -block. The contribution of operators in the $\{2, 3\}$ - and $\{3, 2\}$ -block to the generator are turned off by hand. This generates operators belonging to the $\{0, 3\}$ - and $\{3, 0\}$ -block because the MKU property is lost.

Passive transformation

The behavior of the ROD in Fig. 4.21 shows that especially the terms in the $\{2, 3\}$ - and $\{3, 2\}$ -block hinder a successful transformation. The energetic situation is such that the MKU scheme has to rearrange the energies of the states of different quasiparticle number according to their quasiparticle number. In this process the ROD rises again because the three-triplon sector overlaps with the two-triplon sector. Now, we present one way to circumvent this problem. The idea is to delay the transformation of the problematic $\{2, 3\}$ -block to a later stage. In a first step we perform a MKU transformation of all blocks *except* the $\{2, 3\}$ -block. To this end a generator of MKU type is used. However, all contributions from operators in the $\{2, 3\}$ -block to the generator are set to zero by hand. Therefore, these coefficients will not be transformed to zero but will be present also at the end of the flow.

As the generator is modified it loses the MKU property. Commutation with the generator will not only produce terms that change the quasiparticle number by at most two. There will be also terms that change the quasiparticle number by more than two. This is illustrated in Fig. 4.23. The $\{2, 3\}$ -block which does not contribute to the generator is shaded. In addition, the newly produced $\{0, 3\}$ - and $\{3, 0\}$ -blocks are highlighted. In a truncation scheme with block matrix size $N = 3$ these are the only newly generated blocks.

After the transformation the effective Hamiltonian is block-diagonal apart from the terms in the $\{2, 3\}$ -block. They have been kept because their diagonalization within a MKU scheme is problematic. Nevertheless it is advantageous to have a block-diagonal effective Hamiltonian.

Block diagonality is very convenient for the calculation of spectral weights. Otherwise the notion of weight in a certain channel defined by a quasiparticle number is meaningless since the Hamiltonian can transfer weight through terms that are not diagonal in the quasiparticle number.

The $\{2, 3\}$ -block will be eliminated using the Wegner generator. From the results of Sec. 4.1.2.2 we know that the transformation using Wegner's generator is converging slowly but robustly. This combined transformation technique, using a modified MKU generator and in a second step Wegner's generator, and its results will be labeled '*passive*' in the following. Note that the $\{2, 3\}$ -block is not neglected. The terms and their coefficients are kept in the Hamiltonian. Only their contribution to the MKU generator is set to zero. They appear in the flow equation and are renormalized from contributions of other blocks. Hence the naming 'passive' transformation is appropriate. Compared to the plain MKU transformation the passive approach takes a different direction towards block diagonality. First, all blocks except the critical $\{2, 3\}$ -block are eliminated. Second, the Wegner generator is used to eliminate the couplings in this block.

A passive transformation has been carried out for the truncation schemes $N = 3, d = \{6, 6, 6, 3, 3\}$ and $N = 3, d = \{8, 8, 8, 4, 4\}$. In the two steps of the MKU and Wegner transformation the same truncation scheme is used. All calculations converge. The passive treatment of the $\{2, 3\}$ -block circumvents the convergence problems observed for the plain MKU transformation. The results for the passive calculations for the dispersion at $\lambda = 1.0$ are contained in Fig. 4.22. The result for the $N = 3, d = \{6, 6, 6, 3, 3\}$ truncation using the passive scheme is shown as dot-dashed line, the one for the $N = 3, d = \{8, 8, 8, 4, 4\}$ truncation as solid line. The difference to the exact result is again shown in the top graph. The passive calculations give results that are slightly superior to the plain MKU results for momenta around $k \approx 0.5\pi$. They are less accurate at the points $k = 0$ and $k = \pi$ for the same reasons as the MKU calculations. The passive transformation is significantly more robust in the convergence. But, the quantitative results are not decisively better.

4.2.3. Spectral weight

The passive transformation scheme allows a block-diagonalization of the Hamiltonian. Therefore the weight of the observable introduced in Sec. 4.2.1.2 can now be analyzed also for larger values of λ . For a plain MKU calculation this would have been possible only up to intermediate values of λ .

The observable S_z has been defined in terms of triplet operators in Sec. 4.2.1.2. It is transformed with the same generator as the Hamiltonian. Within the passive scheme this means that we have to subject the observable in the first step to the modified MKU transformation and in the second step to the Wegner transformation. The second step eliminates the $\{2, 3\}$ -block in the Hamiltonian.

After the transformation the observable is not block-diagonal but creates and annihilates triplons. The ground state is the triplon vacuum. In this case only the $\{0, n\}$ -blocks of the observable are relevant. The weight contained in the n -quasiparticle channel is fixed by the

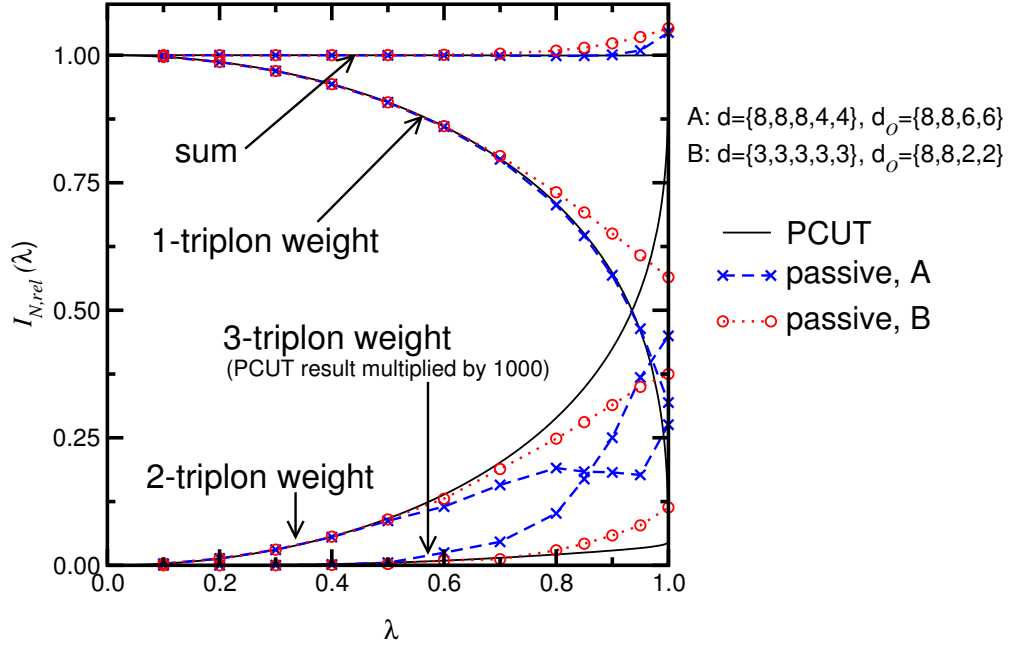


Fig. 4.24: Relative spectral weight $I_{n,\text{rel}}$ in the n -triplon channel. The figure depicts the spectral weights in the one-, two- and three-triplon channel and the sum of the $I_{n,\text{rel}}$. The curves of the various channels are marked with arrows. The PCUT calculation is shown as solid curve. The Hamiltonian and observable extensions of calculations A and B are given above the legend. Calculation A is shown by blue crosses, calculation B by red circles. Note that the PCUT result for $I_{3,\text{rel}}$ has been multiplied by a factor of 1000 for better visibility.

coefficients of the $\{0, n\}$ -block. It is calculated by summing the squares of the coefficients of all terms in the respective block. The total weight is a conserved quantity.

The results for the relative n -triplon spectral weight $I_{n,\text{rel}}$ are shown in Fig. 4.24. The sum of the relative weights should be equal to 1. A deviation from the exact value indicates an inaccuracy in the relative weights due to truncation. Figure 4.24 shows the results of the passive self-similar CUT together with results from the PCUT. The first calculation (in the following calculation A) uses the truncation $N = 3, d = \{8, 8, 8, 4, 4\}$ for the Hamiltonian and the observable truncation $N_{\mathcal{O}} = 2, d_{\mathcal{O}} = \{8, 8, 6, 6\}$. The results are shown with blue crosses. The truncation scheme $N = 3, d = \{3, 3, 3, 3, 3\}$ for the Hamiltonian and the observable truncation $N_{\mathcal{O}} = 2, d_{\mathcal{O}} = \{8, 8, 2, 2\}$ is shown with red circles (in the following calculation B).

The one-triplon spectral weight exhausts the full spectral weight for $\lambda = 0$. It decreases for increasing λ . The PCUT calculation yields a one-triplon spectral weight that vanishes at $\lambda = 1.0$. The two-triplon spectral weight increases with increasing λ . The surprising result is that it takes over almost the full weight at $\lambda = 1.0$. The three-triplon weight is very small. Note that the three-triplon weight is multiplied by a factor 1000 in Fig. 4.24. The sum rule is fulfilled

with good accuracy for all λ .

The one-triplon weight $I_{1,\text{rel}}$ for calculation A follows the results of the PCUT calculation for a wide range of the parameter λ . Even for $\lambda = 0.95$ there is good agreement. There is a sizeable difference for $\lambda = 1.0$. This finding agrees with the good results for the dispersion found in the preceding section. The situation is different for higher triplon channels. The two-triplon weight $I_{2,\text{rel}}$ is close to the PCUT result for $\lambda \leq 0.5$. For larger λ there are sizeable deviations. At the same time we find a comparably large weight in the three-triplon channel. The PCUT calculation finds only very little weight in $I_{3,\text{rel}}$.

The plain MKU transformation $N = 3, d = \{8, 8, 8, 4, 4\}$ exhibits convergence problems for $\lambda = 0.6$, see Fig. 4.20. The passive scheme does not have the convergence problems. The critical $\{2, 3\}$ -block is not diagonalized within the MKU scheme, but only later using Wegner's generator. The uprise in the ROD can be assigned to a reorganization of energy levels according to the quasiparticle number. If we circumvent this problem using a passive transformation it is found that the distribution of weight differs from the one found by the PCUT.

At even larger values of $\lambda \approx 0.8$, non-monotonic behavior of the weights is found. This points towards a loss of accuracy in the transformation. The sum of the relative weights is less affected by increasing λ . It stays close to the correct sum rule up to $\lambda \approx 0.9$.

In Sec. 4.1 it has been shown that smaller truncation schemes are less affected by convergence problems. Therefore, the triplon weights are shown also for truncation B that truncates the operators already at maximal extension 3. The results do not show the discontinuities of the calculation B. They are smooth up to $\lambda = 1.0$. However, the result for $I_{1,\text{rel}}$ deviates from the PCUT results for smaller λ . The results of $I_{2,\text{rel}}$ and $I_{3,\text{rel}}$ are not discontinuous and closer to the PCUT results.

The results shown in Fig. 4.24 have to be interpreted with care. The one-triplon spectral weight is an experimentally observable quantity if the one-particle energies are separated from the multi-particle energies. The weight $I_{1,\text{rel}}$ is found as the weight in a δ -peak at the position of the one-particle energy. The one-particle weight $I_{1,\text{rel}}$ of calculation A (blue crosses) closely follows the PCUT result for $\lambda \leq 0.9$. It is closer to the PCUT result than the more restrictive truncation of calculation B. This improvement of the result for $I_{1,\text{rel}}$ is systematic because there are more terms in calculation A than are in calculation B. The situation is different for the many-particle weights $I_{n,\text{rel}}$ where $n \geq 2$. For these weights calculation B lies closer to the PCUT results. However, the weights $I_{n,\text{rel}}$ where $n \geq 2$ are not physically observable if the energies of the corresponding continua overlap. In this case, n -particle states are allowed to decay into m -particle states. These lifetime effects shift the weight between channels of different quasiparticle number. The analysis of the spectral weight shows that these decay processes are possible for larger λ .

The final distribution of the weight in the two- and three-particle channel is established in the second step of the transformation using the Wegner generator. The lifetime effects are only present for overlapping continua at finite λ . These effects are not captured within the extrapolations of the PCUT approach. Thus, the PCUT produces more continuous results.

But, it neglects the lifetime effects that are present at large values of λ .

In summary, we state that the transformation of observables can be successfully carried out within the self-similar CUT scheme. The distribution of weight can be analyzed to judge the quality of the applied quasiparticle picture. In the case of the spin chain we have seen that there are problems in the transformation for $\lambda \gtrsim 0.6$. Nevertheless the sum rule is fulfilled by the weights $I_{n,\text{rel}}$ with $n \leq 3$ also for large λ . The channels with low triplon number carry the most important contribution to the spectral weight.

4.3. Summary and outlook

In this chapter the self-similar CUT method was applied to one-dimensional spin systems. The starting point both for the spin ladder and the spin chain was the dimerized system. In this limit the spectrum is equidistant. In particular, there is a finite gap that separates the vacuum from the one-particle excitations. The transformation can be applied without problems for large dimerization. Increasing the coupling between the dimers we have observed convergence problems in the spin ladder and the spin chain. For the spin ladder the problematic processes are contained in operators from the $\{2, 4\}$ -block, for the spin chain they are situated in the $\{2, 3\}$ -block.

For the spin ladder we have calculated the one- and two-triplon energies for $x = 0.5$ and 1.0 . In the two-triplon sector the energies of bound states of total spin $S = 0$ and $S = 1$ have been calculated. From a methodical point of view, we have not only derived the effective model but also solved it in the one- and two-quasiparticle sector. The results compare well with the results found by other methods.

The two- and four-triplon continua of the spin ladder show considerable overlap for $x = 1.0$. This induces convergence problems in the transformation. It is an important result of the present chapter that not only a finite one-particle gap is necessary for the self-similar CUT to work. A substantial overlap of multi-particle continua will make it difficult as well to carry out a MKU CUT safely. The MKU transformation sorts the eigenenergies according to the quasiparticle number. A strong overlap of continua makes the re-ordering impossible. If the flow equation is truncated, this process will lead to a loss of accuracy of the effective Hamiltonian. Since truncation is necessary in any real calculation this is an important issue in the context of self-similar CUTs. In Sec. 4.1.5 we have given some suggestions how to handle this problem. One can stop the flow at a minimum of the ROD and treat the remaining elements with another method, e. g. perturbation theory or a numerical technique like Lanczos diagonalization. Another possibility is to circumvent the convergence problems by modifying the course of the unitary transformation. This has been done for the spin chain using a passive transformation.

For the chain system we have calculated the dispersion up to the value $\lambda = 1.0$ which corresponds to the homogeneous spin chain. The transformation is straightforward for small values of λ . For larger values convergence problems show up. To circumvent these problems we take up a strategy proposed in Sec. 4.1.5. In a passive transformation the block that hinders the con-

vergence is excluded from the generator. It is only taken into account within the Hamiltonian. In a subsequent step, this block is transformed using a Wegner generator. The passive transformation converges. However, the passive scheme does not give better results for the dispersion at $\lambda = 1.0$ than the plain MKU scheme that is stopped at a minimum of the ROD. Note that the second step could be replaced also by some other means to deal with the effective Hamiltonian given by the transformation in the first step.

The dispersion of the spin chain is quantitatively determined for values up to $\lambda = 0.6$. For the isotropic case, there are sizeable deviations from the exactly known result. The spectral weights for the observable S_z are calculated using the passive transformation scheme. They coincide with the ones from PCUT up to $\lambda \approx 0.5$. For larger values the passive transformation yields less weight in the two-triplon channel.

For large values of λ there is a considerable overlap of continua of different quasiparticle number. The analysis of the spectral weight for different self-similar transformations shows that this overlap leads to lifetime effects. Multi-triplon states with different quasiparticle number are allowed to decay into each other. This leads to a redistribution of spectral weight between channels of different quasiparticle number.

The transformation of the observable has already been described in the method chapter Chap. 2. For the spin chain it is carried out for the first time within the framework of the self-similar CUT in real space. The transformation of observables is an important ingredient to describe the outcome of experiments. A measured quantity always relates to a certain observable. The following chapter will further pursue this path and compare the results for spectral weights for the bosonic Hubbard model directly to an experimental result.

5. Bosonic atoms in an optical lattice

In the last years, ultracold atoms trapped in optical lattices allowed to perform a new kind of experiments in many-body systems. As the lattice in which the atoms are located is established through adjustable laser beams the system parameters can be tuned [16, 17, 145–148]. In this way it is possible to change the tunneling and the interaction parameter. Recent Bragg spectroscopy experiments [16, 17, 146] found evidence for the transition to a Mott insulating state which is one of the most prominent phenomena in the field of correlated many-body physics. While the interpretation of the experiments as a transition to the Mott state is clear, the distribution of spectral weight on the Hubbard peaks still lacks an explanation.

The aim of this chapter is to explain the distribution of spectral weight on the first and second Hubbard peak in these experiments. To this end, it is necessary to clarify the significance of various excitation processes depending on the kinetic and the interaction energy and on the temperature. A self-similar CUT is used to map the bosonic Hubbard model onto an effective model conserving the number of elementary excitations. Some contributions that are not particle number conserving cannot be rotated away. These introduce small but finite life-time effects that will be neglected. The experimentally relevant observable is transformed. Therewith the spectral weights of the low-energy excitations are successfully calculated.

It will turn out that the results of the calculation have to be extended to finite temperature in order to explain the experiment. An approximate thermodynamics for hard-core bosons is therefore adapted to the present problem. The validity of the approximation is analyzed. Within this approximation evidence for a significant temperature of the order of the interaction parameter is found.

Further support for this finding comes from the analysis of the entropy of bosons confined in optical lattices. This analysis is extended to contain also the Tonks-Girardeau regime of the bosonic Hubbard model [149–152]. The Tonks-Girardeau regime can be treated by a mapping onto free fermions. On the other hand, in the CUT calculation the effect of non-commensurate fillings can be included using the approximate thermodynamics. The temperatures found in this case are of the order of the hopping amplitude. This gives an explanation of the temperatures determined by experiments for the Tonks-Girardeau regime [146]. The results of the two approaches are compared favorably. The obtained results give a consistent picture of the role of temperature in one-dimensional optical lattices in the Tonks-Girardeau and the Mott-insulating regime.

5.1. Bosonic Hubbard model

Bosonic atoms in an optical lattice are described by the bosonic Hubbard model [145]. The Hamiltonian of this model reads

$$H = tH_t + UH_U + \mu H_\mu \quad (5.1.1)$$

$$= -t \sum_i (b_i^\dagger b_{i+1} + b_{i+1}^\dagger b_i) + \frac{U}{2} \sum_i \hat{n}_i(\hat{n}_i - 1) - \mu \sum_i \hat{n}_i. \quad (5.1.2)$$

We will only consider the one-dimensional case. The first term is the kinetic part tH_t and the second term the repulsive interaction UH_U with $U > 0$. The last term accounts for a chemical potential μ . The bosonic annihilation (creation) operators are denoted by b_i (b_i^\dagger), the number of bosons by $\hat{n}_i = b_i^\dagger b_i$. On the same site the bosons repel each other with interaction strength U . In the limit $t/U \rightarrow 0$ a site with n bosons contributes the energy $E(n) = (U/2)n(n-1)$. A deviation from uniform filling costs the energy $E(n+1) + E(n-1) - 2E(n) = U$. For large U and integer filling n it is energetically favorable to put just n bosons on each site. The system is in an insulating state with an energy gap of the order of U . This situation is quite similar to the case of the fermionic Hubbard model described in Chapter 3.

In the opposite limit where t/U is large Bose condensation occurs at low enough temperatures [153]. The condensed bosons are superfluid. The bosonic Hubbard model and its transition from a Mott insulator to a superfluid has been studied with various approaches. Among the extensive literature on the bosonic Hubbard model there are mean-field treatments, e. g. Refs. [145, 154–156], other analytical investigations, e. g. Refs. [153, 157–159], and numerical treatments, e. g. Refs. [160–163]. The phase diagram in the t - μ plane consists of a series of Mott insulating lobes, see Fig. 5.1. The Mott insulating phases correspond to an integer filling per site.

The present chapter is only concerned with the first lobe of the phase diagram where $n = 1$. To set up the self-similar CUT calculation the reference state has to be fixed. For $t/U \rightarrow 0$ and filling $n = 1$ the groundstate of Eq. (5.1.1) is the product state of precisely one boson per site

$$|\text{ref}\rangle = |1\rangle_1 \otimes |1\rangle_2 \dots \otimes |1\rangle_N, \quad (5.1.3)$$

where $|n\rangle_i$ denotes the local state at site i with n bosons. We take $|\text{ref}\rangle$ as the reference state as described in Sec. 2.3.4. The reference state is sketched in Fig. 5.2. Deviations from $|\text{ref}\rangle$ are considered as elementary excitations. The reference state is an eigenstate of H_U . For finite t/U the kinetic part tH_t will cause fluctuations around the reference state.

In principle, each site can be occupied by an infinite number of bosons. The local Hilbert space is infinite dimensional. Consequently, there are also infinitely many linearly independent local operators on this space. The local Hilbert space has to be truncated to set up a real space CUT that uses the method as described in Chapter 2. In the calculations in this chapter the local bosonic Hilbert space is truncated to four local states. Numerical studies using the density-matrix renormalization group (DMRG) have shown that this does not change the relevant physics

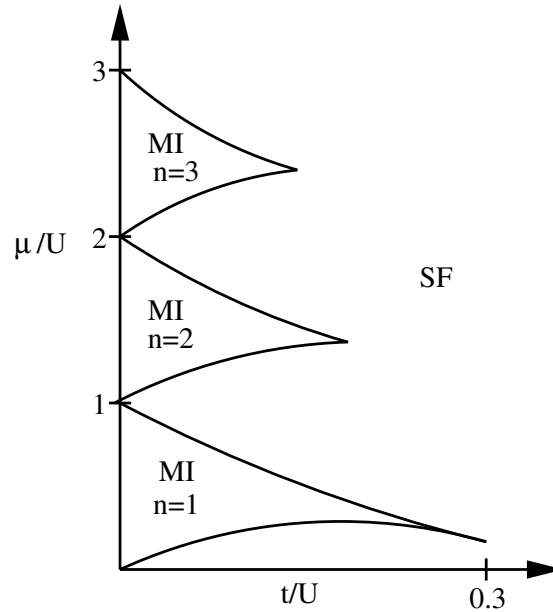


Fig. 5.1: Sketch of the phase diagram of the bosonic Hubbard model in the $(t/U, \mu/U)$ plane [153, 163]. Mott insulating (MI) lobes are surrounded by a superfluid (SF) phase. Inside each MI lobe the filling is fixed at an integer value. This chapter focuses on the MI lobe with filling $n = 1$.

[160–162]. As we are interested in the physical behavior in the first MI lobe where $n = 1$ we will keep the four local states with smallest boson number. These are the states $\{|0\rangle_i, |1\rangle_i, |2\rangle_i, |3\rangle_i\}$. Besides the local reference state $|\text{ref}\rangle_i = |1\rangle_i$, there are three more states and correspondingly three local creation operators. They create local excitations. A hole at site i is created by $h_i^\dagger|1\rangle_i = |0\rangle_i$, a particle by $p_i^\dagger|1\rangle_i = |2\rangle_i$, and $d_i^\dagger|1\rangle_i = |3\rangle_i$ induces another kind of particle at site i . The particle created by d_i^\dagger corresponds to a local occupation of a site by three bosons. This

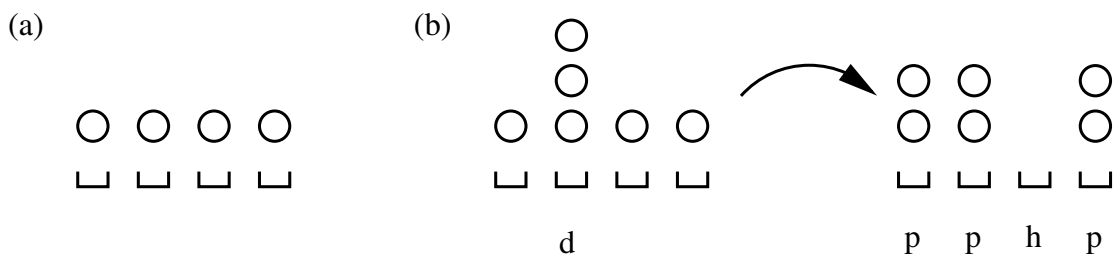


Fig. 5.2: (a) Sketch of the reference state with one atom per site, (b) a process commuting with H_U but not separately conserving the number of h, p and d particles. Starting from a d -excitation one gets to three p - and an h -excitation. The number of bosons is conserved and both states have the energy $3U$. The implications of such processes are further discussed in Sec. 5.1.2.1.

is treated as an independent quasiparticle.

The local bosonic operator b_i^\dagger is thus represented by a four by four matrix

$$b_i^\dagger = \begin{pmatrix} 0 & 0 & 0 & 0 \\ 1 & 0 & 0 & 0 \\ 0 & \sqrt{2} & 0 & 0 \\ 0 & 0 & \sqrt{3} & 0 \end{pmatrix}_i = h_i + \sqrt{2}p_i^\dagger + \sqrt{3}d_i^\dagger p_i. \quad (5.1.4)$$

Equation (5.1.4) implies the representation of the operator b_i as the hermitian conjugate of b_i^\dagger . Note, that this representation of b_i^\dagger and b_i is an approximation. At this point the infinite local Hilbert space is truncated to four states.

The explicit definitions of h_i^\dagger , p_i^\dagger and d_i^\dagger with local matrices are

$$h_i^\dagger = \begin{pmatrix} 0 & 1 & 0 & 0 \\ 0 & 0 & 0 & 0 \\ 0 & 0 & 0 & 0 \\ 0 & 0 & 0 & 0 \end{pmatrix}_i, \quad p_i^\dagger = \begin{pmatrix} 0 & 0 & 0 & 0 \\ 0 & 0 & 0 & 0 \\ 0 & 1 & 0 & 0 \\ 0 & 0 & 0 & 0 \end{pmatrix}_i, \quad d_i^\dagger = \begin{pmatrix} 0 & 0 & 0 & 0 \\ 0 & 0 & 0 & 0 \\ 0 & 0 & 0 & 0 \\ 0 & 1 & 0 & 0 \end{pmatrix}_i. \quad (5.1.5)$$

The operators h , p and d obey the general commutation relations for hard-core bosons, see Eq. (2.3.30) in Sec. 2.3.3. The commutation relations for hard-core bosons differ from those of non-interacting bosons. We give just one example in the language of the present chapter to illustrate this difference explicitly

$$[p_i, p_j^\dagger] = \delta_{i,j}(\mathbf{1} - h_i^\dagger h_i - 2p_i^\dagger p_i - d_i^\dagger d_i), \quad (5.1.6)$$

whereas non-interacting bosons obey $[b_i, b_j^\dagger] = \delta_{i,j}$.

The Hamiltonian is rewritten using Eq. (5.1.4) as

$$H = tH_t + UH_U + \mu H_\mu \quad (5.1.7a)$$

$$H_t = -\sum_i \left(h_i^\dagger h_{i+1} + 2p_i^\dagger p_{i+1} + \sqrt{2}h_i p_{i+1} + \sqrt{2}h_{i+1}^\dagger p_i^\dagger + \sqrt{3}d_i^\dagger h_{i+1}^\dagger p_i + \sqrt{3}h_i^\dagger d_{i+1}^\dagger p_{i+1} + \sqrt{6}d_i^\dagger p_i p_{i+1} + \sqrt{6}d_{i+1}^\dagger p_i p_{i+1} + 3d_i^\dagger p_{i+1}^\dagger p_i d_{i+1} + h.c. \right) \quad (5.1.7b)$$

$$H_U = \sum_i \left(p_i^\dagger p_i + 3d_i^\dagger d_i \right) \quad (5.1.7c)$$

$$H_\mu = -L - \sum_i \left(-h_i^\dagger h_i + p_i^\dagger p_i + 2d_i^\dagger d_i \right) \quad (5.1.7d)$$

where L is the number of lattice sites. The hopping part H_t contains terms that are bilinear, cubic and quartic in the operators h , p and d . The bilinear terms contain hopping and Bogoliubov terms involving h - and p -quasiparticles. Bogoliubov terms are those where a h - and a p -quasiparticle are simultaneously created or annihilated. The cubic and quartic terms always

involve d -quasiparticles. The interaction part H_U takes the form of a bilinear operator in the representation in Eq. (5.1.7). From this representation of the Hamiltonian the self-similar CUT is implemented as described in Chap. 2.

In comparison to the CUTs in previous chapters we find common properties as well as differences. A local representation of operators is used for the bosonic Hubbard model as well as for the fermionic Hubbard model and the spin models. This leads in all cases to operators that fulfill modified local commutation relations. Operators on different sites commute if they are bosonic or anti-commute if they are fermionic. For the spin model and the present bosonic Hubbard model there are only bosonic operators. Thus, the commutation relations are those of hard-core bosons. In the case of the spin models and the fermionic Hubbard model the local Hilbert space has only four states. There is no need to truncate the local Hilbert space. In the present case of an infinite dimensional local Hilbert space we have to truncate the basis to a finite dimension. Concerning the reference state, the situation here is simpler as the one for the Hubbard model. There, the reference *ensemble* is constructed from two local states. For the spin systems in Chap. 4 the CUT is based also on one reference state, the product of local singlets. The local excitation however has been the local triplet with three flavors. For the case of the bosonic Hubbard model the local excitations h^\dagger , p^\dagger and d^\dagger are not related by symmetry.

The full CUT calculation is presented in Sec. 5.1.2. Before, an approximate solution of the problem is given in the next section.

5.1.1. Non-interacting approximation

Inspection of the Hamiltonian (5.1.7) shows that it is bilinear in the p - and h -operators. Cubic and quartic terms always involve d -operators. In a first approximation all terms containing d -operators are neglected. The Hamiltonian then reads

$$\begin{aligned} H = & -t \sum_i \left(h_i^\dagger h_{i+1} + 2p_i^\dagger p_{i+1} + \sqrt{2}h_i p_{i+1} + \sqrt{2}h_{i+1}^\dagger p_i + h.c. \right) \\ & + \sum_i \left(\mu h_i^\dagger h_i + (U - \mu) p_i^\dagger p_i \right) - \mu L \end{aligned} \quad (5.1.8)$$

and after Fourier transformation

$$H = -\mu L + \sum_k \left(a_k h_{-k}^\dagger h_{-k} + b_k p_k^\dagger p_k + c_k p_k^\dagger h_{-k}^\dagger + c_k p_k h_{-k} \right) \quad (5.1.9)$$

with the definitions

$$a_k = \mu - 2t \cos(k) \quad (5.1.10a)$$

$$b_k = U - \mu - 4t \cos(k) \quad (5.1.10b)$$

$$c_k = -2\sqrt{2}t \cos(k). \quad (5.1.10c)$$

Although this Hamiltonian is bilinear it is not easily solvable because the operators involved obey hard-core commutation relations. However, as a second approximation we will replace the

hard-core commutation relations by the commutation relations of non-interacting bosons. The hard-core property of the operators is neglected. Then, a Bogoliubov transformation can be employed to diagonalize the Hamiltonian. To this end the operators p and h are rewritten in terms of new operators \tilde{p} and \tilde{h} as follows

$$p_k^\dagger = \cosh(\alpha_k)\tilde{p}_k^\dagger + \sinh(\alpha_k)\tilde{h}_{-k} \quad (5.1.11a)$$

$$p_k = \cosh(\alpha_k)\tilde{p}_k + \sinh(\alpha_k)\tilde{h}_{-k}^\dagger \quad (5.1.11b)$$

$$h_{-k}^\dagger = \cosh(\alpha_k)\tilde{h}_{-k}^\dagger + \sinh(\alpha_k)\tilde{p}_k \quad (5.1.11c)$$

$$h_{-k} = \cosh(\alpha_k)\tilde{h}_{-k} + \sinh(\alpha_k)\tilde{p}_k^\dagger. \quad (5.1.11d)$$

Here, the angle α_k is a real parameter depending on the momentum k . With the definitions in Eq. (5.1.11) the new operators \tilde{p} and \tilde{h} retain the non-interacting commutation relation. For operators fulfilling hard-core commutation relations it is not possible to set up a Bogoliubov transformation. That is the reason why the hard-core properties of the original operators have been neglected in the present approximation.

The Hamiltonian is rewritten using the definitions in Eq. (5.1.11). The Bogoliubov transformation is realised by demanding that the anomalous terms $p_k^\dagger h_{-k}^\dagger$ and $p_k h_{-k}$ vanish. This is achieved if the condition

$$\tanh(2\alpha_k) = -\frac{2c_k}{a_k + b_k} \quad (5.1.12)$$

is satisfied. For each k this defines the angle α_k . The transformed Hamiltonian has no anomalous terms $p_k^\dagger h_{-k}^\dagger$. It reads

$$\begin{aligned} H = & \sum_k \left(\epsilon_{\text{NI}}^{\text{h}}(k)\tilde{h}_{-k}^\dagger\tilde{h}_{-k} + \epsilon_{\text{NI}}^{\text{p}}(k)\tilde{p}_k^\dagger\tilde{p}_k \right) \\ & + \sum_k \left(-\frac{a_k + b_k}{2} + \frac{1}{2}\sqrt{(a_k + b_k)^2 - 4c_k^2} \right) - L\mu. \end{aligned} \quad (5.1.13)$$

where the dispersion of hole-like quasiparticles $\epsilon_{\text{NI}}^{\text{h}}(k)$ and particle-like quasiparticles $\epsilon_{\text{NI}}^{\text{p}}(k)$ are

$$\epsilon_{\text{NI}}^{\text{h}}(k) = \frac{a_k - b_k}{2} + \frac{1}{2}\sqrt{(a_k + b_k)^2 - 4c_k^2} \quad (5.1.14a)$$

$$\epsilon_{\text{NI}}^{\text{p}}(k) = -\frac{a_k - b_k}{2} + \frac{1}{2}\sqrt{(a_k + b_k)^2 - 4c_k^2}. \quad (5.1.14b)$$

The subscript "NI" indicates that these are the dispersions for the non-interacting approximation.

From the dispersion one can infer the phase diagram. As soon as it costs no energy to reduce or enhance the number of bosons the filling is no longer fixed at the value $n = 1$. The transition from the Mott insulating phase to the superfluid phase takes place. The upper boundary of the MI phase is given by the following condition for the critical chemical potential μ_c

$$\min_k \epsilon^{\text{p}}(k) = 0 \quad \longrightarrow \quad \mu_c^{\text{p}} = \Delta_{\text{NI}}^{\text{p}} \quad (5.1.15)$$

and correspondingly the lower boundary is given by

$$\min_k \epsilon^h(k) = 0 \quad \longrightarrow \quad \mu_c^h = -\Delta_{\text{NI}}^h. \quad (5.1.16)$$

Here we have defined the one-particle gap $\Delta_{\text{NI}}^{\text{p/h}}$ which is the minimum of the dispersion with $\mu = 0$

$$\Delta_{\text{NI}}^{\text{p/h}} := \min_k \{ \epsilon_{\text{NI}}^{\text{p/h}}(k) | \mu = 0 \}. \quad (5.1.17)$$

The difference in sign in Eqs. (5.1.15) and (5.1.16) stems from the fact that a positive chemical potential reduces the energy of a particle while it enhances the energy of a hole. Using the dispersion (5.1.14) one finds

$$\frac{\mu_c^{\text{p/h}}}{U} = \frac{1 - 2\frac{t}{U}}{2} \pm \frac{1}{2} \sqrt{1 - 12\frac{t}{U} + 4\left(\frac{t}{U}\right)^2}. \quad (5.1.18)$$

The Mott insulating region exists only up to a finite value of t_c . If the critical chemical potentials for particles and holes are equal the Mott insulating phase reduces to a single point. The condition for t_c is that $\mu^{\text{p}} = \mu^{\text{h}}$ and we find

$$t_c^{\text{NI}} = \left(\frac{3}{2} - \sqrt{2} \right) U \approx 0.086U. \quad (5.1.19)$$

It is surprising that one finds a critical t_c for the Mott phase and one therefore can describe the phase diagram qualitatively. We postpone further discussion of the results to the next chapter. There, also a comparison to CUT results will be made. The results for the critical chemical potential Eq. (5.1.18) are also found using mean-field theory [154–156, 159]. The mean-field theory in the cited references is based on a decoupling of the hopping part of the Hamiltonian. It introduces a superfluid order parameter. The transition to the Mott phase is defined as the point where the superfluid order parameter vanishes. It is not obvious why our non-interacting approximation and the mean-field treatment give the same results. In both approaches the Hamiltonian is reduced to a bilinear form. This might be the cause for the coinciding results. Now, we turn to the solution of the full problem using a real space CUT.

5.1.2. CUT treatment

The CUT calculation is based on the Hamiltonian (5.1.7). The only approximation made to arrive at this Hamiltonian is the restriction of the local Hilbert space to four states. The hard-core commutation relations are taken into account exactly. The Hamiltonian Eq. (5.1.7) conserves the number of bosons. But it does not conserve the number of the newly introduced h -, p - and d -quasiparticles. For example, the application of H_t to the reference state generates particle-hole pairs. To get rid of the terms that change the number of the h , p and d quasiparticles a MKU generator is chosen as

$$\eta_{i,j}(l) = \text{sgn}(q_i - q_j) H_{i,j}(l) \quad (5.1.20)$$

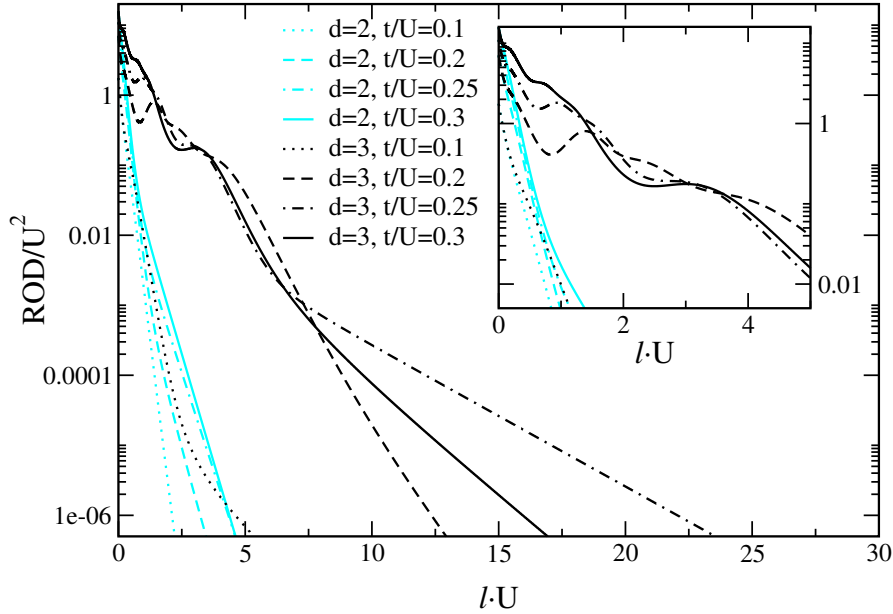


Fig. 5.3: Residual off-diagonality for truncations $d \in 2, 3$ and $t/U \in 0.1, 0.2, 0.25, 0.3$. Note that the vertical axis has logarithmic scale. The inset shows a magnification for small values of the flow parameter l .

in an eigenbasis of H_U ; q_i is the corresponding eigenvalue of H_U [12, 13]. The choice of this generator leads to an effective Hamiltonian commuting with H_U . The transformation eliminates most terms that change the number of quasiparticles. However, there are terms that do not conserve the number of all types of quasiparticles separately, but commute with H_U . They are still present at the end of the flow. These terms are rather complicated and involve at least five local operators. Their structure will be discussed in Sec. 5.1.2.1.

From Eq. (5.1.20) the flow equations are computed. They do not close and therefore one has to truncate the proliferating number of terms. A local truncation scheme is used to truncate the flow equations. The general truncation procedure is described in Sec. 2.3. The maximal distance between two operators in a term in the Hamiltonian is defined to be its *extension*. For the bosonic Hubbard model only the extension is used as a truncation criterion. Terms with an extension larger than a fixed limit value are discarded. No additional constraint for different blocks of the Hamiltonian is imposed as it has been done for the spin systems in Chapter 4. The residual off-diagonality (ROD) is calculated as the sum of the moduli squared of the terms that change the number of quasiparticles. Figure 5.3 shows the ROD for maximal extension $d = 2$ and $d = 3$. For maximal extension $d = 2$ the ROD is a monotonically decaying function for all values of t/U . The Hamiltonian can thus be diagonalized by the CUT. In the ROD for maximal extension $d = 3$ a different behavior is seen. For values $t/U \geq 0.12$ the ROD shows a minimum at l_{\min} . This signals that the intended transformation cannot be performed completely due to

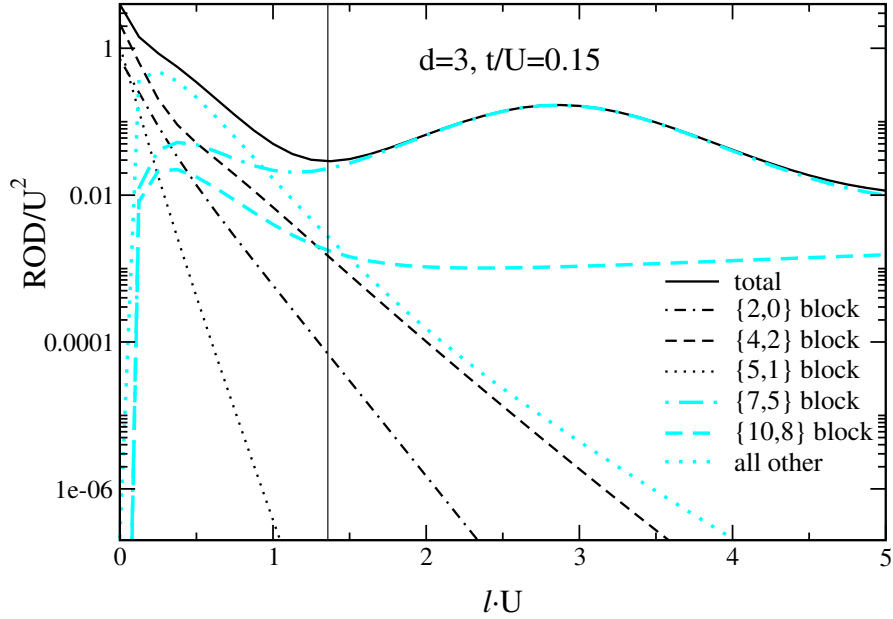


Fig. 5.4: ROD for $d = 3$ and $t/U = 0.15$ separated according to off-diagonal blocks in the Hamiltonian. The scale of the vertical axis is logarithmic. At the minimum of the ROD at $l_{\min} = 1.358$ (indicated by a thin vertical line) practically the whole ROD resides in the $\{7, 5\}$ -block. The ROD in blocks with lower quasiparticle number is much lower.

overlapping higher continua. Overlapping continua introduce finite life-time effects that hinder a unitary mapping onto an effective Hamiltonian that conserves the number of quasiparticles. This effect is also present in the case of the fermionic Hubbard model and in the spin systems, see also the discussion in Sec. 4.1.4.

Fortunately, reliable and quantitative results can be achieved by stopping the flow in the first minimum l_{\min} of the ROD. Even for a value as large as $t/U = 0.2$ the ROD decreases to a value as low as 0.06 times the initial value at l_{\min} . Each individual coefficient is much smaller. In addition, by far the largest contribution to the ROD originates from operators which embody transitions between sectors with high numbers of quasiparticles.

This is clearly seen when the total ROD is classified according to the number of quasiparticles involved in each process. An off-diagonal operator that creates i quanta and annihilates j quanta contributes to the ROD of the $\{i, j\}$ -block. The number of created and annihilated quanta are counted using H_U . Thus, a p^\dagger operator creates one H_U quantum while a d^\dagger operator creates three H_U quanta. The distribution of the ROD over the various blocks is shown in Fig. 5.4 for extension $d = 3$ and hopping parameter $t/U = 0.15$. At $l = 0$ only the blocks $\{2, 0\}$, $\{4, 2\}$ and $\{5, 1\}$ contribute. Their amplitudes decrease quickly and the contribution of other blocks increases. The minimum of the total ROD is at $l_{\min} = 1.358U$. This value is pointed out in Fig. 5.4 by a thin vertical line. At l_{\min} almost the complete ROD is found in the $\{7, 5\}$ -block.

Blocks with small numbers of excitations are reliably separated by the CUT from other blocks. Therefore it is sufficient for the purpose of the present study to stop the CUT at l_{\min} . Remaining off-diagonal operators could be treated in perturbation theory. But, they would only have very small effects because of the small size of the corresponding coefficients.

5.1.2.1. Block-diagonality in a situation with different types of quasiparticles

The MKU generator Eq.(5.1.20) rotates on an effective Hamiltonian that commutes with H_U . Terms in the effective Hamiltonian conserve the eigenvalue q of H_U . In a situation with only one type of quasiparticle, commutation with the corresponding counting operator ensures conservation of the quasiparticle number. This is the case for the fermionic Hubbard model that is studied in Chapter 3. In Chapter 4 the local excitations are the three flavors of a triplet excitation. The excitation of a triplet changes the eigenvalue of the corresponding counting operator by one. This does not depend on the triplet flavor. Therefore, in the case of the spin system only the total triplet number is conserved after the CUT.

In the present case, excitations of the different quasiparticles do not change the eigenvalue of H_U by the same value. Here, we want to investigate to what extent the number of the individual quasiparticles is conserved after the CUT. Let us consider an operator o with (n_h, n_p, n_d) creation operators of h -, p - and d -particles and (m_h, m_p, m_d) annihilation operators of h -, p - and d -particles. Such an operator changes the number of quasiparticles by $d_h = n_h - m_h$, $d_p = n_p - m_p$, $d_d = n_d - m_d$. It commutes with H_U if

$$[H_U, o] = d_p + 3d_d = 0. \quad (5.1.21)$$

An additional constraint on the structure of the operator is given by the conservation of the atom number. The atom number is conserved if

$$[H_\mu, o] = -d_h + d_p + 2d_d = 0. \quad (5.1.22)$$

Equations (5.1.21) and (5.1.22) are solved for given d_d by

$$d_p = -3d_d \quad (5.1.23a)$$

$$d_h = -d_d. \quad (5.1.23b)$$

The first nontrivial operator is found for $d_d = 1$, $d_p = -3$ and $d_h = -1$. The corresponding operator is schematically

$$p_i^\dagger p_j^\dagger p_k^\dagger h_l^\dagger d_m \quad (5.1.24)$$

where i, j, k, l, m are position indices. A sketch of this type of process is shown in Fig. 5.2b on page 121. The only terms which do commute with H_U but do not conserve the quasiparticle number are complicated terms of the type shown in Eq. (5.1.24) or even more complicated ones for $d_d > 1$. Of course, one also finds similar operators for $d_d < 0$. In the present case of different quasiparticles the CUT achieves nearly block-diagonality. Only very complicated

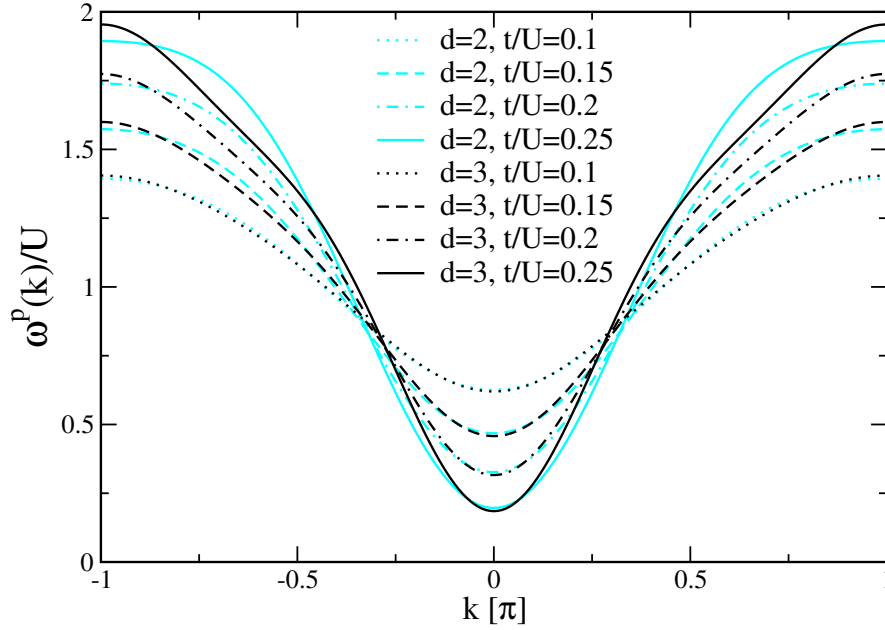


Fig. 5.5: The dispersion of particle-like p -excitations is shown for maximal extensions $d \in \{2, 3\}$ and various values of t/U .

processes changing the number of excitations survive. Most processes changing the number of quasiparticles are rotated away. All sectors with up to three particles of p or h type are separated from the rest of the Hilbert space. In particular, the one p or one h dispersion is perfectly separated. We note that the presence of a decay process of a d -excitation like in Eq. (5.1.24) does not influence the results that are presented in the following.

5.1.3. Dispersion and phase diagram

The dispersion is defined as the one-particle energy with the chemical potential μ set to zero. The dispersion is calculated for extensions $d \in \{2, 3\}$ and $t/U \in \{0.1, 0.15, 0.2, 0.25\}$. Figure 5.5 shows the dispersion of particle-like p -excitations $\omega^p(k)$ and Fig. 5.6 the dispersion of hole-like h -excitations $\omega^h(k)$. The bandwidth of p -particles is larger than the bandwidth of h -particles. This is already clear from the hopping matrix elements which are larger for transitions between states of higher boson occupation, see Eq. (5.1.4).

The results for the p dispersion $\omega^p(k)$ for $t/U = 0.1$ for values of the maximal extension $d = 2$ and $d = 3$ lie on top of each other. For $t/U = 0.15$ and 0.2 there are differences especially for $k \in [0.5\pi, 1.0\pi]$ where the energy of the particles is high. For $t/U = 0.25$ there are sizeable deviations also for smaller k values. At the minimum of the dispersion the agreement of the calculations with extension $d = 2$ and $d = 3$ is very good. The hole dispersion $\omega^h(k)$ for $t/U = 0.1$ coincides well for extensions $d = 2$ and $d = 3$. Again, the discrepancies of the various

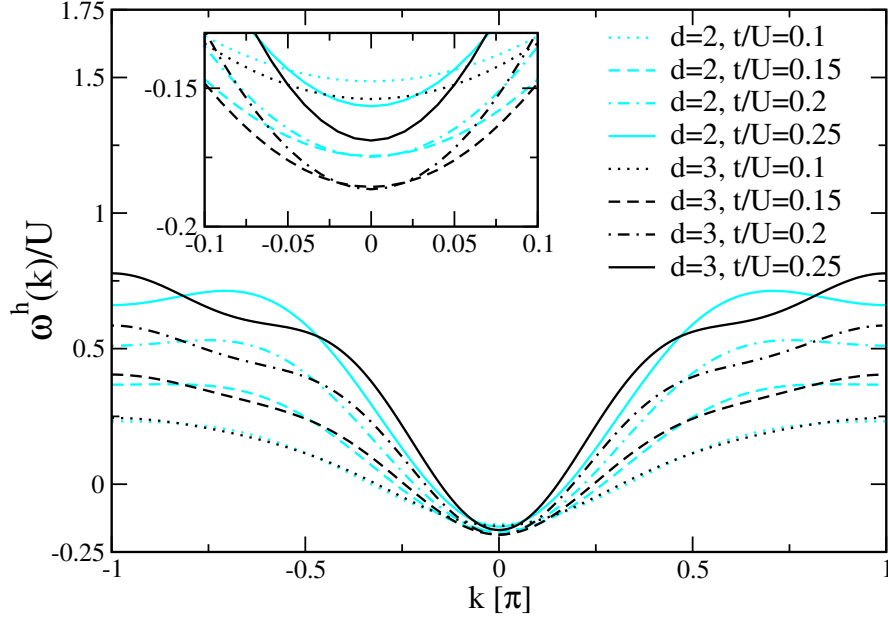


Fig. 5.6: The dispersion of hole-like h -excitations is shown for maximal extensions $d \in \{2, 3\}$ and various values of t/U . The inset shows a magnification of the minimum of the dispersion.

truncation schemes become larger for larger values of t/U , especially at higher energies. The gap value for particle and hole excitations depends only little on the truncation. This observation is exemplified by the two expressions for the dispersion for $t/U = 0.2$ for extension $d = 2$ and $d = 3$

$$d = 2 : \quad \omega^p(k) = (1.156 - 0.706 \cos(k\pi) - 0.123 \cos(2k\pi)) U \quad (5.1.25)$$

$$d = 3 : \quad \omega^p(k) = (1.153 - 0.680 \cos(k\pi) - 0.104 \cos(2k\pi) - 0.0536 \cos(3k\pi)) U \quad (5.1.26)$$

and their minimum values at $k = 0$:

$$d = 2 : \quad \omega^p(0) = 0.315U \quad (5.1.27)$$

$$d = 3 : \quad \omega^p(0) = 0.327U. \quad (5.1.28)$$

The dispersion for extension $d = 2$ has only two cosine terms. However, their prefactor is somewhat larger than in the $d = 3$ result such as to mimic the effect of the third cosine term in the $d = 3$ dispersion. Therefore, the agreement of the gap value for different truncations is much better than the agreement of the coefficients. The states with low energy are energetically far away from the continua. Their energy is very stable compared to the energy of higher lying states.

Also the non-interacting approximation presented in Sec. 5.1.1 yields a result for the dispersion. It is given as an explicit formula in Eq. (5.1.14). Figure 5.7 compares the result of the non-

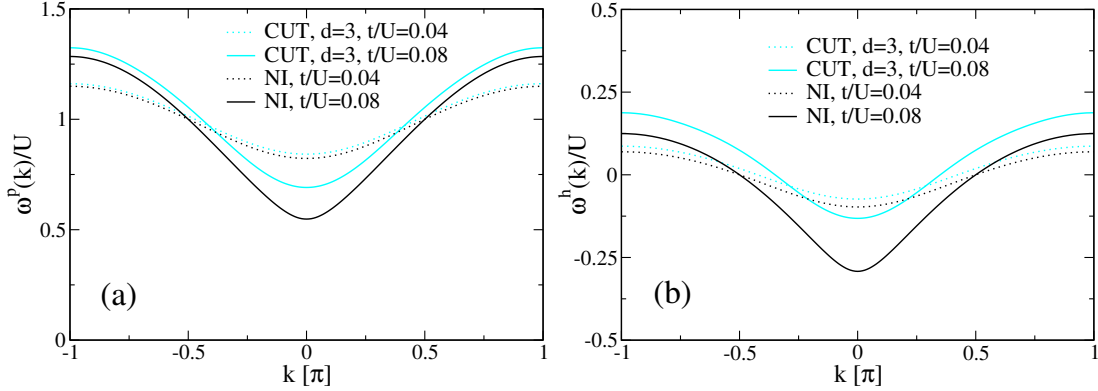


Fig. 5.7: Comparison of the quasiparticle dispersion of the non-interacting approximation (NI) and of the CUT with maximal extension $d = 3$. (a) Dispersion of particle-like p -excitations, (b) Dispersion of hole-like h -excitations. Sizeable differences are seen already for small values of t/U .

interacting approximation (NI) to the CUT result. Figure 5.7a shows the dispersion of p -excitations. For $t/U = 0.04$ the non-interacting approximation is in good agreement with the CUT result. Already for $t/U = 0.08$ the deviations are quite large. The NI dispersion is lower as the CUT result. This is consistent with the observation of a too low critical $t_c^{\text{NI}} = 0.086 U$ found within the NI approximation. The hole dispersion in Fig. 5.7b compares similarly to the CUT results. For $t/U = 0.04$ it is close to, but already below, the CUT-dispersion. Again, the NI dispersion for $t/U = 0.08$ is much too low. In particular, the gap value is off by $0.16 U$. Finally, these deviations lead to a vanishing of the energy for a particle-hole excitation already at $t_c^{\text{NI}} = 0.086 U$.

5.1.3.1. Phase diagram

From the minima of the particle and hole dispersion one can determine the phase diagram, as it has been described in Sec. 5.1.1. We repeat here the necessary definitions. The one-particle gap is defined as

$$\Delta^{p/h} := \min_k \{\omega^{p/h}(k)\}. \quad (5.1.29)$$

Remember that we set the chemical potential to zero in the definition of the dispersion $\omega^{p/h}$. Therewith the critical chemical potential where particle-like excitations become gapless is defined as

$$\mu_c^p = \Delta^p. \quad (5.1.30)$$

The solution of this condition gives the upper boundary of the first Mott-insulating lobe. Correspondingly, the lower boundary is given by the condition that the hole-like quasiparticles become gapless

$$\mu_c^h = -\Delta^h. \quad (5.1.31)$$

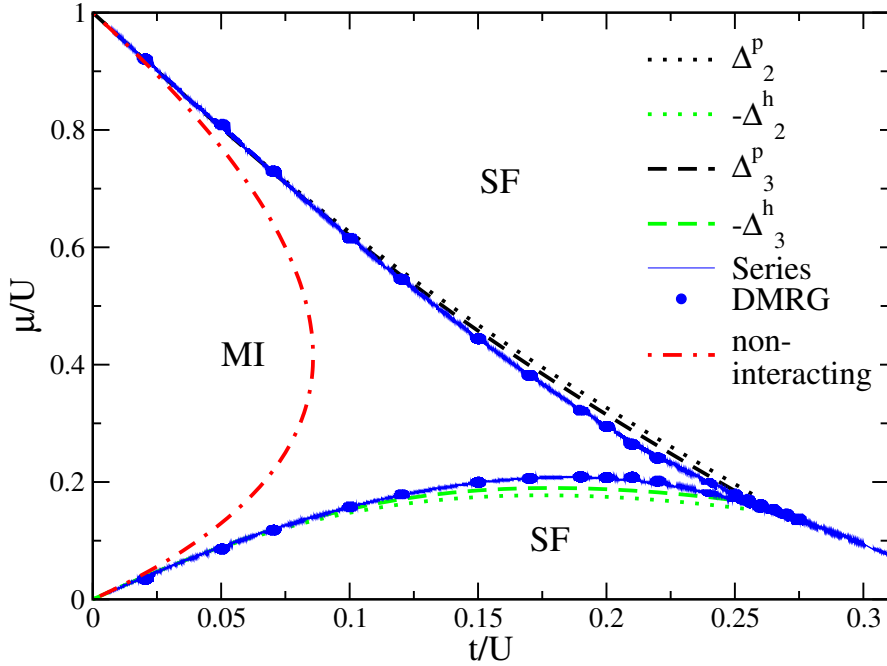


Fig. 5.8: Phase diagram with Mott insulating (MI) and superfluid (SF) phase in the $(t/U, \mu/U)$ plane. Dotted (dashed) lines show CUT results for maximal extension $d = 2$ ($d = 3$). Solid lines (symbols) show series (DMRG) results from Refs. [157, 162]. The result from the non-interacting approximation of Sec. 5.1.1 is shown as dot-dashed line.

The definitions of μ_c^p and μ_c^h differ in sign because a positive chemical potential reduces the energy of a particle while it enhances the energy of a hole. This is directly seen in the Hamiltonian, Eq. (5.1.7). As soon as it costs no energy to reduce or enhance the number of bosons the filling is no longer fixed at the value $n = 1$. The transition from the Mott insulating phase to the superfluid phase takes place.

The reliability of our approach is tested by comparison to results for the phase diagram from other methods. Figure 5.8 shows the phase diagram of the bosonic Hubbard model obtained from the CUT calculation as well as data from DMRG and series expansion [157, 162].

The dotted (dashed) curves result from CUTs for maximal extension $d = 2$ ($d = 3$). For $d = 2$, the CUT can be performed until $l = \infty$; for $d = 3$, the flow is stopped at l_{\min} . Solid curves depict the findings by series expansion, the symbols those obtained by DMRG [157, 162]. The dot-dashed line shows the results from the non-interacting approximation of Sec. 5.1.1. Quite surprisingly, the non-interacting result shows a phase transition to the superfluid regime at $t_c^{\text{NI}} = 0.086 U$. Also the slope of the phase boundaries at $t/U = 0$ is correct in the non-interacting approximation. However, already for small t/U there are sizeable deviations from the more accurate results.

The lower phase boundary stemming from the hole dispersion shows that the gap of the hole-

like excitations depends non-monotonically on the hopping t/U . This is best seen in the inset of Fig. 5.6. The hole gap for $t/U = 0.25$ is *larger* than the one for $t/U = 0.2$. This translates into a reentrant behavior in the phase diagram. Increasing t/U at constant chemical potential $\mu \approx 0.19U$, the Mott insulating phase is left and then entered again for larger values of t/U .

The agreement with the other methods is very good in view of the truncation of the Hilbert space and of the low value of the maximal extension. Note that the $d = 3$ result agrees better than the $d = 2$ result. As expected, the deviations increase for larger values of t/U because longer-range processes become more important. Yet, the values obtained by the CUT for the critical ratio $x_c := t/U$, where the MI phase vanishes, are reasonable. We find $x_c^{(d=2)} = 0.271$ and $x_c^{(d=3)} = 0.258$. By high accuracy density-matrix renormalization $x_c = 0.297 \pm 0.01$ was found, see Ref. [163] and references therein. Series expansion provides $x_c = 0.26 \pm 0.01$ which is very close to our value $x_c^{(d=3)}$. This fact underlines the similarity between the real-space realization of the CUT used here and series expansions.

The transition from the Mott insulator to the superfluid is of the Kosterlitz-Thouless type [153]. This implies an intricate behavior of the gap $\propto \exp(\frac{\text{const}}{\sqrt{x_c - x}})$. For this reason, also DMRG calculations cannot detect the phase transition from the gap value [163]. The critical hopping t_c at the tip of the Mott insulator is determined using the properties of correlation functions. The decay of the correlation functions in the superfluid phase is governed by the Luttinger parameter K . At the transition it is known that $K = 1/2$. Therefore, the transition point can be found by fitting the decay of the correlation functions. In this way the transition point is determined in DMRG calculations [163].

From the findings for the phase diagram in Fig. 5.8 we see that such a peculiar phenomenon as the reentrant behavior of the Mott insulating phase is captured by the CUT approach. The CUT yields quantitative results in a large parameter regime which are in good agreement with the best numerical tools that are available at present. The CUT results are reliable within the MI phase at least for $t \lesssim 0.2U$. On the other hand the mapping to the particle-conserving H_{eff} does not capture the Kosterlitz-Thouless nature of the transition. In the language of the $2D$ XY-model, where it was originally found, the Kosterlitz-Thouless transition is an unbinding transition of vortices [164]. The physics of these complicated objects is not captured by the real space CUT treatment. The reason is that the real space CUT tries to map the problem to an effective Hamiltonian which is rather local. The largest maximal extension used is $d = 3$. The processes included within this maximal extension do not reproduce the physics of the Kosterlitz-Thouless transition.

5.2. Experiment and relevant observable

The calculations in this chapter aim to explain the experimental results of *Stöferle et al.* [17, 148]. This section describes the experiment and explains which observable is the experimentally relevant one.

In the experiment Rubidium atoms are cooled to very low temperatures until they Bose

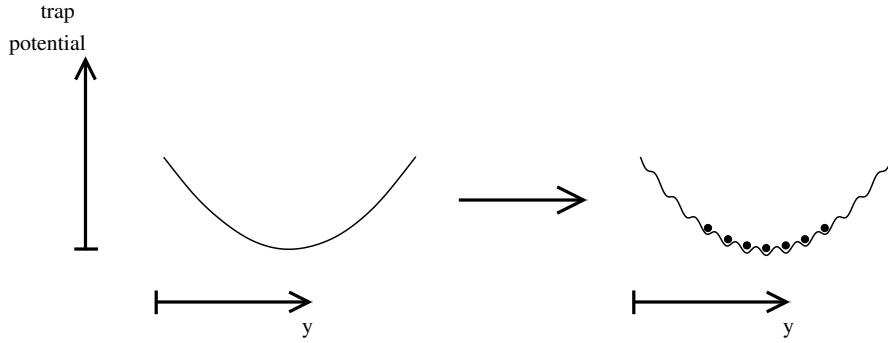


Fig. 5.9: Process of loading the bosonic atoms into an optical lattice. On the left the parabolic trapping potential is shown. In the process of loading an additional modulation of the potential produces an artificial lattice. The minima of the potential correspond to lattice sites. This situation is sketched on the right. In the Mott insulating phase the atoms are localized in the minima of the lattice. This is indicated in the figure by black circles.

condense. They are loaded into a magnetic trap. An artificial lattice is formed by an additional periodic optical potential. The atoms in this lattice are described by the bosonic Hubbard Hamiltonian [145]. The dimensionality of the artificial lattice can be tuned by an anisotropic lattice potential. In the one-dimensional case a potential is produced with large potential depths in x - and z -directions which produce extremely small tunnelling rates in these directions. In the y -direction the potential is ramped to a lower value $V_{\text{ax},0}$. A one-dimensional Bose system in the tubes along the y -axis is formed. The loading of the atoms into the artificial lattice is schematically shown in Fig. 5.9. After the preparation of the one-dimensional Bose system the spectroscopic experiment is performed. Two-photon Bragg spectroscopy is used to measure the energy-dependent response of the system. The lattice potential $V_{\text{ax},0}$ is periodically modulated with amplitude A_{mod} and frequency ν_{mod}

$$V_{\text{ax}}(t, y) = (V_{\text{ax},0} + A_{\text{mod}} \sin(2\pi\nu_{\text{mod}}t)) \sin^2(ky). \quad (5.2.32)$$

The amplitude of the modulation is $A_{\text{mod}} = 0.2V_{\text{ax},0}$. Thus it represents a large perturbation of the system. The frequency ν_{mod} determines the energy of the excitation. After the modulation the lattice potential is gradually switched off and an absorption image of the expanding atom cloud is taken. The width of the central momentum peak is a measure of the spectral weight of the excitation at the respective energy. The experiment has been performed for several values of t/U from the superfluid to the Mott insulating regime.

The results for the spectral weights taken from Ref. [17] are shown in Fig. 5.10. One clearly sees the qualitative change in the measured spectra: from a broad response in the superfluid phase to a discrete spectrum in the Mott phase. The discrete spectrum consists of two peaks. The first is close to the energy given by the interaction strength U , the second is at $\approx 1.9U$. These peaks are the first and second Hubbard peak.

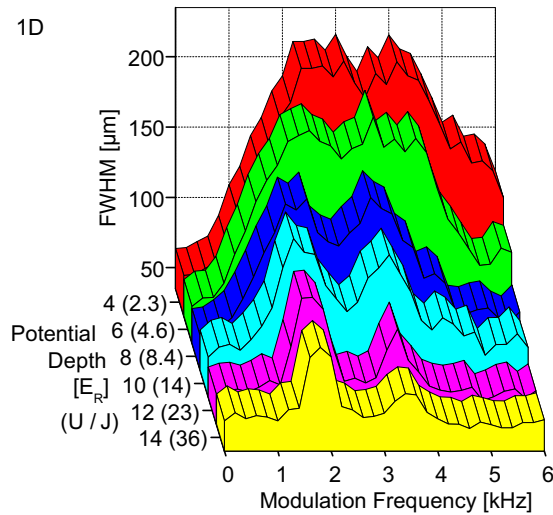


Fig. 5.10: Figure taken from *Stöferle et al.* [17]. It shows the experimental result for the excitation spectrum of bosonic atoms confined to 1D. The values of U/J are given in brackets. Note that $t = 2J$. Therefore, the lowest curve corresponds to $U/t = 72$. One clearly sees the transition from a two peak structure at small t/U to a broad spectrum at larger t/U .

In the present work, we will only deal with the spectroscopic response in the MI region. For references dealing with the experiment in the superfluid regime, see Refs. [165–167]. There is also recent theoretical work dealing with energy absorption experiments in optical lattices in the MI regime [165, 167, 168]. However, references [165, 168] do not use the observable relevant for the experiment in Ref. [17]. Therefore, these references can not reproduce the spectral weight that is present in the experiment. For the MI region, reference [167] deals only with the weight in the first peak.

The aim of this chapter is to explain the surprisingly large spectral weight in the second Hubbard peak. We will not discuss the relative position of the two peaks. From the experimental data shown in Fig. 5.10 the ratio of the weight in the first peak S_1 and in the second peak S_2 can be estimated to be $0.25 < S_2/S_1 < 0.5$ for values of $t/U = 1/46$ and $t/U = 1/72$. It is absolutely unclear why such small values of t/U should produce so much weight in the second Hubbard peak.

Processes contributing to the weight S_2 have energy $2U$. This energy can be realized either by additional creation of a particle-hole pair or by higher processes in the action of the observable. In perturbation theory both contributions are one order smaller in t/U than the leading processes that give rise to the weight S_1 . As the experiment is performed at very small t/U the large ratio of S_2/S_1 is incompatible with the perturbative reasoning.

For the explicit calculation of the spectral weight in this experiment one first has to find the relevant observable. The modulation of the lattice potential changes the depth of the wells and the tunneling rates between adjacent wells of the lattice. Therefore, the observable changes the microscopic parameters U and t and is of the following form

$$\mathcal{O} \propto \delta t H_t + \delta U H_U. \quad (5.2.33)$$

Since multiples of the Hamiltonian do not induce excitations we consider

$$\mathcal{O} \rightarrow \mathcal{O} - (\delta U/U)H, \quad (5.2.34)$$

so that the relevant part of the observable at the beginning of the flow is proportional to the kinetic part of the Hamiltonian

$$\mathcal{O}(l=0) \propto H_t. \quad (5.2.35)$$

The observable in Eq. (5.2.35) acts on the bonds between two sites. The total effect of the observable on all bonds is written as a sum of the local observables (see also Sec. 2.3.5)

$$\mathcal{O}(l) = \sum_{\mathbf{r} \in i+1/2} \mathcal{O}(l, \mathbf{r}) \quad (5.2.36)$$

where i denotes lattice sites. For flow parameter $l=0$ this is the initial observable, for $l=\infty$ it is the effective observable after the transformation. The local observable reads

$$\mathcal{O}(l, \mathbf{r}) = \sum_{\{i, \alpha\}} \hat{c}(l, \{i, \alpha\}) o_{i_1+r, \alpha_1} \cdots o_{i_n+r, \alpha_n} \quad (5.2.37)$$

with the multi-index $\{i, \alpha\}$ summing over all combinations of site indices $\{i\}$ and operator indices $\{\alpha\}$ where we use the notation of Sec. 2.3.5. The right hand side of Eq. (5.2.37) can be rewritten using the specific quasiparticle creation and annihilation operators

$$\begin{aligned} \mathcal{O}(l, \mathbf{r}) = \sum_{\{i, i', j, j', k, k'\}} c(l, \{i, i', j, j', k, k'\}) & h_{i_1+r}^\dagger \cdots h_{i_{n_h}+r}^\dagger h_{i'_1+r} \cdots h_{i'_{m_h}+r} \times \\ & p_{j_1+r}^\dagger \cdots p_{j_{n_p}+r}^\dagger p_{j'_1+r} \cdots p_{j'_{m_p}+r} \times \\ & d_{k_1+r}^\dagger \cdots d_{k_{n_d}+r}^\dagger d_{k'_1+r} \cdots d_{k'_{m_d}+r} \end{aligned} \quad (5.2.38)$$

where (n_h, n_p, n_d) are the number of (h, p, d) quasiparticles created and (m_h, m_p, m_d) are the number of (h, p, d) quasiparticles annihilated. Although the formula is rather lengthy, it allows to easily read off the type of process described by each term in the observable. The powers of creation and annihilation operators in (5.2.38) is collected in the *type*

$$(\bar{n}; \bar{m}) = (n_h \text{h } n_p \text{p } n_d \text{d}; m_h \text{h } m_p \text{p } m_d \text{d}) \quad (5.2.39)$$

characterising the operator. The CUT transforms the observable $\mathcal{O}(l=0)$ into the effective observable $\mathcal{O}^{\text{eff}} = \mathcal{O}(l=\infty)$.

The flow equation for the observable does not close. The generation of terms contributing to the effective observable has to be truncated. For the details of the truncation of the observable see Sec. 2.3.5 where general aspects are explained. Here, we want to repeat just the main aspects of the truncation procedure for the observable. For the Hamiltonian the largest distance between two operators in each term is used as the truncation criterion. This is not possible for the observable. The local observable Eq. (5.2.37) acts on one definite bond \mathbf{r} . Therefore, the coefficient of a term depends on its position relative to the bond \mathbf{r} . This has to be included in the estimation of the importance of a process. We define an integer $d_{\mathcal{O}}$ and compare it to the sum of the distances of all local operators o_i in a certain term in Eq. (5.2.37). If the sum is smaller than or equal to $d_{\mathcal{O}}$ the term is kept, otherwise discarded. The value $d_{\mathcal{O}}$ defines the truncation. For the observable in Eq. (5.2.36) transformations with $d_{\mathcal{O}} = 2, 3, 4$ have been carried out.

5.3. Spectral weights at zero and finite temperature

The momentum and frequency resolved spectral density $S(\mathbf{k}, \omega)$ for the observable \mathcal{O} is defined as

$$S(\mathbf{k}, \omega) = -\frac{1}{\pi} \text{Im} G_{\mathcal{O}}^+(\mathbf{k}, \omega) = -\frac{1}{\pi} \text{Im} \left\langle 0 \left| \mathcal{O}^\dagger(\mathbf{k}) \frac{1}{\omega - [H(\mathbf{k}) - E_0] + i0^+} \mathcal{O}(\mathbf{k}) \right| 0 \right\rangle \quad (5.3.40)$$

where $G_{\mathcal{O}}^+$ is the retarded zero-temperature Green's function. It describes the response of the system for positive energy ω at momentum \mathbf{k} . The energy of the particles introduced by the observable \mathcal{O} determines the energy dependence of $S(\mathbf{k}, \omega)$. A quantity that is the result of an integration of the spectral density is called *spectral weight*.

In order to explain the experiment the distribution of spectral weight has to be calculated for the observable Eq. (5.2.36). The observable in Eq. (5.2.36) gives only rise to spectral weight with momentum $k=0$. An observable with a contribution at finite momentum would include a k -dependent phase factor e^{ikr} .

A sketch of the spectral weight $S(k=0, \omega)$ for this observable is shown in Fig. 5.11. There is a first continuum at U and a second one at $2U$. For small t/U they are well separated. The integral over the spectral density in the first continuum defines the spectral weight S_1 . Correspondingly, S_2 is the spectral weight in the second continuum. For $t/U=0$ the spectral weight consists of δ -functions at multiples of U . The energy of a process is solely determined by H_U . At finite t/U the δ -peaks are broadened to continua. As we are interested in the regime of small t/U the continua do not overlap. It is sufficient to take H_U to measure the energy of an excitation to assign its weight to S_1 or S_2 . Here it is important to note that the assignment to the spectral weight in S_1 or S_2 can only be done after the CUT. Only then, the effective Hamiltonian commutes with H_U and a fixed H_U quantum number can be assigned to every state.

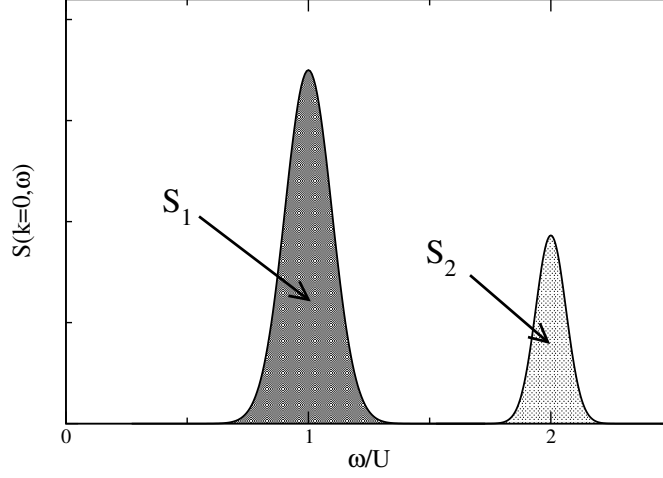


Fig. 5.11: Sketch of the distribution of spectral weight $S(k=0, \omega)$. The weight centered around $\omega = U$ is attributed to S_1 , the weight around $\omega = 2U$ to S_2 .

The aim of the present study is to clarify the distribution of the integrated weights S_1 and S_2 . For this purpose, it is not necessary to calculate the lineshape of $S(k, \omega)$. Of course, the actual lineshape would be an interesting topic on its own.

To obtain further insight we compute the spectral weight of various processes separately. The *type* of an operator in the observable has been defined in the context of Eq. (5.2.38). The type $(\bar{n}; \bar{m}) = (n_h, h, n_p, p, n_d, d; m_h, h, m_p, p, m_d, d)$ collects the numbers of creation and annihilation operators in the term. We define the weight corresponding to a type $(\bar{n}; \bar{m})$ as

$$I_{(\bar{n}; \bar{m})}^{\text{eff}}. \quad (5.3.41)$$

These weights are calculated after the transformation. Therefore, they carry a superscript "eff". The weight $I_{(\bar{n}; \bar{m})}^{\text{eff}}$ is calculated by summing the moduli squared of all coefficients of the given type $(\bar{n}; \bar{m})$.

At zero temperature, only processes that do not annihilate the vacuum contribute. They are of the type $(\bar{n}; 0)$. As the number of bosons is conserved one hole (*h*-particle) has to be generated together with each *p*-particle and two holes together with each *d*-particle. In the first place, the observable introduces particle-hole pairs (type $(1h, 1p; 0)$). Their energy is about U . Higher processes introducing n particle-hole pairs $(n_h, h, n_p, p; 0)$ have the energy nU . The first processes involving a *d* particle are of type $(2h, 1d; 0)$ at energy $3U$. Thus, the relative spectral weight S_2/S_1 at zero temperature is calculated from the weights $I_{(1h, 1p; 0)}^{\text{eff}}$ and $I_{(2h, 1d; 0)}^{\text{eff}}$. These weights are plotted in Fig. 5.12a for the truncations $d_{\mathcal{O}} = 2, 3, 4$. The convergence with the truncation criterion $d_{\mathcal{O}}$ is very good in both cases. The curve for $d_{\mathcal{O}} = 4$ is on top of the $d_{\mathcal{O}} = 3$ curve. The spectral weight $I_{(2h, 2p; 0)}^{\text{eff}}$ which is situated at an energy of $2U$ is very small. Note that the curves for different observable extension are on top of each other. Thus the large experimental value

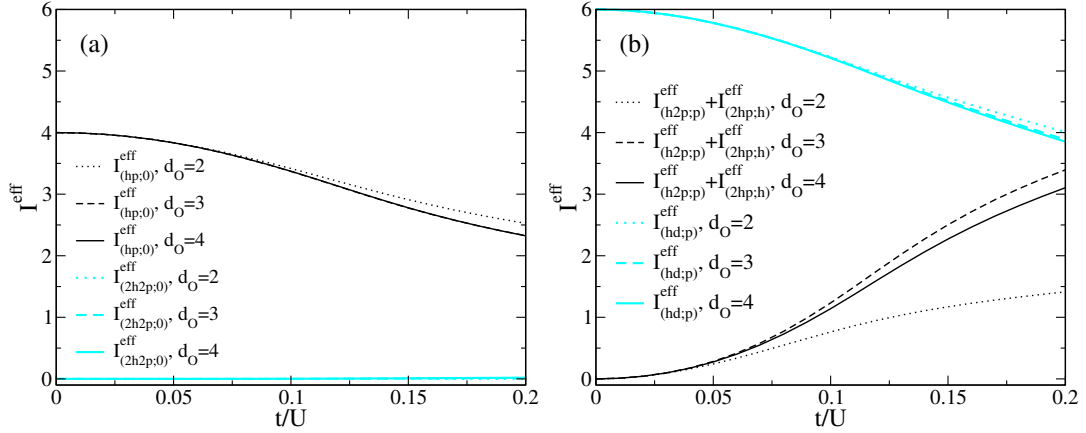


Fig. 5.12: Spectral weights of various processes for the truncations $d_{\text{O}} = 2, 3, 4$ in dotted, dashed and full lines, respectively. (a) shows contributions from processes starting from the vacuum: $I_{(\text{hp};0)}^{\text{eff}}$ which gives spectral weight at energy U (black line), $I_{(2\text{h}2\text{p};0)}^{\text{eff}}$ with energy position $2U$ (gray/cyan line). (b) contributions from processes for one particle present: $I_{(\text{h}2\text{p};\text{p})}^{\text{eff}} + I_{(2\text{h}\text{p};\text{h})}^{\text{eff}}$ (contributes at U) (black line), and $I_{(\text{hd};\text{p})}^{\text{eff}}$ (at $2U$) (gray/cyan line).

of S_2/S_1 cannot be explained in a translational invariant system at zero temperature. However, the experiment is performed in a finite trap. The finite system size leads to an inhomogeneous distribution of the atoms. The possible implications of the inhomogeneity are discussed later in this section.

In Fig. 5.12b the contributions to the spectral weight are plotted for processes that start from one excitation. This excitation can be a particle or a hole. The contributions to the spectral weight at U are $I_{(\text{h}2\text{p};\text{p})}^{\text{eff}}$ and $I_{(2\text{h}\text{p};\text{h})}^{\text{eff}}$. Their sum is depicted by the black curves. Convergence is not fully reached but the small difference between the dashed curve for $d_{\text{O}} = 3$ and the solid curve for $d_{\text{O}} = 4$ indicates that the $d_{\text{O}} = 4$ result is already very close to the true solution. A large contribution of spectral weight at $2U$ is found from processes of the type $(\text{hd};\text{p})$. This channel is a candidate to support the experimental finding of large S_2/S_1 .

Processes of the type $(\text{hd};\text{p})$ contribute spectral weight only if p -excitations are present. This is not the case for the case of zero temperatures that has been discussed up to now. However, quasiparticles are present at finite temperatures. At not too high temperatures, independent particles p and holes h are the prevailing excitations. The presence of p -excitations in the groundstate at finite temperature can give rise to enhanced spectral weight S_2 at $2U$. The increase of spectral weight S_2 with increasing temperature is calculated in the next section. Other excitations, for instance d^\dagger or $(p^\dagger)^2$, are higher in energy and thus much less likely.

That adjacent pairs of singly and doubly occupied sites are at the origin of the high energy peak has already been suggested in Refs. [16, 17]. However, the presence of these defects deep inside the Mott insulating regime has to be explained. At zero or at very low temperature, the inhomogeneity of the parabolic trap can imply a spatially inhomogeneous distribution of

the bosons. Plateaus of various occupations $\langle n \rangle \in \{0, 1, 2, \dots\}$ are found, depending on the total filling [169, 170]. The plateaus correspond to local Mott insulating situations with particle density $n = 1$, $n = 2$, and so on. In the transition region from one integer value of $\langle n \rangle$ to the next, defects occur which lead to excitations at $2U$. But it is unlikely that this mechanism explains the experimental finding since the transition region is fairly short at small temperatures T/U and small values of t/U [169, 170]. The plateaus prevail clearly, while the high energy peak at $2U$ has only by a factor 2 to 5 less weight than the low energy peak at U . It is not plausible that these "steps" govern the behavior of the spectroscopic response of the bulk system. Therefore, it is unlikely that the inhomogeneity of the trap is sufficient to account for the experimental finding. At higher temperatures, thermal fluctuations are the likely candidate for the origin of the defects. The next section is devoted to the calculation of the effect of a finite temperature on the spectral weights.

5.3.1. Finite temperature

At finite temperatures, the system is not in its $T = 0$ groundstate. Excitations are present. This changes the distribution of spectral weight of the effective observable. To quantify the modification of spectral weight the occupation numbers of the excitations have to be calculated. The statistics of hard-core particles is complicated and thus a direct evaluation of the partition function is not easily tractable. Therefore, we will approximate the hard-core statistics in a way introduced in Ref. [171]. The occupation number of an excitation depends on its energy. As the one-particle energies are given in momentum space the effective observable has to be Fourier transformed partially such that it is clear which energy the annihilated particles have.

Approximation for finite temperature

This section will adapt the calculation from Ref. [171] for hard-core boson at finite temperatures for our purpose. In Ref. [171] the triplet excitations above a singlet product state of a spin ladder are treated. In our case the relevant excitations are one-particle and one-hole excitations. Multiple p and h excitations and excitations of d -type are much less relevant because of their high energy. Therefore, we will neglect d -excitations and correlated excitations of more than one particle or hole in the following. Uncorrelated multiple excitation of p - and h -excitations will be taken into account.

We will now use the statistics of non-interacting boson to approximate the statistics of hard-core bosons. It is a bad approximation to substitute the hard-core statistics by the statistics of non-interacting boson without any modification because non-interacting bosons have no restriction on the occupation number. An incorrect number of states would contribute in the partition sum and would lead to an incorrect entropy. The idea is now to reweight all contributions to the partition sum such that they contribute the correct amount of entropy. Therefore, we have to calculate the correct number of states with particle and hole excitations.

The number of possibilities to distribute N bosonic excitations on $2L$ places is

$$g_B(L, N) = \binom{2L + N - 1}{N}. \quad (5.3.42)$$

In contrast, the correct number of possibilities of N hard-core excitations of two kinds on L sites is

$$g(L, N) = 2^N \binom{L}{N}. \quad (5.3.43)$$

Now, the N -boson part in the partition sum is reweighted such that it contributes the correct number of states, namely $g(L, N)$. This ensures that the N -particle part of the partition function contributes the correct entropy. We start from the following partition function for a system of size L and N particles

$$Z'(L, N) = \prod_{j=1}^N \sum_{k_j} \left[\exp(-\beta(\omega^p(k_j) - \mu^p)) + \exp(-\beta(\omega^h(k_j) - \mu^h)) \right]. \quad (5.3.44)$$

Here, a chemical potential for particles μ^p and for holes μ^h is introduced to keep the notation transparent. They are defined as

$$\mu^p = -\mu^h = \mu. \quad (5.3.45)$$

The sum goes over all momenta k_j . Here, $\omega^p(k_j)$ is the energy of a particle with momentum k_j , $\omega^h(k_l)$ the energy of a hole with momentum k_l . The partition function in Eq. (5.3.44) contains $(2L)^N$ terms. The reweighted partition function reads

$$\tilde{Z} = \sum_{N=0}^L \frac{g(L, N)}{(2L)^N} Z'(L, N). \quad (5.3.46)$$

This equation can be rewritten as

$$\tilde{Z} = \sum_{N=0}^L \frac{\binom{L}{N}}{L^N} \prod_{j=1}^N \sum_{k_j} \left[\exp(-\beta(\omega^p(k_j) - \mu^p)) + \exp(-\beta(\omega^h(k_j) - \mu^h)) \right] \quad (5.3.47)$$

$$= \left(1 + \frac{1}{L} \sum_{k_j} \exp(-\beta(\omega^p(k_j) - \mu^p)) + \frac{1}{L} \sum_{k_l} \exp(-\beta(\omega^h(k_l) - \mu^h)) \right)^L \quad (5.3.48)$$

where k_j and k_l run over all particle and hole momenta, respectively. The power $(1 + \dots)^L$ reproduces all terms that are present in Eq. (5.3.47) with the correct multiplicity $\binom{L}{N}$. If we define a partition function for each type of particle $\sigma \in \{p, h\}$ as

$$z^\sigma = \frac{1}{2\pi} \int_0^{2\pi} e^{-\beta(\omega^\sigma(k) - \mu^\sigma)} dk, \quad (5.3.49)$$

equation (5.3.48) reads finally

$$\tilde{Z} = (1 + z^p + z^h)^L. \quad (5.3.50)$$

This approximate partition function in Eq. (5.3.50) has the following properties. For zero doping, the density of particles and holes vanishes as we approach zero temperature. In the limit of low particle density the hard-core interaction between the bosons becomes less relevant and they behave like non-interacting particles. Therefore, the approximate partition function Eq. (5.3.50) will display the correct behavior for $T \rightarrow 0$. For high temperature the reweighting in Eq. (5.3.46) ensures that the correct number of states contribute. Thus the approximate partition function, Eq. (5.3.50), has also the correct behavior for $T \rightarrow \infty$.

For non-zero doping, the particle density does not go to zero for $T \rightarrow 0$. Therefore, it is not ensured that the behavior for low temperatures is correct. Indeed we will see later that for non-zero doping and at very low temperatures the partition function Eq. (5.3.50) produces spurious results. The high temperature limit is correct also for non-zero doping.

Although the partition function in Eq. (5.3.50) is correct in certain limits it is only an approximation for hard-core particles. The sum in Eq. (5.3.44) contains contributions from unphysical states. States with two particles having the same quantum numbers are included in Eq. (5.3.44) although they are not allowed for hard-core particles. In addition it is assumed that all excitations can be described by non-interacting multi-particle excitations.

The free energy per site f is computed from Eq. (5.3.50) as

$$f = -\frac{T}{L} \ln \tilde{Z} = -T \ln(1 + z^p + z^h). \quad (5.3.51)$$

A certain filling is realized by choosing the chemical potential μ appropriately. For filling $n = 1$, i. e. zero doping, the chemical potential μ is determined such that as many particles as holes are excited. The average occupation number n_k^σ of the $\sigma \in \{p, h\}$ excitations with momentum k is

$$\langle n_k^\sigma \rangle = -\frac{\partial f}{\partial \omega^\sigma(k)} = \frac{e^{-\beta(\omega^\sigma(k) - \mu^\sigma)}}{1 + z^p + z^h} \quad (5.3.52)$$

and the probability to find no excitation, and thus the vacuum state, is

$$\langle n^{\text{vac}} \rangle = 1 - \sum_k \langle n_k^p \rangle - \sum_k \langle n_k^h \rangle = \frac{1}{1 + z^p(\beta) + z^h(\beta)}. \quad (5.3.53)$$

With the knowledge of the occupation numbers the effective spectral weight for finite temperature is calculated in terms of the $T = 0$ spectral weight. A contribution to a spectral weight of type $(\bar{n}, 0) = (n_h, n_p, n_d; 0)$ has to be multiplied by the probability to find $n_h + n_p + n_d$ times the local vacuum state on a site. Only then the corresponding operator does not annihilate the given state and contributes to the spectral weight. Hence, the effective finite temperature spectral weights relevant for vacuum processes are

$$I_{(\bar{n}; 0)}^{\text{eff}, T} = I_{(\bar{n}; 0)}^{\text{eff}} \langle n^{\text{vac}} \rangle^{n_h + n_p + n_d}. \quad (5.3.54)$$

At finite temperature there are excitations present in the ground state. Not only the spectral weights of processes starting from the vacuum are relevant. There are also contributions from processes that need to have a particle or hole present in the initial state. The most important

contributions come from processes that need to have only one quasiparticle present. These are the spectral weights $I_{\bar{n},p}^{\text{eff},T}$ and $I_{\bar{n},h}^{\text{eff},T}$. The spectral weight at finite temperature for processes starting from a one-particle or one-hole state reads

$$I_{(\bar{n};\sigma)}^{\text{eff},T} = \frac{\langle n^{\text{vac}} \rangle^{n_h+n_p+n_d}}{2\pi} \int_0^{2\pi} I_{(\bar{n};\sigma)}^{k,\text{eff}} \langle n_k^\sigma \rangle dk. \quad (5.3.55)$$

The occupation number $\langle n_k^\sigma \rangle$ can be calculated from Eq. (5.3.52) using the results for the dispersion $\omega^\sigma(k)$ from the CUT. The effective spectral weight $I_{(\bar{n};\sigma)}^{k,\text{eff}}$ contains contributions from all processes that start from a particle of type σ with momentum k and end in a state of type \bar{n} . The upper index k in the spectral weight $I_{(\bar{n};\sigma)}^{k,\text{eff}}$ indicates the dependence on the momentum of the annihilated particle. The CUT is implemented in real space. Therefore, the effective observable \mathcal{O}^{eff} in Eq. (5.2.38) has to be Fourier transformed such that it depends on momentum. Then, the spectral weight $I_{(\bar{n};\sigma)}^{k,\text{eff}}$ is obtained as the sum of the moduli squared of all contributions with momentum k that are of type $(\bar{n};\sigma)$. It is sufficient to Fourier transform the effective observable partially because only the momentum of the annihilated particle is needed to calculate the necessary occupation numbers.

Partial Fourier transform

The partial Fourier transform of the observable is exemplified by the $(2ph;p)$ amplitudes. The local observable for $(2ph;p)$ processes is

$$\mathcal{O}_{(2p\ h;p)}(r) = \sum_{i_1, j_1, j_2, j'_1} c(l, i_1 - r, j_1 - r, j_2 - r, j'_1 - r) h_{i_1}^\dagger p_{j_1}^\dagger p_{j_2}^\dagger p_{j'_1}. \quad (5.3.56)$$

The observable \mathcal{O} is obtained by summation

$$\mathcal{O}_{(2p\ h;p)} = \sum_r \mathcal{O}_{(2p\ h;p)}(r). \quad (5.3.57)$$

Now, this expression can be rewritten using the coefficients that are Fourier transformed in the index of the annihilated particle

$$\mathcal{O}_{(2p\ h;p)} = \sum_r \mathcal{O}_{(2p\ h;p)}(r) \quad (5.3.58a)$$

$$= \sum_{r, i_1, j_1, j_2, j'_1} c(l, i_1 - r, j_1 - r, j_2 - r, j'_1 - r) h_{i_1}^\dagger p_{j_1}^\dagger p_{j_2}^\dagger p_{j'_1} \quad (5.3.58b)$$

$$= \sum_k \sum_{i_1, j_1, j_2} h_{i_1}^\dagger p_{j_1}^\dagger p_{j_2}^\dagger p_k \underbrace{\sum_{r, j'_1} e^{ikj'_1} c(l, i_1 - r, j_1 - r, j_2 - r, j'_1 - r)}_{\tilde{c}(i_1 - r, j_1 - r, j_2 - r, k)} \quad (5.3.58c)$$

$$= \sum_k \sum_{i_1, j_1, j_2} \tilde{c}(i_1 - r, j_1 - r, j_2 - r, k) h_{i_1}^\dagger p_{j_1}^\dagger p_{j_2}^\dagger p_k. \quad (5.3.58d)$$

The partially Fourier transformed coefficient used in the last line is defined as

$$\tilde{c}(i_1 - r, j_1 - r, j_2 - r, k) = \sum_{r, j'_1} e^{ikj'_1} c(l, i_1 - r, j_1 - r, j_2 - r, j'_1 - r). \quad (5.3.59)$$

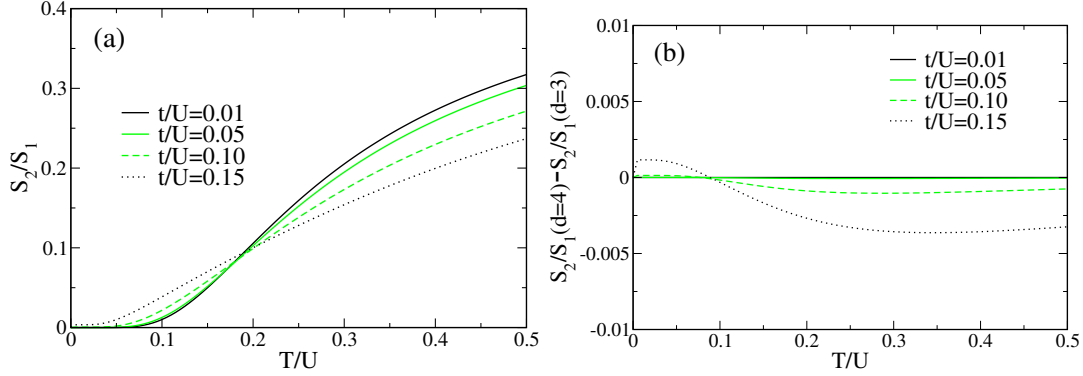


Fig. 5.13: (a) The ratio S_2/S_1 plotted against temperature for the observable truncation $d_{\mathcal{O}} = 4$. S_2/S_1 is shown for fixed values of $t/U \in \{0.01, 0.05, 0.1, 0.15\}$. (b) shows the difference of the result for S_2/S_1 between the truncation $d_{\mathcal{O}} = 4$ and $d_{\mathcal{O}} = 3$. The difference between the two truncation schemes is very small. The deviations increase for increasing t/U and for increasing temperature.

From these coefficients, the $I_{(\bar{n};\sigma)}^{k,\text{eff}}$ are obtained as the sum of the moduli squared of all $\tilde{c}(i_1 - r, j_1 - r, j_2 - r, k)$ with momentum k that are of type $(\bar{n}; \sigma)$. The calculation for processes of type $(p \ 2h; h)$ is done in the same way. Using the partial Fourier-transform and Eq. (5.3.55) the spectral weights $I_{(\bar{n};\sigma)}^{\text{eff},T}$ at finite temperature can be calculated.

5.3.2. Results

Processes of type $(h \ p; 0)$, $(h \ 2p; p)$, and $(2h \ p; h)$ contribute to the spectral weight at energy U . The temperature dependent spectral weight at energy U is

$$S_1 = I_{(h \ p; 0)}^{\text{eff},T} + I_{(h \ 2p; p)}^{\text{eff},T} + I_{(2h \ p; h)}^{\text{eff},T}. \quad (5.3.60)$$

The spectral weight S_2 at $2U$ is made up of the types $(2h \ 2p; 0)$ and $(h \ d; p)$ and therefore the temperature dependent weight at $2U$ is

$$S_2 = I_{(2h \ 2p; 0)}^{\text{eff},T} + I_{(h \ d; p)}^{\text{eff},T}. \quad (5.3.61)$$

To include the second type of processes $(h \ d; p)$ is consistent with the approximation for finite temperature - that included only thermal population of one p- and one h-states - because it starts from a one-particle state. The d -type particle is created by application of the effective observable.

The ratio S_2/S_1 as a function of T/U is shown in Fig. 5.13. Figure 5.13a displays S_2/S_1 for fixed values of $t/U \in \{0.01, 0.05, 0.1, 0.15\}$ for the observable truncation $d_{\mathcal{O}} = 4$. Two regimes can be distinguished in the results for S_2/S_1 . For low values of $T \lesssim 0.19 U$, the ratio S_2/S_1 increases on increasing t/U because the particle gap Δ^p decreases so that $\langle n_{k \approx 0}^p \rangle$ grows. For higher values of $T \gtrsim 0.19 U$, the increase of $\langle n_{k \approx 0}^p \rangle$ is overcompensated by the decrease of

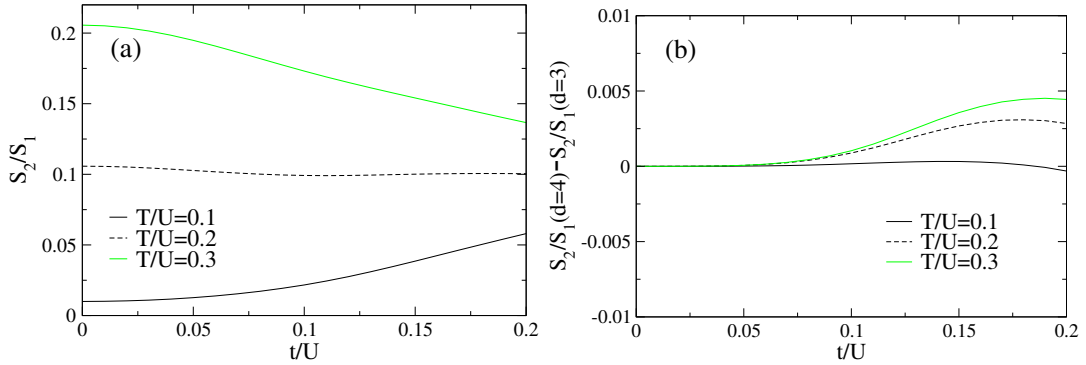


Fig. 5.14: (a) The ratio S_2/S_1 plotted against the hopping amplitude t/U . S_2/S_1 is shown for observable truncation $d_{\mathcal{O}} = 4$ and fixed $T/U \in \{0.1, 0.2, 0.3\}$. (b) The difference between the truncations $d_{\mathcal{O}} = 4$ and $d_{\mathcal{O}} = 3$ against t/U .

the weights $I_{(2h\ 2p;0)}^{\text{eff},T} + I_{(h\ d;p)}^{\text{eff},T}$ and the increase of the weights $I_{(h\ p;0)}^{\text{eff},T} + I_{(h\ 2p;p)}^{\text{eff},T} + I_{(2h\ p;h)}^{\text{eff},T}$ (see Fig. 5.12) so that the relative spectral weight decreases on increasing t/U . Around $T = 0.19U$, the ratio is fairly independent of t/U .

Figure 5.13b shows the difference of S_2/S_1 of the truncations $d_{\mathcal{O}} = 4$ and $d_{\mathcal{O}} = 3$. The difference between the results are very small. The deviations increase for increasing hopping and for increasing temperature. Already the spectral weights of the various processes, shown in Fig. 5.12, displayed only small deviations between the truncations $d_{\mathcal{O}} = 3$ and $d_{\mathcal{O}} = 4$. The total spectral weights S_1 and S_2 are aggregate quantities. They are even less sensible to the truncation scheme than the spectral weights for the various separate processes shown in Fig. 5.12.

The two regimes with different behavior are also clearly seen in Fig. 5.14a where S_2/S_1 is plotted against t/U for fixed temperature. The dashed curve for $T/U = 0.2$ stays fairly constant. For a small temperature $T/U = 0.1$ the relative weight S_2/S_1 increases with increasing t/U , while for $T/U = 0.3$ the ratio S_2/S_1 decreases. Figure 5.13b shows the difference of S_2/S_1 plotted against t/U for different truncations of the observable, $d_{\mathcal{O}} = 4$ and $d_{\mathcal{O}} = 3$. Again, we see that the deviations are small.

The experimental value of S_2/S_1 [17] is about $0.2 - 0.5$ for small values of t/U ($t \leq 0.014U$). It increases on approaching the superfluid phase. Hence, our estimate for S_2/S_1 from the results in Fig. 5.13 implies a significant temperature $T \approx U/3$ in the MI phase. We postpone the discussion of this remarkable result to Sec. 5.5. Before, we try to get further insight into the temperatures realized in the system by looking at entropy properties.

5.4. Entropy

The temperature of $T \approx U/3$ that is found from the analysis of spectroscopic weights is at first sight surprisingly high. In a correlated solid state system the interaction parameter U is

typically of the order of several electron volts [60]. A temperature of this size would be far above the melting temperature of a typical crystal. It has to be checked if a temperature of this size is reasonable in the systems of optically trapped atoms. To this end, this section investigates the entropy of the system before and after loading into the optical lattice. Also situations with fillings different from one particle per site are considered. This calculation will support the finding that the temperatures in the Mott regime is of the order of the interaction parameter.

This section is organised as follows. First, we analyze the entropy of the bosons in a trap without lattice potential. Then, we consider the so-called Tonks-Girardeau(TG) limit. The entropy in this parameter regime is calculated. This leads to an estimation of the temperature found in the TG limit. Using these results the validity of the approximated thermodynamics introduced in Chapter 5.3.1 is checked. Finally, the entropy in the Mott regime is calculated.

5.4.1. Entropy in a harmonic trap

In the experiment the gas of atoms is in the beginning confined in a magnetic trap. The trapping potential is harmonic. Then, the optical lattice is produced by switching on an additional periodic potential. The loading process is schematical shown in Fig. 5.9 on page 134. The loading is performed adiabatically [17]. This means that the entropy S/N remains constant during loading. It is insightful to calculate the entropy of the Bose gas before loading to see at which temperature this entropy is realized after loading.

The calculation of the entropy of a non-interacting Bose gas in a three dimensional harmonic oscillator potential is explicitly done in Appendix B. The entropy per particle depends only on the fraction f_0 of bosons that are condensated

$$\frac{S}{N} = \frac{2\pi^4}{45\zeta(3)}(1 - f_0) \quad (5.4.62)$$

where $\zeta(x)$ is the Riemann ζ -function. The condensate fraction in the experiment [172] is typically about $f_0 = 0.9$. Therefore, we will discuss in the following condensate fractions $f_0 \in \{0.95; 0.9; 0.8\}$. For these condensate fractions the entropy per particle is $\{0.09; 0.18; 0.36\}$, respectively.

5.4.2. Tonks-Girardeau regime

The Tonks-Girardeau (TG) regime of the bosonic Hubbard model is the limit of infinite U at an average filling of less than one boson per site. The only parameter in the system is the hopping amplitude t . The TG regime is studied in Ref. [146] where a temperature of multiples of the microscopic parameter t is found. In the limit of $U \rightarrow \infty$ only empty or singly occupied sites are realized. In one dimension the system of hard-core bosons can be mapped onto a free Fermi system [146, 150, 173, 174]. This mapping allows to calculate the entropy for the TG regime from the free Fermi gas. This is done in Appendix B where also the explicit formulae are found.

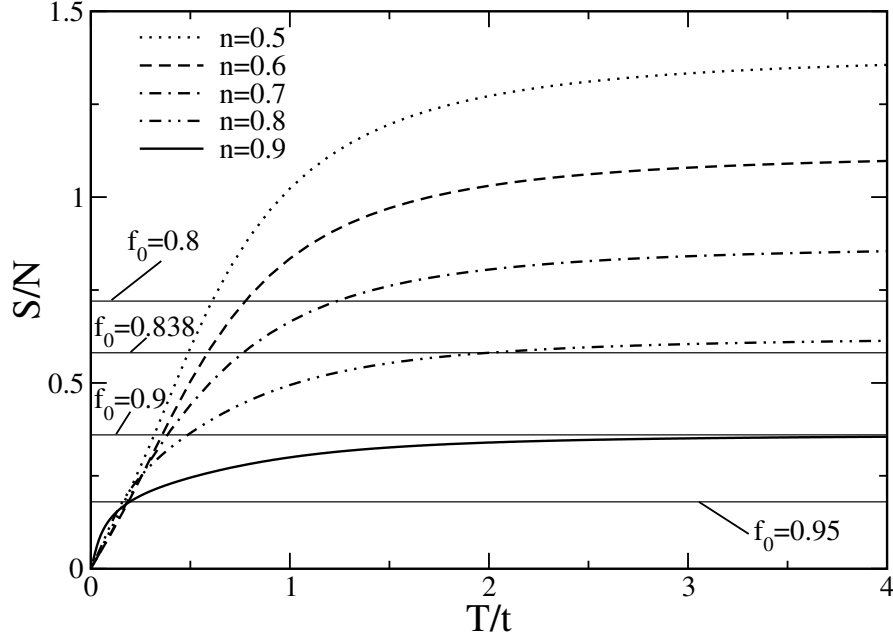


Fig. 5.15: Entropy in the Tonks-Girardeau regime for various fillings. The entropy per particle of the three-dimensional harmonic oscillator for condensate fractions $f_0 = \{0.95; 0.9; 0.8\}$ and $f_0 = 0.838$ is included as horizontal lines.

The entropy per particle is calculated using the derivative of the free energy per particle f with respect to temperature

$$\frac{S}{N} = -\frac{1}{n} \frac{\partial f}{\partial T}. \quad (5.4.63)$$

Here, the number of bosons is denoted by N . The filling n is defined as

$$n = \frac{N}{L}, \quad (5.4.64)$$

which is the ratio of the number of bosons N and the number of lattice sites L . Figure 5.15 shows the entropy per particle against T/t in the TG regime for fillings $n \in \{0.5, 0.6, 0.7, 0.8, 0.9\}$. After a steep increase the entropy approaches its saturation value of

$$\frac{S(T = \infty)}{N} = -\log(n) - \left(\frac{1}{n} - 1\right) \log(1 - n). \quad (5.4.65)$$

Filling $n = 0.5$ shows the largest saturation value. It decreases when the filling is increased.

In addition, the entropy per particle of the three-dimensional harmonic oscillator is plotted for condensate fractions $f_0 = \{0.95; 0.9; 0.8\}$ and $f_0 = 0.838$ as horizontal lines. The conservation of entropy allows to determine the temperature that results for these condensate fractions after loading into the optical lattice in the TG regime. For half filling, $n = 0.5$, the temperatures are $T/t = \{0.17; 0.32; 0.61\}$ for $f_0 = \{0.95; 0.9; 0.8\}$. Also temperatures of multiples of the hopping parameter are possible, e. g. for $f_0 = 0.838$ and $n = 0.8$ the temperature is $T/t = 2$.

Again, the temperatures are of the size of the microscopic system parameter t . This agrees well with the temperature estimated in Ref. [146]. There, the temperature has been determined from the measured momentum profiles. For higher filling the entropy saturates at a lower value. For filling $n = 0.8$ it does not rise up to the value of the harmonic oscillator for $f_0 = 0.8$. Thus in a process of adiabatic loading one can not achieve a filling of $n = 0.8$ when starting with a condensate fraction of $f_0 = 0.8$.

5.4.3. Reliability of the approximation for finite temperatures

In Chapter 5.3.1 the zero-temperature results from the CUT have been extended to finite temperatures. An approximate expression for the partition function of the hard-core bosons has been introduced. This approximate partition function reproduces correctly the high temperature limit. The low temperature limit is correct only if the number of excitations vanishes for $T = 0$. As our reference state is the product state of singly occupied sites this is only the case if the filling $n = 1$.

In this section we check the validity of this approximation. The results for the TG regime from the previous chapter, Sec. 5.4.2, are used as a benchmark. In particular, the quality of the approximation for low temperatures and fillings $n \neq 1$ is addressed.

For this purpose, we introduce a toy model which corresponds to the situation in the TG regime. The approximate thermodynamics has been introduced in Chap. 5.3.1 for the bosonic Hubbard model in the Mott-insulating regime. The reference state is the product of singly occupied local states. Above the reference state there exist particle- and hole-like excitations. These two types of excitations have been included in the approximate partition function.

The toy model includes only hole-like quasiparticle excitations. The free energy from Eq. (5.3.51) simplifies to the free energy of the toy model

$$f_{\text{Toy}} = -T \ln(1 + z^h). \quad (5.4.66)$$

where

$$z^h = \frac{1}{2\pi} \int_0^{2\pi} e^{-\beta(\omega^h(k) - \mu^h)} dk. \quad (5.4.67)$$

Because only hole-like excitations are contained in the toy model the filling is $n \leq 1$. The dispersion contains only one cosine-term

$$\omega^h(k) = -2t \cos(k). \quad (5.4.68)$$

This corresponds to hard-core bosons with nearest-neighbor hopping only. With these definitions the toy model describes the TG regime. For the dispersion in Eq. (5.4.68) the partition function Eq. (5.4.67) can be evaluated analytically. It reads

$$z^h = e^{\beta\mu^h} I_0(2\beta t), \quad (5.4.69)$$

where $I_n(z)$ is the modified Bessel function of the first kind. The entropy per particle reads

$$\frac{S}{N} = -\frac{1}{n} \frac{\partial f}{\partial T} = -\beta e^{\beta\mu^h} \frac{2t I_1(2\beta t) + \mu^h I_0(2\beta t)}{n(1 + e^{\beta\mu^h} I_0(2\beta t))} + \frac{1}{n} \log \left(1 + e^{\beta\mu^h} I_0(2\beta t) \right). \quad (5.4.70)$$

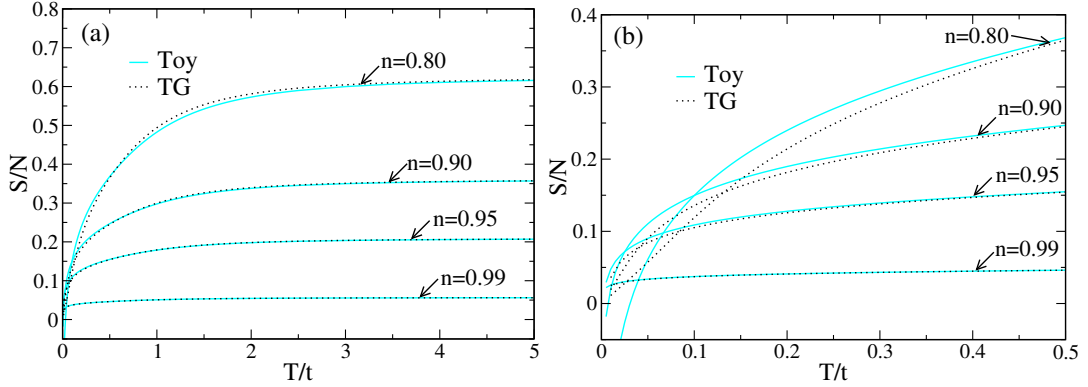


Fig. 5.16: (a) Comparison of the entropy per particle at small temperatures calculated for the TG regime. The entropy of free fermions is shown as black dotted curves. Results from the toy-model calculation are shown in gray (cyan). (b) Same as (a), however the plotting interval has been changed such that the low temperature region is better visible.

The total number of hole excitations divided by the number of lattice sites reads

$$\delta = -\frac{\partial f}{\partial \mu^h} = \frac{e^{\beta\mu^h} I_0(2\beta t)}{1 + e^{\beta\mu^h} I_0(2\beta t)}. \quad (5.4.71)$$

Since the excitations are holes the quantity δ is just the amount of doping with holes. It is related to the filling by

$$\delta = 1 - n. \quad (5.4.72)$$

The doping is determined by the chemical potential. A doping value δ is found for a chemical potential

$$\mu^h = T \log \left(\frac{\delta}{(1 - \delta) I_0(2\beta t)} \right). \quad (5.4.73)$$

The results for the entropy of the toy model are shown in Fig. 5.16 for various fillings. For comparison, the entropy for the TG regime calculated from the free fermion formula is included in the figure. Figure 5.16a shows the entropy for temperatures $T/t \in [0, 5]$. After a steep increase the entropy saturates for high temperatures. The agreement with the free Fermion result is very good. Also for filling $n = 0.8$ which corresponds to a rather large doping of $\delta = 0.2$ the agreement is good for temperatures of the order of the hopping parameter. However, deviations are found for low temperatures. Therefore, the limit of $T/t \rightarrow 0$ is now further investigated. Figure 5.16b shows the entropy for low temperatures, $T/t \in [0, 0.5]$. In this temperature range sizeable deviations are found. They appear especially at low temperatures and are increasing with doping. The entropy even becomes negative for fillings $n = 0.9$ and $n = 0.8$. This behavior is unphysical. It is an artifact of the approximate thermodynamics for hard-core bosons.

As the deviations are small the relative deviation of the entropy

$$\frac{\Delta S}{S} = \frac{S_{\text{Toy}} - S_{\text{TG}}}{S_{\text{TG}}} \quad (5.4.74)$$

is plotted in Fig. 5.17a. For $n = 0.8$ the difference of the entropies has a maximum at $T/t \approx 0.08$, then it drops and becomes even negative at very low temperatures because S_{toy} becomes negative for $T \rightarrow 0$. This is an unphysical artifact of the approximate thermodynamics for hard-core bosons. For $n \rightarrow 1$ the maximum of the relative deviation is lower and shifted to lower temperatures. But artificial negative entropy behavior is still found for very low T .

In Sec. 5.3.1 we argued that the approximate partition function displays the correct zero-temperature behavior if the particle density vanishes for $T \rightarrow 0$. This is not the case for non-zero doping. Thus, deviations in the entropy are found for $T \rightarrow 0$.

To investigate systematically, below which temperature the approximate thermodynamics becomes significantly wrong, we define the temperature T^{dev} , at which the relative deviation $\Delta S/S$ exceeds 10%. It is displayed in Fig. 5.17b as a function of $\delta^2 = (1 - n)^2$. In addition, the temperature T^{neg} is shown which is defined as the temperature where the entropy of the toy model becomes negative. The temperatures T^{dev} and T^{neg} characterize the limit of applicability of the approximate thermodynamics.

The two temperatures T^{dev} and T^{neg} are compared in Fig. 5.17b to the temperature T^{clas} which results from equating the thermal de Broglie wave length

$$\lambda_T = \hbar \sqrt{\frac{2\pi}{mk_B T}} \quad (5.4.75)$$

to the average distance $1/\delta$ between two hole excitations h . The inverse mass $1/m$ is given by $2t$ which is the value of the second derivative at the band minimum. The excellent agreement in the proportionality $T \propto \delta^2$ and the very good agreement of T^{clas} and T^{dev} clearly show that the approximate thermodynamics is a classical treatment, which is valid as long as the gas of excitations is dilute enough. This argument quantifies the limitations of the approximate thermodynamics that has been introduced in Sec. 5.3.1. For very low temperatures the results become unphysical. On the other hand, we have shown that the results obtained for intermediate and high temperatures agree very well with the exact behavior in the TG regime.

5.4.4. CUT treatment

We have already learned that the temperature of the bosons in the optical lattice depends strongly on the regime of the system (Mott insulator or TG regime). The crucial point is whether the energetically low-lying states realize the initially present entropy or not. In the following, we investigate the entropy at finite t/U for the effective model obtained by the CUT calculation and evaluated at finite temperatures by the approximate statistics for hard-core bosons.

The CUT has been used in Sec. 5.1.2 to derive an effective quasiparticle conserving model for the bosonic Hubbard model. The focus of this chapter is on entropy properties calculated using the CUT results. In Sec. 5.3.1 an approximate formalism has been introduced to describe the hard-core bosons at finite temperature. The formulae obtained from this approximate formalism are now evaluated and discussed. The entropy per particle $S/N = -\partial f/\partial T/n$ has been defined

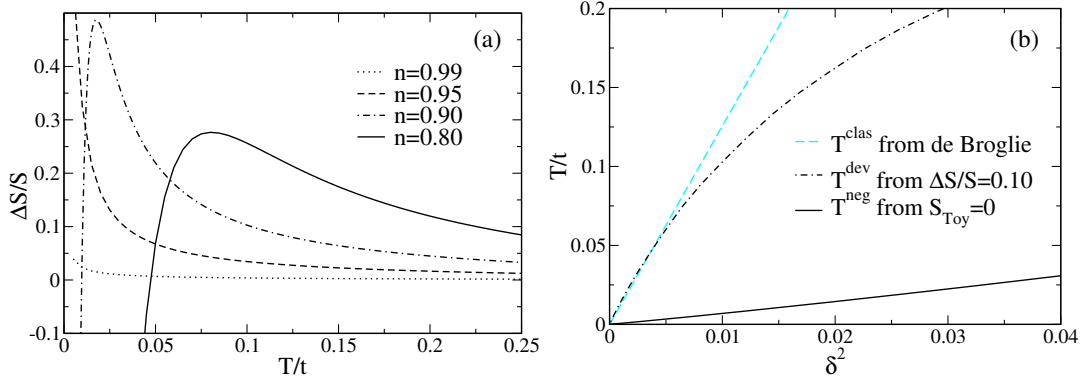


Fig. 5.17: (a) Relative deviation $\frac{\Delta S}{S} = (S_{\text{Toy}} - S_{\text{TG}})/S_{\text{TG}}$ of the entropy of the toy-model from the TG result. (b) Temperature for which deviations become large plotted against $\delta^2 = (1 - n)^2$. For explanation, see text.

in Eq. (5.4.63). The free energy is given by Eq. (5.3.51). The entropy per particle is shown in Fig. 5.18 for three values of t/U and for fillings $n = 1$ and $n = 0.9$. The experimental value of t/U is ≈ 0.013 . The entropy does not change significantly for the values of t/U that are shown because all of them are still deep in the Mott insulating phase. The entropy per particle before loading is $\{0.09; 0.18; 0.36\}$ for condensate fractions $f_0 = \{0.95; 0.9; 0.8\}$, respectively. These values are included as horizontal lines in Fig. 5.18.

As the entropy is conserved, the condensate fraction before loading determines the temperature after loading. For hopping parameter $t/U = 0.02$ the temperatures are $T/U = \{0.12; 0.16; 0.27\}$ for $f_0 = \{0.95; 0.9; 0.8\}$. This is very much in the range of temperatures that were found by the analysis of spectral weights in the preceding section. This seemingly large value for the temperature is needed because the groundstate of the Mott-insulating phase at zero doping is unique and separated by a large gap from the first excited states. The gap is of the order of U for small t/U . The entropy has to be produced by the excited states which have an energy of $\approx U$. This is only possible if also the temperature is of the order of U . The temperature determined from the spectroscopic experiment is $T \approx U/3$. This is higher than the temperature estimated from the entropy. Possible reasons for this deviation are discussed in the next section, Sec. 5.5. In a recent publication *A. M. Rey et al.* studied the change of temperature during the loading [175]. Assuming the conservation of entropy they find results for the temperature in agreement with the results of this thesis. The authors point out that the superfluid-like component that is present in finite traps could allow for lower final temperatures.

The CUT calculation yields also results for the TG regime. In the limit of small t/U the transformation is done without problems. The results for the Mott phase are obtained for commensurate filling $n = 1$. Other fillings can be achieved by tuning the chemical potential μ in Eq. (5.3.49) such that the appropriate numbers of holes and particles are excited. Then, the entropy is calculated with Eq. (5.4.63). The CUT results are calculated using the reference state

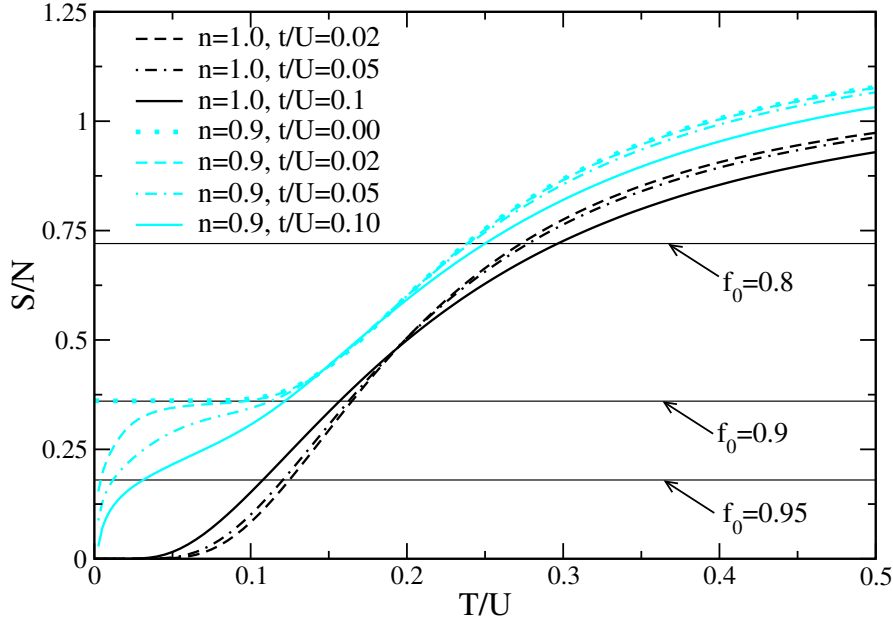


Fig. 5.18: Entropy per particle as function of temperature for $t/U = \{0.00, 0.02, 0.05, 0.1\}$ and filling $n = \{1.0, 0.9\}$. In addition the value for the entropy per particle of the three-dimensional harmonic oscillator with condensate fractions $f_0 = \{0.8, 0.9, 0.95\}$ is given.

in Eq. (5.1.3). Doping is included on the level of the approximated thermodynamics.

Results for filling $n = 0.9$ are shown in Fig. 5.18 as gray(cyan) curves. In this figure the temperature is given in units of U . Clearly several differences from the $n = 1$ result can be identified. At finite doping and zero hopping the entropy has a plateau at low temperatures. The reason for this behavior is the degeneracy of the groundstate. This degeneracy stems from the different possibilities to distribute N atoms on L lattice sites. After the plateau the entropy increases with temperature and saturates at high temperatures. The fact that the plateau value is the same as the entropy for condensate fraction $f_0 = 0.9$ is purely coincidental. At finite doping and small values of t/U remnants of this plateau can still be seen. But, the finite dispersion leads to a unique groundstate. The groundstate degeneracy is lifted and therefore the entropy goes to zero for $T/U \rightarrow 0$.

Next, we consider again the temperature realized after the loading of the atoms into the lattice. The conservation of entropy determines this temperature. It can change dramatically with doping. If the entropy before the loading reaches a value close to the plateau value, the realized temperature is shifted to significantly lower values. Such a situation can be seen in Fig. 5.18 for condensate fraction $f_0 = 0.9$ and filling $n = 0.9$. The temperature after the loading decreases from a value of the order of U to a value of the order of t . This is the mechanism which is most probably observed in the experiment in Ref. [146].

The results in the TG regime are now further analyzed. In Figure 5.19 the results for the

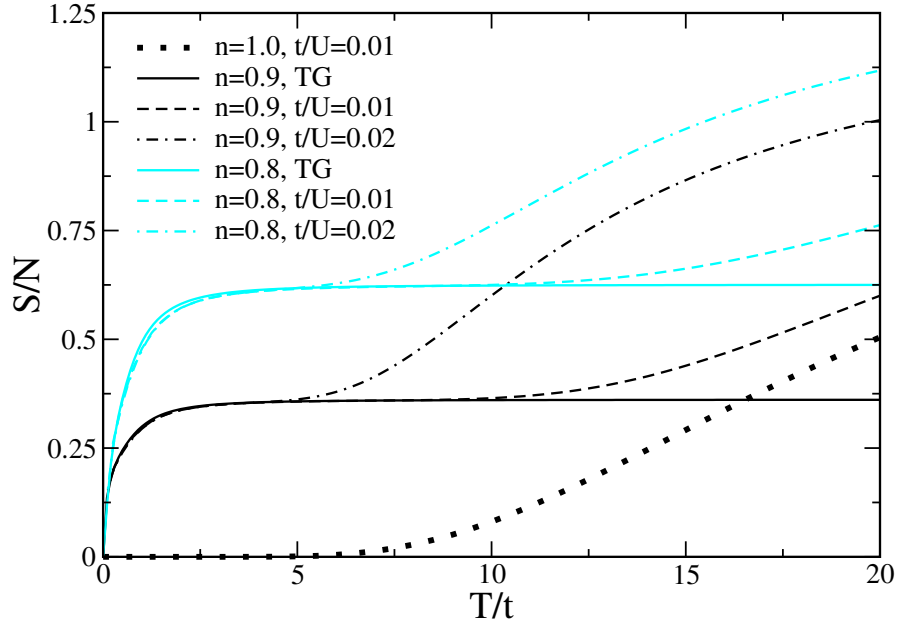


Fig. 5.19: Entropy per particle for $t/U = \{0.00, 0.02, 0.05, 0.1\}$ and filling $n = \{1.0, 0.9, 0.8\}$. The results for the TG regime are included for comparison. The temperature is given in units of t .

entropy per particle from the CUT are compared with the free fermion results. The temperature T is given in units of t in this figure. The figure shows results for $t/U = 0.01$ and $t/U = 0.02$. This translates into a parameter $\gamma = U/t$ where the TG gas is realized [146, 176]. The thick dotted curve shows the entropy per particle for $t/U = 0.01$ for filling $n = 1$. The increase of entropy with temperature is much slower for $n = 1$ than for fillings $n = 0.9$ (black curves) and $n = 0.8$ (gray/cyan curves). At incommensurate filling the possible distributions of the particles introduce additional entropy. For filling $n = 0.9$ surprisingly good agreement is found for low temperatures. The CUT results reproduce nicely the entropy in the TG regime. Good agreement is found up to temperatures of the order of $T/t \approx 10$. Here, the TG result has already saturated at its high temperature limit. On the other hand the CUT results start to feel the presence of the additional Hubbard bands. Therefore, they deviate from the TG result. A temperature of, e. g., $10t$ corresponds to $T/U = 0.1$ for $t/U = 0.01$ but to $T/U = 0.2$ for $t/U = 0.02$. This is the reason why the results for $t/U = 0.02$ show deviations already for $T/t \approx 5$. A similar behavior can be seen for filling $n = 0.8$. For this filling the approximate treatment of doping shows up in small deviations also for low temperatures.

The CUT results reproduce what we found for the TG in Sec. 5.4.2. The conclusions of that section also apply to the CUT calculation. In particular, from the conservation of entropy we find again temperatures that are of the size of the hopping parameter t . Using self-similar CUTs in real space we have obtained results which are valid for the TG as well as for the Mott-

insulating regime. A unifying description of the thermodynamics of the one-dimensional Bose gas is achieved.

5.5. Discussion

The results of this chapter show that it is realistic to find temperatures of the order of the microscopic couplings in atomic Bose gases loaded into optical lattices. This has not been expected. Therefore, we want to recall the conditions under which this result is found.

At first, there are approximations within the calculation. The local Hilbert space has been restricted to four states. In Refs. [160–162] it has been shown that this approximation is sufficient to describe the system. In addition, the truncation of the Hamiltonian and the observable are possible sources of inaccuracies. However, the results for the Hamiltonian in Fig. 5.5 and Fig. 5.6, and the observable, Fig. 5.12 and Fig. 5.13, show that the results do not depend significantly on the truncation. The approximate thermodynamics is tested using the exact results for the TG regime. While there are deviations for very low temperatures the approximate thermodynamics yields good results for the temperatures that are of interest in the present discussion.

The conservation of entropy enforces a sizeable temperature both in the Tonks-Girardeau and in the Mott-Hubbard regime. We found a physically relative simple and consistent picture by more or less purely thermodynamic considerations. The temperature in the undoped Mott insulator is of the order U . Here, the groundstate is a single state and it can not carry any entropy. The initially present entropy has to be distributed over excited states which demands a large temperature of the order of the gap. This is different when studying the doped Mott insulator. In this case the finite amount of holes or particles to be distributed in the groundstate contains a finite amount of entropy. At a certain doping level nearly the whole entropy that is present before the loading process is realized by the groundstate subspace and only a temperature of the order of t is realized.

From this perspective the temperature found from the calculation of the ratio of spectral weights S_2/S_1 at $2U$ and U is very plausible. It gives a natural explanation of the experimental results found in Ref. [17]. It also explains why recent QMC results for the dynamic structure factor do not find appreciable weight at $2U$ (Ref. [170]). At temperatures at which the QMC calculation in Ref. [170] is done there is only little weight at $2U$, as can be seen Fig. 5.18. Our result in Fig. 5.18 show also that more weight at $2U$ and a larger ratio S_2/S_1 is found at temperatures $T \approx U/3$.

In the experiment the atoms are confined by a harmonic trapping potential. It is beyond the scope of the present work to treat the combined effect of the optical lattice and the inhomogeneity of the trap. The trapping potential has definitely some influence on the physical behavior. For example, the system does not undergo true phase transitions since it is finite [169]. In Sec. 5.3 we have argued that it is not plausible that the inhomogeneity is the source of the large spectral weight at high energies. The inhomogeneity indeed introduces steps in the local density of atoms [169, 170]. In the transition regions the occupation changes from one integer value to

the next. This gives rise to excitations with energy $2U$. However, as we are deep in the Mott-insulating regime the transition regions are very small. It is unlikely that they dominate the spectroscopic response of the whole system.

Another aspect in the analysis of the Bragg spectroscopy in Ref. [17] is that the system was shaken fairly strongly. Though it is ascertained that the experiment has been conducted in the linear regime it might be that the system is heated by the probe procedure. This could be the reason why the adiabatic estimate results in $T \approx U/6$ while the spectroscopic estimate implies $T \approx U/3$.

In view of its pronounced T dependence, see Fig. 5.13, the relative spectral weight in combination with spectroscopic measurements of good quality can be used as a thermometer for bosons in optical lattices. In this way the temperature of these artificial condensed-matter systems could be determined reliably. Therefore, Figure 5.13 provides the calibration of the thermometer to measure the temperature in Bose gases in the Mott-Hubbard regime.

5.6. Summary and outlook

In this chapter the method of self-similar CUTs in real space has been applied to the problem of bosonic atoms in an optical lattice. The Mott insulating state with filling one is used as reference state. The excitations around this state are successfully described by hard-core quasiparticles.

Methodically, this chapter is an application of knowledge gathered in the preceding sections. The range of small t/U which is relevant for the experiment is safely treated by the CUTs. For larger truncations the residual off-diagonality displayed non-monotonic behavior. The flow is stopped in the first minimum of the residual off-diagonality and the corresponding coefficients are used in the effective Hamiltonian. This is a good approximation since off-diagonal elements are already very small at this value of the flow parameter. The effective Hamiltonian is already sufficiently diagonalized. The observable is transformed with the same transformation as the Hamiltonian. Both, the Hamiltonian and the observable exhibit good convergence with truncation. Overlapping continua have been shown to generically introduce problems in the CUT treatment. These problems are less harmful in the analysis of the bosonic Hubbard model as the focus is only on small values of t/U .

The results are extended to finite temperature and non-commensurate filling by an approximate treatment of the thermodynamics of the hard-core quasiparticles. The approximate thermodynamics is tested by comparison with exact results for the TG regime. For very small temperatures, the approximation leads to unphysical behavior. However, for the temperatures of interest to explain the experiment the approximate treatment of the thermodynamics yields reliable results.

Results are obtained for the dispersion and the spectral weight of the observable describing the experiment. The phase diagram is in good agreement with high accuracy numerical treatments. The location of the Kosterlitz-Thouless phase transition is underestimated by about 20%. The experimental finding of large spectral weight at energy $2U$ is explained by a temperature of the

order of $U/3$. These findings are supported by calculations for the entropy of one-dimensional bosonic systems. For the Mott-Hubbard regime the conservation of entropy leads to an estimated temperature of $\approx U/6$. The temperature found in the analysis of the spectral weight is higher than the one found from entropy considerations. The reason could be that the spectroscopic experiment modulates the lattice quite strongly. In the TG regime temperatures of the size of the hopping parameter are found in accordance with experiment.

Using the method of CUTs we find a unifying picture of the temperatures found in one-dimensional Bose gases in the TG and the Mott-insulating regime. Both, the analysis of spectral weights and of entropy properties give rise to a sizeable temperature that is of the order of the microscopic parameters.

Further promising investigations are possible in this field of research. At first one could resolve the energy and momentum dependence of the dynamic structure factor $S(k, \omega)$. Also other observables and thus other experimental setups can be studied. An example is the density operator \hat{n} . Yet, the operator \hat{n} yields no response at zero momentum; it gives a finite signal only at non-zero momentum. The treatment of finite doping could be improved by changing the CUT to use a doping dependent reference ensemble. However, this is left for future research.

6. Summary

The present thesis presents the method of self-similar continuous unitary transformations (CUTs) in real space. In this summary we concentrate on conceptual aspects because the content of each chapter has already been summarized on its own at the end of the chapter.

In this work we develop a novel realization of the method of CUTs. CUTs are in general used to derive an effective Hamiltonian systematically. In this thesis the CUT method is used in a self-similar fashion, i.e. the operators retained in the construction of the flow equation are kept according to a truncation criterion. The renormalization of the coefficients is determined by the flow equation. The truncation scheme is based on the locality of operators written in their second-quantized form. To this end, a reference ensemble is defined. All operators are normal-ordered with respect to this reference ensemble. The extension of an operator is the maximal distance of two local operators.

The choice of the reference ensemble is an important step in the calculation. Quasiparticles are deviations from the reference ensemble. Therefore, the choice of the reference ensemble also determines the quasiparticles. A successful description of a physical system often relies on the proper choice of the quasiparticles. The majority of results presented in the present work are found using the MKU generator. It has the advantageous property to conserve block-band diagonality within the flow. The effective Hamiltonian is block-diagonal. Thus, the subsectors with different numbers of quasiparticles are separated. This enables the analysis of the effective model using the quasiparticle number as a conserved quantity.

In Chapter 2 we present a detailed description how to implement self-similar CUTs in real space on a computer. Special emphasis is put on how to realize an efficient implementation and how to take advantage of symmetry properties.

The two-dimensional Hubbard model is the first model to which the self-similar CUT in real space is applied in this thesis. In Chap. 3 we derive an effective model, namely a generalized t - J -model, for the Hubbard model that does not change the number of doubly occupied sites. For half-filling the effective model reduces to a pure spin model. However, our derivation of the effective model also takes into account the motion and the interaction of charges.

The self-similar CUT gives quantitatively reliable parameters of the effective model in a wide range of t/U . The results are convergent in the range of applicability while the series given by perturbation theory is less stable. This shows that the self-similar approach can be used to determine the effective model reliably in a case where it is hard to find quantitative results by perturbation theory. The transformation breaks down if the bandwidth of the system becomes too large. Then, the continua of different quasiparticle number overlap. This hinders the ordering

of the energy of the states according to their quasiparticle number. It is possible to analyze at which point the transformation breaks down.

The quasiparticle concept is further exploited in Chap. 4 that deals with one-dimensional spin systems. The CUT enables the calculation of the energy properties in the one- and two-triplon sector of the spin ladder. In the two-triplon sector, also the energy of bound states is determined. For the spin ladder the transformation is only possible for a certain parameter regime. If the leg coupling is equal to the rung coupling we observe non-monotonic behavior in the residual off-diagonality. Further analysis shows that the convergence problems are related to overlapping multi-triplon continua. For the spin ladder the two- and four-triplon continua have considerable overlap. The degeneracy or nearly degeneracy of levels of different quasiparticle number is problematic because the MKU generator sorts the energy of the levels according to their quasiparticle number. Therefore, not only a vanishing one-particle energy will complicate the transformation. One has to pay attention to the energy situation in higher particle channels as well.

For the spin chain we calculate the one-triplon dispersion and the spectral weights of the observable S_z . For the calculation of spectral weights we have used a passive transformation that first eliminates the unproblematic blocks using a MKU generator and in a second step eliminates the remaining block using a Wegner generator. The distribution of spectral weight over channels with different quasiparticle number deviates from the result of a perturbative CUT. Because the transformation that achieves block-diagonality in the quasiparticle number is not unique, the CUT finds different spectral weights for different transformations. The issue of overlapping continua is found to play a role also in this case. In the presence of overlapping continua lifetime effects can lead to a redistribution of spectral weight. For the spin chain substantial redistribution of spectral weight is observed between the two- and three-triplon weights.

The spin systems have been studied extensively within the perturbative approach to CUTs [30, 41]. The PCUT approach combined with extrapolation techniques yields results for parameters that are not accessible within the present self-similar CUT. The reason lies in the problem of overlapping continua. The PCUT is not so much affected by the energetic vicinity of different quasiparticles sectors. The expansion is formally done around a point where there are no overlapping continua. The self-similar approach is more sensitive to these problems. The higher sensitivity is also an advantage. The non-analytic behavior for a certain parameter regime can be captured in a self-similar approach whereas it cannot be seen in a perturbative treatment.

In Sec. 4.1.5 we point out some means how to deal with the convergence problems. The remaining off-diagonal elements can be treated by perturbation theory or within a numerical scheme such as Lanczos diagonalization. Another way is to account for the problematic blocks in a passive transformation as described in Sec. 4.2. In a second step we treat the remaining block using a more robust Wegner generator.

In Chap. 5 it has been possible to make direct contact to experimental results that have been found for atom gases confined in optical lattices. The system is described by a bosonic

Hubbard model. The spectral weight determined in a spectroscopic experiment is explained using the self-similar CUT. We find that the temperature in the trapped Bose system is of the order of the microscopic parameters. The convergence issue is circumvented in this problem by stopping the flow at a minimum of the residual off-diagonality. The smallness of the remaining off-diagonal coefficients justifies this procedure. The findings for the temperature in the atom trap is corroborated by thermodynamic considerations.

In conclusion, the method of self-similar CUTs in real space developed in this thesis has been proven to yield new and reliable results. Our applications have focused around strongly correlated systems in low dimensions. However, we stress that the application of the method is not restricted to such systems. Whenever a problem can be phrased within a local Hamiltonian, it can be rewarding to tackle the problem by mapping it first onto an effective Hamiltonian using a self-similar CUT approach in real space.

6.1. Outlook

The topics addressed in the present thesis can be investigated further in many ways. Here, we want to point out only a few. It is promising to study the derivation of the effective model for the Hubbard model away from half filling. To this end one has to modify the reference ensemble as to represent the finite doping level. Studies in this direction are on the way [177].

For the bosonic Hubbard model the calculation of spectral densities can resolve the full frequency- and momentum-dependence of the spectroscopic experiments. The coefficients of the effective observable provide all the necessary information to do so. An experimental check of these results might come into range soon in view of the rapid experimental developments in this field.

Another issue to be studied further is the problem of overlapping continua. In the present thesis we have only performed first investigations of ways to circumvent these problems by applying a passive transformation. Further work in this direction could significantly enhance the set of problems to which the self-similar CUT scheme is applicable.

A. The Lanczos technique

The Lanczos technique is an efficient method to calculate numerically physical quantities such as the ground state energy [77, 78]. It is now commonly used in condensed matter physics and it will only be described briefly in the present appendix. The Lanczos technique can be implemented using the Liouville formalism [79]. The problem of a double occupancy moving in a reference ensemble encountered in Chap. 3 is treated using the Liouville formalism. The reference ensemble used in Chap. 3 is characterized by a statistical operator. It is not a single state. One particle electron (hole) excitations are introduced in the reference ensemble by application of a creation (annihilation) operator to this ensemble. Therefore, it is advantageous to analyze the energy of these excitation within the Liouville formalism that is applicable to operators. Since this technique is less common it is briefly presented in this appendix.

The problem under consideration shall be given by its Hamiltonian H . Often a full diagonalization of the Hamiltonian is not feasible even for small finite systems. The Lanczos technique yields numerical results for eigenvalues and correlation functions. It is especially efficient for sparse matrices. The starting point is a trial state

$$|f_0\rangle. \tag{A.1}$$

Then, one generates a set of orthogonal states that are defined as

$$|f_{n+1}\rangle = H|f_n\rangle - a_n|f_n\rangle - b_n^2|f_{n-1}\rangle, \tag{A.2}$$

where the coefficients a_n and b_n are defined through the relations

$$a_n = \frac{\langle f_n|H|f_n\rangle}{\langle f_n|f_n\rangle} \tag{A.3}$$

$$b_{n+1}^2 = \frac{\langle f_{n+1}|f_{n+1}\rangle}{\langle f_n|f_n\rangle} \tag{A.4}$$

$$b_0 = 0. \tag{A.5}$$

The states $\{|f_0\rangle, H|f_0\rangle, H^2|f_0\rangle, \dots\}$ span a subspace of the full Hilbert space. This subspace is enlarged by successive application of H . The states $|f_n\rangle$ are mutually orthogonal because of the implicit Gram-Schmidt orthogonalization in Eq. (A.2). In the basis $\{|f_n\rangle\}$ the Hamiltonian is a tridiagonal matrix where the a_n are the diagonal matrix elements and the b_n are the elements on the secondary diagonal.

A.1. Liouville formulation of the Lanczos technique

In Chapter 3 the Liouville formalism is appropriate since the problem does not involve simple states in a Hilbert space. The reference ensemble is a statistical mixture of many states. The plain Lanczos formalism presented above is not applicable in this case.

The operators \mathcal{O}_i correspond to the vectors $|f_n\rangle$ in the Lanczos technique. The aim is to follow the dynamics of the excitations induced by \mathcal{O}_i . For our application this excitation is a single double occupancy with momentum \mathbf{k} moving in a paramagnetic spin background. The starting operator is

$$\mathcal{O}_0 := \frac{1}{\sqrt{N}} \sum_{\mathbf{r}} e^{i\mathbf{k}\mathbf{r}} n_{\mathbf{r},\downarrow} c_{\mathbf{r},\uparrow}^\dagger, \quad (\text{A.6})$$

where the number of sites is denoted by N and the sum extends over the whole lattice. The effective Hamiltonian acts by commutation as a super-operator on the operators. This defines the action of the Liouville operator

$$\mathcal{L} := [H, \cdot]. \quad (\text{A.7})$$

A “scalar product” is defined as

$$(A|B) = \text{Tr}(A^\dagger B \hat{\rho}_0). \quad (\text{A.8})$$

The paramagnetic reference ensemble is built into this scalar product by the statistical operator $\hat{\rho}_0$. The operator $\hat{\rho}_0$ is defined in Eq. (3.2.6). Note that this scalar product is only positive semi-definite. There are operators whose norm vanishes. An example for an operator with vanishing norm is $\bar{n}_j c_{i,\uparrow}^\dagger = (n_{j,\uparrow} + n_{j,\downarrow} - \mathbf{1}_j) c_{i,\uparrow}^\dagger$, where we have used the notation introduced in Tab. 3.1 of Sec. 3.2.1. The operator \bar{n}_j has non-zero matrix elements only with the empty or doubly occupied local states. It annihilates the singly occupied states in the local basis. Therefore it annihilates the reference ensemble and thus its norm is zero. With these definitions the modified equations read

$$\mathcal{O}_{n+1} = \mathcal{L}\mathcal{O}_n - a_n \mathcal{O}_n - b_n^2 \mathcal{O}_{n-1}, \quad (\text{A.9})$$

and

$$a_n = \frac{(\mathcal{O}_n | \mathcal{L}\mathcal{O}_n)}{(\mathcal{O}_n | \mathcal{O}_n)}, \quad (\text{A.10a})$$

$$b_{n+1}^2 = \frac{(\mathcal{O}_{n+1} | \mathcal{O}_{n+1})}{(\mathcal{O}_n | \mathcal{O}_n)}, \quad b_0 = 0. \quad (\text{A.10b})$$

They replace A.2 through A.4 of the conventional Lanczos technique. In this basis the Liouville operator is again a tridiagonal matrix. Note that the application of \mathcal{L} derived from the effective Hamiltonian *after* the CUT does not change the number of DOs. The application of the Liouville operator shifts the DO and changes the spin background. The iteratively built basis $\{\mathcal{O}_n\}$ describes a single DO (charge excitation) at momentum \mathbf{k} including its magnetic dressing.

B. Entropy of bosons in a three-dimensional harmonic oscillator and in the Tonks-Girardeau regime

In this appendix the formulae for the entropy of bosons in a harmonic trap and for the free fermi gas are derived. The hamiltonian for bosons in a harmonic trap reads ($\hbar = 1$)

$$H = \omega_0 \sum_{j=1}^d a_j^\dagger a_j. \quad (\text{B.1})$$

The situation with many bosons loaded in the harmonic trap is considered. The energy ω_0 is small. Therefore, sums over multiples of ω_0 can be rewritten as integrals. The groundstate is macroscopically occupied with a fraction

$$f_0 = \frac{N_0}{N}, \quad (\text{B.2})$$

where N is the total number of particles and N_0 is the number of bosons in the condensate. The total number of particles is calculated to be

$$N = N_0 + \sum_{m=1}^{\infty} n_B(m\omega_0)D(m\omega_0) \quad (\text{B.3a})$$

$$= Nf_0 + \int_0^{\infty} n_B(\omega)D(\omega)d\omega \quad (\text{B.3b})$$

with use of the density of states $D(\omega)$ and the boson occupation number $n_B(\omega) = \frac{1}{e^{\beta\omega} - 1}$. The density of states counts the number of possible states at a given energy. To realize the energy $m\omega_0$ one has to distribute m energy quanta in d oscillators. The number of possibilities is (consider all arrangements of m bosons and $d - 1$ walls between them)

$$D(m\omega_0) = \binom{m+d-1}{d-1} = \frac{(m+d-1)(m+d-2)\cdots(m+1)}{(d-1)!} \quad (\text{B.4})$$

which yields

$$D(\omega) = \frac{1}{(d-1)!} \left(\frac{\omega}{\omega_0}\right)^{d-1} \quad (\text{B.5})$$

in leading order in $m = \omega/\omega_0$ ($m \gg 1$). From now on, the special case of $d = 3$ will be considered. Equation (B.3b) is rewritten with the previous expression for $D(\omega)$ as

$$N = Nf_0 + \frac{T^3}{2} \int_0^{\infty} \frac{x^2}{e^x - 1} dx = Nf_0 + T^3 \zeta(3), \quad (\text{B.6})$$

where $x = \beta\omega$ and $\zeta(z)$ is the Riemann ζ -function. The partition function of a single boson is

$$Z = \sum_{n=0}^{\infty} e^{-n\beta\epsilon} = \frac{1}{1 - e^{-\beta\epsilon}} \quad (\text{B.7})$$

and the entropy

$$S = -\langle \ln \rho \rangle = -\sum_{n=0}^{\infty} p_n \ln p_n = -\sum_{n=0}^{\infty} \frac{e^{-n\beta\epsilon}}{Z} (-n\beta\epsilon - \ln Z), \quad (\text{B.8})$$

where ρ is the density operator and the p_n the probabilities to find the n -th state. The entropy can be rewritten as

$$S = -\ln(1 - e^{-\beta\epsilon}) + \beta\epsilon n_B(\epsilon) \quad (\text{B.9})$$

such that the total entropy is

$$S_{\text{tot}} = S_{\text{cond}} + \int_0^{\infty} S(\epsilon) = \frac{2\pi^4}{45} T^3, \quad (\text{B.10})$$

where we have used integration by parts and the fact that the condensate is one macroscopic quantum state and therefore has vanishing entropy, $S_{\text{cond}} = 0$. In a last step the entropy per particle is calculated with Eq. (B.6) to be

$$\frac{S}{N} = \frac{2\pi^4}{45\zeta(3)} (1 - f_0) \approx 3.60(1 - f_0), \quad (\text{B.11})$$

which is the formula used in Sec. 5.3.2 as Eq. (5.4.62).

Entropy in the Tonks-Girardeau regime

In the discussion in Sec. 5.4.2 also the question of the temperature in the Tonks-Girardeau regime is adressed. This regime is the limit of infinite U . Only empty and singly occupied sites are present. In one dimension this problem can be mapped onto the free fermion case [150, 173, 174]. To know which temperature is realized after adiabatic loading into the Tonks-Girardeau regime one needs to know the entropy of the free fermion gas. The formulae for the free Fermi gas are given here. In one dimension the dispersion of fermions with only nearest-neighbor hopping is

$$\epsilon(k) = -2t \cos(k). \quad (\text{B.12})$$

The free energy per site is

$$f = \frac{F}{L} = -\frac{k_B T}{L} \sum_k \ln(1 + e^{-\beta\epsilon(k)}) \quad (\text{B.13})$$

$$= -\frac{k_B T}{2\pi} \int_{-\pi}^{\pi} \ln(1 + e^{-\beta\epsilon(k)}) dk, \quad (\text{B.14})$$

where L is the number of sites. For N particles on L sites the filling is $n = N/L$. The entropy per particle is calculated as the derivative of the free energy with respect to temperature

$$\frac{S}{N} = \frac{1}{n} \frac{S}{L} = -\frac{1}{n} \frac{\partial f}{\partial T} \quad (\text{B.15})$$

$$= \frac{1}{\pi} \int_{-\pi}^{\pi} \left(\ln(1 + e^{-\beta\epsilon(k)}) + \frac{\epsilon(k)}{T(1 + e^{-\beta\epsilon(k)})} \right) dk. \quad (\text{B.16})$$

This is the formula used to calculate the results for the Tonks-Girardeau regime shown in Sec. 5.4.2. In the limit of high temperatures the entropy per site is

$$\frac{S}{L} = -n \log(n) - (1 - n) \log(1 - n), \quad (\text{B.17})$$

which is just the entropy of one state with occupation probability n . The entropy per particle is accordingly

$$\frac{S}{N} = -\log(n) - \left(\frac{1}{n} - 1\right) \log(1 - n). \quad (\text{B.18})$$

This formula explains the saturation value of the entropy shown in Fig. 5.15.

Bibliography

- [1] N. W. Ashcroft and N. D. Mermin, *Solid State Physics*, Saunders College Publishing, 1976.
- [2] E. H. Lieb and F. Y. Wu, *Phys. Rev. Lett.* **20**, 1445 (1968).
- [3] A. Georges, G. Kotliar, W. Krauth, and M. J. Rozenberg, *Rev. Mod. Phys.* **68**, 13 (1996).
- [4] J. W. Negele and H. Orland, *Quantum Many Particle Systems*, Reading: Addison-Wesley, 1988.
- [5] K. G. Wilson, *Rev. Mod. Phys.* **47**, 773 (1975).
- [6] R. Shankar, *Rev. Mod. Phys.* **66**, 129 (1994).
- [7] D. Zanchi and H. J. Schulz, *Phys. Rev. B* **61**, 13609 (2000).
- [8] C. J. Halboth and W. Metzner, *Phys. Rev. B* **61**, 7364 (2000).
- [9] M. Salmhofer and C. Honerkamp, *Prog. Theor. Phys.* **105**, 1 (2001).
- [10] M. Salmhofer, C. Honerkamp, W. Metzner, and O. Lauscher, *cond-mat/0409725* (2004).
- [11] F. J. Wegner, *Ann. Physik* **3**, 77 (1994).
- [12] A. Mielke, *Eur. Phys. J. B* **5**, 605 (1998).
- [13] C. Knetter and G. S. Uhrig, *Eur. Phys. J. B* **13**, 209 (2000).
- [14] F. J. Wegner, *Physics Reports* **348**, 77 (2001).
- [15] F. Wegner, *cond-mat/0511660* (2005).
- [16] M. Greiner, O. Mandel, T. Esslinger, T. W. Hänsch, and I. Bloch, *Nature* **415**, 39 (2002).
- [17] T. Stöferle, H. Moritz, C. Schori, M. Köhl, and T. Esslinger, *Phys. Rev. Lett.* **92**, 130403 (2004).
- [18] S. D. Glazek and K. G. Wilson, *Phys. Rev. D* **48**, 5863 (1993).
- [19] S. D. Glazek and K. G. Wilson, *Phys. Rev. D* **49**, 4214 (1994).

- [20] H. Fröhlich, Proc. Roy. Soc. A **215**, 291 (1952).
- [21] J. R. Schrieffer and P. A. Wolff, Phys. Rev. **149**, 491 (1966).
- [22] A. B. Harris and R. V. Lange, Phys. Rev. **157**, 295 (1967).
- [23] M. Takahashi, J. Phys. C **10**, 1289 (1977).
- [24] A. H. MacDonald, S. M. Girvin, and D. Yoshioka, Phys. Rev. B **37**, 9753 (1988).
- [25] P. Lenz and F. Wegner, Nucl. Phys. B **482** [FS], 693 (1996).
- [26] J. Stein, J. Stat. Phys. **88**, 487 (1997).
- [27] K. W. Becker, A. Hübsch, and T. Sommer, Phys. Rev. B **66**, 235115 (2002).
- [28] A. Hübsch and K. W. Becker, Eur. Phys. J. B **33**, 391 (2003).
- [29] C. Knetter, K. P. Schmidt, and G. S. Uhrig, J. Phys.: Condens. Matter **36**, 7889 (2003).
- [30] C. Knetter, K. P. Schmidt, and G. S. Uhrig, Eur. Phys. J. B **36**, 525 (2004).
- [31] S. Dusuel and G. S. Uhrig, Journal of Physics A: Math. Gen. **37**, 9275 (2004).
- [32] S. Dusuel and J. Vidal, Phys. Rev. B **71**, 224420 (2005).
- [33] S. Dusuel, J. Vidal, J. M. Arias, J. Dukelsky, and J. E. Garcia-Ramos, Phys. Rev. C **72**, 064332 (2005).
- [34] C. P. Heidbrink and G. S. Uhrig, Phys. Rev. Lett. **88**, 146401 (2002).
- [35] C. P. Heidbrink and G. S. Uhrig, Eur. Phys. J. B **30**, 443 (2002).
- [36] S. K. Kehrein and A. Mielke, J. Phys. A: Math. Gen. **27**, 4259 (1994).
- [37] S. Kehrein, Phys. Rev. Lett. **83**, 4914 (1999).
- [38] S. Kehrein, Nucl. Phys. B **592**, 512 (2001).
- [39] I. Grote, E. Körding, and F. Wegner, J. Low Temp. Phys. **126**, 1385 (2002).
- [40] V. Hankevych and F. Wegner, Eur. Phys. J. B **31**, 497 (2003).
- [41] K. P. Schmidt and G. S. Uhrig, Mod. Phys. Lett. B **19**, 51179 (2005).
- [42] K. P. Schmidt, C. Knetter, and G. S. Uhrig, Phys. Rev. B **69**, 104417 (2004).
- [43] S. Kehrein, cond-mat/0410341 (2004).
- [44] S. Kehrein and A. Mielke, Ann. d. Physik **252**, 1 (1996).
- [45] T. Stauber and A. Mielke, Phys. Lett. A **219**, 313 (1996).

- [46] T. Stauber and A. Mielke, Phys. Lett. A **305**, 275 (2002).
- [47] C. Knetter, K. P. Schmidt, M. Grüninger, and G. S. Uhrig, Phys. Rev. Lett. **87**, 167204 (2001).
- [48] K. P. Schmidt, C. Knetter, and G. S. Uhrig, Europhys. Lett. **56**, 877 (2001).
- [49] S. Kirschner, *diploma thesis*, Univ. of Cologne, 2004.
- [50] A. Hübsch and K. W. Becker, Eur. Phys. J. B **33**, 391 (2003).
- [51] W. H. Press, B. P. Flannery, S. A. Teukolsky, and W. T. Vetterling, *Numerical Recipes in C*, Cambridge University Press, 1993.
- [52] Further references on OpenMP can be found at <http://www.openmp.org/>.
- [53] J. Hubbard, Proc. Roy. Soc. London Ser. A **276**, 238 (1963).
- [54] J. Hubbard, Proc. Roy. Soc. London **281**, 401 (1964).
- [55] M. C. Gutzwiller, Phys. Rev. Lett. **10**, 159 (1963).
- [56] J. Kanamori, Prog. Theor. Phys. **30**, 275 (1963).
- [57] F. Gebhard, *The Mott Metal-Insulator Transition*, volume 137 of *Springer Tracts in Modern Physics*, Springer Verlag, Berlin, 1997.
- [58] M. Imada, A. Fujimori, and Y. Tokura, Rev. Mod. Phys. **70**, 1039 (1998).
- [59] P. W. Anderson, Phys. Rev. **115**, 2 (1959).
- [60] E. Dagotto, Rev. Mod. Phys. **66**, 763 (1994).
- [61] D. J. Klein and W. A. Seitz, Phys. Rev. B **8**, 2236 (1973).
- [62] F. H. L. Essler, H. Frahm, F. Göhmann, A. Klümper, and V. E. Korepin, *The One-Dimensional Hubbard Model*, Cambridge University Press, Cambridge, 2005.
- [63] M. P. Eastwood, F. Gebhard, E. Kalinowski, S. Nishimoto, and R. M. Noack, Eur. Phys. J. B **35**, 155 (2003).
- [64] M. Karski, C. Raas, and G. S. Uhrig, Phys. Rev. B **72**, 113110 (2005).
- [65] R. B. Laughlin, private communication (2003).
- [66] N. D. Mermin and H. Wagner, Phys. Rev. Lett. **17**, 1133 (1966).
- [67] The Hamiltonian Eq. (3.1.1) changes the number of DOs only by a single absolute value, namely 2. So the only difference between the matrix elements $\text{sign}(d_i - d_j)H_{ij}$ and $(d_i - d_j)H_{ij}$ in an eigen basis of \hat{D} is a factor of 2.

- [68] A. Gutmann, Asymptotic analysis of power-series expansions, in *Phase Transition and Critical Phenomena*, edited by C. Domb and J. Leibovitz, volume 13, chapter 1, Academic Press, New York, 1989.
- [69] W. F. Brinkmann and T. M. Rice, *Phys. Rev. B* **2**, 1324 (1970).
- [70] I. M. Lifshitz, *Advan. Phys.* **13**, 483 (1969).
- [71] W. Metzner, P. Schmit, and D. Vollhardt, *Phys. Rev. B* **45**, 2237 (1992).
- [72] P. van Mieghem, *Rev. Mod. Phys.* **64**, 755 (1992).
- [73] E. Müller-Hartmann and C. I. Ventura, *Phys. Rev. B* **50**, 9235 (1994).
- [74] K. A. Hallberg, E. Müller-Hartmann, and C. A. Balseiro, *Phys. Rev. B* **52**, 4396 (1995).
- [75] Q. F. Zhong and S. Sorella, *Phys. Rev. B* **51**, 16135 (1995).
- [76] Q. F. Zhong, S. Sorella, and A. Parola, *Phys. Rev. B* **49**, 6408 (1994).
- [77] D. G. Pettifor and D. L. Weaire, *The Recursion Method and its Applications*, volume 58 of *Springer Series in Solid State Sciences*, Springer Verlag, Berlin, 1985.
- [78] V. S. Viswanath and G. Müller, *The Recursion Method; Application to Many-Body Dynamics*, volume m23 of *Lecture Notes in Physics*, Springer Verlag, Berlin, 1994.
- [79] P. Fulde, *Electron Correlations in Molecules and Solids*, volume 100 of *Solid State Sciences*, Springer Verlag, Berlin, 1993.
- [80] M. Roger and J. M. Delrieu, *Phys. Rev. B* **39**, 2299 (1989).
- [81] H. J. Schmidt and Y. Kuramoto, *Physica* **B163**, 443 (1990).
- [82] J. Lorenzana, J. Eroles, and S. Sorella, *Phys. Rev. Lett.* **83**, 5122 (1999).
- [83] R. Coldea et al., *Phys. Rev. Lett.* **86**, 5377 (2001).
- [84] Y. Mizuno, T. Tohyama, and S. Maekawa, *J. Low Temp. Phys.* **117**, 389 (1999).
- [85] E. Müller-Hartmann and A. Reischl, *Eur. Phys. J. B* **28**, 173 (2002).
- [86] C. Calzado, C. de Graaf, E. Bordas, R. Caballol, and J.-P. Malrieu, *Phys. Rev. B* **67**, 132409 (2003).
- [87] A. A. Katanin and A. P. Kampf, *Phys. Rev. B* **66**, 100403 (2002).
- [88] A. A. Katanin and A. P. Kampf, *Phys. Rev. B* **67**, 100404 (2003).
- [89] G. S. Uhrig, private communication (2003).

- [90] P. Horsch and W. Stephan, *Physica B* **199&200**, 325 (1994).
- [91] L. F. Feiner, J. H. Jefferson, and R. Raimondi, *Phys. Rev. B* **53**, 8751 (1996).
- [92] V. I. Belinicher, A. L. Chernyshev, and V. A. Shubin, *Phys. Rev. B* **54**, 14914 (1996).
- [93] H. Eskes and A. M. Oleś, *Phys. Rev. Lett.* **73**, 1279 (1994).
- [94] H. Eskes, A. M. Oleś, M. B. J. Meinders, and W. Stephan, *Phys. Rev. B* **50**, 17980 (1994).
- [95] S. Nishimoto, F. Gebhard, and E. Jeckelmann, *J. Phys.: Condens. Matter* **16**, 7063 (2004).
- [96] E. Müller-Hartmann, in *Proceedings of the V. Symposium "Physics of Metals"*, edited by E. Talik and J. Szade, Symposium "Physics of Metals", Ustron-Jaszowiec, Poland, page 22, 1991.
- [97] G. S. Uhrig, *Phys. Rev. Lett.* **77**, 3629 (1996).
- [98] E. Müller-Hartmann, *Z. Phys. B* **74**, 507 (1989).
- [99] R. Bulla, T. A. Costi, and D. Vollhardt, *Phys. Rev. B* **64**, 045103 (2001).
- [100] D. J. Garcia, K. Hallberg, and M. J. Rozenberg, *cond-mat/0403169* (2004).
- [101] N. Blümer and E. Kalinowski, *Phys. Rev. B* **71**, 195102 (2004).
- [102] M. S. Windt, *Optical Spectroscopy of Spin Ladders*, PhD thesis, Universität zu Köln, 2002.
- [103] M. Windt et al., *Phys. Rev. Lett.* **87**, 127002 (2001).
- [104] A. Reischl, E. Müller-Hartmann, and G. S. Uhrig, *Phys. Rev. B* **70**, 245124 (2004).
- [105] R. S. Eccleston et al., *Phys. Rev. Lett.* **81**, 1702 (1998).
- [106] S. Brehmer, H. J. Mikeska, M. Müller, N. Nagaosa, and S. Uchida, *Phys. Rev. B* **60**, 329 (1999).
- [107] M. Matsuda, K. Katsumata, R. S. Eccleston, S. Brehmer, and H. J. Mikeska, *J. Appl. Phys.* **87**, 6271 (2000).
- [108] T. S. Nunner, P. Brune, T. Kopp, M. Windt, and M. Grüninger, *Phys. Rev. B* **66**, 180404 (2002).
- [109] A. Gößling et al., *Phys. Rev. B* **67**, 052403 (2003).
- [110] K. P. Schmidt, C. Knetter, M. Grüninger, and G. S. Uhrig, *Phys. Rev. Lett.* **90**, 167201 (2003).
- [111] T. Barnes, E. Dagotto, J. Riera, and E. S. Swanson, *Phys. Rev. B* **47**, 3196 (1993).

-
- [112] D. G. Shelton, A. A. Nersesyan, and A. M. Tsvelik, Phys. Rev. B **53**, 8521 (1996).
- [113] M. Greven, R. J. Birgeneau, and U.-J. Wiese, Phys. Rev. Lett. **77**, 1865 (1996).
- [114] K. P. Schmidt, H. Monien, and G. S. Uhrig, Phys. Rev. B **67**, 184413 (2003).
- [115] A. Läuchli, G. Schmid, and M. Troyer, Phys. Rev. B **67**, 100409(R) (2003).
- [116] K. P. Schmidt, C. Knetter, and G. S. Uhrig, Acta Physica Polonica B **34**, 1481 (2003).
- [117] C. Knetter, K. P. Schmidt, and G. S. Uhrig, J. Phys. A: Math. Gen. **36**, 7889 (2004).
- [118] E. Dagotto and T. M. Rice, Science **271**, 618 (1996).
- [119] R. Eder, Phys. Rev. B **57**, 12832 (1998).
- [120] K. P. Schmidt, *Spectral Properties of Quasi One-dimensional Quantum Antiferromagnets*, PhD thesis, Universität zu Köln, 2004.
- [121] G. S. Uhrig and H. J. Schulz, Phys. Rev. B **54**, R9624 (1996), Erratum: Phys. Rev. B **58**, 2900 (1998).
- [122] K. Damle and S. Sachdev, Phys. Rev. B **57**, 8307 (1998).
- [123] V. Kotov, O. Sushkov, and R. Eder, Phys. Rev. B **59**, 6266 (1999).
- [124] C. Jurecka and W. Brenig, Phys. Rev. B **61**, 14307 (2000).
- [125] S. Trebst, H. Monien, C. J. Hamer, Z. Weihong, and R. R. P. Singh, Phys. Rev. Lett. **85**, 4373 (2000).
- [126] T. Nunner and T. Kopp, Phys. Rev. B **69**, 104419 (2004).
- [127] S. Kirschner, *Multi-Particle Spectral Densities*, Diploma Thesis, Universität zu Köln, 2004.
- [128] M. E. Zhitomirsky, cond-mat/0601405 (2006).
- [129] M. Karbach, G. Müller, A. H. Bougourzi, A. Fledderjohann, and K. H. Mütter, Phys. Rev. B **55**, 12510 (1997).
- [130] K. P. Schmidt and G. S. Uhrig, Phys. Rev. Lett. **90**, 227204 (2003).
- [131] J. des Cloizeaux and J. J. Pearson, Phys. Rev. B **128**, 2131 (1962).
- [132] L. D. Faddeev and L. A. Takhtajan, Phys. Lett. **85A**, 375 (1981).
- [133] J. D. Johnson, B. M. McKoy, and C. K. Lai, Phys. Lett. **38A**, 143 (1972).
- [134] J. D. Johnson, S. Krinsky, and B. M. McKoy, Phys. Rev. Lett. **29**, 492 (1972).

-
- [135] J. D. Johnson, S. Krinsky, and B. M. McKoy, Phys. Rev. **A8**, 2526 (1972).
- [136] H. Bethe, Z. Phys. **71**, 205 (1931).
- [137] L. Hulthen, Ark. Mat. Astron. Fys. A **26**, 11 (1938).
- [138] C. N. Yang and C. P. Yang, Phys. Rev. **150**, 321 and 327 (1966).
- [139] R. J. Baxter, *Exactly Solvable Models in Statistical Mechanics*, Academic Press, London, 1982.
- [140] J. des Cloizeaux and M. Gaudin, J. Math. Phys. **7**, 1384 (1996).
- [141] F. D. M. Haldane, Phys. Rev. B **25**, 4925 (1982).
- [142] A. B. Harris, Phys. Rev. B **7**, 3166 (1973).
- [143] W. Zheng, C. J. Hamer, and R. R. P. Singh, Phys. Rev. Lett. **91**, 037206 (2003).
- [144] C. J. Hamer, W. Zheng, and R. R. P. Singh, Phys. Rev. B **68**, 214408 (2003).
- [145] D. Jaksch, C. Bruder, J. I. Cirac, C. W. Gardiner, and P. Zoller, Phys. Rev. Lett. **98**, 3108 (1998).
- [146] B. Paredes et al., Nature **429**, 277 (2004).
- [147] T. Kinoshita, T. Wenger, and D. S. Weiss, Science **305**, 1125 (2004).
- [148] M. Köhl, H. Moritz, T. Stöferle, C. Schori, and T. Esslinger, J. Low Temp. Phys. **138**, 635 (2005).
- [149] P. Jordan and E. Wigner, Z. Phys. **47**, 42 (1928).
- [150] M. Girardeau, J. Math. Phys. **1**, 516 (1960).
- [151] L. Tonks, Phys. Rev. **50**, 955 (2002).
- [152] E. H. Lieb and W. Liniger, Phys. Rev. **130**, 1605 (1963).
- [153] M. P. A. Fisher, P. B. Weichman, G. Grinstein, and D. S. Fisher, Phys. Rev. B **40**, 546 (1989).
- [154] W. Krauth, M. Caffarel, and J.-P. Bouchaud, Phys. Rev. B **45**, 3137 (1992).
- [155] K. Sheshadri, H. R. Krishnamurthy, R. Pandit, and T. V. Ramakrishnan, Europhys. Lett. **22**, 257 (1993).
- [156] D. van Oosten, P. van der Straten, and H. T. C. Stoof, Phys. Rev. A **63**, 053601 (2005).
- [157] N. Elstner and H. Monien, Phys. Rev. B **59**, 12184 (1999).

- [158] W. Krauth, Phys. Rev. B **44**, 9772 (1991).
- [159] D. B. M. Dickerscheid, D. van Oosten, P. J. H. Denteneer, and H. T. C. Stoof, Phys. Rev. A **68**, 043623 (2003).
- [160] R. V. Pai, R. Pandit, H. R. Krishnamurthy, and S. Ramasesha, Phys. Rev. Lett. **76**, 2937 (1996).
- [161] V. A. Kashurnikov and B. V. Svistunov, Phys. Rev. B **53**, 11776 (1996).
- [162] T. D. Kühner and H. Monien, Phys. Rev. B **58**, R14741 (1998).
- [163] T. D. Kühner, S. R. White, and H. Monien, Phys. Rev. B **61**, 12474 (2000).
- [164] P. M. Chaikin and T. C. Lubensky, *Principles of condensed matter physics*, Cambridge University Press, Cambridge, 1995.
- [165] A. M. Rey, P. B. Blakie, G. Pupillo, C. J. Williams, and C. W. Clark, Phys. Rev. A **72**, 023407 (2005).
- [166] C. Tozzo, M. Kraemer, and F. Dalfovo, Phys. Rev. A **71**, 061602 (2005).
- [167] A. Iucci, M. A. Cazalilla, A. F. Ho, and T. Giamarchi, cond-mat/0508054 (2005).
- [168] D. van Oosten, D. B. M. Dickerscheid, B. Farid, P. van der Straten, and H. T. C. Stoof, Phys. Rev. A **71**, 021601(R) (2005).
- [169] G. G. Batrouni et al., Phys. Rev. Lett. **89**, 117203 (2002).
- [170] G. G. Batrouni, F. F. Assaad, R. T. Scalettar, and P. J. H. Denteneer, Phys Rev A **72**, 031601(R) (2005).
- [171] M. Troyer, H. Tsunetsugu, and D. Würtz, Phys. Rev. B **50**, 13515 (1994).
- [172] T. Stöferle, private communication (2005).
- [173] M. Girardeau, Phys. Rev. B **139**, 500 (1965).
- [174] V. I. Yukalov and M. D. Girardeau, Laser Phys. Lett. **2**, 375 (2005).
- [175] A. M. Rey, G. Pupillo, and J. V. Porto, Phys. Rev. A **73**, 023608 (2006).
- [176] S. Wessel et al., J. Phys. Soc. Jpn. Suppl. **74**, 10 (2005).
- [177] G. S. Uhrig and N. Lorscheid, private communication (2006).

Abstract

In this thesis the method of self-similar continuous unitary transformations (CUTs) in real space is developed. It is applied to various models from the field of strongly correlated solid state physics and optical lattices.

The CUT method maps a given Hamiltonian to an effective Hamiltonian which is in some respect simpler. In a self-similar CUT the truncation scheme relies on the structure of the operators. The real space approach put forward in this thesis truncates the operators according to their extension in real space. We mainly use a MKU generator to derive an effective model which is block-diagonal in the number of quasiparticles. We give a detailed description of the method. The transformation of the Hamiltonian and of the observables is explained. The implementation on a computer and the optimization of the programs are extensively discussed.

The first application of the method deals with the fermionic Hubbard model. We derive an effective Hamiltonian, a generalized t - J -model, which conserves the number of doubly occupied sites. The effective model includes beyond the well-known Heisenberg term also further two-spin and four-spin terms. In addition, the charge motion and interaction within the effective model is addressed. In the context of the Hubbard model we discuss the question if an effective model that conserves the number of double occupancies can be derived in principle.

The antiferromagnetic spin ladder and spin chain are treated from the viewpoint of a dimerized system. For the spin ladder we calculate the dispersion, the two-particle energies including bound states and the multi-particle continua. The discussion of multi-particle continua shows that the order of the energy levels is important for the convergence of the transformation. For the spin chain the dispersion is calculated. In addition, the transformation of an observable yields the corresponding spectral weights. The spectral weights are compared to results from a perturbative CUT.

For the bosonic Hubbard model we calculate the dispersion and determine the phase diagram. The spectral weight of a certain observable is calculated in order to explain the outcome of a recent experiment that measures the spectroscopic response of atoms confined in optical traps. The distribution of spectral weight is analyzed also at finite temperatures. We find evidence for a substantial temperature of the size of the microscopic parameters. This finding is supported by purely thermodynamic considerations.

Zusammenfassung

In der vorliegenden Arbeit wird die Methode der selbstähnlichen kontinuierlichen unitären Transformationen (CUT) im Ortsraum entwickelt. Sie wird auf verschiedene Modelle aus dem Gebiet der stark korrelierten Festkörpersysteme und der optischen Gitter angewendet.

Die Methode der CUT bildet einen gegebenen Hamiltonoperator auf einen einfacheren effektiven Hamiltonoperator ab. Eine selbstähnliche Realisierung der CUT verwendet ein Trunkierungsschema, das auf der Struktur der auftretenden Operatoren fußt. In dieser Arbeit wird ein MKU-Generator verwendet, um ein effektives Modell zu erhalten, das Block-diagonal in der Zahl der Quasiteilchen ist. Die Arbeit enthält eine detaillierte Beschreibung der Methode der selbstähnlichen CUT im Ortsraum, wobei die Transformation sowohl des Hamiltonoperators als auch der Observablen besprochen wird. Ein Schwerpunkt der Arbeit ist die Implementierung der Methode auf dem Computer und die Optimierung der Computerprogramme.

Die erste Anwendung der Methode stellt das fermionische Hubbard-Modell dar. Es wird ein effektiver Hamiltonoperator konstruiert, der die Zahl der Doppeltbesetzungen im System erhält. Dieser effektive Hamiltonoperator stellt ein verallgemeinertes t - J -Modell dar. Zusätzlich zum bekannten Heisenberg-Term enthält das effektive Modell auch Zwei-Spin-Kopplungen von weiter entfernten Plätzen und Vier-Spin-Terme. Außerdem werden Terme diskutiert, die die Bewegung und die Wechselwirkung von Ladungen beschreiben. Im Zusammenhang mit dem Hubbard-Modell wird die Frage der prinzipiellen Möglichkeit der Herleitbarkeit eines effektiven Modells diskutiert, das die Zahl der Doppeltbesetzungen erhält.

Eine weitere Anwendung sind eindimensionale Spinsysteme. Sie werden vom Standpunkt vollständig dimerisierter Systeme betrachtet. Für die Spinleiter werden die Dispersion, die Zweiteilchenenergien und Vielteilchenkontinua berechnet. Die Berechnung der Zweiteilchenenergien schließt die Analyse von gebundenen Zuständen mit ein. Die Diskussion der Vielteilchenkontinua zeigt, dass für die Konvergenz der Methode die Anordnung der Energiezustände mit verschiedenen Teilchenzahlen essentiell ist. Im Fall der Spinkette wird die Dispersion berechnet. Die spektralen Gewichte einer Observablen werden bestimmt und mit den entsprechenden Ergebnissen einer perturbativen CUT verglichen.

Schließlich wird im letzten Abschnitt das bosonische Hubbard-Modell behandelt. Die Dispersion der Quasiteilchen und das Phasendiagramm werden berechnet. Die Berechnung spektraler Gewichte ermöglicht die Erklärung eines aktuellen Experimentes an Atomen, die in einer optischen Falle gefangen sind. Die Verteilung des spektralen Gewichts auch bei endlicher Temperatur gibt Aufschluss darüber, welche Temperatur in dem experimentellen System realisiert ist. Die Temperatur ist von der Größenordnung der mikroskopischen Parameter des Modell-Hamiltonoperators. Diese Ergebnisse werden untermauert durch weitere rein thermodynamische Überlegungen.

Danksagung

An dieser Stelle möchte ich mich herzlich bei Herrn Professor Dr. G. S. Uhrig für die Übernahme und Betreuung dieser Doktorarbeit bedanken. Sein physikalisches Interesse und seine Gesprächsbereitschaft waren ein wichtiger Motor für den Erfolg der Arbeit.

Professor Dr. E. Müller-Hartmann danke ich für die durchgängige Unterstützung und für die Begutachtung dieser Arbeit. Ein weiterer Dank gilt Professor Dr. M. Braden für die Übernahme des Prüfungsvorsitzes.

Für das Korrekturlesen bedanke ich mich bei Dr. Carsten Aits, Alexander Gößling und meinem Bruder Andreas Reischl. Ein weiteres Dankeschön gilt den Mitgliedern der Arbeitsgruppe für die angenehme und hilfsbereite Atmosphäre. Für die Bereitstellung von experimentellen Daten danke ich Dr. Thilo Stöferle.

Dr. Sébastien Dusuel und Dr. Kai P. Schmidt danke ich für zahlreiche interessante Diskussionen. Dr. Kai P. Schmidt gilt ein zusätzlicher Dank für die Bereitstellung seiner Ergebnisse und die Zusammenarbeit beim letzten Projekt dieser Dissertation.

Meiner Familie danke ich für die Unterstützung während der gesamten Arbeit. Verena und Jakob insbesondere gilt der herzlichste Dank für die gemeinsame Zeit in Köln.

Erklärung

Ich versichere, dass ich die von mir vorgelegte Dissertation selbständig angefertigt, die benutzten Quellen und Hilfsmittel vollständig angegeben und die Stellen der Arbeit - einschließlich Tabellen, Karten und Abbildungen -, die anderen Werken im Wortlaut oder dem Sinn nach entnommen sind, in jedem Einzelfall als Entlehnung kenntlich gemacht habe; dass diese Dissertation noch keiner anderen Fakultät oder Universität zur Prüfung vorgelegen hat; dass sie - abgesehen von unten angegebenen Teilpublikationen - noch nicht veröffentlicht worden ist sowie, dass ich eine solche Veröffentlichung vor Abschluss des Promotionsverfahrens nicht vornehmen werde. Die Bestimmungen dieser Promotionsordnung sind mir bekannt. Die von mir vorgelegte Dissertation ist von Herrn Prof. Dr. Götz S. Uhrig betreut worden.

Köln, den 15. März 2006

Teilpublikationen

- A. Reischl, E. Müller-Hartmann, and G. S. Uhrig, Systematic mapping of the Hubbard model to the generalized t - J -model, Phys. Rev. B **70**, 245124 (2004), and: cond-mat/0401028.
- A. Reischl, K. P. Schmidt, and G. S. Uhrig, Temperature in one-dimensional bosonic Mott insulators, Phys. Rev. A **72**, 063609 (2005), and: cond-mat/0504724.
- K. P. Schmidt, A. Reischl, and G. S. Uhrig, Thermodynamics of Adiabatically Loaded Cold Bosons in the Mott Insulating Phase of One-Dimensional Optical Lattices, Eur. Phys. J. D **38**, 343 (2006), and: cond-mat/0510461.

Lebenslauf

Persönliche Daten

Name	Alexander Reischl
Geburtsdatum	6.8.1973
Geburtsort	Pforzheim
Familienstand	verheiratet, ein Kind
Staatsangehörigkeit	deutsch

Schulbildung

1980-1984	Grundschule Pforzheim
1984-1985	Kepler-Gymnasium, Pforzheim
1985-1993	Markgraf Ludwig Gymnasium, Baden-Baden
6/1993	Abschluss: Abitur

Zivildienst

7/1993-9/1994	Arbeiterwohlfahrt Baden-Baden
---------------	-------------------------------

Studium

10/1994-9/1995	Philosophie, Politik und VWL an der Universität Freiburg
10/1995-9/1997	Physik an der Universität Freiburg
10/1997-8/2001	Physik an der Universität zu Köln
8/2000	Beginn der Diplomarbeit bei Prof. Dr. E. Müller-Hartmann
7/2001	Abschluss: Diplom Physik
seit 10/2001	Anfertigung der vorliegenden Dissertation

Arbeitsverhältnisse

7/2000-7/2001	Studentische Hilfskraft am Institut für Theoretische Physik der Universität zu Köln
seit 10/2001	Wissenschaftlicher Mitarbeiter am Institut für Theoretische Physik der Universität zu Köln

